The Evolution of the Tully-Fisher Relation at Redshift $z \sim 1$

DISSERTATION
der Fakultät für Physik
an der Ludwig-Maximilians-Universität München

vorgelegt von
MARCO BARDEN
aus Koblenz

Januar, 2004

Erstgutachter:	Prof. Dr. Reinhard Genzel
Zweitgutachter:	Prof. Dr. Andreas Burkert

Tag der mündlichen Prüfung:	19.10.2004

Zusammenfassung

Seit langem ist die Tully-Fisher Relation, eine empirische Beziehung zwischen der Rotationsgeschwingigkeit und der absoluten Helligkeit von Scheibengalaxien, ein wichtiges Werkzeug der beobachtenden Kosmologie. Allerdings ist es bisher nicht gelungen eine schlüssige Erklärung für die Entwicklung von Scheibengalaxien bei hoher Rotverschiebung zu finden. In dieser Arbeit soll gezeigt werden wie die Vermessung von räumlich aufgelösten Rotationskurven bei der Ruhewellenlänge von Hα zur Klärung dieser Frage beitragen kann. Insbesondere soll hier eine Auswahl von 22 Scheibengalaxien vorgestellt werden, die im Mittel eine Rotverschiebung $z \sim 0,9$ aufweisen. Dies ist die bisher größte Entfernung von solchen Galaxien, für die die Messung von Rotationskurven erfolgreich war.

Ausgewählt wurden diese Objekte insbesondere aufgrund ihrer Größe, gemessen innerhalb der Isophoten bei einer scheinbaren Flächenhelligkeit von 25 mag pro Quadratbogensekunde. Diese Galaxien sind morphologisch vergleichbar mit der Milchstraße. Sie weisen die größten Skalenlängen auf, die bei Scheibengalaxien bekannt sind, sogar im Vergleich mit lokalen Objekten.

Allein aus dieser Tatsache können wir schließen, dass das erste Erscheinen von solch großen Scheibengalaxien weiter zurück liegen muss als acht Milliarden Jahre. Wir errechnen für diese Gruppe von Scheibengalaxien scheinbare zentrale Scheibenflächenhelligkeiten, die wesentlich größer sind (um 1,44 Magnituden) als eine lokale Vergleichsgruppe mit ähnlicher Ausdehnung. Dabei ist ihre absolute Helligkeit im Mittel allerdings nur wenig größer als die der lokalen Vergleichsgalaxien. Kombiniert man die Ergebnisse aus der Entwicklung in Helligkeit, Größe und zentraler Flächenhelligkeit, erkennt man, dass ein Szenario, in dem sich Galaxien "von innen nach außen" entwickeln, d.h. die Scheibenskalenlängen wachsen mit der Zeit, wahrscheinlicher ist als eine hypothetische selbst-ähnliche Entwicklung, bei der die Scheibenskalenlängen konstant bleiben und lediglich die zentrale Flächenhelligkeit mit der Zeit abnimmt.

Weiterhin sind die Rotationsgeschwindigkeiten der hoch rotverschobenen Galaxien systematisch niedriger als die der entsprechenden lokalen Objekte. Daraus ergibt sich eine im Mittel um einen Faktor zwei niedrigere Masse für die Galaxien im frühen Universum. Kombiniert man die beiden Resultate, niedrigere Masse bei gleichzeitig leicht größerer absoluter Helligkeit, ergibt sich eine Verschiebung der Tully-Fisher-Beziehung bei hoher Rotverschiebung zu größeren Absoluthelligkeiten von $\Delta_{TF} = 1,44$ mag im Vergleich zur lokalen Relation.

Darüber hinaus haben wir vergleichbare Daten aus der Literatur zusammen getragen um ein umfassenderes Bild von der Entwicklung dieser Verschiebung der Tully-Fisher Relation zu erhalten. Es scheint, dass sich die Tully-Fisher Beziehung systematisch mit der Zeit zu ihrer heutigen Position bewegt hat, gemäß der Gleichung: $\Delta_{TF} = -(0,19 \pm 0,19) - (1,40 \pm 0,32) \times z$. Dieses Ergebnis beruht auf der Annahme, dass die Steigung der Tully-Fisher Relation während der ganzen Zeit konstant geblieben ist. Sogar wenn man sämtliche Literaturdaten zusammen betrachtet, ist es nicht möglich die Steigung in den einzelnen Rotverschiebungsgruppen entscheidend einzugrenzen.

Im Vergleich mit semi-analytischen Modellen lässt sich keine Übereinstimmung mit dem hier beobachteten Trend einer sich verschiebenden Tully-Fisher Relation finden. Jedoch sagen die numerischen Modelle von Steinmetz und Navarro (1999), obwohl ihr Ordinatenabschnitt sowohl für lokale wie auch für ferne Galaxien nicht mit den Beobachtungen übereinstimmt, eine Verschiebung von derselben Größe voraus wie sie oben angegeben wurde. Aus diesen Simulationen wird auch ersichtlich, dass die Steigung der Tully-Fisher Relation mit der Zeit konstant bleibt.

Contents

1 Abstract **9**

2 Introduction **11**
2.1 The Formation and Evolution of Disc Galaxies 11
2.2 The Tully-Fisher Relation 12

3 The Data and Analysis **15**
3.1 Motivation 15
3.2 Sample Selection 16
3.2.1 The High Redshift Sample 16
3.2.2 The Local Comparison Sample 17
3.3 Observations 30
3.4 Data Reduction 31
3.4.1 ISAAC Spectroscopy 32
3.4.2 Ground-Based Imaging 34
3.4.3 HST Imaging 37
3.4.4 B-Band Images for Local Galaxies 37
3.5 Data Analysis 38
3.5.1 Distance Estimators 38
3.5.2 Surface Brightness Profile Fits 40
3.5.3 Inclinations 54
3.5.4 Rotation Speeds 56
3.5.5 Absolute Magnitudes and Colours 58
3.6 Truncation Effects 65
3.6.1 Surface Brightness Effects 65
3.6.2 Morphological Dependence of the Inclination 74
3.6.3 Morphological Dependence of the Disc Scale Length 76
3.6.4 Morphological Dependence of the Central Surface Brightness 79
3.6.5 Morphological Dependence of the Isophotal Radius 81
3.6.6 Morphological Dependence of the Absolute Magnitude 85
3.6.7 Resolution Effects 85
3.6.8 Summary of Surface Brightness and Resolution Effects 88

4 Results **89**
4.1 The Isophotal Radius R_{25} 89
4.2 The Disc Scale Length R_d 92
4.3 The Absolute Magnitude M_B^{rest} 92
4.4 The Central Surface Brightness μ_d^{rest} 97
4.5 Morphological Evolution 97
4.6 The Rotation Speed v_{rot} and Mass $M_{2.2}$ 108
4.7 The Tully-Fisher Relation 118
4.7.1 The Tully-Fisher Offset 118

    4.7.2 Phenomenological Explanation of the Tully-Fisher Relation 118
  4.8 Colours and Mass-to-Light-Ratios 122
  4.9 Dynamical Evolution 124

5 Discussion **135**
  5.1 Comparison with Observations 135
    5.1.1 The Vogt et al. Data 135
    5.1.2 The Ziegler et al. Data 139
    5.1.3 The Milvang-Jensen et al. Data 139
    5.1.4 Intercomparison and Redshift Evolution 142
  5.2 Comparison with Theory 149
    5.2.1 Evolution of the Disc Scale Length 149
    5.2.2 Evolution of the Absolute Magnitude 149
    5.2.3 Evolution of the Central Surface Brightness 149
    5.2.4 Evolution of the B-V Colour 153
    5.2.5 Evolution of the Tully-Fisher relation 153

6 Conclusions **161**

7 Acknowledgements **165**

Bibliography **167**

A Statistical Tests **173**

B Bulge-to-Disc Ratios **195**

C The Atlas **203**

List of Figures

3.1 Inclination angles i . . . 18
3.2 Apparent sizes of high redshift galaxies. . . . 19
3.3 Terminal and peak velocities . . . 22
3.4 Comparison of the RC3 with the local sample: R_{25} . . . 27
3.5 Comparison of the RC3 with the local sample: M_B . . . 28
3.6 Comparison of the RC3 with the local sample: v_{rot} . . . 29
3.7 Extraction of a rotation curve . . . 35
3.8 Seeing Comparison . . . 36
3.9 Tully-Fisher relation of the local sample . . . 39
3.10 Histogram of the photgraphic plate scale parameter β . . . 42
3.11 Ratio of the extent of DSS and CCD profiles . . . 43
3.12 Splicing of CCD and DSS profiles . . . 44
3.13 Difference of the limiting surface brightnesses of the DSS and CCD profiles . . . 45
3.14 Impact of limiting surface brightness on fitting parameters . . . 47
3.15 R_{lim} versus R_{25} . . . 48
3.16 Histograms of R_{lim} . . . 49
3.17 Limiting surface brightnesses μ_{lim} . . . 50
3.18 Disc scale lengths as a function of wavelength . . . 52
3.19 Apparent versus isophotal sizes of the high redshift galaxies. . . . 53
3.20 The effect of profile truncation on inclination . . . 55
3.21 The Tully fisher relation and the impact of seeing . . . 57
3.22 Radial compared to optical extent of the high-z rotation curves . . . 59
3.23 Radial extent compared to expected peak of rotation of the high-z rotation curves 60
3.24 Intrinsic consistency of the data quality of the high-z rotation curves . . . 61
3.25 SEDs of the high redshift sample . . . 64
3.26 Estimation of extinction coefficients . . . 66
3.27 Relative B to V extinction . . . 67
3.28 B-V colour versus $R_d^{z=0}$ . . . 68
3.29 B-V colour versus $M_{B_T}^{i,z=0}$ . . . 69
3.30 B-V colour versus v_{rot} . . . 70
3.31 Ratio of R_{max} over R_{lim} for the local sample . . . 71
3.32 R_{max} of local and distant galaxies . . . 72
3.33 Light profile of NGC4178 . . . 73
3.34 Δi as a function of i . . . 75
3.35 The effect of profile truncation on disc scale length . . . 77
3.36 ΔR_d as a function of R_d . . . 78
3.37 The effect of profile truncation on central surface brightness . . . 80
3.38 $\Delta \mu_d$ as a function of μ_d . . . 82
3.39 The effect of profile truncation on the isophotal radius . . . 83
3.40 ΔR_{25} as a function of R_{25} . . . 84
3.41 The effect of profile truncation on the absolute magnitude . . . 86
3.42 ΔM_B as a function of M_B . . . 87

4.1 Histograms of the isophotal radii . . . 90
4.2 Histograms of the isophotal radii after matching the samples . . . 91
4.3 Histograms of the disc scale lengths . . . 93
4.4 R_d as a function of R_{25} . . . 94
4.5 Histograms of the disc scale lenghts after matching the samples . . . 95
4.6 Histograms of the absolute magnitudes . . . 96
4.7 M_B^{rest} as a function of R_{25} . . . 98
4.8 Histograms of the absolute magnitudes after matching the samples . . . 99
4.9 Histograms of the central surface brightnesses . . . 100
4.10 μ_d^{rest} as a function of R_{25} . . . 101
4.11 Histograms of the central surface brightnesses after matching the samples . . . 102
4.12 Histograms of the matched disc scale lengths . . . 104
4.13 Histograms of the isophotal sizes after matching R_d . . . 105
4.14 Histograms of the absolute magnitudes after matching R_d . . . 106
4.15 Histograms of the central surface brightnesses after matching R_d . . . 107
4.16 Histograms of the rotation speeds . . . 109
4.17 v_{rot} as a function of R_{25} . . . 110
4.18 Histograms of the rotation speeds after matching the samples . . . 112
4.19 Histograms of the rotation speeds after matching R_d . . . 113
4.20 Histograms of the disc mass within 2.2 disc scale radii . . . 114
4.21 $M_{2.2}$ as a function of R_{25} . . . 115
4.22 Histograms of the enclosed mass after matching the samples . . . 116
4.23 Histograms of the enclosed mass after matching R_d . . . 117
4.24 The Tully-Fisher relation . . . 119
4.25 The offset from the Tully-Fisher relation . . . 120
4.26 The Tully-Fisher relation and the impact of profile truncation . . . 121
4.27 Histograms of the B-V colours . . . 123
4.28 Histograms of stellar mass-to-light ratio . . . 125
4.29 Histograms of stellar mass-to-light ratio . . . 126
4.30 Histograms of dynamical mass-to-light ratio . . . 127
4.31 Histograms of the mass ratios ρ . . . 128
4.32 R_d as a function of v_{rot} . . . 130
4.33 Histograms of the specific angular momenta . . . 131
4.34 Histograms of j_d after matching the samples . . . 132
4.35 j_d as a function of R_{25} . . . 133

5.1 Tully-Fisher relation for Vogt et al. (1993; 1996; 1997) . . . 136
5.2 Tully-Fisher relation for Vogt (1999, 2000, 2001a,b) . . . 137
5.3 Tully-Fisher relation for Vogt (1999, 2000, 2001a,b) . . . 138
5.4 Tully-Fisher relation for Ziegler et al. (2002) . . . 140
5.5 R_d versus v_{rot} for the Ziegler et al. (2002) data . . . 141
5.6 Tully-Fisher relation for Milvang-Jensen (2003) . . . 143
5.7 R_d as a function of redshift . . . 144
5.8 M_B as a function of redshift . . . 145
5.9 v_{rot} as a function of redshift . . . 147
5.10 The Tully-Fisher offset as a function of redshift . . . 148
5.11 Evolution of the disc scale length . . . 150
5.12 Evolution of the absolute magnitude . . . 151
5.13 Evolution of the central surface brightness . . . 152
5.14 Evolution of the B-V colour . . . 154
5.15 Evolution of the Tully-Fisher relation . . . 155
5.16 The size-rotation velocity relation . . . 156
5.17 The magnitude-size relation . . . 158
5.18 The Tully-Fisher relation for the Steinmetz and Navarro (1999) data . . . 159

6.1 Mass as a function of disc scale length 163

A.1 Random Gaussian distribution of variable x 174
A.2 Sum of 1000 random Gaussian distributions of variable x 175
A.3 Random variable y versus x 177
A.4 Sum of 10 random distributions of variable y versus x 178
A.5 Random Gaussian distribution of variable y 179
A.6 Sum of 1000 random Gaussian distributions of variable y 180
A.7 T-test probability distribution of L_x and H_x 181
A.8 RS-test probability distribution of L_x and H_x 182
A.9 FV-test probability distribution of L_x and H_x 183
A.10 KS-test probability distribution of L_x and H_x 184
A.11 T-test probability distribution of L_y and H_y 185
A.12 RS-test probability distribution of L_y and H_y 186
A.13 FV-test probability distribution of L_y and H_y 187
A.14 KS-test probability distribution of L_y and H_y 188
A.15 T-test probability distribution of the “reduced” L_y and H_y 190
A.16 RS-test probability distribution of the “reduced” L_y and H_y 191
A.17 FV-test probability distribution of the “reduced” L_y and H_y 192
A.18 KS-test probability distribution of the “reduced” L_y and H_y 193

B.1 R_{25} as a function of B/T 196
B.2 R_d as a function of B/T 197
B.3 μ_d as a function of B/T 198
B.4 M_B as a function of B/T 199
B.5 B-V as a function of B/T 200
B.6 v_{rot} as a function of B/T 201
B.7 $M_{2.2}$ as a function of B/T 202

C.1 Calibration for local galaxies 204
C.1 Calibration for local galaxies 205
C.1 Calibration for local galaxies 206
C.1 Calibration for local galaxies 207
C.1 Calibration for local galaxies 208
C.1 Calibration for local galaxies 209
C.1 Calibration for local galaxies 210
C.1 Calibration for local galaxies 211
C.1 Calibration for local galaxies 212
C.1 Calibration for local galaxies 213
C.1 Calibration for local galaxies 214
C.2 Calibration for distant galaxies 215
C.2 Calibration for distant galaxies 216
C.3 Light profiles of nearby galaxies 217
C.3 Light profiles of nearby galaxies 218
C.3 Light profiles of nearby galaxies 219
C.3 Light profiles of nearby galaxies 220
C.3 Light profiles of nearby galaxies 221
C.3 Light profiles of nearby galaxies 222
C.3 Light profiles of nearby galaxies 223
C.3 Light profiles of nearby galaxies 224
C.3 Light profiles of nearby galaxies 225
C.3 Light profiles of nearby galaxies 226
C.3 Light profiles of nearby galaxies 227
C.4 Light profiles of distant galaxies 228

C.4 Light profiles of distant galaxies . . . 229
C.5 Rotation curves of the high redshift galaxies . . . 230
C.5 Light profiles of distant galaxies . . . 231
C.6 Spectrum of CFRS-00.0137 . . . 232

List of Tables

3.1 The High Redshift Sample - Basic Data 20
3.2 The Local Sample - Basic Data 23
3.2 *Continued* 24
3.2 *Continued* 25
3.2 *Continued* 26
3.3 The Observations 31
3.4 Inclination corrections for high-z targets with ground-based images 56
3.5 Spectral Classification of the High Redshift Sample 63
3.6 Morphological Dependence of Inclination 74
3.7 Morphological Dependence of Disc Scale Length 79
3.8 Morphological Dependence of Central Surface Brightness 81
3.9 Morphological Dependence of Isophotal Radius 85
3.10 Morphological Dependence of Absolute Magnitude 88

5.1 MS1054-03 1403 142

A.1 Random Distributions 176

Chapter 1

Abstract

The power of the Tully-Fisher relation as a tool of observational cosmology has long been acknowledged. However, all attempts of unravelling the evolution of disc galaxies at high redshift have proven inconclusive. We demonstrate how rotation curves measured at the rest-wavelength of Hα can successfully shed some light unto the topic. Our sample of 21 galaxies at a mean redshift of $z = 0.9$, the most distant sample so far, consists of mainly large isophotally selected late disc galaxies comparable to the Milky Way. These are amongst the largest in terms of disc scale lengths even compared to local galaxies. From this we conclude that the appearance of large disc galaxies must lie further back than $\sim$ 8Gyr. We find that these galaxies have much higher surface brightnesses (1.44mag) than a local set of galaxies with similar sizes. Their absolute magnitudes are only slightly brighter, though. Furthermore, combining the evolution in magnitude, size and surface brightness, we find that a scenario where galaxies grow inside-out is more consistent with the data than self-similar evolution. Moreover, the rotation velocities of the distant sample are systematically lower than the local sample, resulting in a lower average mass by a factor of 2. The combination of those two effects results in an offset from the local Tully-Fisher relation of $\Delta_{TF} = -1.44$mag towards brighter magnitudes. Compared to similar data in the literature we find a consistent picture for the evolution of the Tully-Fisher relation with redshift: $\Delta_{TF} = -(0.19 \pm 0.19) - (1.40 \pm 0.32) \cdot z$. Total source numbers in the individual redshift bins are too small even taking all the available data together to meaningfully constrain the slope of the Tully-Fisher relation at high redshifts. The observed offset from the TullyFisher relation is in good agreement with the offset derived from numerical simulations by Steinmetz and Navarro (1999) at a redshift $z \sim 1$.

Chapter 2

Introduction

2.1 The Formation and Evolution of Disc Galaxies

In recent years a lot of progress has been made in understanding the formation and evolution of galaxies. In the emerging standard picture of galaxy and structure formation very weak initial density perturbations of dark matter are sufficient to determine the evolution of the primordial gas into the clusters and galaxies we see today. Such Gaussian density fluctuations were generated during inflation and gravitational instabilities magnified them leading to the formation of dark matter haloes with a certain mass spectrum. Structure is built up hierarchically in the sense that small objects, like galactic haloes, formed first and as time evolves gravitational forces lead to the assembly of larger and larger structures, including galaxy clusters and super-clusters. Therefore, with time small haloes merge to bigger entities and the galaxies we see today are the merging products of several smaller progenitors.

The spectrum of initial halo masses is understood on one hand in linear terms as a part of the Press-Schechter formalism (Press and Schechter, 1974; Bond et al., 1991; Bower, 1991; Lacey and Cole, 1993). On the other hand N-body simulations were very successful in describing the merging of dark haloes and the construction of large merger trees. Both methods agree remarkably well. The dark matter haloes were initially modelled as isothermal spheres, but more detailed N-body studies found that this was a rather poor approach (Frenk et al., 1988; Efstathiou et al., 1988; Dubinski and Carlberg, 1991) and today the density profile by Navarro, Frenk and White, the NFW-profile, is widely used as a better approximation, although it still may not be the complete solution (Navarro et al., 1995, 1996, 1997).

The haloes are mostly made up of “dark” matter with a fraction of 5-10% of normal baryonic material. Once the dark matter halo has virialised, the gas inside starts to collapse dissipatively and forms galaxies. White and Rees (1978) have modelled this process and derived a luminosity function for galaxies in good agreement with observations. Since this collapse is a smooth process, properties of the haloes and the discs are related (Fall and Efstathiou, 1980; Faber, 1982). Before collapse, the halo is filled with shock-heated gas at the virial temperature. As the gas cools down it radiates its binding energy, but retains its angular momentum (Fall, 1983). Finally it settles into a rotationally supported flat star forming disc with an exponential light profile and a flat rotation curve (Dalcanton et al., 1997; Mo et al., 1998). During this process of gas falling into the centre, forming the disc, the halo responds adiabatically and contracts in the regions surrounding the disc.

When a critical gas density threshold is reached star formation ignites. The first high mass stars formed in the disc will impact on their surrounding by enriching the interstellar medium and even the hot halo gas with metals, which then will affect the gas cooling rates and the subsequent infall of more gas. Furthermore, the injected kinetic energy will regulate star formation by inhibiting further infall into the respective star forming region. It is this interplay between stability of the interstellar medium and porosity, which regulates star formation in a disc (Silk, 1997). The ejected metals will also influence the properties of the next generation of stars that are formed.

As time progresses the disc grows not only by accreting gas from the immediate surroundings, but also from neighbouring dwarf galaxies. Those neighbours live in the same halo as the central galaxy and the whole ensemble of objects inside the halo live on different orbits circling the centre of mass of the halo. As a result of dynamical friction several individual galaxies will spiral down to the centre and merge with the most massive member. Any discs involved in such merging events will only survive if the mass ratio of the merger is high (e.g. 1:10). The small partner in such a collision gets destroyed and swallowed by the primary object and may settle in the centre of that galaxy forming a bulge (Abadi et al., 2003). If the mass ratio gets too large (>1:3) no disc will survive the event and the resulting object will most probably resemble an elliptical galaxy (Kormendy, 1989; Bender et al., 1992; Naab et al., 1999).

Theorists have developed basically two different techniques to model the evolution of galaxies in detail. On one hand there are extensive numerical simulations. Those are usually based on numerical N-body integrators in combination with smoothed particle hydrodynamics (SPH) codes that include the effects of gravity, gas dynamics, radiative cooling and heating processes (Steinmetz and Navarro, 1999). Star formation is included making phenomenological assumptions (Navarro and White, 1993; Steinmetz and Mueller, 1994). The advantage of such codes is the direct treatment of the physical equations concerning gravity and gas cooling without having to appeal to assumptions or simplistic scaling relations. However, this comes at great computational cost and as a result of this detailed simulations are either very limited in volume or have only a very coarse spatial and/or temporal resolution. Furthermore, star formation and feedback, i.e. the (self-) regulation of the star formation rate resulting from the injection of supernova energy into the interstellar medium, still rely on recipes with simplified assumptions. Examples for such codes can be found in e.g. Evrard et al. (1994); Navarro and White (1994); Steinmetz and Mueller (1994); Tissera et al. (1997); Domínguez-Tenreiro et al. (1998); Steinmetz and Navarro (1999); Elizondo et al. (1999); Abadi et al. (2003). On the other hand detailed semi-analytical models have been developed. They contain simplified prescriptions for the various processes that are acting during the formation of a galaxy like the formation and evolution of dark matter haloes, the gas cooling inside the haloes, the infall of the gas forming a disc and the subsequent evolution of the disc, star formation and feedback, the impact of metallicity effects, mergers of galaxies and spheroid formation, galaxy properties like luminosities and colours. The advantage of semi-analytical models is that they can be performed at almost any resolution and that they are highly flexible. However, the latter point may also be interpreted as a disadvantage, though, since the freedom in input parameters may soften conclusions drawn from the models. Therefore, they rely heavily on observations to calibrate them. Furthermore, they cannot treat the gas cooling in a self-consistent hydrodynamical sense, but have to make again simplifying assumptions. Examples for such models can be found in Kauffmann et al. (1993, 1994, 1997); Kauffmann (1995a,b); Mo et al. (1998, 1999); Mao et al. (1998); Cole et al. (1994, 2000); Heyl et al. (1995); Baugh et al. (1996b,a, 1998); Guiderdoni et al. (1998); Somerville and Primack (1999); van den Bosch (2000, 2002); van den Bosch et al. (2002), and references therein. Encouragingly, comparisons of the two techniques, semi-analytical modelling and numerical simulations, show general agreement Pearce et al. (1999); Benson et al. (2001); Helly et al. (2003).

2.2 The Tully-Fisher Relation

Tully and Fisher (1977) found a very remarkable relation between the total luminosity and rotation speed of disc galaxies. This Tully-Fisher relation is one of the cornerstones of the measurement of the cosmological distance scale and hence is a very useful tool in investigating large-scale dynamics and in the determination of the Hubble constant. However, the Tully-Fisher relation is purely an empirical relationship and has not yet received a comprehensive physical explanation. Its universal validity across a wide range of spiral masses must have fundamental implications for the relationship between the mass of the galaxy, its star-formation history, specific angular momentum and dark matter content and distribution. Both slope and zeropoint have to be explained by the standard picture introduced above. It is therefore an important tool for constraining models of disc formation (van den Bosch, 2000).

Broadly speaking, there are basically two competing models to explain the Tully-Fisher relationship. The first of these is that the Tully-Fisher relation is a consequence of self-regulated star formation in discs with different masses (e.g. Silk, 1997; Heavens and Jimenez, 1999), i.e. the competition of disc instability (which promotes star formation) with porosity (which inhibits star-formation) regulates the star formation. The model is not the complete answer, however, since it does not explain things like the mass-to-light ratios or the scale-lengths of the discs. In the second broad category of models the Tully-Fisher relation is a direct consequence of the cosmological equivalence between mass and circular velocity (e.g. Mo et al., 1998; Steinmetz and Navarro, 1999). This formalism is part of what has become the standard model for the growth of structure - the hierarchical merging model in which the gravitational effects of dark matter drive the evolution of galaxies and large-scale structure (e.g. Kauffmann et al., 1993). Models of this type have the advantage of providing testable predictions about the sizes, surface densities, and rotation curves of galaxies as a function of redshift. However, as emphasised by Steinmetz and Navarro (1999), although the Tully-Fisher relation can naturally be explained by hierarchical merging models, the normalisation and evolution of the Tully-Fisher relation depend strongly on the prescription used for the star-formation and on the cosmological parameters.

The existence of a relation between luminosity and velocity was predicted from simulations very early on by Fall and Efstathiou (1980); Faber (1982). It was found to hold over a wide range of wavelengths. With increasing wavelength its intrinsic scatter decreases since extinction gets lower and the slope of the relation gets steeper (Aaronson et al., 1979; Visvanathan, 1981; Tully et al., 1982; Pierce and Tully, 1988; Gavazzi, 1993; Verheijen, 1997; Strauss and Willick, 1995; Willick et al., 1997). However, moving to rest-frame near-infrared wavelengths does not improve the scatter further, since especially in the K-band the sky gets very unstable (sky brightness changes on time-scales of minutes) and magnitudes get affected more by stellar population effects than in the optical I-band (Regan and Vogel, 1994; Courteau, 1997; Rhoads, 1998). In fact, r and I-band Tully-Fisher relations have yielded similar (or even lower) scatters as the near-infrared calibrations (Willick, 1991; Han, 1991; Courteau, 1992; Mathewson et al., 1992; Pierce and Tully, 1992; Peletier and Willner, 1993; Schommer et al., 1993; Bernstein et al., 1994; Raychaudhury et al., 1997; Giovanelli et al., 1997). It was also looked into whether the Tully-Fisher scatter was a function of a “third parameter” like surface brightness, bulge-to-disc ratio, rotation curve shape, colour or morphological type. No such parameter was found, though (Strauss and Willick, 1995; Courteau, 1997). Furthermore, the slope of the Tully-Fisher relation depends on the estimator used for the measurement of the rotation velocity (Verheijen, 1997; Willick et al., 1997; Courteau and Rix, 1999). And even worse, evolution and environmental effects were also suggested to affect its shape (Courteau, 1997). Although progress has been made in modelling the Tully-Fisher relation semi-analytical models still fail to predict simultaneously the galaxy luminosity function and the zeropoint and slope of the Tully-Fisher relation. Semi-analytical models are either calibrated to match the luminosity function or the Tully-Fisher relation, but could not get both right, so far. Furthermore, numerical models suffer from the so-called angular momentum problem and in connection to that fail to reproduce the observed TullyFisher relation. In those codes, the material that settles onto a disc looses to much angular momentum and as a result of that the model galaxies fall off the relations observed in local galaxies (e.g. Sommer-Larsen et al., 1999; Elizondo et al., 1999; Steinmetz and Navarro, 1999).

Chapter 3

The Data and Analysis

There have been many different approaches to address the issue of quantifying the evolution of spiral galaxies. Various authors appealed to large redshift surveys to study the change of the star formation rate, luminosity functions or surface brightnesses with time. Others invoked smaller samples of disc galaxies to measure the evolution of the dynamical properties with redshift. Neither of these attempts could so far provide a coherent picture of both morphological and dynamical evolution of spirals. The purpose of this work is to combine different morphological indicators such as structural parameters with dynamical information from spectroscopic observations for two different sets of galaxies.

3.1 Motivation

As the tracer of the rotation of galaxies a variety of spectroscopic features exists. One might use spatially resolved velocity information from neutral hydrogen or carbon monoxide in the radio and millimetre wavelength regimes or stellar absorption features or nebular emission lines in the optical and near-infrared. With the advent of the 8m-class telescopes redshifts as high as $z \approx 1-3$ are now accessible for rotation curve studies. However, most of the indicators mentioned are well out of reach for the observer at these distances (with few exceptions like e.g. luminous galaxies at z>3 obtained from CO interferometry). The only promising candidates that remain are the strongest nebular emission lines like [OII], [OIII] or Balmer emission lines like Hα or Hβ.

With currently available optical multi-object spectrographs it has become an easy task to observe large numbers of objects simultaneously and to derive rotation speeds from the resulting spectra. However, with increasing distance the diagnostic lines get shifted to longer and longer wavelengths. This imposes a considerable challenge to the observer especially in the I-band where the night sky lines get strong enough to interfere with the detection of the target galaxies as the sensitivity of the detectors diminishes. As a result, observation of Hα, the strongest diagnostic, becomes almost impossible at redshifts $z \gtrsim 0.3$ in the optical. Attempting higher redshifts from the optical necessitates the use of "bluer" spectroscopic features. However, with [OII] a natural limit is reached, which pushes optical rotation curve observations out to $z \approx 1.2$ corresponding to an age of the universe of ~ 5 Gyrs.

This does not imply an end to the distance ladder, though. Although near-infrared spectrographs cannot compete with optical instruments in object numbers, the general-purpose long-slit mode, where one target is observed at a time, has become quite comparable in sensitivity, being mostly limited by the sky brightness and not the detector. Another factor that helps detecting fainter spectroscopic lines is the seeing, which changes with wavelength $\propto \lambda^{-1/5}$ or even faster. As a result of this under the same atmospheric conditions a spectroscopic line will be more concentrated and therefore have a higher peak flux at longer wavelengths. This factor becomes critical when high redshift rotation curves are to be observed. Since at redshifts of $z \approx 1$ a Milky-Way sized galaxy only has a visible diameter of ≈ 2 arcsec on the sky resolving a rotation curve is only possible for relatively large objects under good seeing conditions. In fact, the different seeing FWHM may be the crucial factor not only of resolving, but also detecting the target.

At a redshift $z \gtrsim 0.6$ Hα gets shifted into the from the ground well accessible J-band. Using the near-infrared to observe Hα a whole new range opens up for dynamical studies of disc galaxies. A theoretical limit is reached only at a redshift $z \approx 2.4$ when the universe was only ~ 3 Gyrs old. A disadvantage of the near-infrared instruments is the limited wavelength coverage, though. In the optical the usable range extends usually over several thousand Ångstroems while in the near-infrared at the same resolution only a few hundred are available (with current detectors). This is a direct result of the size of the detectors used. Optical detectors typically have 4-32 times more pixels. Therefore, the observer cannot stare blindly at a target anymore hoping that it has the proper distance, but he has to know its precise redshift beforehand.

In principle observing in the near-infrared allows pushing the measurement of resolved rotation curves to higher redshifts. The requirement of an a priori knowledge of redshifts with the limited spectral range of currently available detectors puts some severe constraints on the limit $z \approx 2.4$, though. Since photometric redshifts usually are not accurate enough one is bound to redshift surveys, which for obvious reasons (multi-object capability) are done in the optical regime again. Unfortunately, this limits the maximum reachable distance to $z \approx 1.2$. Beyond this redshift indicators become scarce and fewer and fewer galaxies are identified.

Despite these difficulties and compromises we have started a large programme to obtain rotation curves of galaxies beyond $z \gtrsim 0.6$. We have collected a sample of disc galaxies, i.e. objects with exponential light profiles, with known spectroscopic redshifts and accessible HST images. For this high redshift sample ($\langle z \rangle \approx 0.9$) we have obtained resolved near-infrared Hα long-slit spectra from which we extracted rotation curves. To enable a proper comparison of those data we also constructed a local comparison sample. For those galaxies we collected imaging data and resolved spectra. Since the nearby imaging data are much deeper than what one can obtain for distant galaxies, we artificially degraded the extracted light profiles to match the quality of the high redshift sample. This allows us to directly estimate the differences one would measure assuming that we had really deep data for the distant galaxies as well. Therefore, we have direct means at hand to evaluate the impact of surface brightness dimming with redshift. We will characterise the morphological and dynamical properties of the high redshift and a matched local comparison sample in the following chapters.

3.2 Sample Selection

In order to study the evolution of the Tully-Fisher relation the first ingredients one needs are two fairly matched samples at low and high redshift that are then compared with each other. To this end we have selected a sample of galaxies at high redshift suited for measuring rotation curves by means of longslit spectroscopy at the redshifted wavelength of Hα. The second sample consists of a set of local galaxies, for which rotation velocities from resolved rotation curves are already available in the literature.

3.2.1 The High Redshift Sample

As described in Sec. 3.1 we have begun a programme of medium resolution long-slit spectroscopy of the Hα-line in spiral galaxies at redshifts $z \gtrsim 0.6$ to obtain rotation curves. Because of the stringent constraint that the target's distance has to be known relatively precisely we consequently only selected objects with known spectroscopic redshifts. All targets were drawn from the CFRS / LDSS redshift surveys, the clusters MS1054, AC103 and the Hawaii deep field SSA22 (Lilly et al., 1995; Glazebrook et al., 1995; van Dokkum, 1999; Couch et al., 1998; Cowie et al., 1996, respectively, and references therein).

To obtain the rotation speed of a galaxy the velocity difference obtained from the rotation curve has to be corrected for inclination effects. For very low inclinations these corrections can amount to more than a factor of two. Therefore, it becomes important to obtain precise estimates for the inclinations. However, with object sizes of only a few arcseconds the seeing from ground-based observations becomes a limiting factor for the calculation of inclinations. The regions from which we selected our targets were all imaged by Wide Field Planetary Camera 2 (WFPC2) on-board HST. Only four galaxies in our sample have their morphologies derived solely from ground-based ISAAC/VLT imaging. All target galaxies were required to have inclination angles $i > 30°$. The mean of our sample galaxies is $\langle i \rangle \approx 60°$ (see Fig. 3.1).

Another requirement for studying rotation curves successfully is that the objects are spatially resolved in our longslit data. One cannot hope to measure the flat part of the rotation curve, which defines the true rotation speed of the object properly in cases where the galaxy is smaller than the size of the seeing disc. As a result of this we required our target galaxies to have apparent limiting radii $R_{lim}^{app} \gtrsim 1$" (the radius out to which the profile could be traced; see Fig. 3.2). To test the effect of the seeing on the rotation curve we also attempted three objects with apparent limiting radii $R_{lim}^{app} < 1$"

Moreover, encounters between galaxies or merging of galaxies will impact on the rotation curves of the involved objects (Barton et al., 1999). Depending on the relative masses of the participating sources the outcome of such events will differ a lot (e.g. Barnes and Hernquist, 1992; Barnes, 1992; Barnes and Hernquist, 1996). In cases where the mass ratio between the two galaxies is high, the smaller galaxy might either get destroyed completely in the gravitational field of the larger partner or be swallowed. However, for equal mass galaxies the outcome of merging should resemble an elliptical galaxy rather than a spiral and might result in destruction of both discs. Especially in the latter case the corresponding rotation curves are severely affected, while in the first case at least the rotation curve of the secondary should experience some amount of distortion. Although Barton et al. (2001) have shown that the rotation curves of interacting systems in the local universe basically follow the same Tully-Fisher relation as normal galaxies (with very few exceptions, about $\lesssim 10\%$ of their sample), we aimed at selecting mostly normal non-interacting galaxies for our study.

Finally, we required the sample galaxies to exhibit exponential functions over major parts of their surface brightness profiles (as measured from profile fits to HST I-band[1] or VLT J-band images). As a result of this most of our high redshift targets do not have big bulges. Since massive bulges could interfere with the measurement of disc rotation curves or the derivation of morphological quantities we convinced ourselves that the properties of local galaxies even after degrading the data to match the high redshift data quality do not change as a function of bulge mass, i.e. the ratio of bulge to total luminosity (see Appendix B). There is just one other restriction imposed indirectly on our sample: the magnitude limit intrinsic to the photometric surveys used to select our targets. This, however, does not bias the sample in any way since our requirement of selecting big objects correlates with bright magnitudes (see Fig. 4.7). Thus, all our selection criteria put together result in the cleanest, most well defined sample to date.

Besides the targets we drew from the aforemetioned sources we were able to include one target from the VLT science archive[2] (observations by White et al. 1999). This object also had WFPC2/HST images available and the rotation curve was taken in the same observational configuration as our galaxies. Basic parameters for our high redhisft sample are listed in Tab. 3.1.

3.2.2 The Local Comparison Sample

The ability to interpret the results obtained from the high redshift galaxies depends heavily on the proper definition of the local comparison sample. Therefore, we tried to find objects in the literature with the same amount of information as for our high redshift galaxies. This includes images and spatially resolved rotation curves. At the mean redshift of our high redshift sample the I-band HST images sample roughly the rest-frame B-band. Hence, we searched the literature for objects with accessible CCD B-band images (obtained from the NASA Extragalactic Database,

---

[1] Based on observations made with the NASA/ESA Hubble Space Telescope, obtained from the data archive at the Space Telescope Science Institute (STScI). STScI is operated by the association of Universities for Research in Astronomy, Inc. under the NASA contract NAS 5-26555.

[2] Based on observations made with ESO Telescopes at the La Silla or Paranal Observatories under programme ID 63.O-0372.

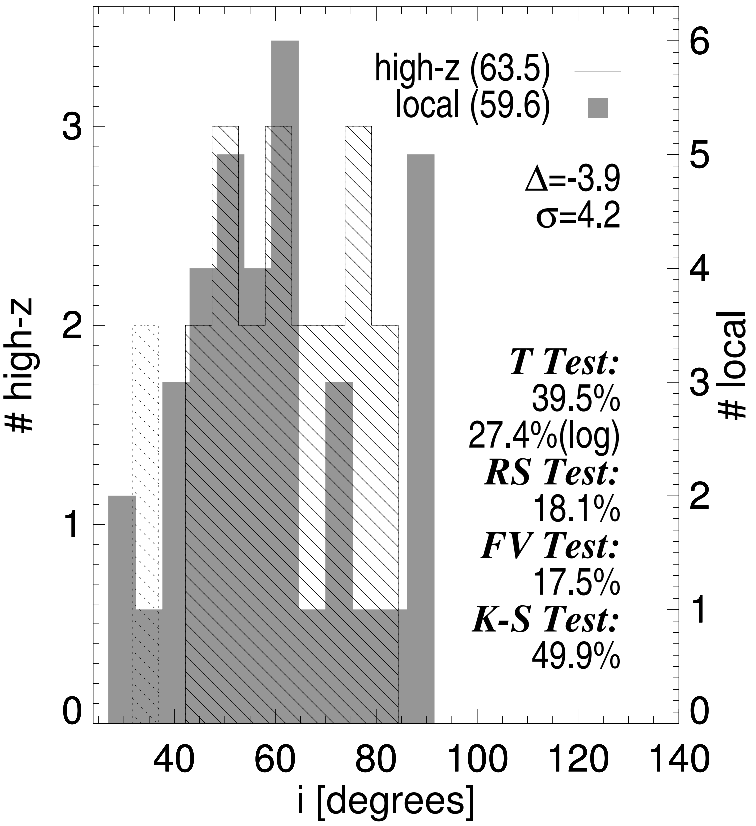

Figure 3.1: Inclination angles i

Histograms of the inclinations of the low (shaded region) and high redshift (striped region) samples. The means for both distributions are indicated in brackets in the upper right corner. The difference of the two means Δ and its 1σ error is shown above a set of statistical tests (lower right), including a student's T-test (on a linear and a logarithmic scale), a rank-sum test, a variance test and a Kolmogorov-Smirnov test, respectively. The dotted high redshift galaxies were excluded from the statistical analysis for not fitting the R_{25} selection criterion (see Sec. 3.2).

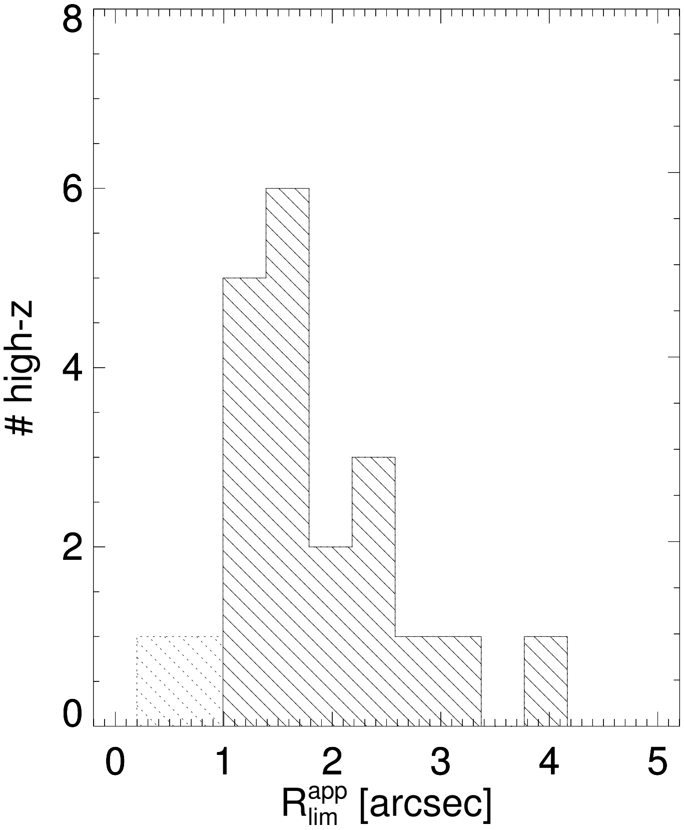

Figure 3.2: Apparent sizes of high redshift galaxies.

The solid area represents a sample of distant galaxies with the same distribution of isophotal radii as the local galaxy population. The dotted regions were excluded from the statistical analysis. The selection criterion imposed on this sample was to have sizes larger than ∼ 1 arcesc.

Table 3.1: The High Redshift Sample - Basic Data

ID (1)	z (2)	R$_{25}$ kpc (3)	R$_d$ kpc (4)	i deg (5)	A$_B^i$ mag (6)	A$_B^g$ mag (7)	μ_d^{rest} $\frac{\mathrm{mag}}{\mathrm{asec}^2}$ (8)	m$_B$ mag (9)	M$_B^{rest}$ mag (10)	v$_{rot}$ km s^{-1} (11)
CFRS-00.0174	0.7838	13.9	2.8	79	0.63	0.14	19.54	22.21	-21.24±0.2	116±40
CFRS-00.0308	0.9704	17.3	4.7	43	0.08	0.13	21.00	23.09	-20.93±0.2	86±20
MS1054-1403	0.8133	39.5	8.4	76	0.54	0.15	19.88	20.24	-23.30±0.1	232±50
MS1054-1733	0.8347	14.4	3.0	60	0.22	0.15	19.81	22.46	-21.16±0.1	133±20
LDSS2-03.219	0.6024	11.4	8.7	57	0.18	0.34	23.58	23.06	-19.69±0.2	101±50
CFRS-03.0999	0.7049	27.5	7.8	78	0.62	0.42	21.19	21.27	-21.89±0.3	223±10
CFRS-03.1393	0.8554	20.9	4.8	83	0.69	0.42	20.24	21.96	-21.72±0.1	187±10
CFRS-03.1650	0.6341	17.0	5.7	72	0.43	0.42	21.74	22.29	-20.60±0.2	165±40
CFRS-22.0953	0.9787	22.1	5.7	68	0.34	0.28	20.76	22.47	-21.57±0.1	144±30
CFRS-22.1313	0.8173	22.7	5.8	74	0.47	0.28	20.74	21.87	-21.69±0.1	120±10
CN84-023	0.6389	25.0	4.9	49	0.12	0.17	19.46	20.35	-22.56±0.4	159±50
CN84-123	0.6776	19.9	3.9	62	0.24	0.17	19.50	21.02	-22.04±0.1	212±40
CSH96-68	1.5625	16.3	2.7	60	0.22	0.29	18.45	23.03	-22.27±0.4	85±50
SA68-5155	1.0521	23.9	5.9	68	0.33	0.22	20.62	22.43	-21.81±0.1	147±50
CFRS-00.0137	0.9512	17.8	3.1	45	0.10	0.14	18.84	21.76	-22.21±0.1	237±40
CSH96-32	1.0215	12.7	2.1	49	0.12	0.30	18.29	22.32	-21.84±0.1	184±20
CSH96-74	1.3633	24.8	5.1	80	0.68	0.29	19.75	22.56	-22.37±0.1	107±30
CFRS-03.0776	0.8835	7.6	1.2	36	0.06	0.42	18.15	22.94	-20.83±0.1	144±10
CFRS-03.1056	0.9392	11.2	2.0	50	0.13	0.42	19.03	22.85	-21.08±0.1	140±10
CFRS-03.1284	0.9393	8.3	1.3	33	0.04	0.42	17.81	22.68	-21.26±0.1	95±20
CFRS-22.0599	0.8856	13.0	2.2	57	0.19	0.29	18.56	22.07	-21.71±0.1	128±30
stat. error		±2	±1	±5			±0.4	±0.2	±0.2	

[a] galaxy observed by White et al. (ESO proposal ID: 63.O-0372(A)), retrieved from the ESO data archive

Note. – (1) galaxy identification (Lilly et al., 1995; Glazebrook et al., 1995; van Dokkum, 1999; Couch et al., 1998; Cowie et al., 1996), (2) redshift z, (3) isophotal radius R_{25}, (4) disc scale length R_d, (5) inclination i, (6) internal extinction A_B^i (Tully and Fouque, 1985), (7) galactic foreground extinction A_B^g (Schlegel et al., 1998), (8) rest-frame central surface brightness μ_d^{rest}, (9) total apparent rest-frame B-band magnitude m_B, (10) total absolute rest-frame magnitude M_B^{rest} plus rough error estimate, (11) inclination corrected rotation velocity v_{rot} plus rough error estimate – the last row shows statistical errors for several variables as derived in Sec. 3.5.

NED, or ESO science archive). Although photographic plate data are available for the whole sky we opted not to use them for two reasons. Firstly, the response of photographic plates is not linear in contrast to CCDs. Even though the plate data are usually linearised using micro densitometers the quality of this linearisation process can vary from frame to frame (see Sec. 3.2.2). Secondly, the centres of bright objects on photographic images are very often over-exposed. For such objects fitting bulges becomes impossible. Therefore, only CCD data can mimic the high redshift data adequately.

To enable comparison of rotation velocities we required our sample objects to either have published HI or Hα rotation curves (Prugniel et al., 1998, and references therein). From these we calculated terminal rotation velocities, i.e. the velocity beyond the turn-over point at 2.2 disc scale lengths R_d where the rotation curve has reached its flat part (Binney and Tremaine, 1987), even in cases where peak rotation velocities were already tabulated. The reason for this was that in the case of the high redshift objects for sensitivity and / or resolution reasons it might be possible that the rotation speed we calculate underestimates the peak rotation velocity. Therefore, the terminal velocity, which is somewhat smaller than the peak velocity results in a more appropriate value for comparison with high redshift galaxies. For a definition of terminal and peak velocity see Fig. 3.3.

Another factor that has to be considered are the distances. For the high redshift data, after settling on a specific world model, the object's redshift can simply be converted to a luminosity distance. Not so for very nearby galaxies. At recession velocities $cz \lesssim 1000$ km s^{-1} gravitational forces from local (super-) structures may heavily affect distance and distance dependent scale measurements. Especially in cases of objects with negative "recession" velocities estimating distances from their redshifts becomes impossible. Amongst the objects with CCD images we therefore only selected those with published distance estimates based on primary or secondary indicators or recession velocities corrected for Virgo-centric infall (Freedman et al., 2001; Pierce and Tully, 1992; Puche and Carignan, 1988; Tully and Pierce, 2000; Ferrarese et al., 2000; Giuricin et al., 2000; Drozdovsky and Karachentsev, 2000; Karachentsev and Sharina, 1997; Karachentsev et al., 2000; Distefano et al., 1990; Abell et al., 1989; Duval and Monnet, 1985; LEDA[3]).

All remaining sample galaxies are listed in the RC3 catalogue (de Vaucouleurs et al., 1991) and LEDA. From these two databases we obtained total apparent magnitudes. Since for many objects multiple values were available for their magnitudes and / or distance estimates, we calculated a Tully-Fisher relation for all objects and compared the various values with the local calibration by Tully and Pierce (2000). We adopted the best matching combination for the subsequent evaluation (also see Sec. 3.5.1 and Fig. 3.9). For almost all objects (97%) a best fitting parameter combination could be found that places them inside the 3σ-limits of the local relation. The adopted values are listed in Tab. 3.2.

The local sample at that stage however, is not guaranteed to be complete in any way and may in fact be biased in various observables. Therefore, we had to normalise our size, magnitude and rotation velocity distributions to a more general and complete data set. To represent the local galaxy population in an unbiased way we selected the RC3 catalogue. The RC3 contains values for the isophotal radius R_{25} measured at a surface brightness of 25 mag arcsec^{-2}, the rotation speed and the total apparent magnitude. We converted the total apparent magnitudes to absolute magnitudes assuming a distance as determined by the recession velocity in the rest-frame of the 3K microwave background radiation, which is also tabulated in the RC3. However, this distance estimate will become meaningless for very nearby galaxies. Therefore, we used only a subsample of the RC3 with recession velocities $cz_{3K} \gtrsim 2000$ km s^{-1}. Since galaxy properties do not change on this distance scale, we do not impose any selection bias by this procedure. Moreover, the rotation speed is only available in the form of HI full width measurements and not as derived from resolved rotation curves. Applying the corrections as given in Tully and Fouque (1985) we converted the HI width at the 20% intensity level W_{20} to a rotation speed and corrected this value for the effect of inclination (for detailed explanations about inclination corrections see Sec. 3.5.3). Finally we rejected all objects where one or more of the necessary variables were missing or were $W_{20} < 100$ km s^{-1} and were the total magnitude was fainter than $M_B^{rest} > -17$. The remaining sample

---

[3] The Lyon Meudon extragalactic database (http://leda.univ-lyon1.fr)

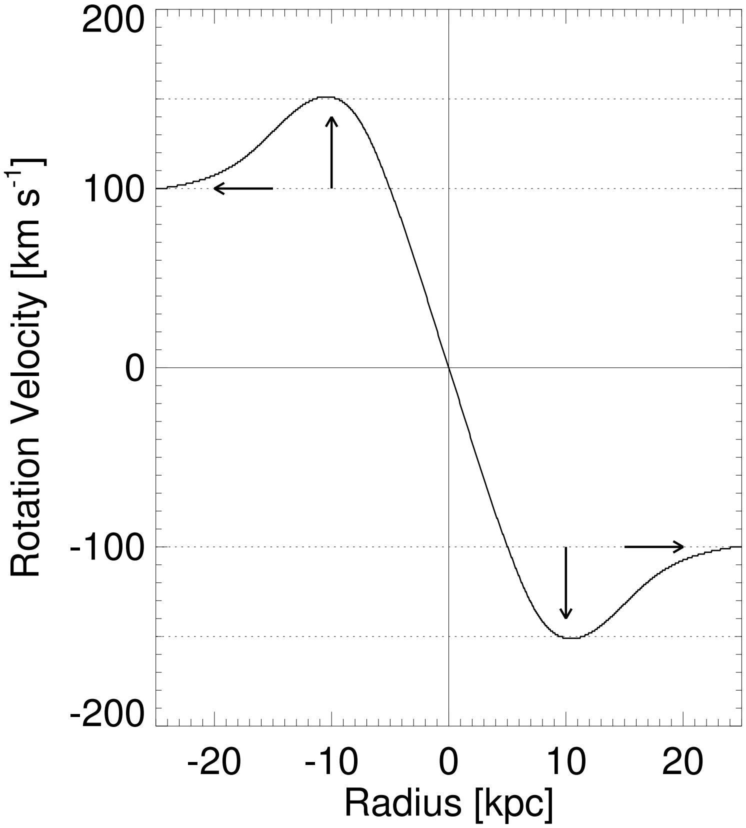

Figure 3.3: Terminal and peak velocities

Position velocity diagram of an artificial galaxy with a disc scale length of ∼ 5kpc. The peak velocity is measured at ∼ 2.2 disc scale lengths (vertical arrow) to be ∼ 150km s^{-1} (top / bottom dotted lines). The terminal velocity is the velocity measured at the outermost accessible radius (horizontal arrow), which is in this case at ∼ 100km s^{-1} (middle dotted lines).

Table 3.2: The Local Sample - Basic Data

ID (1)	cz km s^{-1} (2)	R$_{25}$ kpc (3)	R$_d$ kpc (4)	i deg (5)	A$_B^i$ mag (6)	A$_B^g$ mag (7)	μ_d^{rest} $\frac{\text{mag}}{\text{asec}^2}$ (8)	m$_B$ mag (9)	M$_B^{rest}$ mag (10)	v$_{rot}$ km s^{-1} (11)
NGC0023	4614	12.3	4.3	55	0.16	0.17	21.90	12.69	-21.43±0.17	231
NGC0045	447	5.2	2.3	45	0.10	0.09	22.54	11.22	-17.81±0.08	112
NGC0214	4572	17.2	4.1	49	0.12	0.15	20.40	12.85	-21.25±0.13	223
NGC0247	195	5.6	3.0	72	0.43	0.08	22.95	9.24	-17.98±0.07	105
NGC0266	4719	24.0	6.7	55	0.16	0.30	21.11	12.38	-21.79±0.17	285
NGC0300	168	5.3	1.4	51	0.13	0.05	21.05	8.59	-18.31±0.05	93
NGC0520	2179	12.9	3.1	65	0.29	0.12	20.49	11.95	-20.53±0.13	129
NGC0628	411	7.0	1.9	39	0.07	0.30	21.08	9.88	-18.97±0.10	87
NGC0691	2692	16.2	4.7	44	0.09	0.31	21.26	12.15	-20.79±0.15	202
NGC0765	5120	16.9	5.9	39	0.07	0.44	21.90	13.53	-20.82±0.30	132
NGC0891	821	11.4	2.8	90	0.69	0.28	20.54	10.12	-20.24±0.20	195
NGC1068	1205	15.5	5.4	38	0.06	0.14	21.99	9.55	-21.64±0.10	230
NGC1365	1319	16.8	4.2	43	0.09	0.09	20.70	10.23	-21.15±0.07	245
NGC1448	950	9.6	2.3	79	0.65	0.06	20.43	10.75	-19.92±0.13	186
NGC1512	902	7.8	2.0	59	0.20	0.05	20.68	10.93	-19.63±0.10	146
NGC1532	1172	17.0	4.1	83	0.69	0.07	20.51	9.96	-21.17±0.13	227
NGC1642	4488	14.0	3.4	34	0.05	0.35	20.58	13.25	-20.81±0.13	155
NGC1672	956	13.0	4.3	66	0.31	0.10	21.68	9.97	-20.71±0.09	130
NGC1832	1775	9.7	2.2	48	0.12	0.31	20.12	11.84	-20.19±0.13	187
NGC2280	1310	11.2	2.3	67	0.31	0.44	19.62	10.59	-20.78±0.20	207
NGC2403	237	6.6	1.8	57	0.18	0.17	20.88	8.75	-18.90±0.07	135
NGC2442	1436	18.3	6.4	70	0.38	0.87	21.90	10.86	-20.71±0.13	246
NGC2487	4827	23.8	10.4	58	0.19	0.22	22.53	13.04	-21.18±0.14	158
NGC2541	731	5.6	2.2	63	0.26	0.22	22.19	12.00	-18.10±0.14	95
NGC2595	4329	18.3	5.5	38	0.07	0.17	21.39	12.86	-21.12±0.14	289
NGC2683	902	9.3	1.7	82	0.69	0.14	19.15	9.95	-20.61±0.11	197
NGC2715	1583	14.4	4.8	62	0.24	0.11	21.77	11.55	-20.23±0.14	145
NGC2775	1982	16.3	4.0	39	0.07	0.19	20.60	10.96	-21.31±0.10	315
NGC2835	773	9.3	3.0	49	0.12	0.44	21.61	10.89	-19.33±0.17	101
NGC2903	672	11.7	2.7	62	0.24	0.13	20.28	9.44	-20.47±0.10	193
NGC2976	252	3.5	1.0	67	0.31	0.30	21.37	10.51	-17.28±0.13	60
NGC3031	315	11.9	2.9	56	0.18	0.35	20.70	7.71	-20.55±0.03	242
NGC3034	162	3.0	0.6	79	0.65	0.69	19.13	8.65	-18.18±0.12	112
NGC3079	1334	15.2	4.3	82	0.69	0.05	21.19	10.85	-20.56±0.15	232
NGC3185	1310	6.1	2.0	61	0.23	0.12	21.64	12.76	-18.61±0.07	120
NGC3187	1418	5.9	3.2	73	0.45	0.11	23.04	13.46	-18.08±0.11	64
NGC3198	878	12.1	3.6	69	0.37	0.05	21.34	10.50	-20.00±0.10	153
NGC3223	2632	21.4	7.0	44	0.09	0.47	21.67	11.70	-21.19±0.14	279
NGC3319	917	9.5	2.8	75	0.50	0.06	21.32	10.98	-19.60±0.17	95
NGC3344	962	12.8	3.7	32	0.04	0.14	21.20	10.41	-20.29±0.13	169
NGC3351	947	10.7	3.1	41	0.08	0.12	21.20	10.45	-20.21±0.10	211
NGC3368	1001	11.8	2.8	48	0.11	0.11	21.01	10.00	-20.79±0.13	216

Table 3.2: *Continued*

(1)	(2)	(3)	(4)	(5)	(6)	(7)	(8)	(9)	(10)	(11)
NGC3486	887	7.1	1.6	38	0.06	0.09	20.29	10.99	-19.53±0.10	177
NGC3593	693	6.0	2.1	65	0.29	0.08	21.96	11.57	-18.41±0.08	106
NGC3623	1058	17.6	4.9	72	0.42	0.11	21.16	9.83	-21.07±0.06	261
NGC3628	890	18.4	5.4	89	0.69	0.12	21.27	9.59	-20.94±0.10	213
NGC3631	1004	7.3	1.5	34	0.05	0.07	19.54	10.96	-19.83±0.08	136
NGC3646	4308	38.9	14.4	52	0.14	0.10	22.07	11.64	-22.33±0.13	296
NGC3672	1808	13.7	4.3	61	0.23	0.18	21.51	11.86	-20.21±0.15	210
NGC3675	1271	13.2	3.3	63	0.25	0.09	20.71	10.75	-20.56±0.15	194
NGC3726	1103	14.7	5.0	56	0.18	0.07	21.82	10.73	-20.26±0.07	147
NGC3810	1196	8.4	1.8	40	0.07	0.19	19.97	11.28	-19.89±0.10	187
NGC3877	1181	12.2	3.7	79	0.65	0.10	21.38	11.14	-20.01±0.10	161
NGC3883	6269	12.1	12.8	29	0.03	0.12	24.01	13.83	-20.97±0.10	203
NGC3893	1535	12.2	2.7	44	0.09	0.09	20.07	11.07	-20.65±0.15	183
NGC3917	1196	10.3	5.9	79	0.66	0.09	23.12	11.85	-19.32±0.10	133
NGC3938	884	9.3	2.6	30	0.04	0.09	21.10	10.86	-19.65±0.10	77
NGC3953	1370	17.2	5.4	58	0.20	0.13	21.55	10.64	-20.83±0.10	222
NGC3992	1562	20.8	6.0	57	0.19	0.13	21.28	10.41	-21.34±0.13	240
NGC4013	1298	9.9	2.5	90	0.69	0.07	20.72	11.50	-19.85±0.14	165
NGC4027	842	5.5	1.3	45	0.10	0.18	20.38	11.56	-18.85±0.04	109
NGC4088	1031	10.5	2.7	62	0.24	0.09	20.84	10.91	-19.93±0.09	181
NGC4136	764	5.2	1.6	32	0.04	0.08	21.42	12.06	-18.14±0.17	58
NGC4144	360	3.4	1.1	81	0.69	0.06	21.48	11.36	-17.21±0.13	77
NGC4151	884	6.9	2.3	51	0.13	0.12	21.80	11.37	-19.15±0.20	75
NGC4157	1298	12.3	5.0	90	0.69	0.09	22.32	11.46	-19.89±0.13	184
NGC4175	4059	12.8	4.1	89	0.69	0.09	21.65	13.48	-20.36±0.17	165
NGC4178	947	10.6	5.3	79	0.64	0.12	22.83	11.26	-19.40±0.07	123
NGC4183	1142	8.2	5.3	90	0.69	0.06	23.32	12.17	-18.90±0.13	105
NGC4189	2191	13.6	4.9	47	0.11	0.14	21.95	12.40	-20.09±0.06	161
NGC4192	1148	18.6	6.6	79	0.64	0.15	21.95	10.31	-20.77±0.08	208
NGC4216	1169	13.0	4.0	75	0.51	0.14	21.48	10.48	-20.64±0.09	233
NGC4217	1241	13.5	6.1	89	0.69	0.08	22.60	11.35	-19.90±0.13	186
NGC4237	962	4.4	1.0	54	0.15	0.13	20.27	12.36	-18.34±0.10	133
NGC4254	947	9.6	2.1	32	0.04	0.17	20.00	10.40	-20.26±0.08	184
NGC4258	597	13.2	3.8	64	0.28	0.07	21.74	8.82	-20.84±0.07	216
NGC4302	1214	10.3	7.1	90	0.69	0.15	23.43	11.81	-19.39±0.12	180
NGC4303	1217	15.2	3.4	40	0.07	0.10	20.11	10.11	-21.10±0.09	116
NGC4321	1424	23.5	6.7	45	0.09	0.11	21.22	9.96	-21.59±0.08	172
NGC4388	1589	14.8	4.5	75	0.49	0.14	21.63	11.27	-20.52±0.09	188
NGC4395	282	4.8	2.0	66	0.31	0.07	22.37	10.33	-17.68±0.15	63
NGC4414	1157	9.5	2.0	56	0.18	0.08	19.96	10.78	-20.32±0.13	166
NGC4449	240	2.8	0.5	60	0.22	0.08	19.31	9.77	-17.92±0.13	75
NGC4450	1742	17.4	4.4	54	0.16	0.12	20.67	10.74	-21.25±0.08	173
NGC4490	528	6.2	1.3	58	0.20	0.09	19.78	10.02	-19.37±0.06	94
NGC4496	1037	8.9	3.5	53	0.15	0.11	22.19	11.79	-19.07±0.14	89

Table 3.2: *Continued*

(1)	(2)	(3)	(4)	(5)	(6)	(7)	(8)	(9)	(10)	(11)
NGC4498	1613	8.8	2.6	71	0.40	0.13	21.29	12.39	-19.43±0.15	95
NGC4501	1838	25.1	6.3	61	0.23	0.16	20.69	10.13	-21.97±0.04	275
NGC4527	1562	17.2	5.2	75	0.50	0.09	21.43	10.88	-20.87±0.08	181
NGC4535	1535	23.3	8.6	44	0.09	0.08	22.06	10.50	-21.22±0.08	170
NGC4548	932	10.2	3.0	48	0.11	0.16	21.34	10.85	-19.78±0.07	141
NGC4559	681	10.5	2.9	66	0.30	0.08	21.11	10.16	-19.78±0.11	118
NGC4565	1292	16.6	3.4	89	0.69	0.07	19.96	9.73	-21.61±0.11	254
NGC4569	947	16.2	4.6	68	0.35	0.20	21.21	9.91	-20.75±0.08	183
NGC4579	1625	18.4	4.5	44	0.09	0.18	20.60	10.39	-21.45±0.08	249
NGC4594	1214	25.7	5.0	83	0.69	0.22	20.41	8.29	-22.91±0.10	358
NGC4631	474	13.7	4.6	90	0.69	0.07	21.80	9.06	-20.10±0.18	139
NGC4651	1268	9.8	2.4	50	0.13	0.12	20.66	11.26	-20.03±0.08	195
NGC4654	1091	12.1	3.3	63	0.26	0.11	21.05	10.84	-20.13±0.10	145
NGC4689	1463	12.5	3.8	39	0.07	0.10	21.46	11.53	-20.08±0.07	132
NGC4710	947	6.9	1.5	90	0.69	0.13	20.02	11.22	-19.44±0.16	116
NGC4725	1316	23.1	6.8	63	0.26	0.05	21.32	9.85	-21.53±0.13	202
NGC4731	1136	10.1	2.6	83	0.69	0.14	20.79	11.21	-19.85±0.16	103
NGC4826	531	9.3	2.0	56	0.17	0.18	19.93	9.19	-20.21±0.10	185
NGC4861	1031	3.0	3.3	62	0.25	0.05	24.04	13.66	-17.19±0.30	50
NGC4930	2413	17.2	5.7	49	0.12	0.48	21.73	11.88	-20.82±0.30	216
NGC4939	3073	24.4	8.1	53	0.15	0.18	21.74	11.75	-21.48±0.20	294
NGC5005	1340	15.0	3.6	66	0.31	0.06	20.45	10.30	-21.12±0.08	277
NGC5020	3430	13.8	16.3	63	0.25	0.10	24.08	12.83	-20.64±0.30	116
NGC5033	1136	13.4	4.7	63	0.26	0.05	22.22	10.49	-20.57±0.10	212
NGC5055	711	16.5	4.5	61	0.23	0.08	21.32	9.08	-20.96±0.10	186
NGC5073	2692	14.5	4.5	84	0.69	0.25	21.53	12.61	-20.33±0.20	189
NGC5078	1901	12.8	2.8	87	0.69	0.28	20.49	11.31	-20.87±0.22	281
NGC5161	2263	17.9	5.9	59	0.20	0.25	21.69	11.80	-20.76±0.20	184
NGC5236	417	14.0	3.4	39	0.07	0.28	20.45	8.13	-20.75±0.03	160
NGC5371	2602	28.0	10.5	47	0.11	0.04	22.09	11.21	-21.66±0.14	242
NGC5457	480	19.2	6.2	31	0.04	0.04	21.62	8.27	-20.91±0.09	194
NGC5585	561	5.9	1.9	49	0.12	0.07	21.58	11.08	-18.45±0.14	95
NGC5746	1808	18.5	3.7	89	0.69	0.17	22.06	10.60	-21.47±0.16	300
NGC5907	995	16.5	7.2	89	0.69	0.05	22.51	10.43	-20.34±0.13	220
NGC6015	1151	10.2	3.1	59	0.21	0.05	21.39	11.48	-19.61±0.10	171
NGC6503	387	4.2	0.9	75	0.52	0.14	20.08	10.39	-18.33±0.09	111
NGC6643	1682	14.8	4.4	62	0.24	0.26	21.37	11.49	-20.43±0.13	159
NGC6744	591	17.2	6.0	52	0.14	0.19	21.90	9.00	-20.63±0.17	212
NGC6902	2854	17.5	4.1	42	0.08	0.17	20.44	11.56	-21.51±0.18	285
NGC6946	309	6.7	7.2	63	0.26	1.48	23.98	9.35	-18.88±0.10	112
NGC7184	2401	27.5	14.1	72	0.42	0.14	22.88	11.23	-21.46±0.18	275
NGC7319	6664	15.5	4.6	52	0.14	0.34	21.36	14.31	-20.62±0.15	127
NGC7331	1001	13.6	3.4	75	0.51	0.39	21.12	9.84	-20.94±0.12	238
NGC7412	1526	11.3	3.3	47	0.11	0.05	21.25	11.77	-19.93±0.13	81

Table 3.2: *Continued*

(1)	(2)	(3)	(4)	(5)	(6)	(7)	(8)	(9)	(10)	(11)
NGC7479	2728	21.9	5.6	61	0.23	0.48	20.73	11.37	-21.60 0.06	205
NGC7793	264	5.7	1.7	50	0.13	0.08	21.29	9.50	-18.39 0.05	100
stat. error		±2	±1	±5			±0.4	±0.2	±0.2	

Note. – (1) galaxy identification, (2) adopted redshift cz, (3) isophotal radius R_{25}, (4) disc scale length R_d, (5) inclination i, (6) internal extinction A_B^i (Tully and Fouque, 1985), (7) galactic foreground extinction A_B^g Schlegel et al. (1998), (8) rest-frame central surface brightness μ_d^{rest}, (9) total apparent rest-frame B-band magnitude m_B, (10) total absolute rest-frame magnitude M_B^{rest} plus rough error estimate for M_B^{rest}, (11) adopted inclination corrected rotation velocity v_{rot} – the last row shows statistical errors for several variables as derived in Sec. 3.5.

included still $\sim$ 1900 galaxies, about 8.4% of the full RC3 catalogue, and therefore enough to form an unbiased and complete representation of the local galaxy population.

This representative set of RC3-galaxies was now our basis to normalise our local sample to. Although the data for our local sample galaxies including images and rotation speeds from resolved rotation curves contains much more and more precise information we did not use these data, but the same values from the RC3 to enable a fair comparison. The only exception being the distance, since a lot of our galaxies are closer than v_{3K} = 2000 km s^{-1}, making it necessary to adopt our precise estimates to obtain proper values for related variables like size and absolute magnitude.

One might argue that the RC3 is not complete either. However, this will probably only be true in the case of very small dwarf galaxies. At large distances we will not be able to detect such objects, though. The question now arises what the minimum object size is that we are likely to include in our high redshift sample. Guided by the apparent sizes of our high redshift objects we chose the isophotal radius $R_{25} \geq 12.5$ kpc as our selection criterion for both near and far objects (see Sec. 3.5.2). Moreover, on these scales the RC3 catalogue will indeed be reasonably complete.

Although our local sample now contains the same selection function as our high redshift galaxies we have not matched yet the local sample with the local galaxy population as represented by the RC3. Comparing the isophotal radius R_{25}, absolute magnitude and rotation speed histograms for the RC3 and our local sample we found that the distributions were significantly different in that our catalogue contained many more fast rotators and in relation too many intermediate size objects (12.5 kpc $\lesssim R_{25} \lesssim$ 17.5 kpc). Furthermore, the shape of the absolute magnitude histogram was also distorted. In an iterative process we removed objects from our catalogue trying to bring the two samples into agreement. We preferred to exclude objects with mediocre data (especially shallow images) first, and then to remove as few sources as possible. After this arbitrary process out of our 132 galaxies 86 remained. However, the results presented later on do not depend on the specific target selection in this process. We tested several realisations of this rejection process without altering the individual distributions significantly. After applying the size selection criterion our representative set of local galaxies with $R_{25} \geq 12.5$ kpc contains 36 objects, still almost twice as many as in the high redshift sample. This matches perfectly the corresponding excerpt of the RC3 catalogue of $\sim$ 1200 galaxies ($\sim$ 5% of the complete catalogue).

The final histograms for R_{25}, absolute magnitude and rotation speed for our restricted local sample and the RC3 catalogue are shown in Fig. 3.4, Fig. 3.5 and Fig. 3.6, respectively. We have applied our standard set of statistical tests, a student's T-test with linear and logarithmic scaling, a rank-sum test, a variance test and a Kolmogorov-Smirnov test, to verify that the distributions were drawn from the same sample, i.e. our local galaxies represent a fair match to the local population. Since, as we will also show in our subsequent discussion, other structural and morphological parameters correlate with R_{25}, absolute magnitude and / or rotation speed essentially all variables under consideration are matched. Thus, our restricted ($R_{25} \geq 12.5$ kpc) set of local galaxies fairly

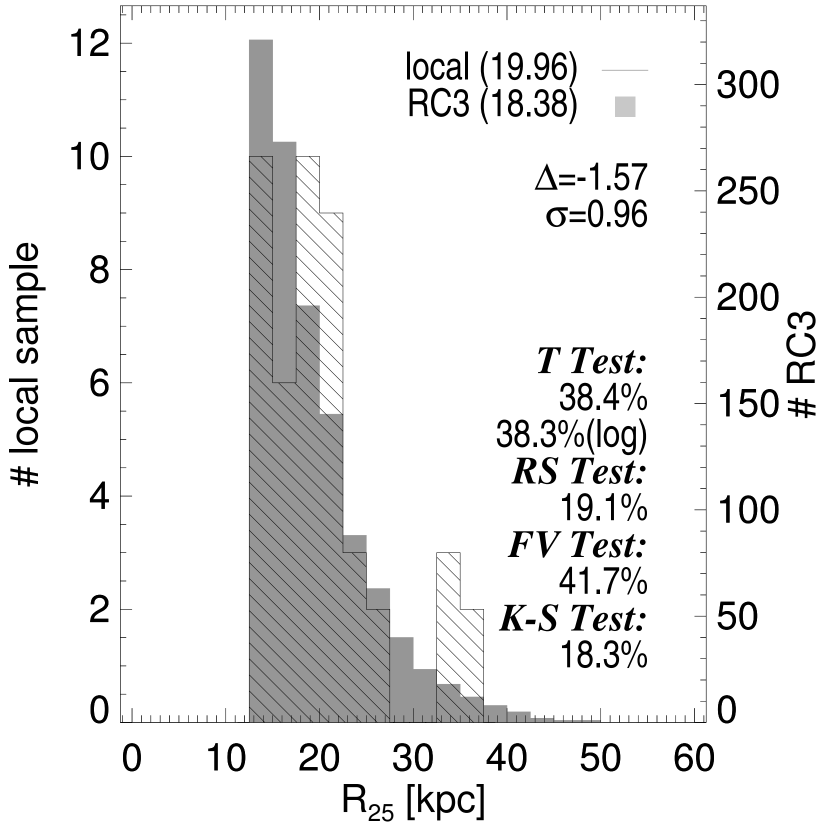

Figure 3.4: Comparison of the RC3 with the local sample: R_{25}

Histograms of the isophotal radius R_{25} for the local galaxy population as represented by the RC3 (shaded region) and our sample of local galaxies (striped region). The means for both distributions are indicated in brackets in the upper right corner. The difference of the means of the two distributions Δ and its 1σ error is shown above a set of statistical tests (lower right), including a student's T-test (on a linear and a logarithmic scale), a rank-sum test, a variance test and a Kolmogorov-Smirnov test, respectively. For an explanation of the interpretation of the tests see Appendix A.

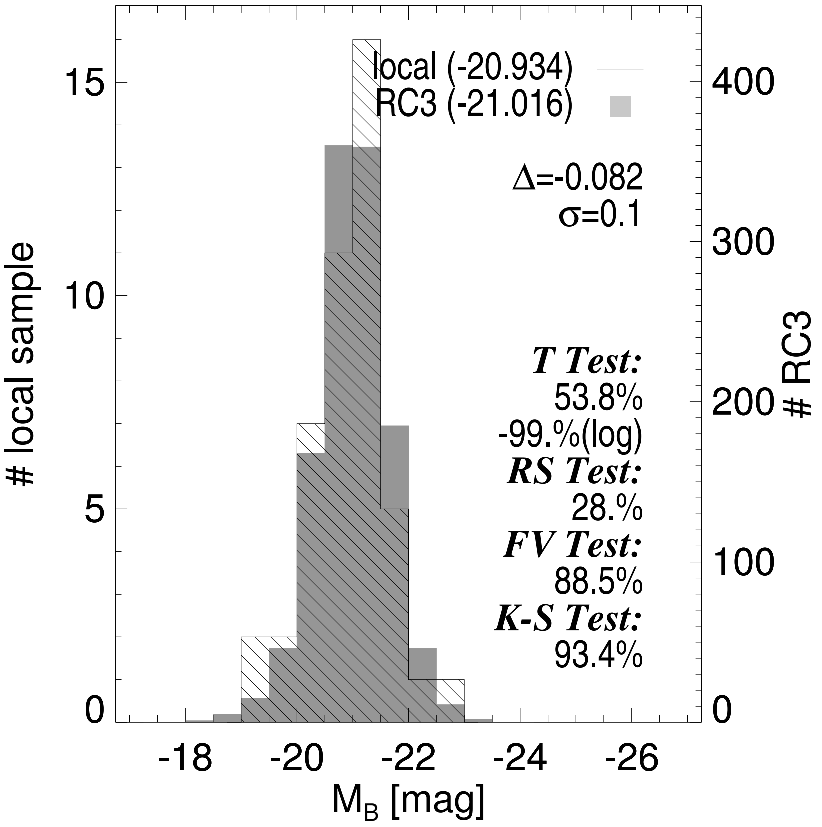

Figure 3.5: Comparison of the RC3 with the local sample: M_B

Histograms of the absolute magnitude M_B for the local galaxy population as represented by the RC3 (shaded region) and our sample of local galaxies (striped region). The means for both distributions are indicated in brackets in the upper right corner. The difference of the means of the two distributions Δ and its 1σ error is shown above a set of statistical tests (lower right), including a student's T-test (on a linear and a logarithmic scale), a rank-sum test, a variance test and a Kolmogorov-Smirnov test, respectively. For an explanation of the interpretation of the tests see Appendix A.

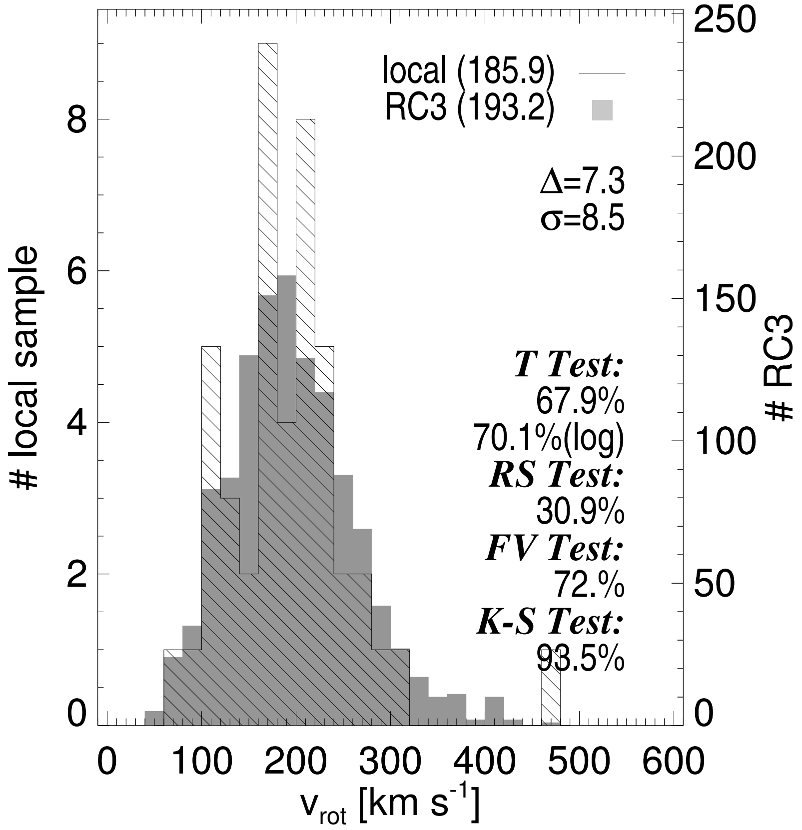

Figure 3.6: Comparison of the RC3 with the local sample: v_{rot}

Histograms of the rotation velocity v_{rot} for the local galaxy population as represented by the RC3 (shaded region) and our sample of local galaxies (striped region). The means for both distributions are indicated in brackets in the upper right corner. The difference of the means of the two distributions Δ and its 1σ error is shown above a set of statistical tests (lower right), including a student's T-test (on a linear and a logarithmic scale), a rank-sum test, a variance test and a Kolmogorov-Smirnov test, respectively. For an explanation of the interpretation of the tests see Appendix A.

matches the local galaxy population and shows the same selection bias, namely the size selection, as our set of high redshift galaxies, and any difference between the two sets of data, therefore, has to result from the evolution of such disc galaxies over the last 6-9 Gyrs. In the following discussion we refer to the restricted set of local galaxies also as the "matched" or "cut" sample. The basic data for the local sample are presented in Tab. 3.2.

3.3 Observations

To obtain Hα rotation curves of high redshift galaxies in the near-infrared J- and H-bands we were granted 12 nights of observing time with ISAAC at the ESO Very Large Telescope (VLT) so far. ISAAC, the Infrared Spectrometer And Array Camera, is the current multi-purpose imaging camera and spectrograph at the Antu/VLT telescope in the wavelength regime from 1 μm $< \lambda <$ 5 μm. It consists of two 1024x1024 pixel arrays, a HAWAII HgCdTl-array for the short wavelengths and an Aladdin InSb-array for the long wavelengths. The field of view for imaging is ∼2.5'x2.5' at a pixel scale of 0.1484"/pix in short wavelength and ∼72"x72" at a pixel scale of 0.071"/pix in long wavelength mode. A large set of broad and narrow-band filters is available for both wavelength regimes. Besides imaging the instrument is capable of polarimetry and spectroscopy. The two spectroscopic modes, low and medium resolution, provide slit-width resolution products of $R \sim 500$ and $R \sim 3100$, respectively (for a slit of 1" width). Four different slits (0.3", 0.6", 1.0", 2") are available.

The first set of data was obtained in service mode in ESO-period 65 (April - September 2000) and was carried over to period 66 (October 2000 - March 2001). As a result of this we did not have the chance to interact with the observing team. Therefore, we fixed the integration times to 3 hours and selected the 0.6"-slit, resulting in a slit-width resolution product of $R \sim 5200$. The targets for this run were selected on the basis of 1" resolution pre-images acquired in the J-band with ISAAC. From these images we also measured inclination angles that were then used to orient the slits for the spectroscopy. In addition to these J-band images we were able to use I-band images of similar quality and resolution taken with the Canada France Hawaii Telescope (CFHT[4]) on a run in 1991 (Observer: Le Fevre). It turned out in the acquisition images of 0.4" seeing (taken prior to positioning the slit) that one source was in fact a merger of two galaxies. Because of strong night sky lines in the spectra it was impossible to distinguish between the two objects and we therefore rejected this source from the following study. During this run we were able to successfully observe three targets at seeing values of typically ∼ 0.8".

The remaining three runs were granted in visitor mode (in fact the first one was also initially scheduled in visitor mode, but got switched to service mode due to problems with the instrument in the beginning of the semester). They were carried out in February 2001, September 2001, and September 2002. However, in contrast to the first run, we recognised the fact that estimation of minor over major axial ratios of very small objects leads to extremely large uncertainties in the inferred inclination angles (see also Sec. 3.5.3). Therefore, the targets for these runs were exclusively selected from WFPC2/HST F814W images. Additionally, we used a slightly wider slit (1" width) this time resulting in an $R \sim 3100$. Furthermore, visitor mode allowed us to vary the integration times in accordance with the actual brightness of the object. We found that usually after integrating for 20 minutes it was already possible to judge whether the spectroscopy would produce a suitable emission line or not. Depending on the signal-to-noise ratio achieved in the pipeline reduced data, which was available immediately after each 10 minutes exposure we integrated on source in between 1 and 3 hours. In contrast to the first observing run this time our objects were so faint that we could not detect them in the acquisition images. Therefore, we measured the proper off-set from a nearby bright star on the HST images and used that star during the observations as our acquisition reference. Using this "blind"-offsetting technique we were able to detect another 3 + 8 + 6 objects in February 2001, September 2001, and September 2002, respectively, with seeing values ranging from 0.4" to 0.8". The varying success rates during

---

[4] Obtained from the Canadian Astronomy Data Center, which is operated by the Dominion Astrophysical Observatory for the National Research Council of Canada's Herzberg Institute of Astrophysics.

these runs resulted from improving our observation and target selection strategy on one hand, and the loss of observing time due to instrument failures and the weather on the other hand. We present the statistics of the individual runs in Tab. 3.3. From those statistics we learn that the crucial factor to successfully observing high redshift rotation curves is flexibility in the exposure times. Especially from the first to the second visitor mode run one notices a steep increase in efficiency. We managed to decrease the effective exposure time per source, i.e. the total exposure time on source including continuum and not detected targets divided by the total number of successful targets, by almost a factor of two. Therefore, with ∼2.5 hours integration time plus overhead and calibration data it is realistic to observe ∼3 rotation curves per night with ISAAC. Although conceptionally the observing setup is not very complicated service mode observtions are not suitable at all for this kind of data since integration times have to be fixed beforehand. The reason for this is that it is almost impossible to hone the sample to a degree that the success rate, i.e. the ratio of successful number of targets over total number of targeted sources, reaches well beyond 60-70% without introducing severe slection biases especially in the form of strong line emitting sources.

Table 3.3: THE OBSERVATIONS

run	1	2	3	4
date	Sep.-Oct. 2000	Feb. 2001	Sep. 2001	Sep. 2002
observing mode	service	visitor	visitor	visitor
pre-images	ISAAC/VLT	WFPC2/HST	WFPC2/HST	WFPC2/HST
slit width	0.6”	1.0”	1.0”	1.0”
spectral resolution	$R \sim 5200$	$R \sim 3100$	$R \sim 3100$	$R \sim 3100$
seeing	$\sim 0.8''$	0.5”-1.2”	0.4”-0.8”	0.5”-0.9”
integration time	3 hours, fixed	1-3h, variable	1-3h, variable	1-3h, variable
time lost	N/A	weather	technical	weather
targets not detected	2	4	3	1
continuum only	2 (on 1 slit)	2	2	0
success rate	50%	33%	62%	86%
effective amount of time per source	6.7 hr	4.4 hr	2.3 hr	2.6 hr
successful targets	3 (+1 excluded)	3	8	6

Together with the source from the ESO data archive we could obtain 21 rotation curves of high redshift disc galaxies so far. However, the ESO time allocation committee granted our project another set of 3 observing nights in September 2003, which should allow us to increase our sample to maybe 30 galaxies.

3.4 Data Reduction

Although a wide variety of data were involved in our study, including spectroscopy, ground-based and HST imaging in the optical and near-infrared, the basic principles of taking and reducing the data were basically the same. Each final frame consists of many single science and calibration exposures. The first problem common to almost all astronomical observations especially in the optical and infrared are cosmic ray events: High energetic particles impact onto the detectors and deposit charges that get interpreted as a signal. These cosmic ray events, or “cosmics”, affect single or even small groups of pixels. To be able to remove them one usually takes several exposures of the same field. With multiple exposures rejection of extraordinarily bright pixels leads to a cosmic ray cleaned image.

Another characteristic of modern detectors is the so-called dark current. Near-infrared and also to some extent optical detectors produce a signal even without being exposed to any light source (emitting in the sensitive wavelength range of the array). This signal results from thermal radiation of the detector and especially the read-out electronics and is proportional to the time. To remove this dark current special dark frames are taken of exactly the same exposure time as the science frames. Using such "darks" the dark current is easily subtracted from the science frames.

Furthermore, the response of individual pixels of an array is usually not uniform across the whole detector area. Sensitivity variations are generally of the order of a few percent around the mean value, but in extrem cases a pixel may only detect a tiny fraction of photons compared to the average pixel. These are called "dark" or "dead" pixels. In contrast to these dark pixels there are also "hot" pixels that constantly show a very strong signal even without being exposed to light. Dead and hot pixels are easily taken care of by flagging them in the science images and taking exposures of one target at slightly different positions.

Additionally, the pixel to pixel variations produce a global pattern of differing sensitivity as a result of the detector itself or even dust grains on lenses, that occasionally produce "donut"-shaped features on the images. To get rid of such variations one takes images of an evenly illuminated surface like a lamp projected onto the inside of the telescpoe dome or the sky during dusk or dawn. Such "dome"- or "sky"-flats first get normalised and then the science frame is divided by the flat to remove the sensitivity variations.

After removing these detector inherent effects one still has to cope with the omni-present sky-background. This background unfortunately also varies with time and the frequency of these changes and the background intensity is higher at longer near-infrared / optical wavelengths. As a result one has to find a compromise between integrating long enough to not be limited by the read noise of the read-out electronics, but short enough to not average over these sky variations. Furthermore, one has to take multiple exposures again at slightly different positions. The shifts in between individual exposures are necessary to create a so-called "sky-frame", which is a mean of several exposures without containing the targets that are to be observed. This object-free sky-frame gets subtracted from the individual science exposures thus removing the sky-background.

Finally, the corrected science frames have to be shifted back onto a common reference frame to be then co-added, resulting in the science image. In the case of spectroscopy basically all these prescriptions apply as well, but shifts can now only be applied along the slit-direction, in order not to put the target out of the slit. This results in special patterns like: position A, position B, position B', position A',... In between position A and position B usually a larger offset of several tens of arcseconds gets applied, whereas position A differs from position A' only by a few acseconds. Consecutive AB pairs are first subtracted from each other to remove the sky background. Then AB and A'B' pairs get shifted onto a common reference frame and finally, the pairs are combined resulting in the output spectrum.

In spectroscopy in addition to dome- or sky-flats, spectra of arc lamps are somtimes taken as a reference to calculate a precise wavelength solution. However, night sky OH-lines in the near-infrared are abundant enough to dispense with such arc-frames and use the science frames directly to calibrate the dispersion axis of the spectra.

3.4.1 ISAAC Spectroscopy

ISAAC scpectroscopy data was primarily taken for one purpose: to extract a rotation speed from the Hα rotation curve of the objects. To achieve this goal, firstly, the data were reduced following the prescriptions outlined in Sec. 3.4 to combine all exposures, remove the sky background, and any instrumental signatures. Next, the resulting rotation curve must be extracted and measured.

Initial Data Reduction

The HAWAII array built into ISAAC consists of a chip divided into four different quadrants. Unfortunately, the read-out electronics couples them in a way producing some charge transfer from the columns of one quadrant into the next. This problem, however, is well behaved and the ESO eclipse software contains a package that removes this so-called "electrical ghost" effect. This tool was applied to all science and calibration frames. Besides eclipse we used standard IRAF packages to reduce the data. Each night three dark frames were taken for spectroscopy. These files were combined rejecting cosmic rays and subtracted from the science frames. Additionally, each day six dome-flats were taken, three with the lamp in the dome turned on and another set of three with the lamp turned off. The "off"-frames were subtracted from the "on"-frames, and the resultant files were combined, again rejecting cosmic rays. After normalising this dome-flat the dark-subtracted science frames were divided by the dome-flat. To remove cosmic rays from the science images we computed a median frame for each exposure and replaced all pixels in the input frames deviating for more than 10σ from the median by the corresponding pixel in the median frame. Especially in the case of the service mode data, where frames for one target were taken on different dates, we checked all files individually for shifts in the wavelength direction due to flexure and applied a reverse shift if necessary. Then we combined all frames and calculated and immediately applied a wavelength solution and distortion correction from the night sky OH-lines. The data set of dark-subtracted, flat-fielded and rectified spectra belonging to one target was then processed by the eclipse package SPJITTER. This task was set to simply subtract AB pairs from each other, to shift frames, and to fold them back together. Finally, we subtracted the residual sky background from the resulting frame by fitting a polynomial to the data along the spatial axis, smoothed the spectrum and extracted a rotation profile.

Evaluation of Line Widths and Equivalent Widths

To extract rotation curves from the spectra two approaches had to be taken. Estimating equivalent widths for the Hα-lines required us to extract one dimensional spectra. The IRAF task APEXTRACT is perfectly suited to this. It sums several pixels along the wavelength direction and tries to estimate the location of the spectra along the spatial axis. Once identified, one has to specify the width of a "pseudo"-slit, which is then used to trace the spectrum along the whole dispersion direction. After tracing the spectrum the profile gets summed over the spatial axis including a weighting scheme. The resulting 1-dimensional spectrum we then used in an attempt to calculate equivalent widths.

However, even with the increased signal-to-noise one gains in the continuum, for the huge majority of our high-z galaxies only lower limits could be derived. Since only for three objects from ground-based J-band images an Hα-continuum flux could be derived, we refrained from a general equivalent width study and defer this topic until deep rest-frame Hα images are taken for these objects.

However, we also used the Hα-profiles to measure line widths comparable to the full width measurements given in the RC3 for the local galaxies. To this end we fitted the 1-dimensional Hα-profiles by several, usually one or two (in the case of a double horned profile), Gaussians. The actual number of Gaussians used depended on the structure of the 1-dimensional Hα-profile. The sum of those was supposed be a reasonable representation of the Hα-profile while keeping the total number of functions used as low as possible. Those Gaussian functions we then deconvolved with a Gaussian with a FWHM of the resolution of the observations. We measured the width of the fits at the two velocities that enclose 20% of the total flux. Finally, we applied the corrections given by Tully and Fouque (1985) to remove the effects of broadening and turbulence.

Extraction of a Resolved Rotation Curve

In almost all cases, however, we did not have rely just on 1-dimensional data, but could derive a resolved rotation curve from the 2-dimensional spectra. To extract the data points that are then used to fit a model rotation curve we developed a special adaptive curve tracing algorithm.

Before applying this technique to a spectrum, only "adequate" data points were extracted, i.e. only the rectangular region of the spectrum containing the Hα emission line is handed to the tracing routine, and in this region all values below roughly 3σ of the background noise were blanked. The algorithm then calculated the intensity weighted mean along the dispersion axis of the smoothed spectra for each column and rejected outlying pixels. This calculation was iterated until 10 pixels remained in the sample. We found this to be a reasonable number including as many pixels as possible while excluding obvious outliers. The intensity weighted mean of the remaining pixels defines a position-velocity data point.

Since this procedure is very unstable in the steep inner parts of the profile, a second refined measurement is started afterwards. Three data points from the first evaluation of the position-velocity data are now used to calculate a slope "before" and "after" the point under consideration. A new position-velocity value is then estimated by evaluating the intensity weighted mean along a line perpendicular to the mean of the two slopes. The effect of this is, that the data points are redistributed along the ridge line of the rotation curve decreasing the average distance to the "real" values. We show an example of how this fitting works in Fig. 3.7. There are several reasons that make applying of such a complicated technique vital to extracting a real rotation curve. First of all, the very low signal-to-noise that one gets, even with the big aperture of the VLT, makes mean, median or weighting techniques prone to noise spikes. And second, in the cases where OH night sky lines cross the Hα-line the signal may get severely distorted, ranging from getting no signal at all (in regions where one would expect something otherwise) to having line flux at positions that clearly do not belong to the line (one can see this clearly in spectra with a continuum). Another reason for this technique is that the seeing is of the order of 4-6 pixels in the spatial direction of the spectra. This corresponds to 4.7-7 kpc at the mean redshift of our sample, which is a reasonable fraction of the disc scale lengths even of our large galaxies.

We then fitted the final position-velocity diagram with a model rotation curve. Since the resolution of our Hα-rotation curves at redshifts $z \approx 0.9$ cannot distinguish between different phenomena in the cores of the galaxies like nuclear rings or warps or even in the outer discs we assume a simple model. It consists of a step-function that is convolved with a Gaussian with a full-width at half maximum of the seeing weighted with an exponential function with a scale-length as measured from our surface brightness fits on the HST / VLT images. Since the seeing conditions cannot be measured accurately during the observations or derived from the final spectrum, we have to rely on the values from the J-band acquisition images before the observations and the values from the seeing monitor in the visual. However, the seeing conditions in the near-infrared change on timescales much smaller than our total integration times (10 minutes compared to typically 120 minutes), and they may even vary independently from the visual wavelength regime, let alone the offset that has to be applied to convert to the near-infrared. Taken together, these facts render the seeing virtually a free parameter. Nevertheless, the values obtained from a free fit correlate well with the "true" seeing values. The parameters that finally go into the model are the rotation speed, the seeing, and the scale length of the optical disc. The only free parameter is the rotation speed as defined by the amplitude of the step function.

3.4.2 Ground-Based Imaging

On our first run at the VLT we were granted 40 minutes of pre-imaging time to select targets from two fields where no HST images were available. Three objects were selected based on these observations. On one of our later runs we took another pre-image and successfully observed one additional object. These images were reduced in exactly the same way as the ISAAC spectra (see Sec. 3.4.1) including ghost removal, dark subtraction, flat-fielding and cosmic ray cleaning. Since the images were dithered heavily, i.e. all consecutive images were taken on slightly different positions, we were able to construct a so-called running sky-flat. Such a sky-flat consists of a combination of a number of images taken right before and after the observed frame. During the combination of these frames it was also possible to flag and remove cosmic ray events in the individual frames. Subtracting the according running sky-flat from each image removed the sky background, but produced a number of dark spots around every object. The sky-image in a perfect

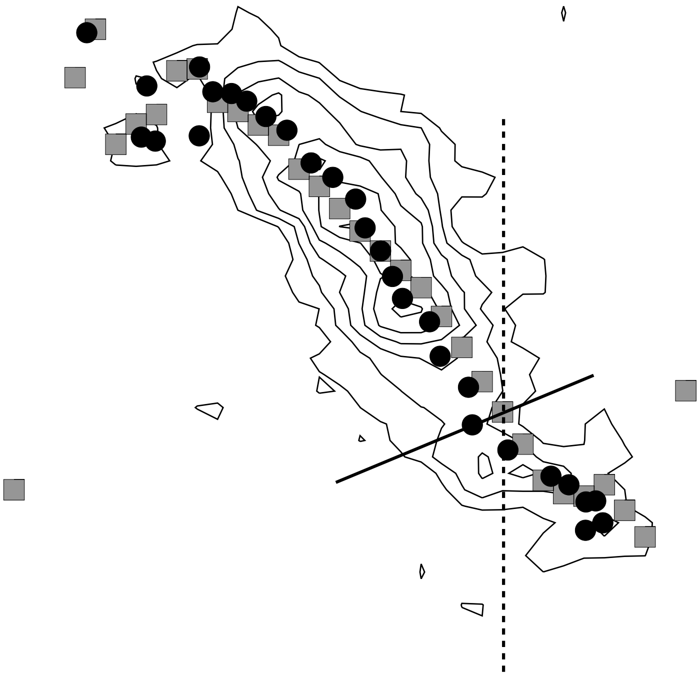

Figure 3.7: Extraction of a rotation curve

We plot the 2-dimensional spectrum of an example galaxy (contours; dispersion axis - vertical, spatial axis - horizontal). Taking outlier resistant intensity weighted mean values along the spatial axis (summing over lines parallel to the dashed one) we obtain the grey position-velocity data points. Since especially in the steep inner parts intensity variations may not allow tracing the "ideal" line, we refine those first values by fitting a new set of points along a line perpendicular to the first data (solid line). The values obtained from this (solid circles) provide a much better estimate for the "ridge-line" of the spectrum.

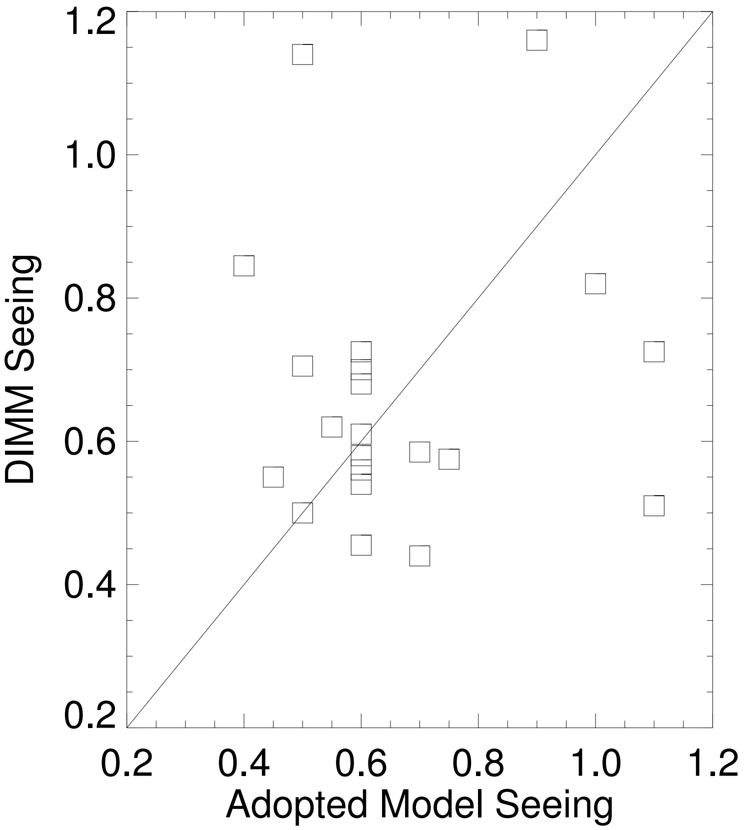

Figure 3.8: Seeing Comparison

Comparison of the seeing values as measured from the optical seeing monitor at the beginning and the end of the observations. More than 3/4 of all targets show reasonable agreement with the adopted model values.

world should only contain sky flux. However, our sky frame still contained some residual flux from the objects contributing more flux than the sky at the actual position. No matter which pixel rejection algorithm one chooses the limitation of only being able to combine a few frames (because of the sky background changing with time) it is impossible to get rid of the objects completely, therefore producing the dark spots when subtracting the sky-frame from an image. After shifting and combining the images the dark spots became even more pronounced, because of the increase in signal-to-noise. However, this frame could now be used as a template to mask all the objects in the frame. In a second step these masks were now used to remove all "object-pixels" when creating the running sky-flat. Using this "object-free" sky-image we could get rid of the dark spots. In an additional step we block-magnified all images by a factor of two before the final shift-and-add process, which produced the science image.

3.4.3 HST Imaging

For more than 80% of our observed targets we were able to obtain HST/WFPC2 F814W images from the STScI's Archive. Similar to the near-infrared (see Sec. 3.4.2) images are taken at slightly different positions to overcome the problems of under-sampling the point spread function (PSF) of HST and to regain information that would otherwise be lost. For our data reduction we used the recipes and procedures as given in Mutchler and Fruchter (1997); Fruchter et al. (1997).

Firstly, the sky background was subtracted from all input images. Next, a new image was created where all pixels in regions where the median was not significantly different from the background (i.e. zero) were blanked. By means of cross-correlation, all images were then compared to find the offsets between them. Since WFPC2 images consist of four different frames, i.e. four individual CCDs, stored in one image, one gets four different shift values for each image. The drift of the chips relative to each other, however, is small enough that it is possible, for sequentially taken images, to neglect the drift altogether and to average the four different measurements of the shifts to improve the overall accuracy. Although WFPC2 suffers from hot pixels, it was not necessary for our purposes to treat these in any special way. Now the images were drizzled onto a new finer output grid including the previously calculated shifts and the distortion information as given in the image header. To remove the cosmic rays in the final image, the drizzled images were median combined rejecting a certain fraction of pixels. This largely cleaned image is then blotted back onto the original frame. Using the information of the derivative of this image (a measure of the steepness of the median image) the blotted image itself and the data image, i.e. the image that was used to create the drizzled frames, all cosmic rays were rejected in the data image. The last step of the calculation consists of the drizzling of the cosmic ray free images onto one output image including shifts and distortions.

3.4.4 B-Band Images for Local Galaxies

To construct a local set of galaxies with which to compare our high redshift sample, we were able to collect B-band images for an ensemble of 132 nearby galaxies. These data were obtained for various purposes at different telescopes (see de Jong, 1996a; Larsen and Richtler, 1999; Howk and Savage, 1999; Cheng et al., 1997; Frei et al., 1996; Tully et al., 1996). Other than the images requested from the ESO science archive, these data were already reduced and no other calibrations were applied. In the case of the images from Frei et al. (1996) even stars were already removed. In addition to these objects, we could include four targets from our own observations at the German / Spanish 2.2m telescope at Calar Alto and the ESO 3.6m telescope at La Silla. These data were flat-fielded using dome-flats, and cosmic rays were removed by a simple rejection algorithm. After shifting the frames onto a common grid they were co-added to obtain the final output image. In the case of the images from the ESO science archive no calibration data were retrieved and the various frames were just shifted and summed, again rejecting cosmic rays. The lack of calibration data does not have an impact on the scientific output extracted from the frames. In order to measure light profiles from these CCD images, we subtracted the sky background carefully before attempting to fit profiles.

In addition to these CCD data, for every object a B- or R-band (in the very few cases were B-band information was not available) Schmidt-plate image from the second generation DSS catalogue[5][6][7] was obtained. The reason for this was the fact that to properly measure surface brightness profiles one needs rather deep images. Unfortunately, most of the data in the literature where taken for different purposes and therefore not deep enough to extend to the very outermost parts of the galaxies. To improve the extent of the CCD surface brightness profiles we therefore used the DSS images. Since these data where linearised we could directly compare the extracted profiles to the CCD data (also see Sec. 3.5.2).

3.5 Data Analysis

3.5.1 Distance Estimators

One of the critical parameters for all of the parameters we explore is the adopted distance to a target. Therefore, we put a lot of effort into the determination of a distance scale. For the high redshift sample we simply adopt a low-density ($\Omega_M = 0.3$), flat ($\Omega_M + \Omega_\Lambda = 1$), Λ-dominated ($\Omega_\Lambda = 0.7$) cosmology with a Hubble constant $H_0 = 70$ km s^{-1} Mpc^{-1}. This world model is in agreement with measurements from the HST Key project to determine the extragalactic distance scale, estimates from large-scale galaxy clustering, the baryon fraction in clusters, the evolution in the abundance of X-ray clusters, estimates from high redshift supernovae and the detection of the first cosmic microwave background Doppler peak (e.g. Freedman et al., 2001; Cole et al., 2000; and references therein). Those results have recently been confirmed with extremely high precision by the Wilkinson Microwave Anisotropy Probe (WMAP; Spergel et al., 2003).

However, for the local galaxies a redshift cannot simply be converted into a distance, because peculiar motions are easily of the order of the recession velocity. There are basically three redshift regimes which have to be treated separately. For very nearby galaxies usually primary distance indicators are available as distance measures like Cepheids, novae, brightest stars and so on. For the “distant” objects of our local sample Virgo-centric infall is the dominant source of the peculiar motions and a dynamical model can correct the recession velocity accurately enough to derive a distance. Unfortunately, these two regimes do not overlap and there is a range of recession velocities where the determination of distances via primary distance indicators becomes scarce and very difficult to perform and where a model of Virgo-centric infall becomes too coarse resulting in strong deviations from the “true” distance.

Since usually multiple values were available for magnitudes, rotation speeds and distances without any hint for the “right” value, we could approach the problem by constructing a Tully-Fisher relation for our local sample galaxies. We plot the Tully-Fisher calibration by Tully and Pierce (2000) in Fig. 3.9 and try to minimise the distance between this relation and our data points. It turns out that the rotation speed and the magnitude estimates usually do not have a large impact on the Tully-Fisher relation. Only the inclination (rotation axis) and the distance (magnitude axis) could significantly impact on the final value. However, since the differences in the inclinations were usually small only the distance remains to obtain a correct Tully-Fisher value. Especially in the intermediate distance regime estimates for distance moduli could show differences

---

[5] The Digitized Sky Survey was produced at the Space Telescope Science Institute under U.S. Government grant NAG W-2166. The images of these surveys are based on photographic data obtained using the Oschin Schmidt Telescope on Palomar Mountain and the UK Schmidt Telescope. The plates were processed into the present compressed digital form with the permission of these institutions.

[6] The Second Palomar Observatory Sky Survey (POSS-II) was made by the California Institute of Technology with funds from the National Science Foundation, the National Aeronautics and Space Administration, the National Geographic Society, the Sloan Foundation, the Samuel Oschin Foundation, and the Eastman Kodak Corporation. The Oschin Schmidt Telescope is operated by the California Institute of Technology and Palomar Observatory.

[7] The UK Schmidt Telescope was operated by the Royal Observatory Edinburgh, with funding from the UK Science and Engineering Research Council (later the UK Particle Physics and Astronomy Research Council), until 1988 June, and thereafter by the Anglo-Australian Observatory. The blue plates of the southern Sky Atlas and its Equatorial Extension (together known as the SERC-J), as well as the Equatorial Red (ER), and the Second Epoch [red] Survey (SES) were all taken with the UK Schmidt.

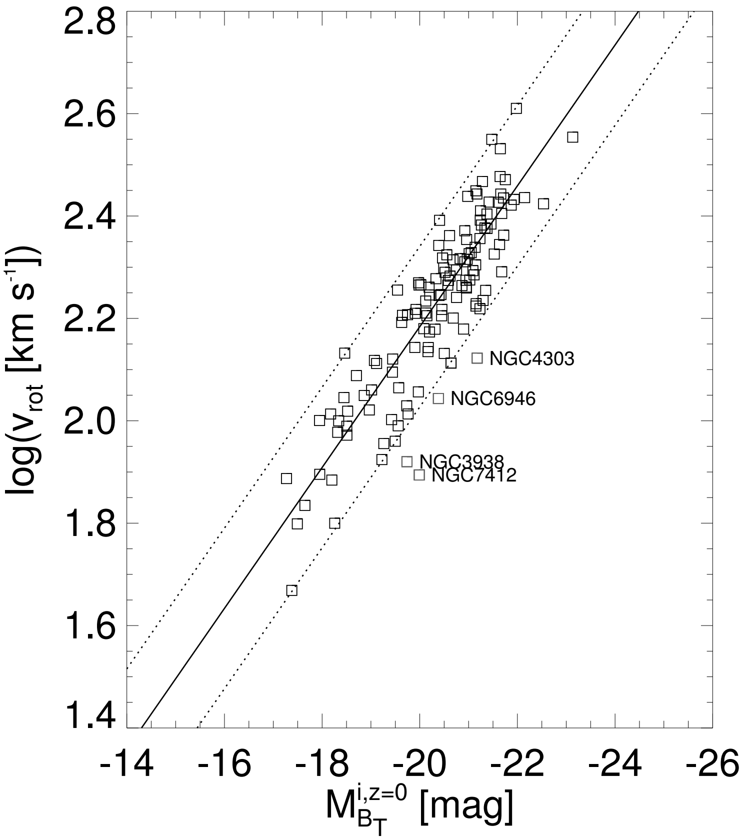

Figure 3.9: Tully-Fisher relation of the local sample

The Tully-Fisher relation of our local galaxy sample. All but 4 objects lie inside the 3σ-limits (dotted lines) of the local Tully-Fisher relation (solid line) by Tully and Pierce (2000). Object identifications of the four outliers are indicated. The reason for the outliers are the very low inclinations of those objects ($\sim 30°$). Therefore, small changes of their inclination could place them within the 3σ-limits.

of more than 2 magnitudes. Therefore, we adopt the distance measure for an object that moves it closest to the calibration line. As a result we obtain a similar scatter for our galaxies as Tully and Pierce (2000) and almost all galaxies (97%) lie within the 3σ confidence interval. Galaxies outside the 3σ-limits all have very low inclinations. A detailed discussion on the impact of inclination measurements is given below (see Sec. 3.6.1). The adopted distances are listed in Tab. 3.2.

3.5.2 Surface Brightness Profile Fits

To measure parameters like e.g. the central surface brightness, the exponential disc scale length or the inclination, the radial surface brightness profiles had to be extracted. We used the STSDAS package ELLIPSE, an add-on to IRAF, to measure iso-contours in the images. The routine creates a table containing the intensity, inclination, position angle and various other geometrical or flux related parameters in dependence of the radius. This table is then input for a routine that fits a bulge and disc to the 1-dimensional light profile.

All images, including HST, ISAAC and DSS data, were carefully background subtracted before attempting to fit profiles. This included in a few cases even removing close companion galaxies, since they would otherwise affect the background measurement of the IRAF ellipse fitting routine that generates the surface brightness profile. For this purpose we used the IRAF imedit task and replaced the objects in question by a fit to the background as estimated from an annulus surrounding this source. In the case of the DSS images we also removed bright stars that show shallow haloes around them in the same way, because they would have a similar effect as a companion galaxy.

In order to obtain the deepest possible data for the local galaxies we combined CCD images with DSS photographic plate data, which were usually deeper. To connect the two sets of data, though, we first had to convert the radii from pixels to arcseconds to get a common length scale. Furthermore, to enable fitting of a bulge, we deleted table entries at the inner edge of the profile according to the seeing or resolution of the images. The resulting table is input for a routine that combines the available photometric data with the surface brightness and distance information, converts the data into physical units and fits an exponential disc and a de Vaucouleurs bulge according to the following formulae:

$$\begin{aligned}
\text{Disc:}\quad \Sigma_d^{rest}(R) &= \Sigma_{0,d}^{rest} \cdot \exp\left(-\frac{R}{R_d}\right) \\
\text{Bulge:}\quad \Sigma_b^{rest}(R) &= \Sigma_{0,b}^{rest} \cdot \exp\left(-7.67\left(\left(\frac{R}{R_b}\right)^{1/4} - 1\right)\right)
\end{aligned} \tag{3.1}$$

with $\Sigma_d^{rest}(R)$, $\Sigma_b^{rest}(R)$, $\Sigma_{0,d}^{rest}$, $\Sigma_{0,b}^{rest}$ being the disc / bulge surface brightness and the central disc / bulge surface brightness, respectively (in $L_\odot$ kpc^{-2}). R is the radius, R_d the exponential disc scale length and R_b the bulge scale length (all in kpc).

Similar to the rescaling of the radii we also had to rescale the intensities of the DSS profiles to match the CD data. There are two major disadvantages, however, that have to be taken into account when dealing with photographic plates: The limited dynamic range and the linearity. The integration times of the DSS all sky survey images are so long that usually the centres of nearby bright galaxies are over-exposed. The region over which one loses density contrast is in many cases big enough that it becomes impossible to fit a bulge. This does not impose much of a problem, though, since the CCD data with their higher resolution and contrast can be used to extract all necessary information. Therefore, we clipped these over-exposed regions before trying to match the profiles. The remaining overlap was sufficient to calculate optimal fits for all of our galaxies and as a result we were able to extend the majority of our profiles by 20-50%. Unfortunately, there is not such an easy solution for correcting the flux linearity problem. Since photographic plates have to be linearised using micro-densitometers, this process of linearisation becomes a source of error itself. Again, one has to compare the photographic plate data with CCD images to quantify to amount of “non-linearity”.

It turned out that not only a scale factor had to be applied to match the CCD frames, but that we also had to correct for differing slopes of the extracted profiles. Fortunately, a simple power law could correct for this “non-linear” effect and match the two profiles perfectly. In general, we applied the following fitting formula to match the two profiles:

$$I_{CCD} = (A \cdot I_{DSS})^{\beta} \tag{3.2}$$

here, I_{CCD} and I_{DSS} denote the intensities measured in the CCD and DSS frames, respectively, and the scale A and slope β are the fit parameters. The slope β varied from galaxy to galaxy, according to the quality of the linearisation of the respective photographic plates. It defines directly the percentage by which an exponential scale length would differ from a CCD measurement. In Fig. 3.10 we present a histogram which shows the distribution of the slope parameter β. Although the mean of the distribution is only offset by $\sim 4\%$ the spread is rather big. The average DSS profile has a measurement error of ±8%, but the individual measurement could easily be off by $\sim 20\%$. Therefore, we conclude that studies of big samples are only marginally affected by the varying quality of the linearisation of the DSS plates. However, single case studies will almost certainly result in rather insecure measurements.

To perform such a profile splicing we assumed that a powerlaw fit like eq. 3.2 can account for the differences in the differing scales and slopes and, furthermore, that there are no higher order non-linearities inherent to the DSS data. However, in the 9 cases where the CCD data were deep enough to span at least the same range of isophotal radii as the DSS images we could prove that this assumption is valid. But even in the cases were the CCD profiles extended only out to 80% of the total combined profile (56% of all local sample galaxies) the agreement of the matched profiles was excellent (see Fig. 3.11). In these cases no major differences were found after applying the fit. Even local variations like spiral arms or dust lanes were reproduced in the DSS profile (see Fig. 3.12). On average the 25% increase in radius corresponds to 1.5 mag deeper surface brightness limits (see Fig. 3.13). In the following discussion all results are based on the combined CCD plus DSS light profiles.

To obtain absolute rest-frame central disc-bulge surface brightnesses, we had to calculate a scale factor S first that converts instrumental counts I (disc / bulge intensity profiles $I_d(\vartheta)$, $I_b(\vartheta)$ depending on the radius ϑ in arcsec and central disc / bulge intensities $I_{0,d}$, $I_{0,b}$; intensities in counts arcsec^{-2}) to physical units (corresponding disc / bulge surface brightness profiles $\Sigma_d^{rest}(\vartheta)$, $\Sigma_b^{rest}(\vartheta)$ and disc / bulge central surface brightnesses $\Sigma_{0,d}^{rest}$, $\Sigma_{0,b}^{rest}$ in $L_\odot$ arcsec^{-2}):

$$\Sigma^{rest} = S \cdot I \tag{3.3}$$

Taking the absolute magnitude M_B^{rest} as the zero-point the scale S follows from the total disc and bulge luminosities:

$$S = \frac{10^{-0.4\left(M_B^{rest} - M_{B,\odot}\right)}}{2\pi \cdot \vartheta_d^2 \cdot I_{0,d} + 7.22\pi \cdot \vartheta_b^2 \cdot I_{0,b}} \tag{3.4}$$

ϑ_d and ϑ_b are the disc and bulge scale radii in arcsec, respectively. We assumed an absolute B-band magnitude of the sun $M_{B,\odot} = 5.54$ mag (Unsöld and Baschek, 1991).

Furthermore, we had to convert the surface brightnesses from a luminosity density (Σ^{rest} in $L_\odot$ arcsec^{-2}) to a magnitude scale (μ^{rest} in mag arcsec^{-2}). This conversion also had to take the dimming of the surface brightness with redshift into account. We derived the following zero-point μ_{zp}:

$$-2.5 \log \Sigma^{rest} + \underbrace{M_{B,\odot} + 5 \log \frac{D}{[\mathrm{Mpc}]} + 25 - 2.5\gamma \log(1+z)}_{\mu_{zp}} = \mu^{rest} \tag{3.5}$$

with the distance D in Mpc to convert the various disc and bulge surface brightnesses ($\Sigma_d^{rest}(\vartheta)$, $\Sigma_b^{rest}(\vartheta)$, $\Sigma_{0,d}^{rest}$, $\Sigma_{0,b}^{rest}$) from a luminosity density to a magnitude and $\gamma = 4$, the exponent for the surface brightness dimming law.

Aside from the surface brightness dimming with redshift, there is another difference between the local and the high redshift data: the limiting surface brightness. After calibrating local and high redshift profiles we found that on average the high redshift profiles just extended out to

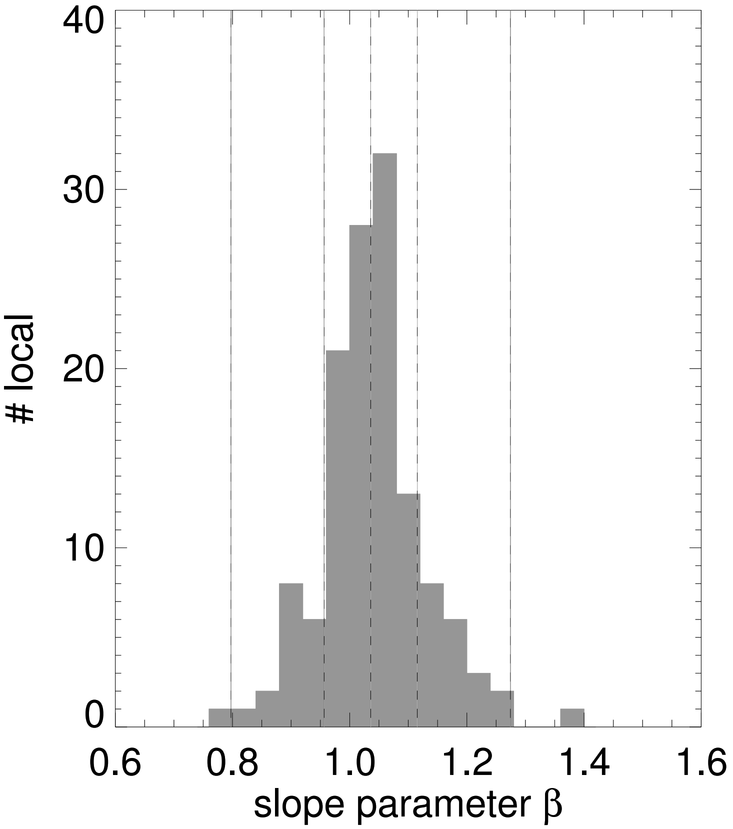

Figure 3.10: Histogram of the photgraphic plate scale parameter β

The scale parameter β (shaded histogram) and the mean, ±1σ and ±3σ uncertainties (vertical lines). About 30% of the data deviate by more than 8% from the mean of the distribution.

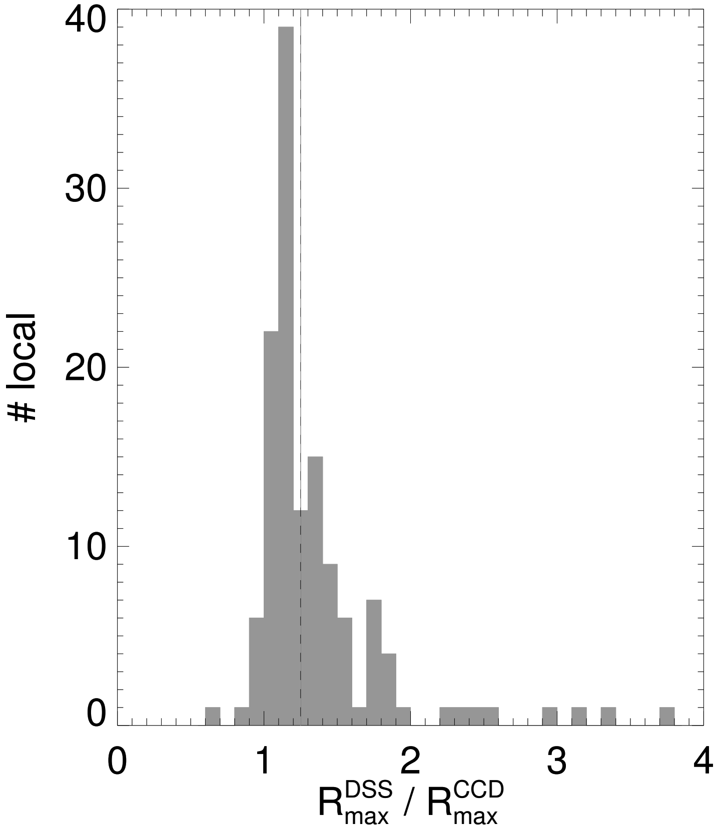

Figure 3.11: Ratio of the extent of DSS and CCD profiles

The ratio of the maximum extent of the DSS profiles and the maximum extent of the CCD profiles illustrates that on average splicing CCD and DSS profiles could increase the radial extent of our profiles by 25%. In the cases were the ratio of the extent of the profiles was smaller than 1 or at least 1.25 (7% and 56% of all galaxies) we could show that correcting the linearity of the photographic plates resulted in excellent agreement between the two profiles.

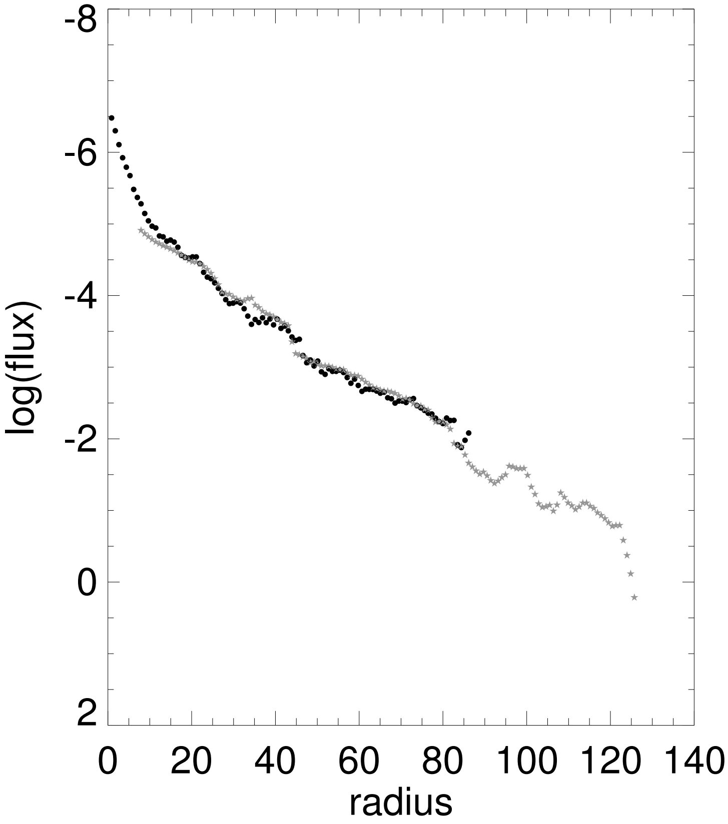

Figure 3.12: Splicing of CCD and DSS profiles

The CCD (black circles) and DSS (grey stars) light profiles of NGC2280 (flux and radius in arbitrary units). After applying our correction the profiles coincide to a very high degree. The central region of the DSS profile was clipped, effectively excluding over-exposed regions.

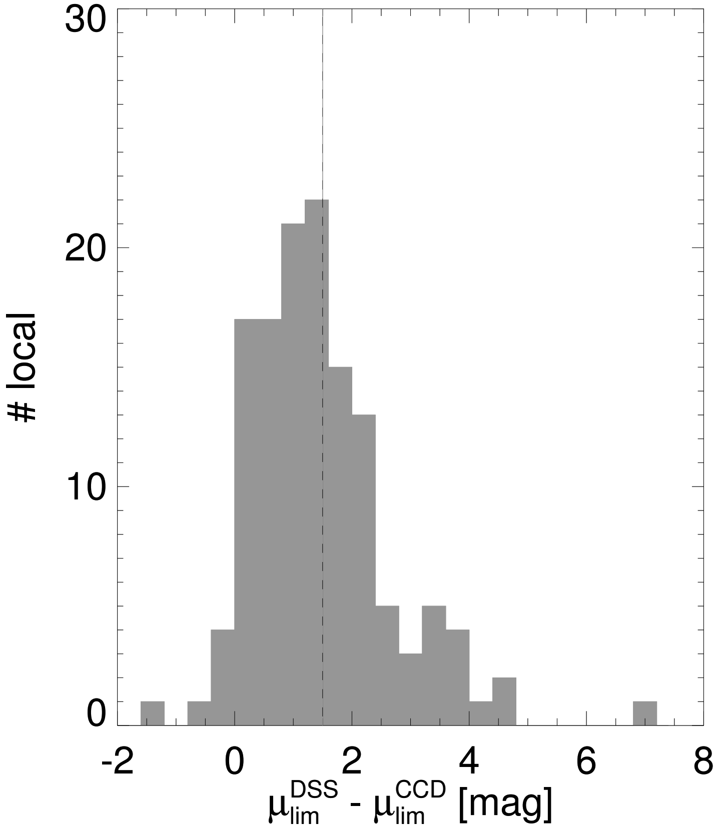

Figure 3.13: Difference of the limiting surface brightnesses of the DSS and CCD profiles

Histogram of the difference of the surface brightness limits of the CCD and photographic plate light profiles. For the cases where the DSS image was deeper than the corresponding CCD frame, we find on average a depth increase of 1.5 mag (vertical line).

limiting surface brightnesses in the rest-frame around 24 mag arcsec^{-2} whereas the local galaxies where easily detectable even at levels as faint as $\sim 26 - 29$ mag arcsec^{-2}. This resulted directly from the surface brightness dimming with redshift. The signal-to-noise ratios of the images of the high redshift galaxies would have had to be much better than that of the local images to achieve the same image quality in terms of depth. However, this would require unreasonably large integration times especially for the HST.

To explore the effect of this on the extracted scale lengths and central surface brightnesses, we artifically truncated the local profiles at different radii. Starting at 10% of the total radius we fitted a disc-bulge model every 5% out to the maximum radius. For the ideal case of an exponential disc with a de Vaucouleurs bulge one should of course not expect any variation of the extracted disc / bulge properties with radius. However, real galaxies with spiral arms and dust lanes or -even worse- varying profile shapes do exhibit such changes with radius. This effect should not be as pronounced for the bulge as for the disc, but since the disc profiles determine the amount of light that is left for a bulge even the quality of the bulge fitting depends to some extent on the limiting radius. Extracting bulge / disc and inclination values at different radii allows us to remove such effects. Where spiral arms and dust lanes should reveal themselves as local increases or dips, profile changes would be measured as global variations of (primarily) the disc parameters. Fitting a quadratic function as a function of limiting radius R_{lim} or surface brightness μ_{lim} to the various parameters excluding obvious outliers has a stabilising effect on the finally adopted parameters. In Fig. 3.14 we plot the measurements of disc scale length, disc central surface brightness, bulge scale length, bulge central surface brightness and inclination (from bottom to top) as a function of limiting surface brightness. The proposed quadratic fit obviously is a perfect method of "smoothing" over local profile features, thus providing a more stable value at the corresponding radius.

We now have to specify the radius or surface brightness at which we measure our model values. Since the high redshift galaxies show a range of different limiting radii R_{lim} we opted against chosing just one fixed R_{lim} for the local sample. To match the depth of the images of the high redshift targets, we chose the mean value of the different surface brightnesses to measure the profiles. Because of the morphological deviations from the ideal form this mean value does not trivially correspond to the middle of the minimum and maximum radius at which we truncated the profiles (see Fig. 3.14). Since the resulting limiting surface brightness was still too faint compared to the high redshift value we subtracted another 0.5 magnitudes. Simply moving to brighter limiting surface brightnesses can be misleading. For very shallow profiles, i.e. objects with extremely large disc scale length, subtracting 0.5 mag could lead to exceeding or at least getting too close to the surface brightness measured at the centre to still allow fitting of the light profile. Fortunately, only in one case we found that this effect severely biased the result.

To demonstrate the result of this scheme, we plot the limiting radius R_{lim} of the high redshift galaxies and the truncated profiles of the local objects versus the isophotal radius R_{25} (see Fig. 3.15). There is one object in this plot that falls below the average correlation between R_{lim} and R_{25}, and this source indeed showed a very steep light profile. Furthermore, as was conjectured in Sec. 3.2.2, after removing the redshift dependence (by converting apparent sizes to kpc) and truncating the local profiles, the limiting radius correlates very well with isophotal size. From Fig. 3.15 we find that all objects lie below or at least very close to the line where $R_{lim} = R_{25}$. As a result of this we can conclude that our estimates of isophotal radii and even more so disc scale lengths (which are generally smaller than R_{25}) are well determined.

The method of truncating the local profiles is not quite perfect, though. Comparing the histograms of R_{lim} of the two samples shows that they agree quite well (see Fig. 3.16). The truncated local sample appears to have a slightly narrower distribution than the high redshift galaxies and their limiting radii seem a little smaller as well (local: 11.6 kpc $\longleftrightarrow$ high-z: 14.1 kpc). This is not really a problem since the effects of limited depth should get more pronounced with smaller limiting radii. Therefore, we rather over- than underestimate the expected effect. Furthermore, we have compared the limiting surface brightness distributions of both samples (see Fig. 3.17). The means of these two distributions coincide closely (local: 23.81 mag $\longleftrightarrow$ high-z: 23.71 mag), but again their variances do not agree. Since the local limiting surface brightnesses are

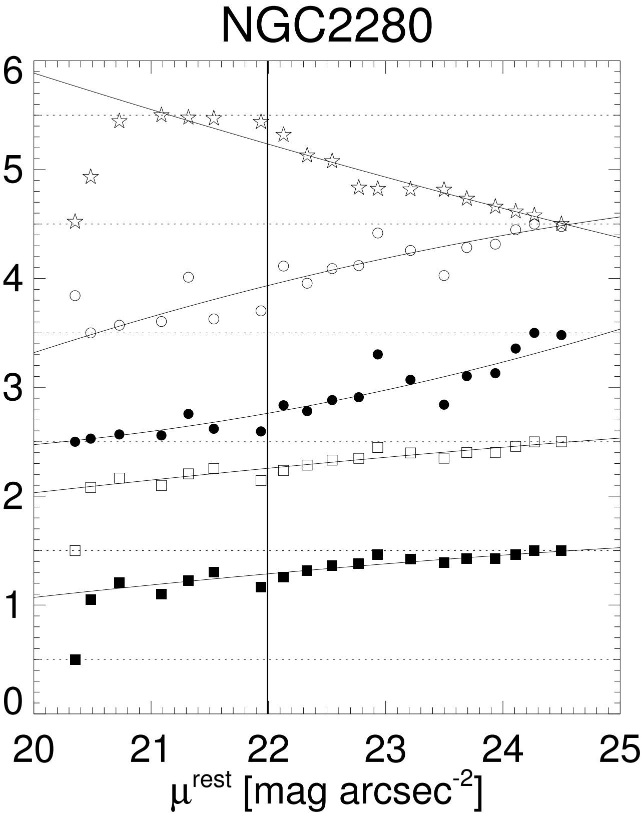

Figure 3.14: Impact of limiting surface brightness on fitting parameters

Resulting disc scale length (filled boxes), central disc surface brightness (open boxes), bulge scale length (filled circles), central bulge surface brightness (open circles) and inclination (open stars) as a function of limiting surface brightness (horizontal axis). The vertical axis is in arbitrary units. The adopted values are taken at the intersection of the quadratic fit (thin solid lines) with the thick vertical line.

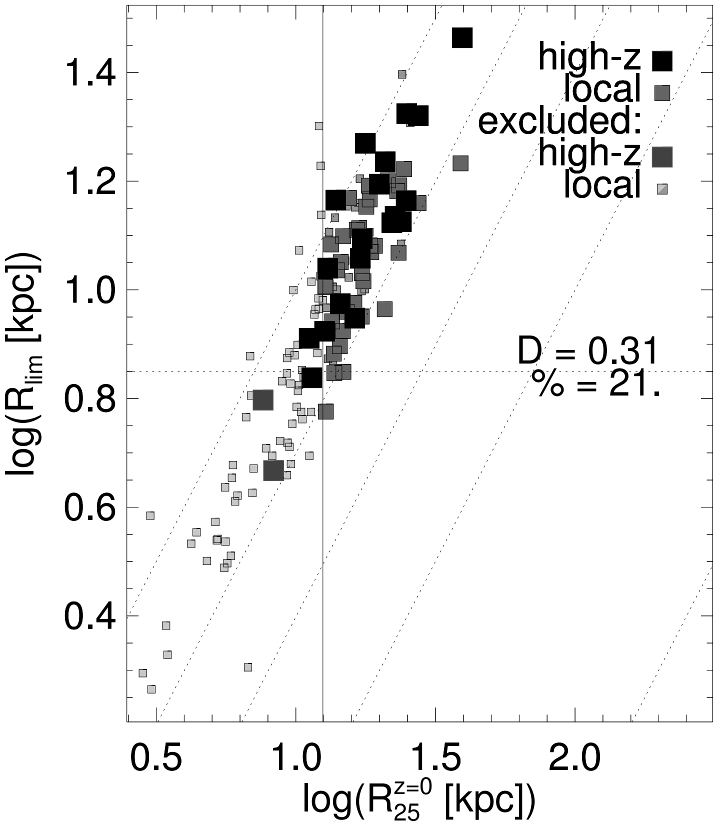

Figure 3.15: R_{lim} versus R_{25}

The limiting radii R_{lim}, which roughly correspond to the apparent sizes on the sky (measured at $\sim 5\sigma$ of the sky background noise), versus the isophotal radii R_{25} for high redshift (large symbols) and local galaxies (small symbols). Large grey boxes represent high redshift galaxies and small light grey boxes symbolise local galaxies that were excluded from the statistical analysis for not fitting the R_{25} selection criterion (see Sec. 3.2). Small dark grey boxes show local galaxies that were rejected from the sample to match the RC3 catalogue distributions of R_{25}, M_B and v_{rot}. The diagonal lines indicates the locus of $R_{lim} = a \times R_{25}$ with a=1, 0.5, 0.25, 0.1, 0.01. For most of our galaxies R_{lim} is between 50% and 100% of R_{25}. The horizontal line is a rough conversion of apparent size to limiting radius (neglecting the redshift dependence). The vertical line marks the $R_{25} > 12.5$ kpc selection criterion. A KS-test indicates that both have the same R_{lim} / R_{25} characteristics (middle right). It should be noted that one cannot infer from this plot the possible locus of objects missed in the two samples. The lowest surface brightness objects e.g. of the local sample have the same distribution as the rest of the sample and are not preferentially found in one of the corners of the plot.

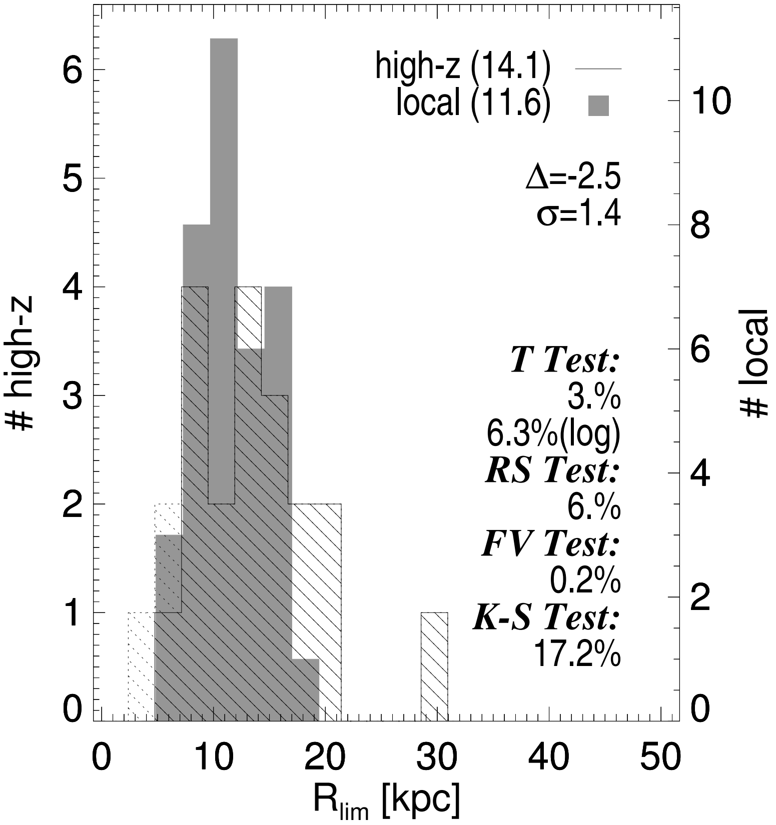

Figure 3.16: Histograms of R_{lim}

Histograms of the limiting radii R_{lim} of the low (shaded region) and high redshift (striped region) samples. The means for both distributions are indicated in brackets in the upper right corner. The difference of the two means Δ and its 1σ error is shown above a set of statistical tests (lower right), including a student's T-test (on a linear and a logarithmic scale), a rank-sum test, a variance test and a Kolmogorov-Smirnov test, respectively. The dotted high redshift galaxies were excluded from the statistical analysis for not fitting the R_{25} selection criterion (see Sec. 3.2).

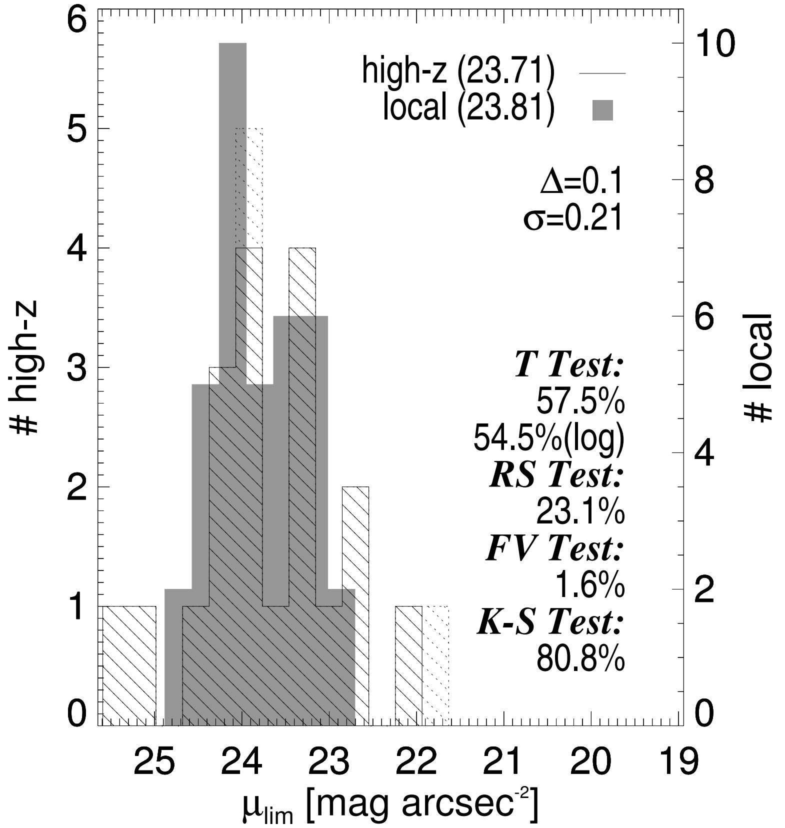

Figure 3.17: Limiting surface brightnesses μ_{lim}

Histograms of the limiting surface brightnesses μ_{lim} of the low (shaded region) and high redshift (striped region) samples. The means for both distributions are indicated in brackets in the upper right corner. The difference of the two means Δ and its 1σ error is shown above a set of statistical tests (lower right), including a student's T-test (on a linear and a logarithmic scale), a rank-sum test, a variance test and a Kolmogorov-Smirnov test, respectively. The dotted high redshift galaxies were excluded from the statistical analysis for not fitting the R_{25} selection criterion (see Sec. 3.2).

a little smaller than the high redshift ones, one could think of trying to shift the local distribution to brighter surface brightnesses. However, this would then also imply moving to smaller limiting radii. We do not have this option, though, since R_{lim} for the local galaxies is already smaller than that for the distant sources. Thus, we conclude that we have found an acceptable compromise to mimic the image quality of the high redshift sample in terms of limiting radii and surface brightnesses by truncating the local galaxies' light profiles.

The procedure of truncating the profiles involved fitting of the measured shape parameters, which had a stabilising effect on the local data. The reason for this was the smoothing of fluctuations in the light profile. Since in the case of the high redshift data one could be affected by the same problem, e.g. in a case where the profile ends right on top of a spiral arm, we adopted a similar technique to stabilise these results as well. In their case, however, we could not afford to "waste" any dynamic range and so we chose our maximum radius as the limit. Furthermore, instead of starting at 10% of the total radius we use at least the outermost 35% of the profile and adopt a spacing of 2.5%. Again, the resulting model parameters are much more robust than the single measurement values and this procedure ensures that we are treating the two samples (high and low redshift) in the same way.

Another difference between the data is that the local galaxies have their scale lengths measured naturally in the rest-frame B-band. On the other hand, the high redshift HST F814W-images do not necessarily cover the rest-frame B-band. Since it is known from local data (e.g. de Jong, 1996b) that disc scale lengths get systematically smaller with wavelength, we have to estimate the magnitude of this effect. We plot the ratio of the disc scale lengths in the B-band over the disc scale lengths measured in the V-, R-, I-, H- and K-band for all 86 galaxies of the de Jong (1996b) sample (see Fig. 3.18). Although a linear relation breaks at rest-frame V-band and the relation at smaller wavelengths gets extremely steep (unfortunately, we do not have the means to model this regime), we find that our redshift range is small enough that the large majority of all high redshift galaxies has their disc scale length measured close enough to rest-frame B-band that errors do not exceed 5%. Only in two cases this systematic error is $\approx 10\%$ and therefore, we can use our F814W-measured disc scale lengths without applying any corrections. Furthermore, the four cases with J-band image-based disc scale lengths also have systematic errors of $\sim 7.5\%$. But although the rest-frame B-band in those cases lies in a region where one could apply a linear fit, we refrain from doing so, since measurement errors are of comparable size and even larger. In summary, the lack of rest-frame measurements of disc scale lengths and also isophotal radii does not impact on our subsequent discussion.

The R_{25} selection

Fortunately, for observational reasons (see Sec. 3.2.1) our high redshift sample was selected to only include objects larger than some minimum apparent size. The problem now is that a direct comparison becomes impossible because of the entirely different distances of the two samples. We have to convert the apparent size first to some intrinsic distance-independent variable. In Fig. 3.19 we plot the apparent sizes of the high redshift galaxies versus the isophotal radius R_{25}. Obviously apparent size on the sky correlates well with R_{25}. This is not surprising, though, since the apparent size depends on redshift and depth of the images only. For objects at the same redshift and with images of the same depth one should find a rather perfect correlation. Therefore, R_{25} seems to be a perfect variable to restrict the local sample in the same fashion as the high redshift galaxies.

But there is even more evidence that the high redshift galaxies appear to be selected by R_{25} rather than by R_{lim} (see Fig. 3.15). A selection in R_{lim} should have resulted in a few objects inside the triangle enclosed by the three lines in Fig. 3.15. Since no such object was selected although we picked up a few objects even smaller, a selection based on R_{25} is justified. Another point to make here is that truncating the local profiles seems to recover exactly the same behaviour as that found for the high redshift galaxies. We do neither observe an offset nor change in slope between the two distributions. Even the scatter appears to be the same and indeed a 2-dimensional K-S test signifies that the two groups cannot be distinguished from each other. Therefore, to impose

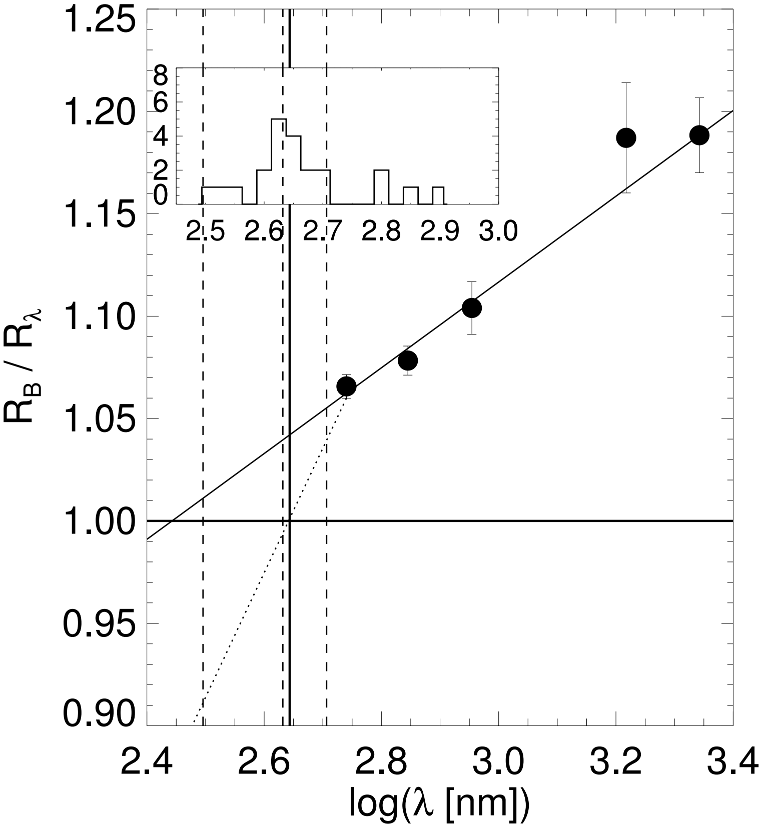

Figure 3.18: Disc scale lengths as a function of wavelength

The means of the disc scale length ratios R_B/R_λ as a function of wavelength (solid circles). The diagonal line is a linear least-squares fit to the data. Unfortunately, the relation breaks down at $\lambda \approx 550$nm. The fit should cross 1 precisely at $\lambda = 440$nm (thick horizontal and vertical lines). We also plot a simple linear extension for $\lambda < 550$nm (dotted line). Since we could not obtain data at smaller wavelength a more complex modelling of this regime becomes impossible. However, our evaluation of observed frame I-band disc scale length should only be minimally affected by this. We mark the range of rest-frame B-band for our high redshift galaxies by the thin vertical dashed lines (minimum, mean, maximum redshift). Furthermore, the inset shows the distribution of rest-frame observed wavelength of the distant sample. The mean is very close to rest-frame B-band and our systematic errors should be smaller than 5% for the majority of the cases with 1 or 2 exceptions as large as ∼10%.

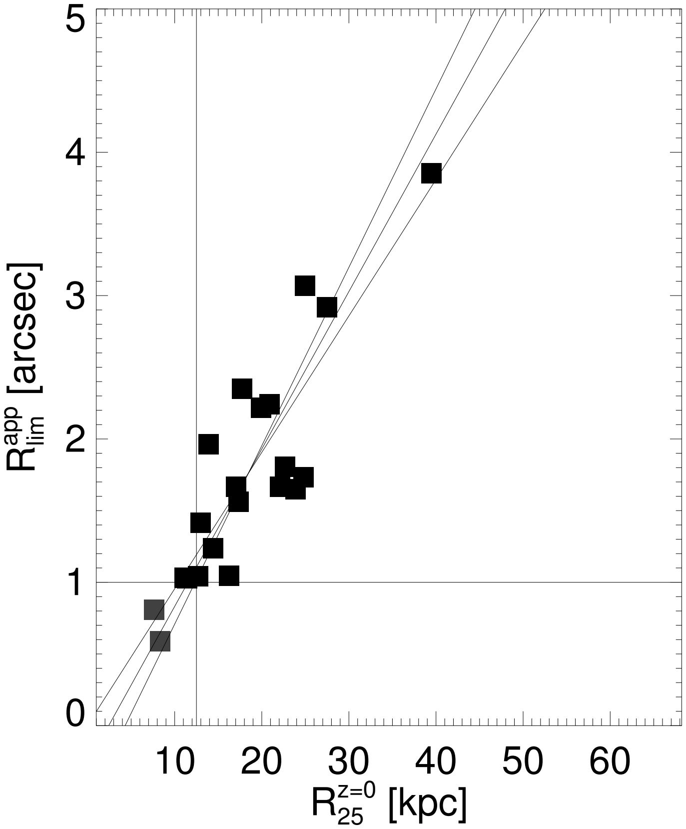

Figure 3.19: Apparent versus isophotal sizes of the high redshift galaxies.

From plotting the apparent sizes of our high redshift galaxies versus their isophotal radii it follows that selecting objects greater than some angular size on the sky is equivalent to applying a cut-off at a certain isophotal radius. Diagonal lines show a bisectorial fit to the data. According to this fit an apparent limiting radius $R_{lim}^{app} = 1''$ corresponds to an isophotal radius $R_{25} = 12.5$ kpc. Grey boxes represent objects that do not fit the selection criteria for being too small ($R_{lim} < 1''$).

the same size selection bias also on our local sample we only included galaxies with $R_{25} \geq 12.5$ kpc.

3.5.3 Inclinations

A proper estimate of the inclination of an object becomes an important issue especially since the Tully-Fisher relation is sensitive to inclination errors. On one hand it is used to correct the rotation velocities to their edge-on values (at an inclination of 30° the inclination correction amounts to a factor of 2) and on the other hand it determines the amount of internal extinction in a spiral galaxy (~ 0.7 mag to correct an edge-on galaxy to face-on, using equation (2) of Tully and Fouque, 1985 for $i = 80°$). Inclinations i are usually derived by measuring the ratio of the minor to the major half-axis $\frac{b}{a}$ of a galaxy. Using Hubble's formula one can then calculate the inclination assuming an intrinsic minimal axis ratio (e.g. Holmberg, 1946):

$$\cos^2(i) = \frac{(b/a)^2 - q_0^2}{1 - q_0^2} \tag{3.6}$$

with $q_0 = 0.2$, the intrinsic axis ratio. For the sake of simplicity we will neglect evolutionary effects of the scale heights of disc galaxies (e.g. Samland and Gerhard, 2003), which could influence the exact value of q_0. Since our high redshift galaxies are usually highly inclined such an increase should not affect the subsequent conclusions. When measuring our surface brightness profiles we also calculated the radial dependence of the intrinsic half-axis ratio and therefore the inclination. We adopted a mean value of the outer half of all measurements as our inclination for a certain limiting radius. Since the radial dependence could impact on the final value of the inclination, we apply the same fitting technique at different radii as for the other bulge and disc parameters (see Sec. 3.5.2). We compared our measurements (without degrading them to match the high redshift data) for the local galaxies with the values given in the RC3 and LEDA at their respective limiting surface brightnesses. No significant differences where found. In the very few cases where the two methods did not agree we took a new approach and measured the axial ratio manually on the image frames. It turned out that on one hand the ellipse fitting algorithm had failed on some isophotes (in these cases our manually derived value was very close to the one from RC3 or LEDA). Fine tuning the ellipse fitting could usually recover the RC3 / LEDA value. On the other hand we found that for very high inclinations both RC3 and the ellipse fitting produced too low values. LEDA gave usually better estimates, but anyhow we calculated new values by following morphological features in some regular galaxies (dust lanes, spiral arms). We found that the LEDA values were very close to ours and therefore adopted their estimate for all highly inclined objects. This problem with highly inclined objects, however, has no impact on subsequent corrections of e.g. the rotation speed. The histogram of the inclinations of local galaxies (see Fig. 3.20) measured after truncation reveals that the mean value is not significantly affected in both cases. The truncation of local profiles results in a mean offset from the "true" value, i.e. the value derived from the full light profile, of $0.09° \pm 0.45°$ while stabilising the high redshift values with the same procedure shifts the values by $0.05° \pm 0.04°$. The individual inclination measurements should on average be accurate to $\pm 5°$.

Since the objects become smaller and fainter with distance we have to worry about the impact of this on our extracted properties. With sizes on the sky of only a few arcseconds, the ground based seeing becomes a limiting factor for extracting e.g. inclinations. With seeing values of half the size of the major axis of the object only lower limits can be computed for the inclination, which will then over-correct the rotation speed for Tully-Fisher relations. Furthermore, with roughly 20-50% of the galaxy being blurred by the seeing fitting a central bulge becomes almost impossible for ground-based data.

Unfortunately, in four cases we had to rely on ground-based images alone to estimate inclinations. Plotting the Tully-Fisher relation for the high redshift galaxies reveals that those objects are amongst the fastest rotators in the respective magnitude bins. This is a direct consequence of overestimating the rotation velocity by using inclinations that are too small. To compensate for

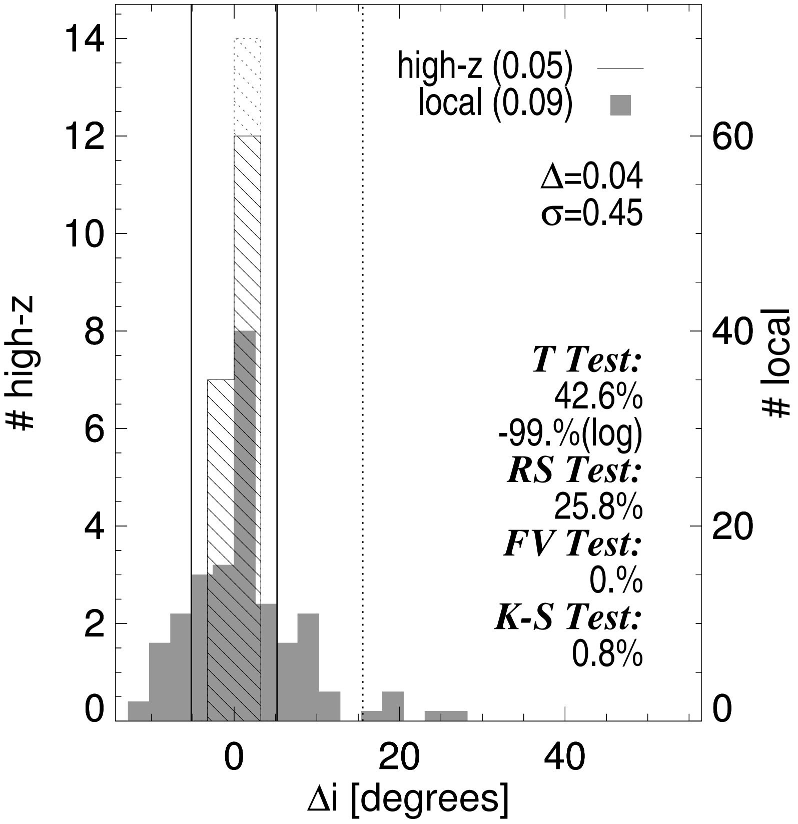

Figure 3.20: The effect of profile truncation on inclination

Histograms of the change of the inclinations after truncation of the light profile of the low (shaded region) and high redshift (striped region) samples. The means for both distributions are indicated in brackets in the upper right corner. The difference of the two means Δ and its 1σ error is shown above a set of statistical tests (lower right), including a student's T-test (on a linear and a logarithmic scale), a rank-sum test, a variance test and a Kolmogorov-Smirnov test, respectively. The dotted high redshift galaxies were excluded from the statistical analysis for not fitting the R_{25} selection criterion (see Sec. 3.2). The solid and dotted vertical lines represent the 1σ and 3σ confidence limits excluding outliers, respectively.

this effect we simulated images of disc galaxies in IRAF with pixel scales similar to WFPC2. These model images were then smoothed according to the seeing and the pixel scale of the ground-based data. After that we extracted a surface brightness profile and compared the light profiles and inclination angles of simulation and observed image. Iteratively, we tried to create an HST image that would match the ground-based frame by adapting the inclination, scale radii and central surface brightnesses of disc and bulge. Once a perfect match was found we compared the "simulated" with the "measured" inclination. The simulated inclinations were on average 35% larger than the measured ones and therefore we adopted these values for the subsequent evaluation. We demonstrate the effect of this by plotting the the Tully-Fisher relation before and after correcting the ground-based data (see Fig. 3.21).

Table 3.4: Inclination corrections for high-z targets with ground-based images

ID (1)	i' deg (2)	i deg (3)	v'_{rot} km s^{-1} (4)	v_{rot} km s^{-1} (5)	$A_B^{i\prime}$ mag (6)	A_B^i mag (7)
CFRS-00.0174	47.8	78.5	154	116	0.11	0.64
CFRS-00.0308	36.8	42.5	96	86	0.06	0.09
LDSS-03.219[a]	56.5	56.5	101	101	0.18	0.18
CFRS-00.0137	36.4	45.1	283	237	0.06	0.10

[a] imaging data were not sufficient for simulation.

Note. – (1) object identification; (2)(4)(6) i', v'_{rot}, $A_B^{i\prime}$ symbolise the uncorrected values from as derived from the ground-based imaging data for inclination, rotation velocity and internal extinction, respectively; (3)(5)(7) i, v_{rot}, A_B^i are the adopted values as obtained from the simulations for inclination, rotation velocity and internal extinction, respectively.

3.5.4 Rotation Speeds

The rotation speed of the high redshift galaxies we estimate by fitting a simple model with a constant terminal velocity (see Sec. 3.4.1). Before using this "measured" rotation velocity v'_{rot} for Tully-Fisher applications, however, one has to correct for the effect of inclination. Since in most cases we do not observe the object completely edge-on, the recession velocities we measure along the target do not only have vectorial components directly towards or away from the observer, but also perpendicular to this direction. Therefore, the component we measure v'_{rot}, gets smaller with decreasing inclination i. However, it is possible to compute the edge-on rotation speed v_{rot} easily by applying a simple formula:

$$v_{rot} = \frac{v'_{rot}}{\sin{(i)}} \tag{3.7}$$

Unfortunately, there is no straightforward way to estimate the error in v'_{rot}. We will therefore assume that the resolution of the detector defines the prime source of error in v'_{rot}. In order to estimate the error of the rotation speed v_{rot} we also have to take the error in the inclination into account. Converting the inclination error from degrees to a rotation speed we find that rotation speed estimates become very insecure when derived for face-on systems ($i < 30°$).

One might argue that although all necessary care was taken in reducing the data and extracting the rotation curves we do not sample the full rotation rotation curve, thus underestimating the true rotation speed. There are several pieces of evidence that our rotation curves are indeed sufficient to obtain proper estimates of the target's rotation speed. First of all we compare the spatial extent of the extracted rotation curves with the limiting radius R_{lim}, which provides a reasonable measure of the spatial extent of the visible part of the targets. We define the (spatial)

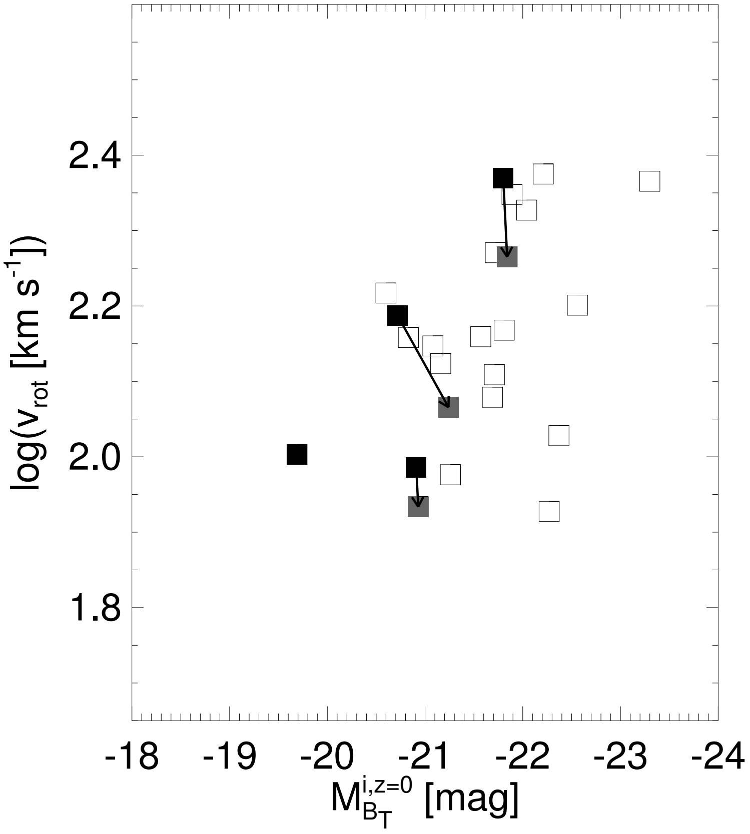

Figure 3.21: The Tully fisher relation and the impact of seeing

The Tully Fisher relation for our high redshift galaxies. For objects with solid symbols we could only obtain ground-based images. Without correcting for the effect of seeing, rotation velocities are too high and absolute magnitudes to faint (internal extinction correction). After correcting for the seeing, those objects (grey solid symbols) are more consistent with the remaining data (open symbols). For one object we could not simulate the "true" inclination (lower left solid object). In this case we adopted the inclination as derived from the ground-based data. Assuming a totally edge-on orientation would place it at a ~ 0.08 dex lower rotation speed and at ~ -0.52 mag brighter absolute magnitude. This object does not fulfil the R_{25}-selection criterion and has therefore no impact on the remaining discussion.

extent of the rotation curve R_v by the minimum and maximum extracted data points, i.e. the "left" and the "right" end, of the rotation curve plus half of the adopted seeing converted to kpc. Plotting the ratio R_v/R_{lim} (see Fig. 3.22) we find that more than 75% of our rotation curves reach out farther than R_{lim} and only $\sim 5\%$ do not reach at least 50% of the optical extent.

Furthermore, rotation curves of disc galaxies are commonly modelled using the following profile (see Binney and Tremaine, 1987):

$$v_{d,circ}^2(R) = 4\pi G\Sigma_0 R_d \cdot y^2 \cdot [I_0(y)K_0(y) - I_1(y)K_1(y)] \tag{3.8}$$

with the rotation speed $v_{d,circ}$ at radius R, the gravitational constant G, the central surface brightness Σ_0, the disc scale radius R_d, $y = R/(2R_d)$ and $I_i(y)$ and $K_i(y)$ with $i = 1,2$ the modified Bessel functions of the first and second kind, respectively. Such a profile peaks in velocity at $R_{2.2} \approx 2.16R_d$. Therefore, plotting the radial extent R_v versus $R_{2.2}$ shows (see Fig. 3.23) that for the majority of our high redshift objects, the rotation speed we derive must indeed be very close to the maximum rotation speed.

Finally, to check the intrinsic consistency of our data, we divided the high redshift galaxies into a high quality and a low quality sample (50% best rotation curves, 50% worst rotation curves). This division is a subjective attempt to measure whether a turn-over or flat part of the rotation curve is visible or not. Plotting the offset –in magnitude space– from the local Tully-Fisher relation by Tully and Pierce (2000) versus the absolute mangitude M_B we find -2.00 ± 0.25 mag for the high quality and -1.68 ± 0.32 mag for the low quality samples (see Fig. 3.24). Therefore, **we conclude that there is also no intrinsic trend inherent in our data that the rotation curves where no turn-over is obvious would systematically show lower rotation velocities than the rotation curves with more prominent flat parts.**

To be conservative with our following discussion of the Tully-Fisher relation, for the local galaxies we did not measure the maximum rotation speed. Instead we used the rotation speed in the flat region of the rotation curves, which is less than the maximum rotation speed (at least for very peaky profiles). This results in a good match with the calibration of the Tully-Fisher relation given in the literature (Tully and Pierce, 2000). And furthermore, since the resolution even in the HST images, is not comparable to the resolution of the local images, where dust lanes and spiral arm structures help in defining a proper inclination, we might be underestimating the inclination angles. This would result in too large corrections for the rotation speeds. Knowing the "true" inclination could therefore only reduce our estimate of the rotation speed. Thus, **any offset seen in our high redshift Tully-Fisher relation in comparison to the local one towards lower rotation speeds / brighter magnitudes cannot be explained with underestimation of the rotation velocity of the high redshift sources due to inclination corrected systematic uncertainties.**

3.5.5 Absolute Magnitudes and Colours

Another quantity has to be described in some detail: the absolut magnitudes. To convert total apparent magnitudes in the observed frame into total rest-frame B-band magnitudes we need to know several additional parameters.

First of all one has to correct the apparent magnitudes for the extinction caused by the interstellar material in our own galaxy. This extinction depends on the wavelength (it gets higher in bluer bands) and therefore has to be applied according to the observed wavelength regime. Furthermore, it strongly depends on the position of the object on the sky, i.e. the position relative to the Milky Way. In the plane of the Milky Way the extinction is extremely high, especially towards the centre, and it decreases considerably towards high galactic latitudes. The amount of extinction in the optical wavelength regime is usually derived from all-sky maps taken at infrared wavelengths (Schlegel et al., 1998). Using NED we could obtain the values calculated by Schlegel et al. (1998) for every object.

Besides the extinction from our own galaxy we have to include also the extinction caused by the target galaxy itself. Unfortunately, this is a rather challenging task, especially for spiral galaxies,

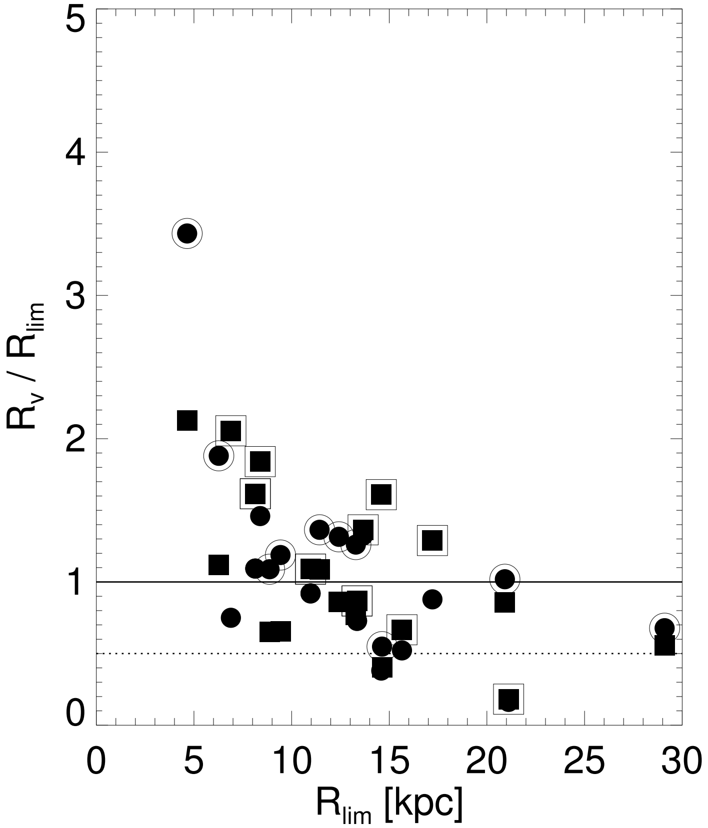

Figure 3.22: Radial compared to optical extent of the high-z rotation curves

Ratio of spatial extent of the high redshift rotation curves R_v and the optical limiting radius R_{lim} as a function of R_{lim}. Boxes and circles represent the minimum ("left") and maximum ("right") ends of the rotation curves. The largest extent for each object is additionally marked by a surrounding square or circle. In more than 75% of all sources R_v is larger than R_{lim} (solid line). Only $\sim 5\%$ of the rotation curves do not reach at least half the optical size (dotted line).

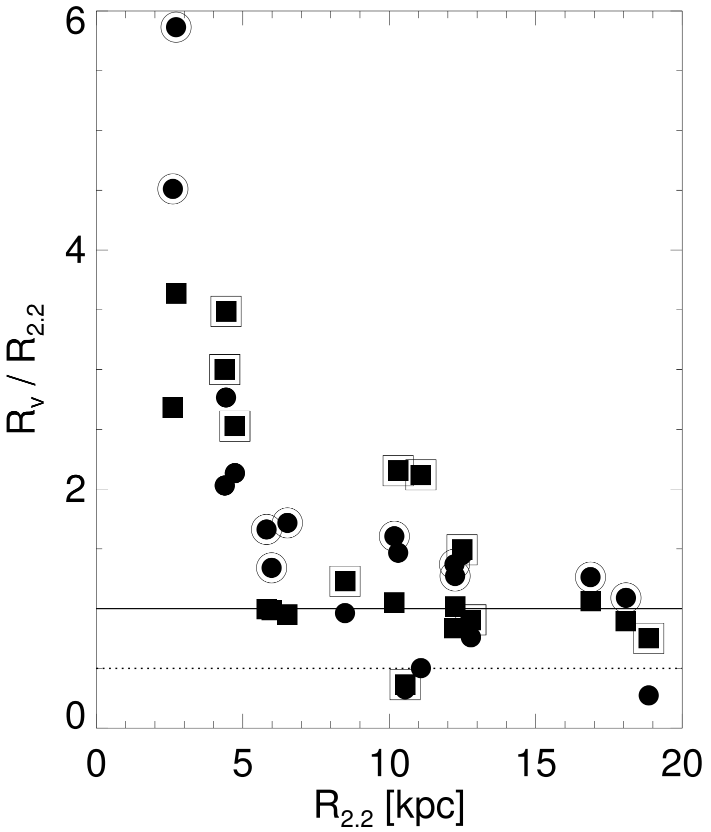

Figure 3.23: Radial extent compared to expected peak of rotation of the high-z rotation curves

Ratio of spatial extent of the high redshift rotation curves R_v and the expected peak of rotation $R_{2.2}$ as a function of $R_{2.2}$. Boxes and circles represent the minimum ("left") and maximum ("right") ends of the rotation curves. The largest extent for each object is additionally marked by a surrounding square or circle. In more than 85% of all sources R_v is larger than $R_{2.2}$ (solid line). Only $\sim 5\%$ of the rotation curves do not reach at least about one disc scale length (dotted line $\sim 1.1 R_d$).

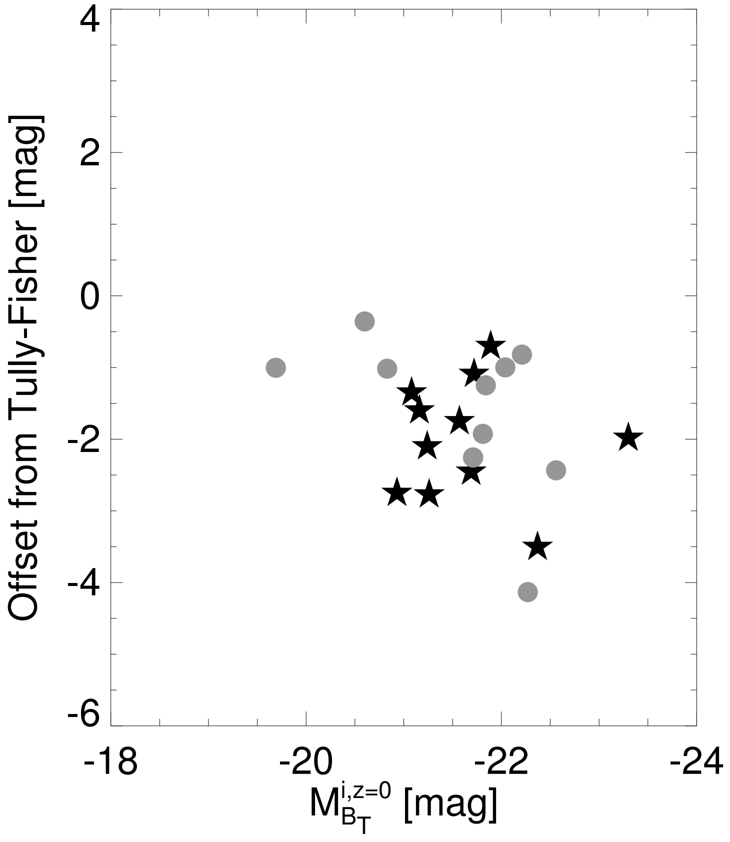

Figure 3.24: Intrinsic consistency of the data quality of the high-z rotation curves

The offset from the local Tully-Fisher relation versus the absolute magnitude M_B. The high redshift data are divided into a better (stars) and worse (circles) half in terms of rotation curve quality. The quality-division is a subjective attempt to judge whether a rotation curve has a more or less clearly discernible turn-over or a flat region. The mean offsets of the high and low quality samples are the same.

because of dust. To obtain a comparable value for every object one would have to measure the galaxy in face-on configuration. The reason for this is that the apparent magnitude is an integral over the total area of the object. Turning a disc from its face-on to its edge-on configuration, however, decreases the visible surface, thus reducing its apparent magnitude. For an ideally optically thin galaxy this should not matter, however, since in any configuration of the object one would measure its total amount of emitted flux and therefore its precise magnitude. Real galaxies, however, are far from that state. The presence of interstellar material like dust or gas makes a galaxy relatively opaque, and thus the dependence of the magnitude with inclination arises. Even in face-on configuration the presence of dust lanes makes it rather impossible to estimate the precise total magnitude of a galaxy. There have been several attempts in the literature (see e.g. Tully and Fouque, 1985; Bottinelli et al., 1995; Tully et al., 1998) to derive empirically formulae for the amount of extinction. For our purposes we will adopt the parameterisation of Tully and Fouque (1985) to correct all our magnitudes to face-on values, but refrain from applying any further corrections to obtain the true intrinsic magnitude:

$$\tilde{A}_B^i = -2.5 \log \left[f \left(1 + e^{-\tau \sec i} \right) + (1-2f) \left(\frac{1 - e^{-\tau \sec i}}{\tau \sec i} \right) \right],$$

where $\tau = 0.55$ and $f = 0.25$. For $i > 80^\circ$ Tully and Fouque (1985) proposed a constant value $\tilde{A}_B^{max} = \tilde{A}_B^{i=80^\circ}$. Since this formula for the true intrinsic magnitude $\tilde{A}_B^i$ is "poorly" determined according to Tully and Fouque (1985) we only correct for an extinction relative to face-on orientation:

$$A_B^i = \tilde{A}_B^i - \tilde{A}_B^{i=0^\circ} = \tilde{A}_B^i - 0.27\mathrm{mag}$$

In lack of better understanding, we adopt this parameterisation for both, the local and distant galaxies, although higher amounts of dust at high redshift could have an impact on this formulation. Furthermore, we note that both Bottinelli et al. (1995) and Tully et al. (1998) find that the internal extinction is somewhat luminosity dependent, in that bright galaxies show a higher extinction than faint ones. However, since their formulae to correct for this effect assume an a priori Tully-Fisher relation, which may not be the same at high and low redshift, we refrain from correcting for luminosity dependent extinction. This should only have a minor impact on our analysis since we apply the same correction consistently to both data sets.

Finally, the distance towards the target influences the estimate of the total magnitude. Since the observed wavelength $\lambda_{obs} = (1+z)\,\lambda_{rest}$ is a function of the rest wavelength λ_{rest} one has to apply a K-correction to the observed luminosities to obtain luminosities at a certain rest wavelength to account for the change of the spectral energy distribution (SED) with wavelength.

For our local galaxies we could obtain total B-band magnitudes from the RC3 and LEDA. Since the K-corrections are tiny at the distances of this sample we did not apply any. We only corrected their magnitudes for galactic foreground and internal extinction. For our distant galaxy sample this is not the case any more, though. Observing a target at $z \sim 0.9$ in the I-band is approximately equivalent to measuring its rest-frame B-band magnitude. For this sample we retrieved total apparent magnitude measurements in several bands from the literature and corrected each of these measurements for galactic foreground extinction. Then we calculated the rest-frame wavelengths corresponding to these magnitudes (in the AB magnitude system) and constructed model SEDs to fit these data points from the templates by Kinney et al. (1996). First we tried to match their early and late type galaxy spectra to our flux measurements. Since this could not provide a perfect fit in most cases we then added varying contributions of four different types of spectra of nuclear or star-forming activities: a LINER-, Seyfert-, weakly extincted starburst and a heavily extincted starburst. Together with the initial early or late type fit we then selected the best match out of these five possibilities to estimate the flux of the object in the rest-frame B-band. Finally this AB-flux was converted to a standard Vega magnitude and then an extinction correction according to the target's inclination was applied. After employing these corrections we can now convert the extinction corrected total apparent rest-frame B-band magnitudes m_B^{rest} to absolute magnitudes

M_B^{rest} using the standard formula for the distance modulus:

$$m_B^{rest} - M_B^{rest} = 5 \log \frac{D}{[\mathrm{Mpc}]} + 25$$

with the distance D in Mpc. Spectral classifications are listed in Tab. 3.5. Although no strong conclusions should be drawn from the resulting SEDs, we find that the majority of our targets is consistent with normal late type spiral galaxies. Our sample does contain some earlier type or starburst type spiral galaxies, though.

Table 3.5: SPECTRAL CLASSIFICATION OF THE HIGH REDSHIFT SAMPLE

ID (1)	ET % (2)	LT % (3)	LIN % (4)	Sey % (5)	HSB % (6)	LSB % (7)	B-V mag (8)
CFRS-00.0174	43.4	56.6	-	-	-	-	0.71
CFRS-00.0308	-	90.1	-	-	-	9.9	0.62
MS1054-1403	12.8	87.2	-	-	-	-	0.71
MS1054-1733	13.1	86.9	-	-	-	-	0.71
LDSS2-03.219	-	26.8	-	-	73.2	-	0.42
CFRS-03.0999	-	15.9	84.1	-	-	-	0.73
CFRS-03.1393	-	60.0	-	-	40.0	-	0.54
CFRS-03.1650	64.4	35.6	-	-	-	-	0.78
CFRS-22.0953	47.6	-	-	-	52.4	-	0.54
CFRS-22.1313	-	1.1	-	98.9	-	-	0.60
CN84-023	59.8	-	40.2	-	-	-	0.79
CN84-123	95.2	-	-	4.8	-	-	0.81
CSH96-68	58.9	-	-	-	41.1	-	0.59
SA68-5155	-	80.4	-	-	-	19.6	0.54
CFRS-00.0137	62.5	-	-	-	-	37.5	0.48
CSH96-32	-	98.2	-	-	-	1.8	0.69
CSH96-74	86.7	-	-	-	-	13.3	0.68
CFRS-03.0776	-	86.7	-	-	-	13.3	0.59
CFRS-03.1056	82.8	-	-	-	-	17.2	0.65
CFRS-03.1284	-	76.1	-	-	-	23.9	0.51
CFRS-22.0599	-	50.1	-	-	49.9	-	0.50

Note. – (1) galaxy identification (Lilly et al., 1995; Glazebrook et al., 1995; van Dokkum, 1999; Couch et al., 1998; Cowie et al., 1996); (2)-(7) fraction of the total SED for early type (2), late type (3), LINER (4), Seyfert (5), high extinction starburst (6) and low extinction starburst; (8) rest-frame B-V colour

For both samples, at high and low redshift, we have tabulated B-V colours (see Tab. 3.5). The majority of the colours for the nearby sample are listed in the RC3 with a few additions from LEDA. V-band magnitudes for the high redshift sample we calculated in a similar fashion as our B-band rest-frame magnitudes. Since the inclination corrections in the B and V bands are different we adopt the following scheme to derive at least rough extinction estimates for our high redshift galaxies in V. Tully et al. (1998) tabulate extinction corrections A_λ^i as a function of wavelength λ as:

$$A_\lambda^i = \gamma_\lambda \cdot \log\left(\frac{a}{b}\right) \tag{3.9}$$

with $\gamma_\lambda = a_\lambda + b_\lambda \cdot (\log(2 \cdot v_{rot}) - 2.5)$ and the axial ratio a/b which is connected to the inclination as described in eq. 3.6. Since Tully et al. (1998) do not tabulate values for the V-band we plot

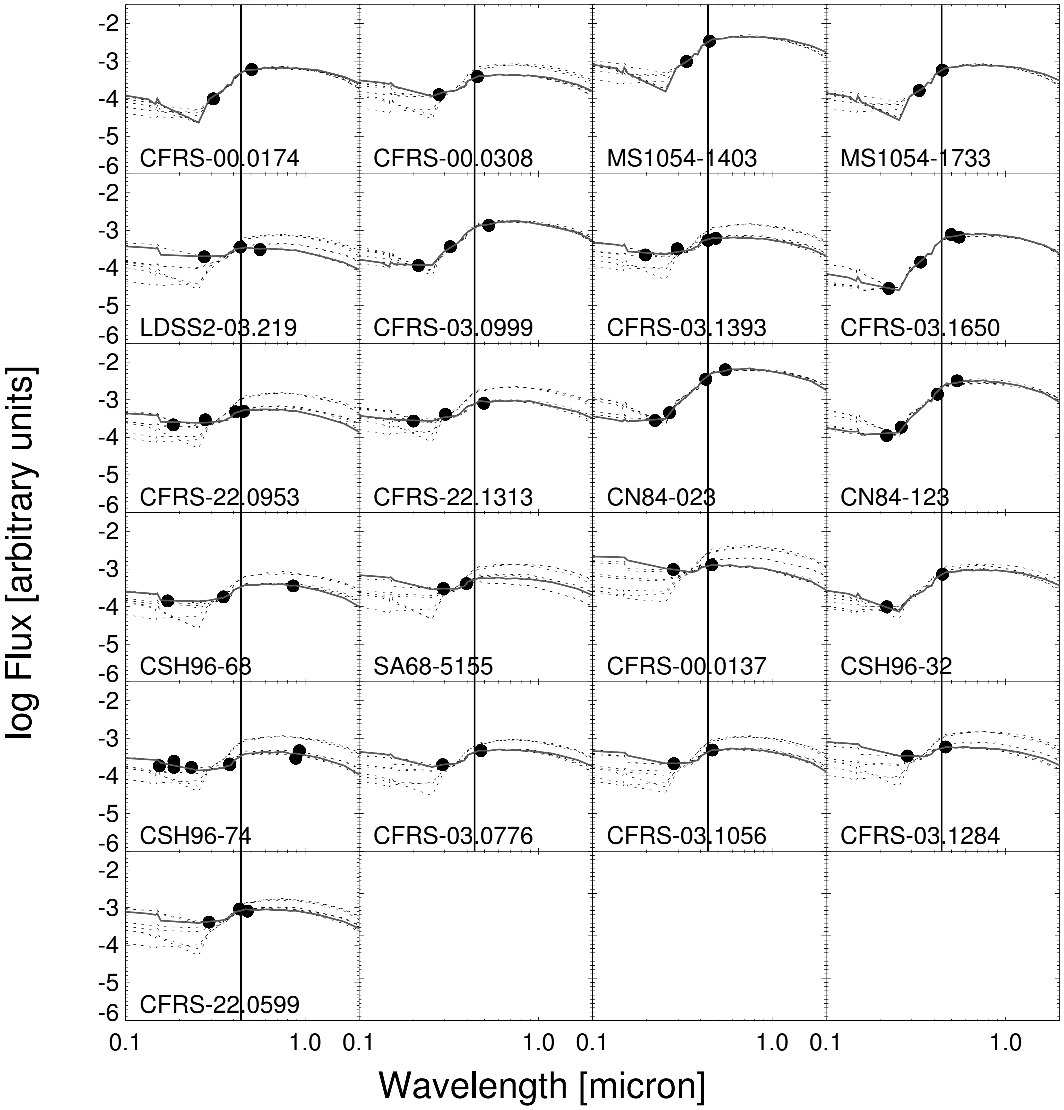

Figure 3.25: SEDs of the high redshift sample

Here we show the available observed total source fluxes (corrected for galactic extinction) of the high redshift sample converted to rest-frame at the respective redshift as a function of wavelength. The wavelength axis ranges from 0.1 to 2 μm. The Flux axis is in arbitrary units. Various template SEDs (as listed in Sec. 3.5.5) are shown (dotted lines). We indicate the best fit two-component model by a thick solid line (see also Tab. 3.5). As can be seen from the vertical line (corresponding to 440nm), our rest-frame B-band magnitude estimates should be fairly robust, since in almost all cases an observed magnitude estimate is fairly nearby. Only at the highest redshifts extrapolation is required.

their values for a_λ and b_λ as a function of λ (see Fig. 3.26). From a linear fit we read off values at the V-band (550nm) of $a_\lambda = 1.36$ and $b_\lambda = 2.35$. Next we calculate the mean difference between A^i_B and A^i_V:

$$A^i_B - A^i_V = (\gamma_B - \gamma_V) \cdot \log\left(\frac{a}{b}\right) = ((a_B - a_V) + (b_B - b_V) \cdot (\log(2 \cdot v_{rot}) - 2.5)) \cdot \log\left(\frac{a}{b}\right)$$

Since the spread of $A^i_B - A^i_V$ for any sensible combination of inclination $30 < i < 90$ and rotation speed $100 < v_{rot} < 250$ is only ± 0.05 we adopt a global value $A^i_B - A^i_V = 0.2$ (see Fig. 3.27). We will use this value to correct our high redshift B-V colours obtained from the formulae by Tully and Fouque (1985):

$$\text{B-V} = \left(B - A^i_B\right) - \left(V - A^i_V\right) = B - V - \left(A^i_B - A^i_V\right) = B - V - 0.2$$

These colours demonstrate that none of our main diagnostic measurements depend on the specific spectral type of the selected sample (see Fig. 3.28, 3.29, 3.30).

3.6 Truncation Effects

Basically, all our conclusions are based on the comparison of a local with a distant sample. Therefore, it is of utmost importance to assure that on one hand the samples were picked in the same way and that on the other hand the quality of data used to extract the information is equivalent. Therefore, before launching into the discussion of the data we will first study the impact of truncating the profiles of the local galaxies in some detail. We will analyse the local sample before and after truncation to evaluate the reasons for outliers. Furthermore, this procedure will provide us with reasonable error estimates for inclination, disc scale length, central surface brightness, isophotal radius, and absolute magnitude.

3.6.1 Surface Brightness Effects

Since the objects get fainter with redshift it becomes difficult to reach the same limiting surface brightnesses in the images of the distant sample as for the local galaxies. In fact, the maximum radius out to which we can measure the profiles of local galaxies is usually twice as large as the maximum radius for the high redshift galaxies (see Fig. 3.31). From the histograms of the maximum radii R_{max} out to which the ellipse fitting routine could trace the light profile we find $\langle R_{max} \rangle = 25.7$ kpc for the local and $\langle R_{max} \rangle = 14.1$ kpc for the distant galaxies (see Fig. 3.32). To compensate for this difference we truncate the local profiles at a characteristic radius R_{lim}. Therefore, for the high redshift galaxies $R_{lim} = R_{max}$, while for the local galaxies $R_{lim} < R_{max}$.

Furthermore, we know from the deep local data that galaxy profiles do not necessarily follow pure exponential profiles, but might exhibit two different exponential scale lengths or even curved profiles (see e.g. Fig. 3.33). It is for this reason that it becomes important at what limiting surface brightness one measures the profile. As explained in Sec. 3.5.2 we truncate our local profiles at various radii and take the mean limiting surface brightness to measure our profile properties. Since adopting a mean value cannot quite recover the distribution of limiting surface brightnesses at high redshift we subtract another 0.5 magnitudes to derive the final limiting surface brightness (see Fig. 3.17). We show in Fig. 3.16 that this results in limiting radii very similar to the limiting radii of the high redshift sources. In fact, the mean limiting radius of our local galaxies ($\langle R_{lim} \rangle = 11.6$ kpc) is actually a little smaller than the mean limiting radius of the distant sample ($\langle R_{lim} \rangle = 14.1$ kpc). However, the smallest limiting radii of the local galaxies are not smaller than the smallest high redshift ones ($R_{lim} \gtrsim 6$ kpc). The difference of the means of the two samples therefore arises from the fact that the variance of our truncated local sample is slightly smaller than that of the high redshift distribution. However, by accepting these values we take a rather conservative approach, which could, if anything, result in a slightly larger scatter in the properties of the local galaxies. Furthermore, the low end tail of the limiting radius distribution of our local galaxies is set such that a reasonably good agreement in the limiting surface brightness distributions is

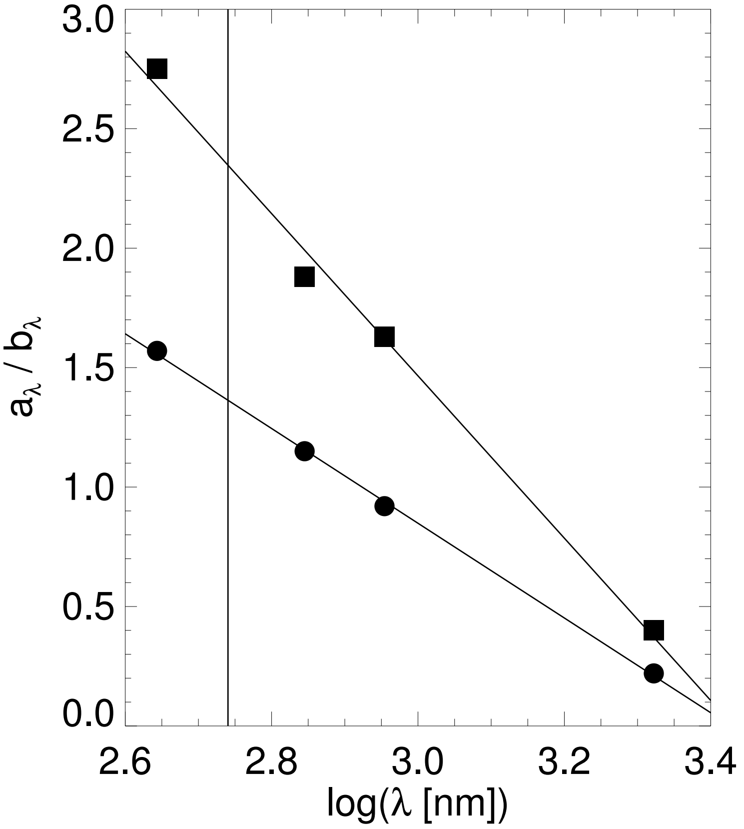

Figure 3.26: Estimation of extinction coefficients

Extinction coefficients a_λ (cirlces) and b_λ (squares) as a function of wavelength and corresponding fits (diagonal lines). The vertical lines indicate the V-band.

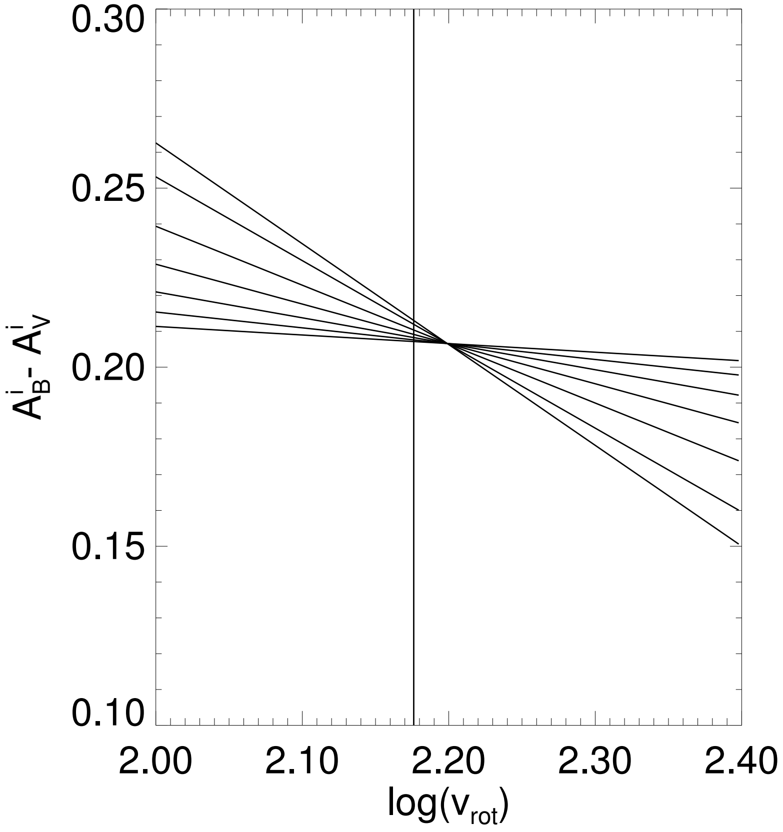

Figure 3.27: Relative B to V extinction

The difference between the estimated extinction coefficients in B and V as a function of rotation speed v_{rot} and inclination i (different lines; $30 < i < 90$). We adopt $A^i_B - A^i_V = 0.2$ as a global mean difference. The vertical line indicates the mean rotation velocity of our high redshift sample.

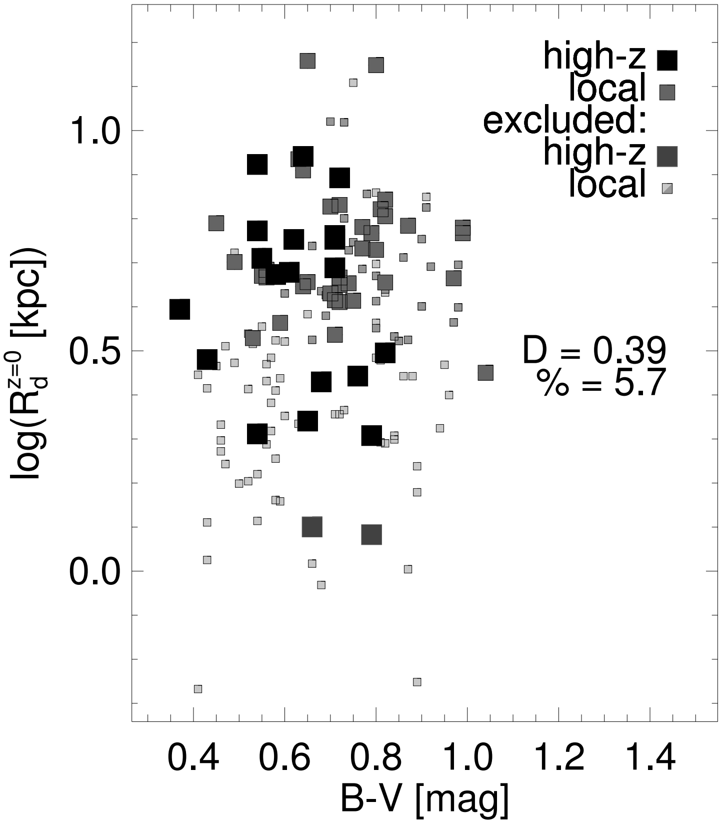

Figure 3.28: B-V colour versus $R_d^{z=0}$

Disc scale length $R_d^{z=0}$ as a function of B-V rest-frame colour. There is no obvious systematic trend for the high redshift galaxies. For details on the symbols see caption of Fig. 4.1.

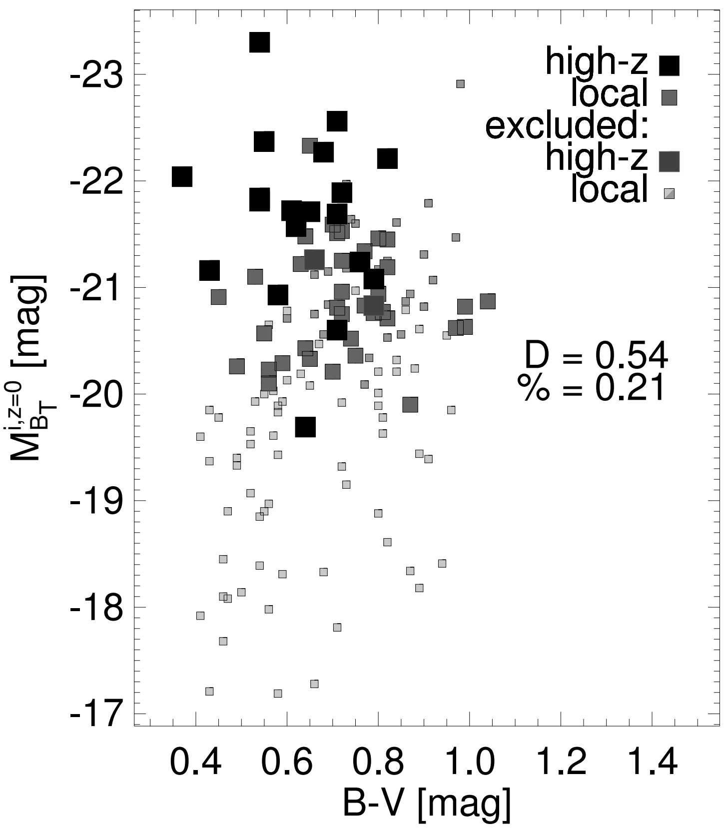

Figure 3.29: B-V colour versus $M_{B_T}^{i,z=0}$

Absolute rest-frame $M_{B_T}^{i,z=0}$ as a function of B-V rest-frame colour. Again, we do not find systematic trends for the high redshift galaxies. For details on the symbols see caption of Fig. 4.1.

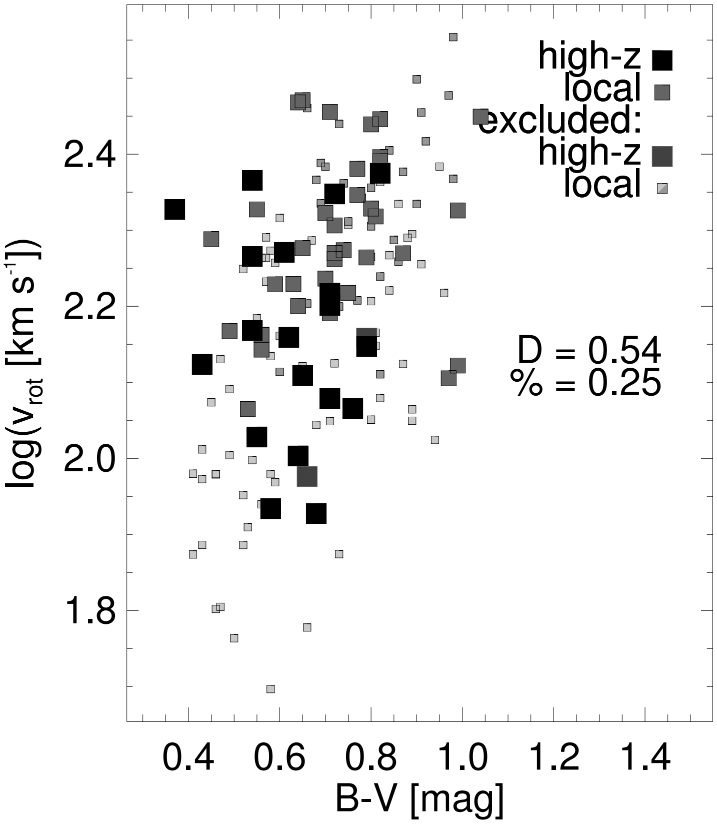

Figure 3.30: B-V colour versus v_{rot}

Rotation velocity v_{rot} as a function of B-V rest-frame colour. The rotation velocity does not change with colour for the high redshift galaxies. For details on the symbols see caption of Fig. 4.1.

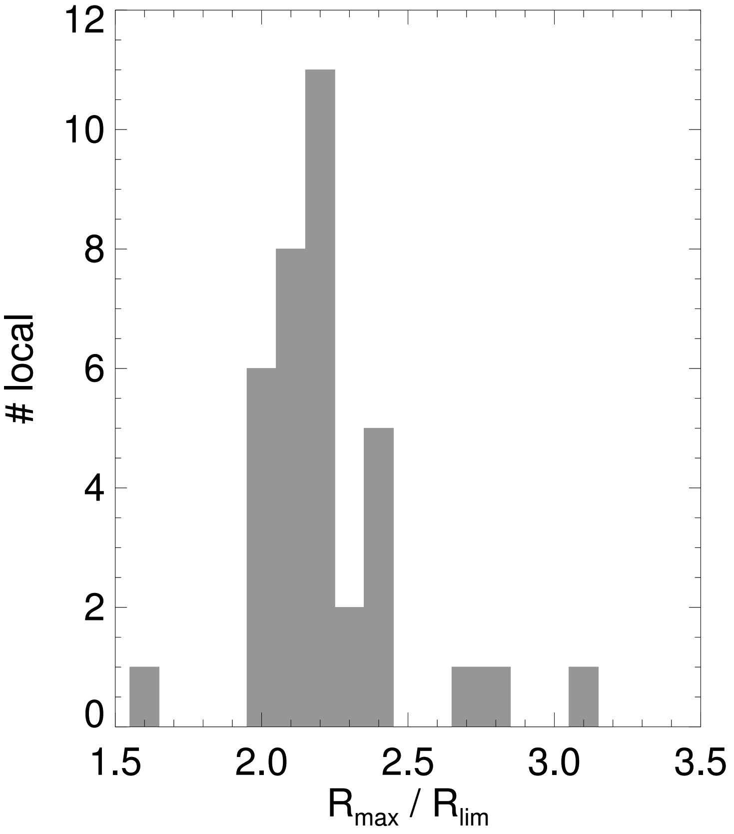

Figure 3.31: Ratio of R_{max} over R_{lim} for the local sample

The ratio of the maximal accessible radius R_{max} over the limiting radius R_{lim} for local galaxies. R_{lim} for local sources is equivalent to their maximal accessible radius, if they were shifted out to a distance $z \sim 0.9$. In the local universe it is possible to trace the light profiles of disc galaxies twice as far out as in the the case of distant objects.

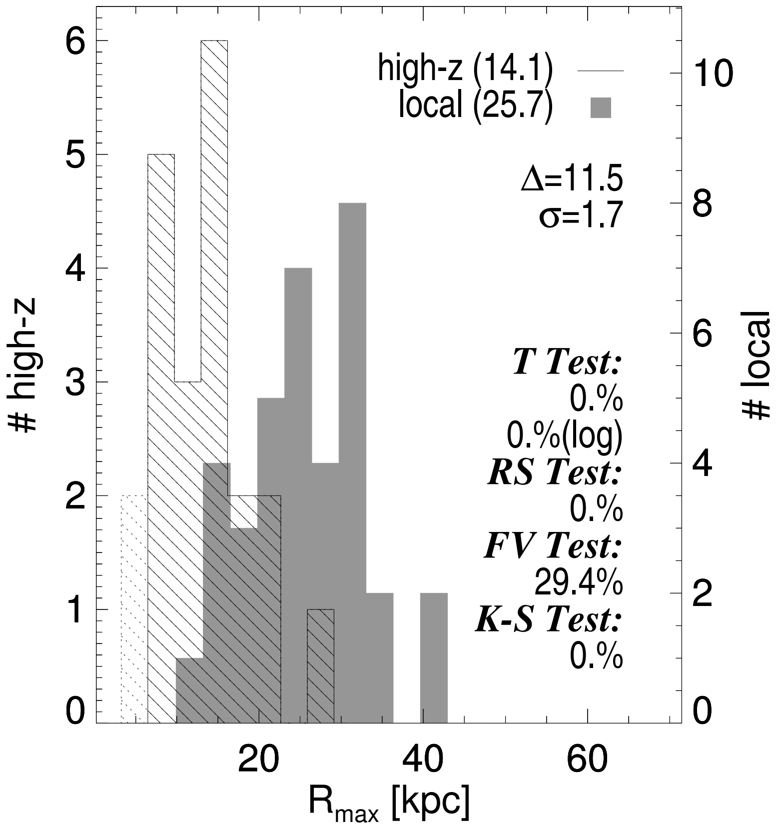

Figure 3.32: R_{max} of local and distant galaxies

Histograms of the maximum radii R_{max} of the low (shaded region) and high redshift (striped region) samples. The means for both distributions are indicated in brackets in the upper right corner. The difference of the two means Δ and its 1σ error is shown above a set of statistical tests (lower right), including a student's T-test (on a linear and a logarithmic scale), a rank-sum test, a variance test and a Kolmogorov-Smirnov test, respectively. The dotted high redshift galaxies were excluded from the statistical analysis for not fitting the R_{25} selection criterion (see Sec. 3.2).

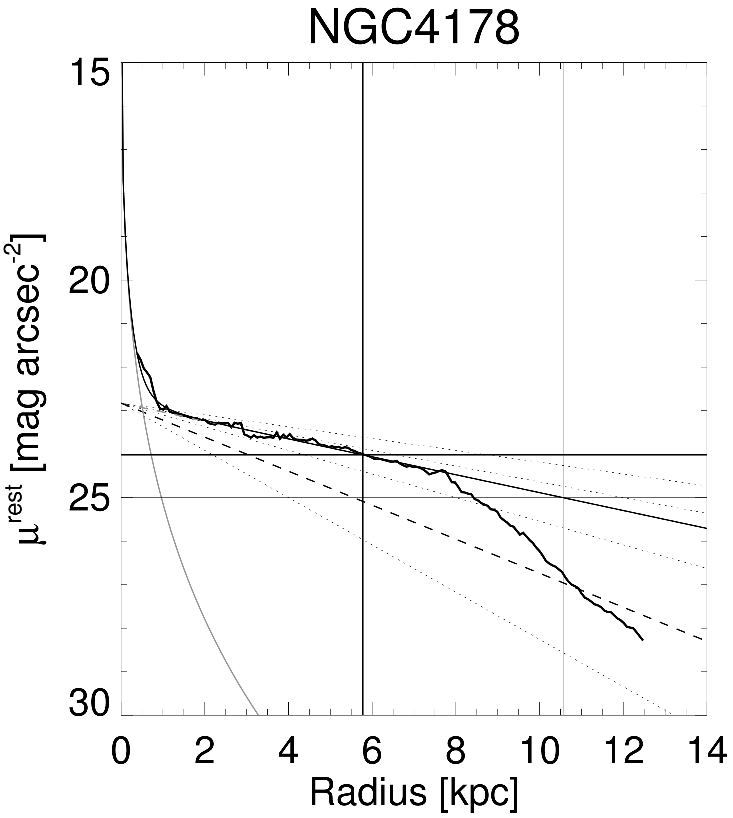

Figure 3.33: Light profile of NGC4178

Light profile (thick solid line) of an example galaxy with a double exponential law. An exponential (grey dashed line) and a de Vaucouleurs (grey solid line) model was fitted out to a radius of $R_{lim} \sim 5.75$kpc (thick vertical and horizontal lines). The combined model defines R_{25} (thin horizontal and vertical lines). Using the total profile out to $R_{max} = 12.5$kpc one would measure a disc scale length as indicated by the black dashed line. Apparently, a better fit would be obtained, by using two exponentials, since the profile breaks at $R \sim 8$kpc. The thin dotted lines indicate disc scale lengths of 2, 4, 6, 8 kpc.

just reached (see Fig. 3.17). The means of the two limiting surface brightness distributions are the same, though ($\langle \mu_{lim}\,(local) \rangle$ = 23.81 mag, $\langle \mu_{lim}\,(high-z) \rangle$ = 23.71 mag). Increasing the limiting radius of the local objects would increase their limiting surface brightness. However, the local galaxies' limiting surface brightnesses cannot be increased by large amounts since that would immediately brake the agreement with the high redshift distribution. We conclude that in terms of limiting radii and limiting surface brightnesses the two samples can be made to agree fairly well.

Using our prescription to truncate the local profiles now enables us to compare the cut with the full profiles to quantise in how far scale radii or central surface brightnesses or even inclinations, which also depend on the radius, change during this process.

3.6.2 Morphological Dependence of the Inclination

Firstly, we plot the difference of inclination before and after truncation of the profile Δi versus the finally adopted inclination (see Fig. 3.34). We find that the majority of the data (95%) do not have their inclinations changed by the process by more than 15°. Interestingly, apparently all outliers with $\Delta i > 15°$, i.e. with offsets from the mean larger than 3σ, had their inlinations increased by the truncation. A closer inspection of the images of these objects (NGC0266, NGC1672, NGC2487, NGC4496A, NGC5236, NGC7479) reveals that they all have a similar morphology (classification adopted from RC3): all exhibit a prominent bar (NGC5236 only shows a weak bar, i.e. type AB), half of them are S-shaped (two spiral arms forming an S-shape), two show an S-shape and an inner ring structure (tightly wound spiral arms forming a ring) and only one of them shows neither of these two features (NGC2487). These results are listed in Tab. 3.6. They are all of relatively late type (1 Sab, 2 Sb, 2 Sc, 1 Sm).

Table 3.6: Morphological Dependence of Inclination

S	outliers (6)		local sample (127)	
		%		%
(1)	(2)	(3)	(4)	(5)
A	0	0	53	42
B	5	83	31	24
AB	1	17	43	34
0	1	17	9	7
S	3	50	59	46
R	0	0	15	12
T	2	33	44	35

Note. – (1) morphological feature: A - no bar, B - strong bar, AB - weak bar, 0 - no ring or S-shape, S - S-shape, R - inner ring, T - mixed (ring + S-shape); (2)-(3) total number and relative fraction with respective morphological feature of outliers; (4)-(5) total number and relative fraction with respective morphological feature of all local galaxies.

At a first glance one finds that the combination of an S-shape and a bar results in a faint "halo" surrounding the galaxy. This halo however is the main inclination defining feature, without which one mainly measures the inner region. Since the objects have positive values of Δi this implies that the inner region is on average higher inclined than the outer parts. However, although the absence of the halo in the shallow images removes the inclination defining feature of the targets, it is not the driving factor of this process. Especially the fact, that only positive outliers in Δi are observed, results solely from the barredness of the objects. The ellipse fitting routine gets fooled by the bar and assumes the bar to be a highly inclined edge-on disc rather than an overall weakly inclined source. This result gets supported by the fact that the fractions of objects with S-shapes and of objects with S-shapes and inner rings is the same within the outlier group (50% and 33%)

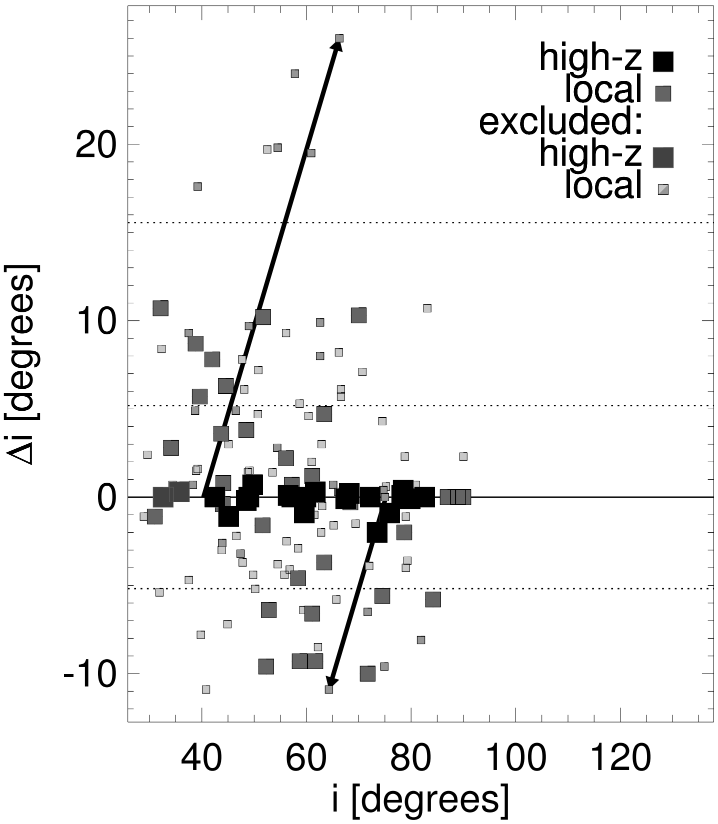

Figure 3.34: Δi as a function of i

The change of the inclinations after truncation of the light profile Δi as a function of inclination i for high redshift (large symbols) and local galaxies (small symbols). Large grey boxes represent high redshift galaxies and small light grey boxes symbolise local galaxies that were excluded from the statistical analysis for not fitting the R_{25} selection criterion (see Sec. 3.2). Small dark grey boxes show local galaxies that were rejected from the sample to match the RC3 catalogue distributions of R_{25}, M_B and v_{rot}. The arrows indicate the original value of i before truncation of the light profile.

and the local sample (47% and 35%, respectively). We are considering here (and in the following discussion) all local galaxies without ambiguities in their morphological classification from RC3, i.e. 127 objects out of 132 in total.

Thus, the resulting higher "apparent" inclination leads to a lower rotation velocity value. Therefore, the occurence of many such objects would have a dramatical impact on the Tully-Fisher relation since these points would be measured as sources with rotation speeds that are too low for their absolute magnitude or with magnitudes that are too bright for their rotation speed, depending on the point of view. Fortunately, unless the morphological mix at redshifts $z \sim 0.9$ changes dramatically towards containing many more barred objects statistically speaking less than ~ 1.5 objects of the high redshift sample may fall into that category. The possibility of bars promoting the occurence of erroneous inclination measurements gets supported by the fact that only 24% of all our local sample galaxies show a strong bar in the sense that if the same effect would happen with non-barred objects it should be weaker by at least an order of magnitude. Apparently, every $\sim$5th barred galaxy shows an abnormal inclination.

Furthermore, we do not find any correlation of Δi with inclination. One might naively expect inclination errors to increase with decreasing inclination, since it gets more difficult to measure inclinations of face-on targets. However, such a trend is not observed. The restricted sample does, however, exhibit more highly inclined objects with their inclinations being overestimated and more face-on galaxies with their inclinations being underestimated than expected. The reason for this is the selection of our targets, though, and will therefore not impact on the overall evaluation of the stability and errors of the high redshift sample. From the histogram of Δi (Fig. 3.20) we could derive a mean error for the measurement of individual inclination angles under conditions (imaging quality) of our high redshift galaxies of $\pm 5^\circ$.

3.6.3 Morphological Dependence of the Disc Scale Length

Next, we will present a similar assessment for the disc scale lengths R_d. In this variable we find 11 outliers with deviations from the mean larger than 3σ, i.e. $\Delta R_d > 3$ kpc. The objects are NGC2487, NGC3646, NGC3883, NGC4258, NGC4565, NGC4930, NGC5020, NGC5371, NGC5746, NGC6902 and NGC7184. A quick glance at the histogram of the deviations ΔR_d from the "true" R_d reveals that the disc scale lengths do not get scattered to one side of the distribution, but to both. The morphological types of the outliers show 36% barred and 27% non-barred objects, the rest being of a mixed type, i.e. with a weak bar. 18% exhibit an S-shape, 27% an inner ring and 45% both features. Only 9% of the outliers show neither an inner ring nor an S-shape (see Tab. 3.7). Overall the R_d-peculiar objects are of slightly earlier type than the inclination-outliers (6 Sb, 4 Sbc, 1 Sc).

One might be tempted to assume that barredness may have a similarly destabilising effect on the disc scale lengths as on the inclinations. However, the percentages of barred, non-barred and mixed types is the same within the outliers (27%, 36% and 36%) and the overall local sample (24%, 42% and 34%, respectively). On the other hand, we find an overabundance of sources with inner rings (outliers: 27%, total sample: 12%) and too few objects with S-shapes (outliers: 18%, total sample: 46%). The fraction of sources without inner rings nor an S-shape is the same in both samples (outliers: 9%, total sample: 7%) while we find slightly more objects that show both features amongst the outliers (46% $\longleftrightarrow$ 35%). We conclude that bars and the presence of two spiral arms forming an S-shape does not have a major impact on the stability of disc scale length measurements. The driving factor for disc scale length errors is the presence of inner rings. In those cases it seems that even the fitting procedure is not capable to remove the effect of the spiral arms completely. Overall, again assuming a roughly time-independent morphological mix, we expect statistically ~ 2.3 objects influenced by this effect in the high redshift sample. We calculate a mean error for the disc scale length measurements of high redshift galaxies of ± 1 kpc (see Fig. 3.35).

Plotting the change of the disc scale length ΔR_d versus the finally measured disc scale length R_d (see Fig. 3.36) we primarily find two things: On one hand there are more objects that get scattered to larger values of R_d in the process of truncating the profile than vice versa. On the other hand,

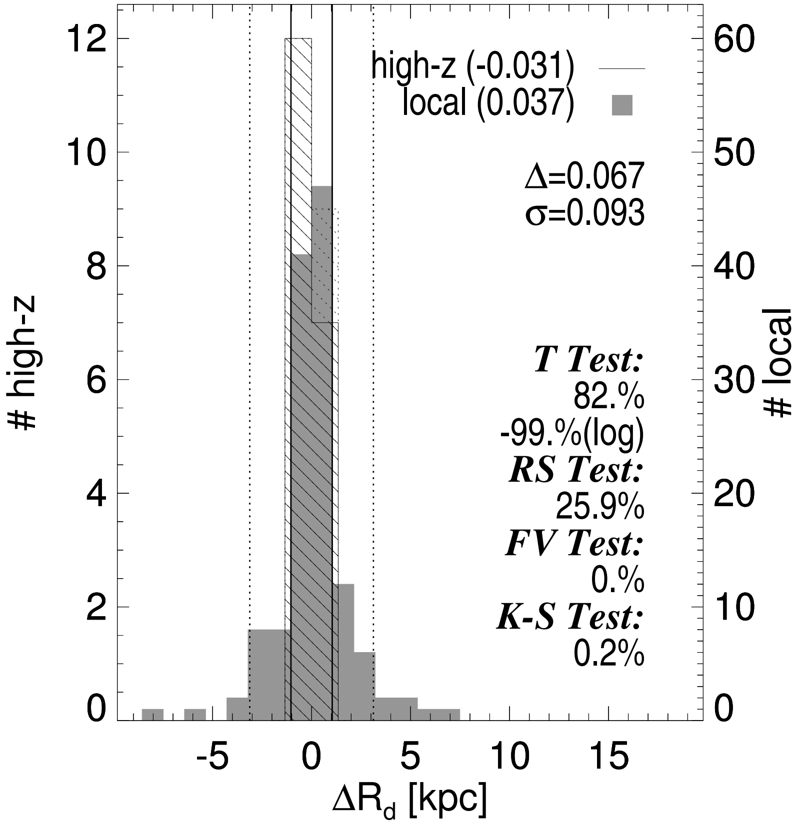

Figure 3.35: The effect of profile truncation on disc scale length

Histograms of the change of the disc scale lengths after truncation of the light profile of the low (shaded region) and high redshift (striped region) samples. The means for both distributions are indicated in brackets in the upper right corner. The difference of the two means Δ and its 1σ error is shown above a set of statistical tests (lower right), including a student's T-test (on a linear and a logarithmic scale), a rank-sum test, a variance test and a Kolmogorov-Smirnov test, respectively. The dotted high redshift galaxies were excluded from the statistical analysis for not fitting the R_{25} selection criterion (see Sec. 3.2). The solid and dotted vertical lines represent the 1σ and 3σ confidence limits excluding outliers, respectively.

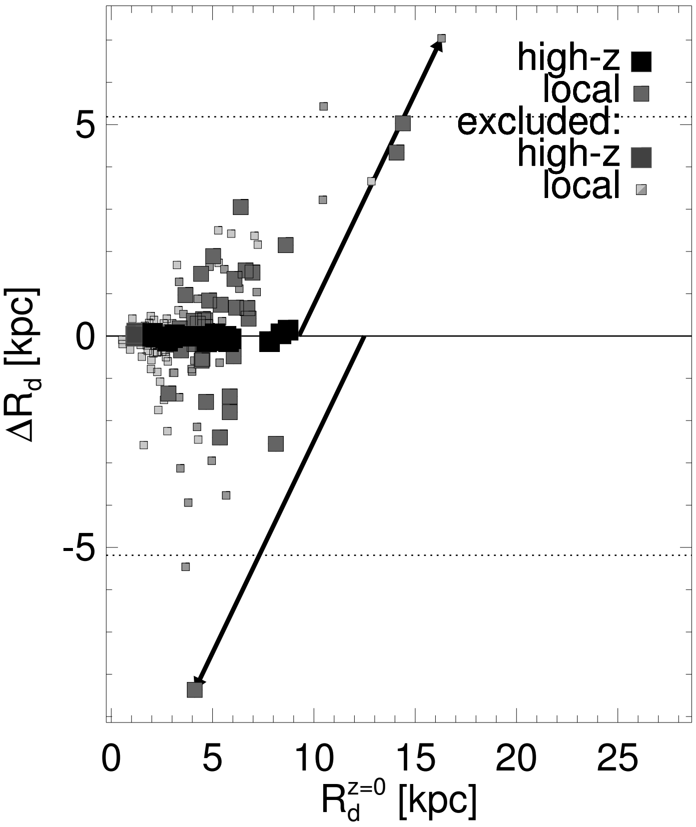

Figure 3.36: ΔR_d as a function of R_d

The change of the disc scale lengths after truncation of the light profile ΔR_d as a function of disc scale length R_d for high redshift (large symbols) and local galaxies (small symbols). Large grey boxes represent high redshift galaxies and small light grey boxes symbolise local galaxies that were excluded from the statistical analysis for not fitting the R_{25} selection criterion (see Sec. 3.2). Small dark grey boxes show local galaxies that were rejected from the sample to match the RC3 catalogue distributions of R_{25}, M_B and v_{rot}. The arrows indicate the original value of R_d before truncation of the light profile.

Table 3.7: Morphological Dependence of Disc Scale Length

S	outliers (6)		local sample (127)	
		%		%
(1)	(2)	(3)	(4)	(5)
A	3	27	53	42
B	4	36	31	24
AB	4	37	43	34
0	1	9	9	7
S	2	18	59	46
R	3	27	15	12
T	5	45	44	35

Note. – (1) morphological feature: A - no bar, B - strong bar, AB - weak bar, 0 - no ring or S-shape, S - S-shape, R - inner ring, T - mixed (ring + S-shape); (2)-(3) total number and relative fraction with respective morphological feature of outliers; (4)-(5) total number and relative fraction with respective morphological feature of all local galaxies.

those sources that had their disc scale lengths increased the most were mainly the biggest objects. At disc scale lengths beyond 10 kpc we only see sources with positive ΔR_d. This has an important implication for our high redshift objects: Since those galaxies were measured on only "shallow" images, statistically speaking we have likely overestimated rather than underestimated their disc scale length. Especially in the case of the three sources with relatively large disc scale length ($R_d > 7$ kpc), we have underestimated at most the scale length of one galaxy while overestimating two. Depending on the relative fraction of nearby objects with ΔR_d larger and smaller than zero a similar statement is probably also true for the smaller high redshift galaxies. As a result of this the mean disc scale length measured for the high redshift sample may be slightly increased as a result of the imaging quality.

3.6.4 Morphological Dependence of the Central Surface Brightness

Another parameter we sought to stabilise by the fitting procedure was the central surface brightness. In this case 12 objects are scattered outside the 3σ range. Their $\Delta\mu_d$'s are larger than ± 1.1 mag arcsec^{-2}. The outliers are NGC0023, NGC3368, NGC3486, NGC4151, NGC4258, NGC4565, NGC4594, NGC4651, NGC5078, NGC5746, NGC6902 and NGC7331. Again, all outliers are predominantly found on one side of the distribution. It is somewhat harder, though, to find an explanation for this phenomenon. Although we do not have any objects without inner rings and S-shapes amongst the outliers (7% were expected), the relative fractions of sources with either of the two features (inner ring: 17% $\longleftrightarrow$ 12%, S-shape: 50% $\longleftrightarrow$ 46%, for outliers and total sample, respectively) or both (outliers: 33%, total sample: 35%) are roughly the same for both samples (see Tab. 3.8). Furthermore, the influence of a bar is also not too obvious. We find a slightly higher fraction of objects without (50% and 42%) or only weak bars (42% and 34%) amongst the outliers while there are fewer barred sources amongst them (8% and 24%). Therefore, we conclude that generally galaxies without bars are a little more vulnerable to false central surface brightness measurements than barred ones. An explanation for this could be that the ellipse fitting routine performs slightly better on the prominent structure of a bar in terms of central surface brightnesses while it has to struggle more with spiral arms. For the high redshift sample we expect that for ~ 1.9 objects we have measured a wrong central surface brightness, i.e. a central surface brightness that is off by more than ± 1.1 mag arcsec^{-2}. If ring structures or S-shapes were the driving factor of this effect we would expect ~ 2.4 erroneous measurements. The mean error for a central surface brightness measurement is ± 0.4 mag arcsec^{-2} (see Fig. 3.37).

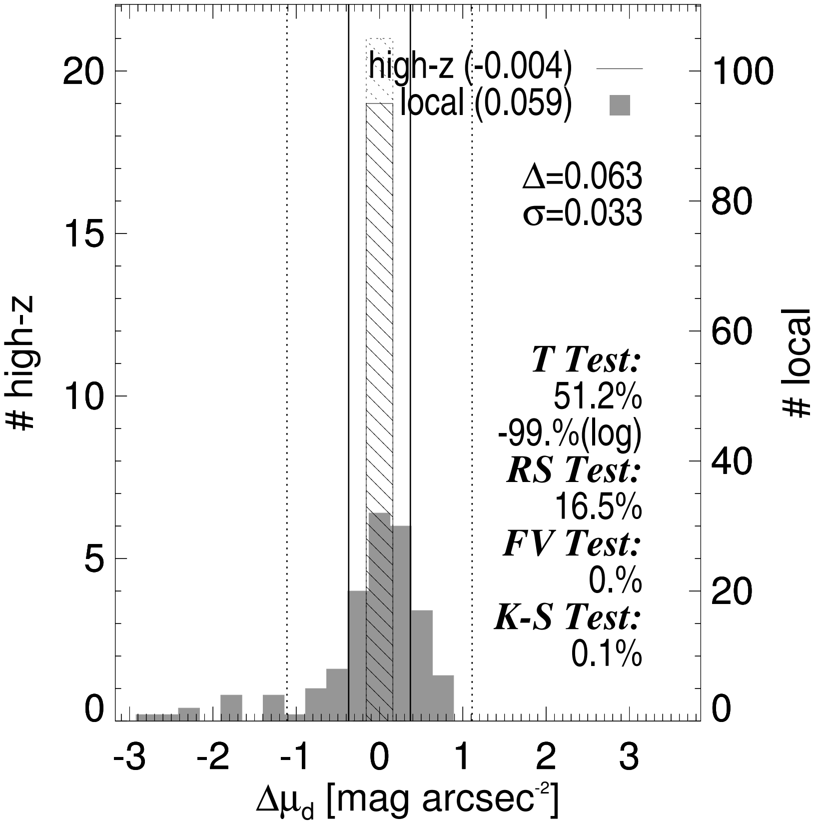

Figure 3.37: The effect of profile truncation on central surface brightness

Histograms of the change of the central surface brightness after truncation of the light profile of the low (shaded region) and high redshift (striped region) samples. The means for both distributions are indicated in brackets in the upper right corner. The difference of the two means Δ and its 1σ error is shown above a set of statistical tests (lower right), including a student's T-test (on a linear and a logarithmic scale), a rank-sum test, a variance test and a Kolmogorov-Smirnov test, respectively. The dotted high redshift galaxies were excluded from the statistical analysis for not fitting the R_{25} selection criterion (see Sec. 3.2). The solid and dotted vertical lines represent the 1σ and 3σ confidence limits excluding outliers, respectively.

Table 3.8: Morphological Dependence of Central Surface Brightness

S	outliers (6)		local sample (127)	
		%		%
(1)	(2)	(3)	(4)	(5)
A	6	50	53	42
B	1	8	31	24
AB	5	42	43	34
0	0	0	9	7
S	6	50	59	46
R	2	17	15	12
T	4	33	44	35

Note. – (1) morphological feature: A - no bar, B - strong bar, AB - weak bar, 0 - no ring or S-shape, S - S-shape, R - inner ring, T - mixed (ring + S-shape); (2)-(3) total number and relative fraction with respective morphological feature of outliers; (4)-(5) total number and relative fraction with respective morphological feature of all local galaxies.

The plot of $\Delta\mu_d$ versus μ_d (see Fig. 3.38) reveals more information about the probable errors in the measurement of high redshift central surface brightnesses. A closer inspection shows a slight tendency of decreasing $\Delta\mu_d$ with increasing (brightening) central surface brightnesses. Objects with surface brightnesses of $\mu_d > 22$ have predominantly positive $\Delta\mu_d$ while sources with $\mu_d < 20$ have largely negative values of $\Delta\mu_d$. Furthermore, all outliers also have negative $\Delta\mu_d$'s. As a result of this the central surface brightness estimates of the high redshift galaxies are mostly lower limits, i.e. the value given indicates more likely a limit towards the bright end of possible central surface brightnesses. Unfortunately, one would rather be interested in a faint end limit for the high redshift surface brightness to clearly discriminate between local and distant galaxies in the case of a brightening of disc galaxies with redshift.

3.6.5 Morphological Dependence of the Isophotal Radius

Since R_{25} is calculated from a profile with the truncated values for R_d / μ_d and R_b / μ_b the error in R_{25} is a combination of the errors of those four variables. Therefore, the change in R_{25} may be related to the effects discussed so far. We find only six 3σ outliers, though: NGC2442, NGC3628, NGC3646, NGC4930, NGC5371 and NGC6902. From Fig. 3.39 we deduce an average error of $1\sigma = \pm 2$ kpc for R_{25}. The morphological types of the outliers are roughly consistent with the local sample in terms of barredness (A: 50% $\longleftrightarrow$ 42%, B: 17% $\longleftrightarrow$ 24%, AB: 33%$\longleftrightarrow$ 34%; outliers $\longleftrightarrow$ local targets). However, we find fewer objects with S-shapes (17% and 46%) and a larger number of sources with inner rings amongst the outliers (33% and 12%). The number of sources with both, inner rings and S-shapes, (33% and 35%) and without those features (17% and 7%) is roughly the same for both samples (see Tab. 3.9). Statistically speaking ~ 1.8 high redshift galaxies may be affected by the same effect. Interestingly, the measurement of isophotal radii is not as vulnerable to outliers as the disc scale lengths or central surface brightnesses. For this reason it appears that correlations based on isophotal radii are more robust than those derived from disc scale lengths or surface brightnesses alone.

Furthermore, the distribution of positive and negative ΔR_{25} is not as uneven as in the case of the central surface brightnesses (see Fig. 3.40). The average isophotal radii deduced from these measurements are therefore relatively close to the “true” values as inferred from perfect data. There is a slight tendency left to over-estimate the size of distant objects.

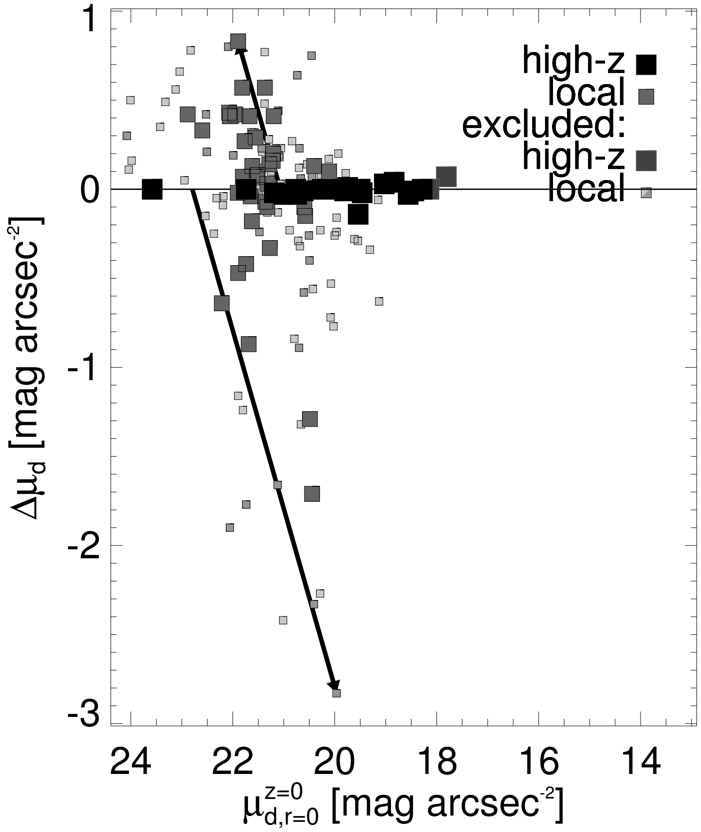

Figure 3.38: $\Delta\mu_d$ as a function of μ_d

The change of the central surface brightness after truncation of the light profile $\Delta\mu_d$ as a function of central surface brightness μ_d for high redshift (large symbols) and local galaxies (small symbols). Large grey boxes represent high redshift galaxies and small light grey boxes symbolise local galaxies that were excluded from the statistical analysis for not fitting the R_{25} selection criterion (see Sec. 3.2). Small dark grey boxes show local galaxies that were rejected from the sample to match the RC3 catalogue distributions of R_{25}, M_B and v_{rot}. The arrows indicate the original value of μ_d before truncation of the light profile.

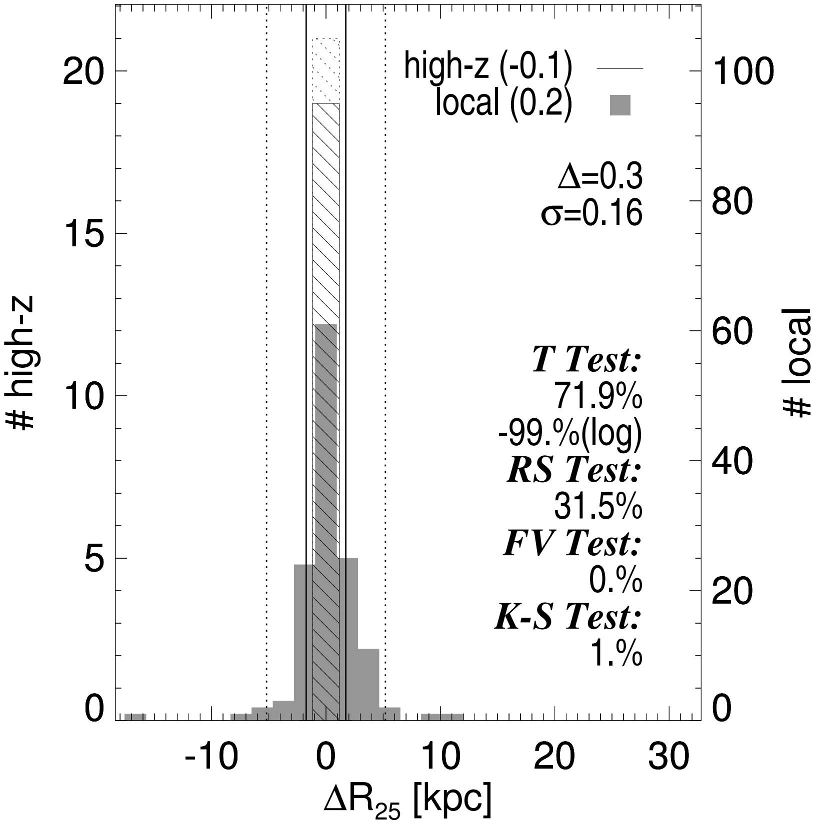

Figure 3.39: The effect of profile truncation on the isophotal radius

Histograms of the change of the isophotal radius after truncation of the light profile of the low (shaded region) and high redshift (striped region) samples. The means for both distributions are indicated in brackets in the upper right corner. The difference of the two means Δ and its 1σ error is shown above a set of statistical tests (lower right), including a student's T-test (on a linear and a logarithmic scale), a rank-sum test, a variance test and a Kolmogorov-Smirnov test, respectively. The dotted high redshift galaxies were excluded from the statistical analysis for not fitting the R_{25} selection criterion (see Sec. 3.2). The solid and dotted vertical lines represent the 1σ and 3σ confidence limits excluding outliers, respectively.

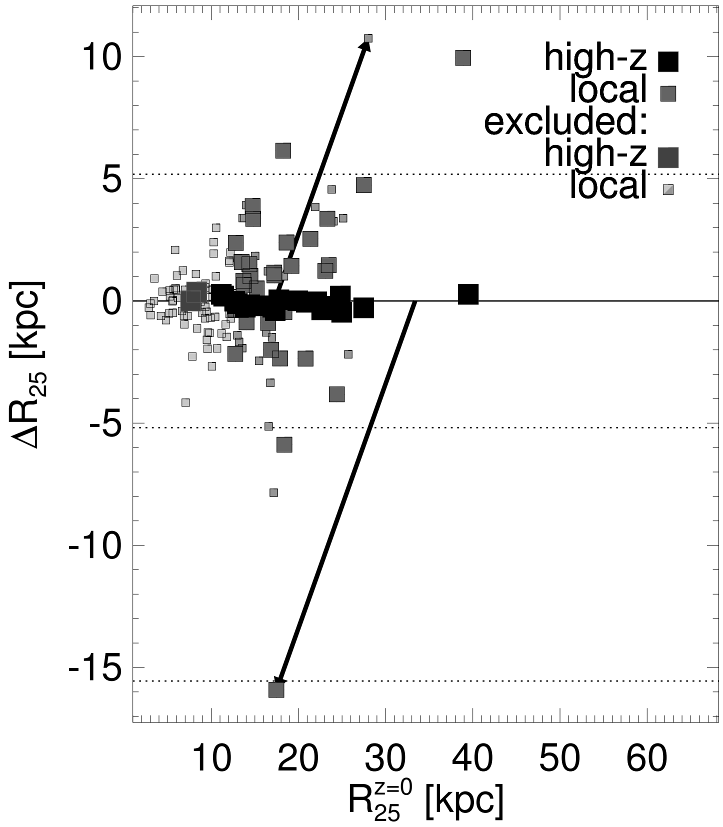

Figure 3.40: ΔR_{25} as a function of R_{25}

The change of the isophotal radius after truncation of the light profile ΔR_{25} as a function of isophotal radius R_{25} for high redshift (large symbols) and local galaxies (small symbols). Large grey boxes represent high redshift galaxies and small light grey boxes symbolise local galaxies that were excluded from the statistical analysis for not fitting the R_{25} selection criterion (see Sec. 3.2). Small dark grey boxes show local galaxies that were rejected from the sample to match the RC3 catalogue distributions of R_{25}, M_B and v_{rot}. The arrows indicate the original value of R_{25} before truncation of the light profile.

Table 3.9: Morphological Dependence of Isophotal Radius

S	outliers (6)		local sample (127)	
		%		%
(1)	(2)	(3)	(4)	(5)
A	3	50	53	42
B	1	17	31	24
AB	2	33	43	34
0	1	17	9	7
S	1	17	59	46
R	2	33	15	12
T	2	33	44	35

Note. – (1) morphological feature: A - no bar, B - strong bar, AB - weak bar, 0 - no ring or S-shape, S - S-shape, R - inner ring, T - mixed (ring + S-shape); (2)-(3) total number and relative fraction with respective morphological feature of outliers; (4)-(5) total number and relative fraction with respective morphological feature of all local galaxies.

3.6.6 Morphological Dependence of the Absolute Magnitude

Besides R_{25}, the absolute magnitude M_B^{rest} implicitely also depends on the disc profile parameters R_d / μ_d and R_b / μ_b. We find 10 3σ-outliers with $|\Delta M_B^{rest}| > 0.57$ mag: NGC23, NGC3187, NGC3486, NGC3883, NGC4178, NGC4930, NGC5020, NGC5371, NGC6902 and NGC6946. From the histogram of ΔM_B^{rest} (see Fig. 3.41) we derive an average error for the measurement of M_B^{rest} excluding the outliers of $1\sigma = \pm 0.2$ mag. To pin-point which morphological feature is responsible for these outliers is not trivial, though. On one hand we find (again) an over-abundance of barred objects (40% and 24%). At the same time the number of objects with weak bars (40% and 34%) stays roughly constant while there are fewer sources without bars (20% and 42%). If bars were the driving feature for the outliers we would expect ~ 1.7 objects affected by this in the high redshift sample. On the other hand we find fewer objects with S-shapes (20% and 46%) amongst the outliers and too many sources with both, inner rings and S-shapes, (60% and 35%). The numbers of galaxies without rings and S-shapes (0% and 7.1%) and with inner rings only (20% and 12%) are about the same in the outlier and local sample. Apparently, the presence of inner rings enhances the probability for large errors in the measurement of absolute magnitudes especially in combination with an S-shape. We expect ~ 2.2 objects to be scattered outside the 3σ range in the high redshift sample. Overall we conclude that morphologically peculiar objects with bars and/or rings and S-shapes are prone to erroneous measurements of their absolute magnitude, which is perhaps not too surprising.

In the 2-dimensional plot of ΔM_B^{rest} versus M_B^{rest} we do not find extremely prominent trends (see Fig. 3.42). The number of negative values of ΔM_B^{rest} appears to be slightly bigger than the number of positive values, though. Again, this will result in slightly too bright estimates of the absolute magnitude.

3.6.7 Resolution Effects

All these surface brightness effects taken into account, our local data now mimic the quality of the high redshift data in almost every respect. Only the intrinsically higher spatial resolution of the data remains. Since the local galaxies are several ten or even hundred times larger on the sky we are able to observe them in much more detail than the distant objects. However, most of the information hidden in the higher resolution gets smoothed over in the process of computing the 1-dimensional profiles, anyway. We have tried to simulate this resolution effect by reducing the

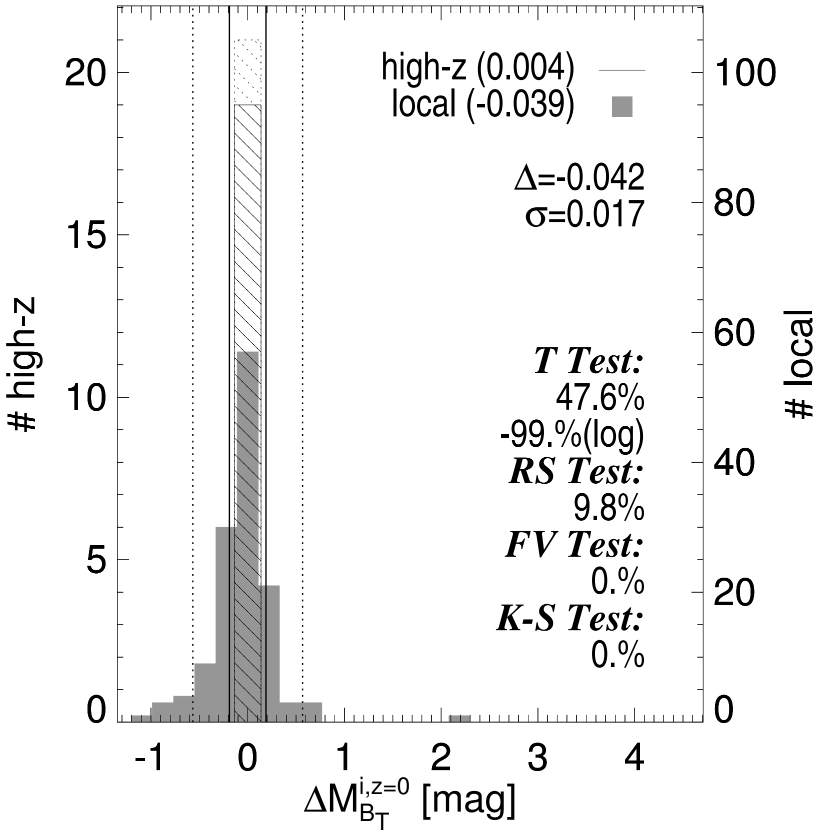

Figure 3.41: The effect of profile truncation on the absolute magnitude

Histograms of the change of the absolute magnitude after truncation of the light profile of the low (shaded region) and high redshift (striped region) samples. The means for both distributions are indicated in brackets in the upper right corner. The difference of the two means Δ and its 1σ error is shown above a set of statistical tests (lower right), including a student's T-test (on a linear and a logarithmic scale), a rank-sum test, a variance test and a Kolmogorov-Smirnov test, respectively. The dotted high redshift galaxies were excluded from the statistical analysis for not fitting the R_{25} selection criterion (see Sec. 3.2). The solid and dotted vertical lines represent the 1σ and 3σ confidence limits excluding outliers, respectively.

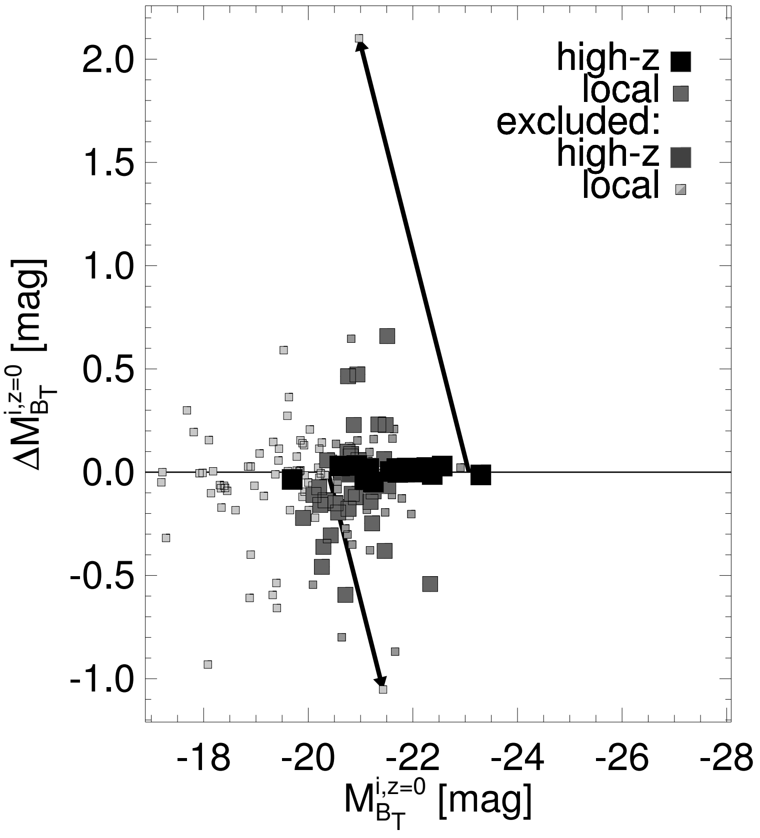

Figure 3.42: ΔM_B as a function of M_B

The change of the absolute magnitude after truncation of the light profile ΔM_B as a function of absolute magnitude M_B for high redshift (large symbols) and local galaxies (small symbols). Large grey boxes represent high redshift galaxies and small light grey boxes symbolise local galaxies that were excluded from the statistical analysis for not fitting the R_{25} selection criterion (see Sec. 3.2). Small dark grey boxes show local galaxies that were rejected from the sample to match the RC3 catalogue distributions of R_{25}, M_B and v_{rot}. The arrows indicate the original value of M_B before truncation of the light profile.

Table 3.10: Morphological Dependence of Absolute Magnitude

S	outliers (6)		local sample (127)	
		%		%
(1)	(2)	(3)	(4)	(5)
A	2	20	53	42
B	4	40	31	24
AB	4	40	43	34
0	0	0	9	7
S	2	20	59	46
R	2	20	15	12
T	6	60	44	35

Note. – (1) morphological feature: A - no bar, B - strong bar, AB - weak bar, 0 - no ring or S-shape, S - S-shape, R - inner ring, T - mixed (ring + S-shape); (2)-(3) total number and relative fraction with respective morphological feature of outliers; (4)-(5) total number and relative fraction with respective morphological feature of all local galaxies.

size of the images in such a way that the source after resampling extends over a similar number of pixels as a typical high redshift target. In fact, we reduced it even to only half that size, in order to increase the effect of such an image degradation. After this we magnified the image again by a factor of 1.5 in order to mimic the effect of drizzling. This image now looks very similar compared to a high redshift frame. Measuring the radial profile in the degraded image and then scaling the resulting profile back to the original size one essentially gets back the same profile. Therefore, the resolution of the high redshift images is high enough even for objects with sizes of only two to four arcseconds and thus our two samples can be assumed equal from the observational point of view.

3.6.8 Summary of Surface Brightness and Resolution Effects

The following discussion of the differences between the local and the high redshift sample will heavily depend on our ability to characterise the local comparison sample. We found that the higher spatial resolution of the images of local galaxies does not impact dramatically on the data, however, there are several issues concerning the limited depth of the high redshift galaxy imaging data. Basically **all variables deduced from light profiles, like inclinations, disc scale lengths, central surface brightnesses, isophotal radii and absolute magnitudes, suffer from limited dynamic range, i.e. radial extent**. In some cases we find a general trend to over- or under-estimate the “true” value of the variable in question, sometimes even depending directly on the magnitude of the variable itself. In all cases we find several outliers, i.e. objects in excess of a standard Gaussian distribution beyond the 3σ-level. These **outliers were mainly induced by special morphological features like bars or rings and S-shapes. Overall, ~ 2 high redshift objects ($< 10\%$) could be such outliers in each variable, assuming a morphological mix roughly constant with time**. In fact, e.g. Abraham et al. (1999) find that bar fractions -if anything- drop at higher redshifts $z \sim 1$. However, we will not be affected by these effects to a large extent, since we are mainly interested in relative statements. Only when comparing our samples (especially the local galaxies) to data in the literature some care has to be taken, and one has to account for the various effects of imperfect data/measurements.

Chapter 4

Results

4.1 The Isophotal Radius R_{25}

Selecting the samples on the isophotal size R_{25} one should first use this variable for comparison. We find that the minimum sizes of the two samples are indeed the same as required by construction (see Fig. 4.1). Furthermore, although no other restriction was imposed on our high redshift sample, we notice that the overall distributions of isophotal size of the two samples are very similar. In fact, the statistical tests confirm that mean and variance are about the same. Including all high redshift galaxies with isophotal sizes $R_{25} > 12.5$ kpc, results in significances of 31%, 39%, 23%, 13%, 12% and 36% for the linear and logarithmic student's T-test, the Wilcoxon's rank-sum RS-test, the linear and logarithmic F-variance FV-test and the Kolmogorov-Smirnov KS-test, respectively. Values exceeding 5% have to be interpreted as a non-rejection of the null-hypothesis, i.e. the tested variable –in this case the isophotal size– is the same for both samples.

One might argue now that finding the same sizes for both samples is a direct result of our size selection criterion. However, we would like to stress that this selection only affects the low end of the distribution. It is striking that the high redshift galaxies do span the same range of sizes as the local population. This illustrates that the galaxy population sampled by our high redshift galaxies has not evolved very much in isophotal size since $z \sim 0.9$. In the case of strong size evolution one would expect that the largest objects at high redshift were smaller than the largest local galaxies. Since we have probably picked the biggest galaxies for our high redshift sample, simply for observability reasons, this means that objects of the size of the biggest local galaxies already existed at a time when the universe was roughly half its current age. Furthermore, since the high redshift sample could be biased towards brighter objects also for observability reasons, this would imply that we have selected the biggest objects at these redshifts, because of the very strong correlation between absolute magnitude M_B^{rest} and isophotal size R_{25} (see Fig. 4.7). Therefore, we conclude that **large spiral galaxies have not evolved substantially in isophotal size since z=0.9**. Actually, the variance test indicates that the scatter and therefore to some extent even the shape of the two distributions are the same.

Since our prime selection criterion was R_{25} we will now try to achieve an even better match of our local sample with the high redshift data by removing a small number of targets. The reason for doing this is that since we are pushing the limits of the statistical tests (see Appendix A) they will fail to indicate differences of two samples that are smaller than the dynamical range of the data. Therefore, by slightly narrowing the dynamical range of the data we basically get a second measurement (though, with slightly increased noise, due to the smaller number of sources). If the test results of that data set are dramatically different from those of the full data set, we know that those results cannot be statistically significant. Removing four objects from the high redshift data is sufficient to get a perfect agreement (see Fig. 4.2). The difference between the means of the two populations is now tiny, compared to an offset of a little more than 1σ before removing the four sources.

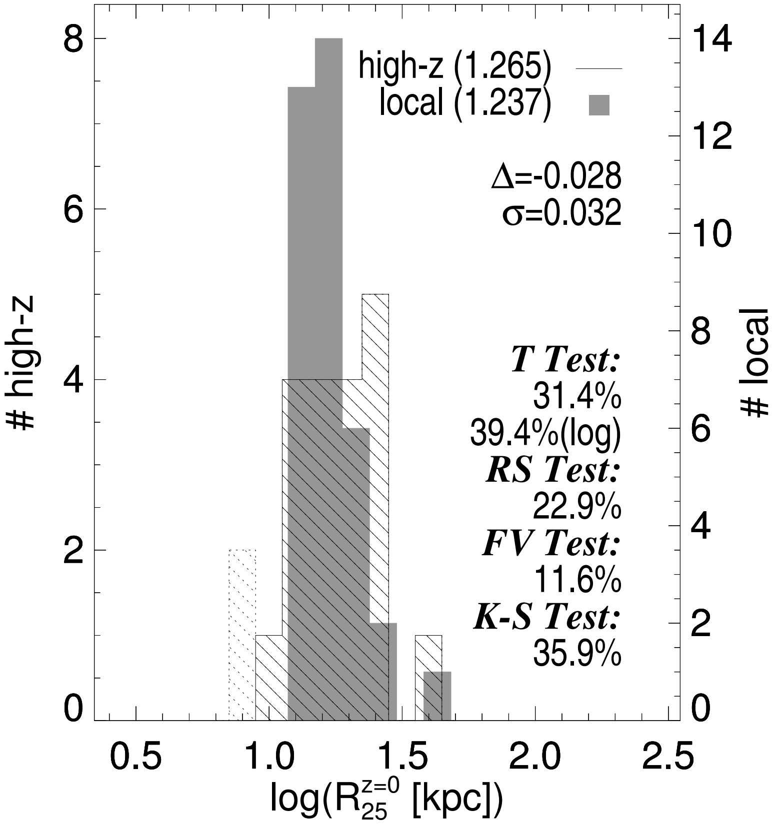

Figure 4.1: Histograms of the isophotal radii

Histograms of the isophotal radii R_{25} of the low (shaded region) and high redshift (striped region) samples. The means for both distributions are indicated in brackets in the upper right corner. The difference of the two means Δ and its 1σ error is shown above a set of statistical tests (lower right), including a student's T-test (on a linear and a logarithmic scale), a rank-sum test, a variance test and a Kolmogorov-Smirnov test, respectively. The dotted high redshift galaxies were excluded from the statistical analysis for not fitting the R_{25} selection criterion (see Sec. 3.2). The tests show that the two samples are the same. The difference between the means of the two samples is slightly larger than 1σ.

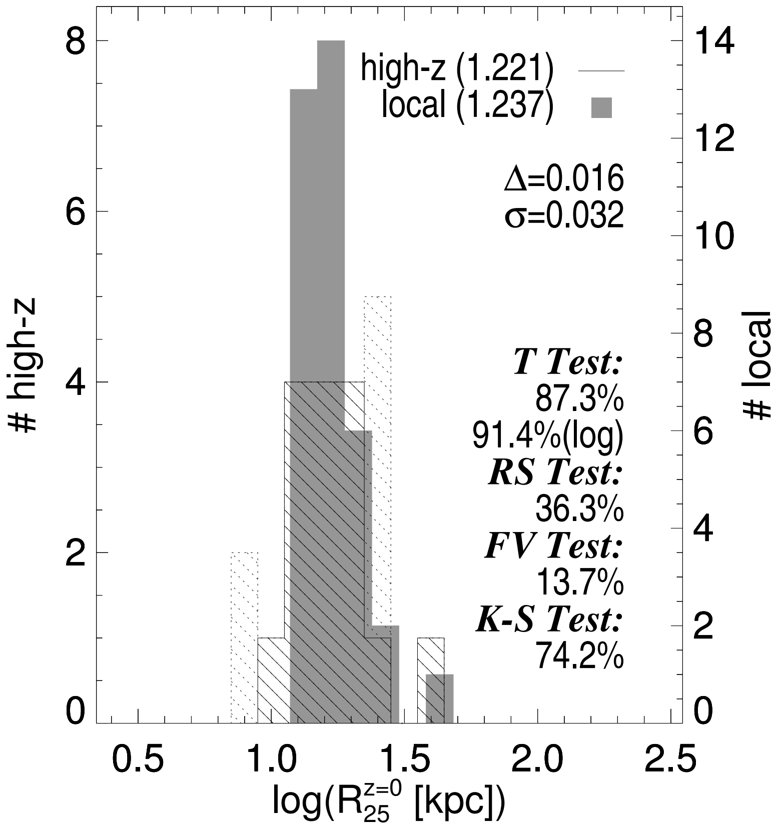

Figure 4.2: Histograms of the isophotal radii after matching the samples

Same plot as Fig. 4.1. Additionally, four high redshift galaxies were removed, to minimise the difference between the means of the two distributions. The subsequent discussion of this reduced high redshift data set does not depend on the specific choice of those galaxies.

4.2 The Disc Scale Length R_d

The next variable we would like to focus on is the disc scale length R_d. Figure 4.3 shows that both samples overlap almost perfectly. All tests indicate that mean and variance of the two distributions cannot be distinguished from each other at the 5% level (13%, 4%, 8%, 46%, 12%, 9% for lin. / log. T-test, RS-test, lin. / log. FV-test, KS-test). From this plot alone we have to conclude that spiral galaxies also did not evolve in disc scale length. However, the agreement is not as good as in the case of the isophotal size. Objects at high redshift appear to be somewhat smaller than objects in the local universe. Since we know (see Appendix A) that the tests will fail to indicate small differences, we will now examine whether R_{25} and R_d are related (see Fig. 4.4). We find that both data sets follow a tight sequence. Objects with large isophotal radii also have large disc scale lengths; sources with small disc scale lengths have small isophotal radii. A closer inspection reveals, that this is a result of the particular choice of our samples. The lines of constant central disc surface brightness indicate that on the lower right side we are hitting a high surface brightness limit while on the opposite side the surface brightness gets too low to detect anything. It should be stressed, though, that this surface brightness difference has to be intrinsic to the samples since the data sets were matched in isophotal size (see Sec. 4.1). This in mind, despite the inability of the tests to confirm this result it is a little surprising that the mean galaxy at high redshift has a smaller disc scale length than the mean local galaxy while at the same time it has a similar isophotal size. Figure 4.4 obviously demonstrates that the two distributions do not overlap. A 2-dimensional KS-test confirms that the two samples are marginally different. Therefore, we will now try to discern how the disc scale lengths differ at a constant isophotal radius. To this end, we first fit the local data with the following relation:

$$R_d = A \cdot R_{25}^B \;\longleftrightarrow\; \log R_d = \log A + B \cdot \log R_{25} \tag{4.1}$$

which produces a linear graph in a log-log space with the zero-point $\tilde{A} = \log A$ and the slope B. Since the local data span a larger range in R_{25} we will measure the slope from the complete local data set iteratively excluding outliers and then use it for the high redshift sample as well. Nevertheless, a free bisectorial fit to the high redshift data agrees quite well with the local fit. From the fit to the local galaxies we calculate a slope $B = 1.293$. Using this slope we can now minimise in a chi-squared sense the differences from the fit and the data. We find $\left[\tilde{A}\right]_{local} = -0.877 \rightarrow [A]_{local} = 0.133$ and $\left[\tilde{A}\right]_{highz} = -1.056 \rightarrow [A]_{highz} = 0.088$. The ratio $\alpha \equiv [R_d]_{highz} \,/\, [R_d]_{local} = [A]_{highz} \,/\, [A]_{local} = 0.66 \pm 0.03$ at a constant R_{25} indicates that galaxies of the same isophotal size had a smaller disc scale length at high redshift than today.

One might suspect that the tests did not confirm this result since the selection of high redshift galaxies was a little larger (in isophotal size) than the local average. Indeed removing four objects from the high redshift sample to match the local average in isophotal size (see Fig. 4.2) results in the disc scale length means tests to also drop below the 5% limit (see Fig. 4.5). Only the linear T-test (6%) still disagrees with the remaining tests (log. T-test: 1%, RS-Test: 2%, KS-test: 2%). This shows, that the removal of four sources from the high redshift sample to match the local data still has some impact on the outcome of the statistical tests. In this case, only after adjusting the sample, the tests could confirm the offset we found in the 2-dimensional plot. We conclude that **at high redshift objects with the same isophotal size as local galaxies had slightly smaller disc scale lengths than the nearby ones.** Nevertheless, the biggest high redshift galaxies have similar disc scale lengths as the largest local objects.

4.3 The Absolute Magnitude M_B^{rest}

Now we will inspect the absolute magnitude distributions of the two samples. The histograms of M_B^{rest} (see Fig. 4.6) indicate a clear result. All tests signal that the distributions are different ($\sim 0\%$). The FV-test indicates that the shapes of the distributions are marginally different. As in the case of the disc scale lengths, we analyse a 2-dimensional plot as well. Figure 4.7 demonstrates

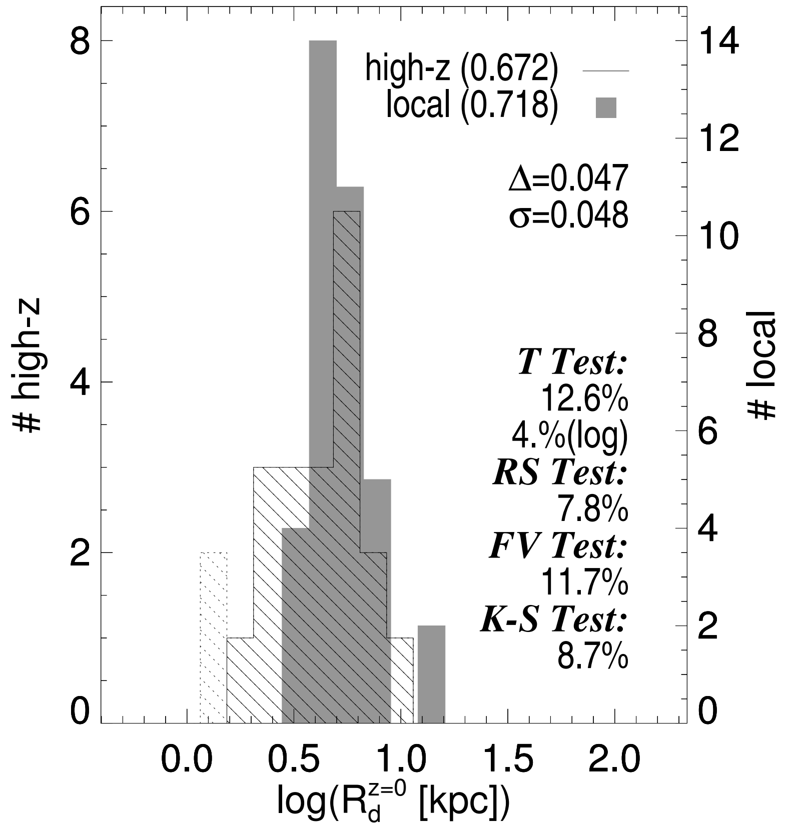

Figure 4.3: Histograms of the disc scale lengths

Histograms of the disc scale length R_d of the low (shaded region) and high redshift (striped region) samples. The symbols and annotations are the same as in Fig. 4.1. The difference of the means of both distributions is about 1σ. This gets confirmed by the statistical tests.

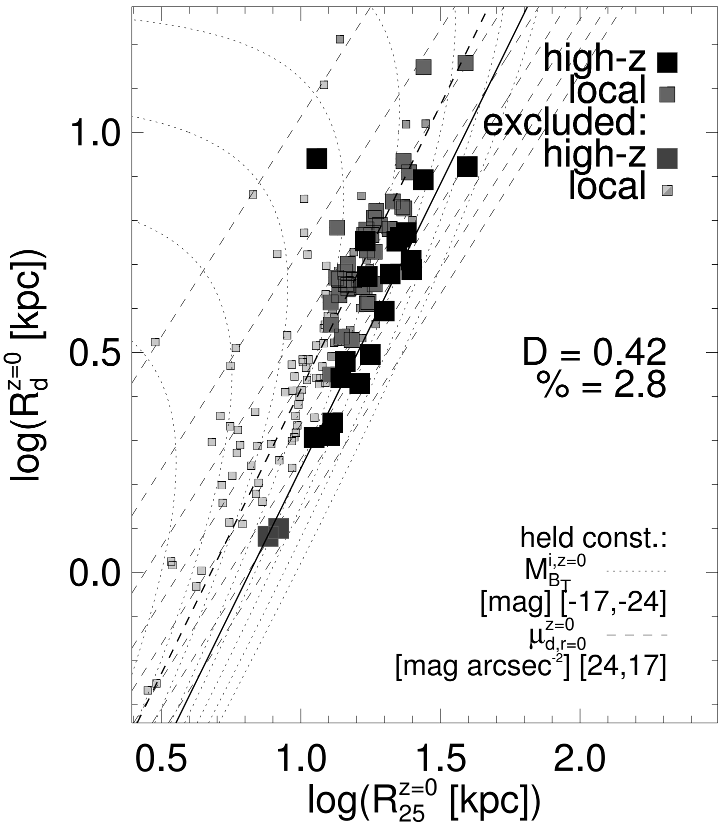

Figure 4.4: R_d as a function of R_{25}

The disc scale length R_d versus the isophotal radius R_{25} for high redshift (large symbols) and local galaxies (small symbols). Large grey boxes represent high redshift galaxies and small light grey boxes symbolise local galaxies that were excluded from the statistical analysis for not fitting the R_{25} selection criterion (see Sec. 3.2). Small dark grey boxes show local galaxies that were rejected from the sample to match the RC3 catalogue distributions of R_{25}, M_B and v_{rot}. The dotted and thin dashed lines are lines of constant absolute magnitude ranging from $-17 < M_B < -24$ and constant central disc surface brightness ranging from $24 < \mu_d < 17$, respectively. The thick dashed and solid lines are fits to the local and high redshift data, respectively. A KS-test indicates that both samples are marginally different (middle right).

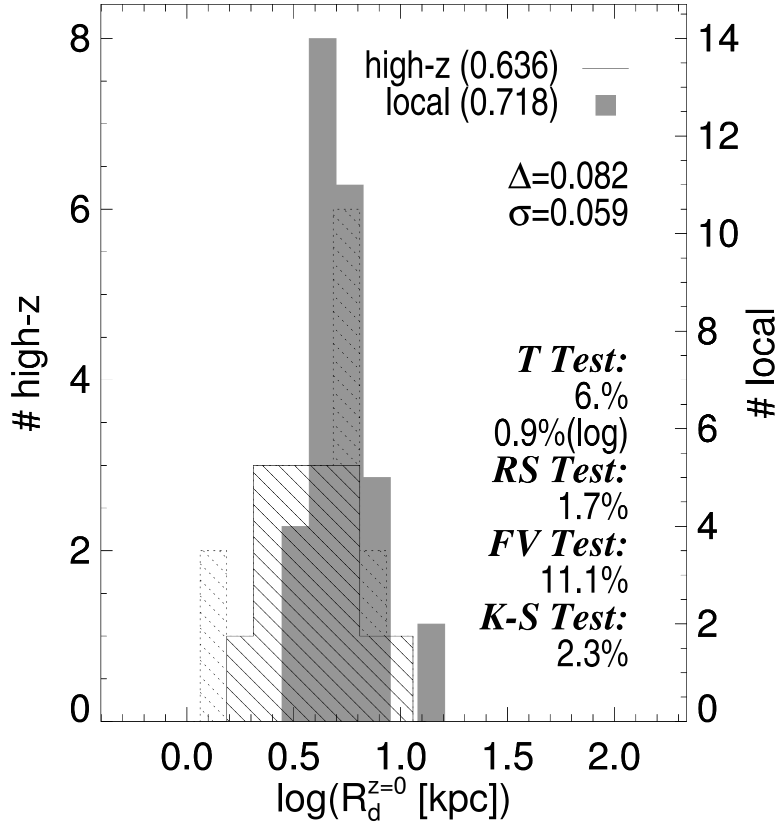

Figure 4.5: Histograms of the disc scale lenghts after matching the samples

Same plot as Fig. 4.3. The same four high redshift galaxies as in Fig. 4.2 were removed. While the variance of the two samples seems very similar (FV- test), the means of the two distributions are apparently different (almost 1.5σ; T-, RS-, KS-test).

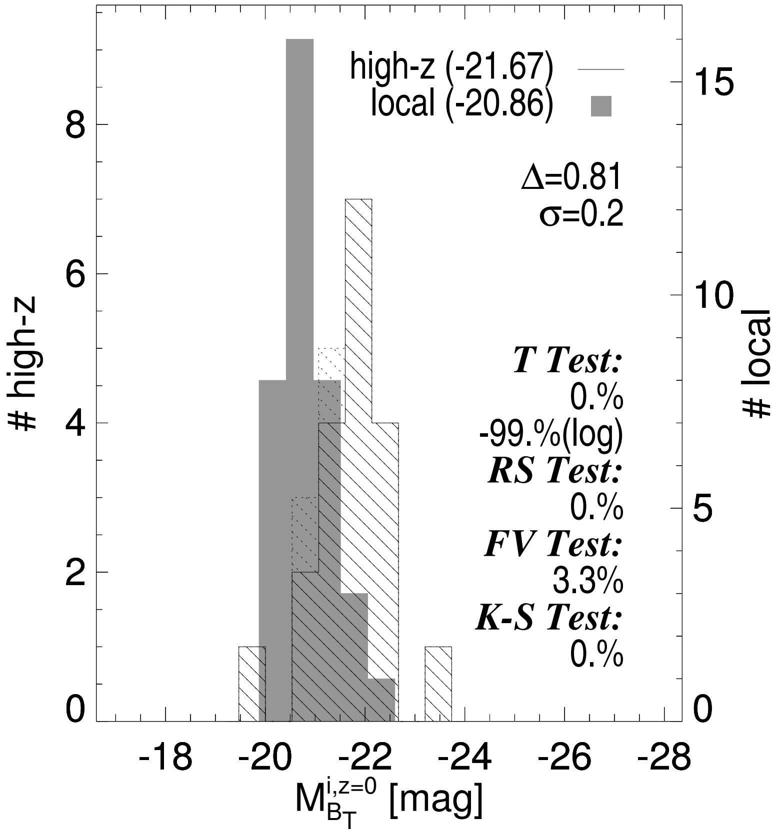

Figure 4.6: Histograms of the absolute magnitudes

Histograms of the absolute magnitudes M_B^{rest} of the low (shaded region) and high redshift (striped region) samples. The symbols and annotations are the same as in Fig. 4.1. The difference of the means of both distributions is a little more than 4σ. All tests confirm this result. The FV-test indicates that the variances of the two samples are marginally different.

that absolute magnitudes and isophotal sizes correlate well. A 2-dimensional KS-test ($\sim 0\%$) again indicates a clear difference between the two samples. A fit following the same prescription as in Sec. 4.2 quantifies the offset in absolute magnitude between local and distant galaxies at the same isophotal size:

$$M_B^{rest} = A + B \cdot \log R_{25}$$

For a constant R_{25} and assuming that $B = -5.304$ is the same for local and high redshift galaxies we find $[A]_{local} = -14.39$ and $[A]_{highz} = -15.07$. The difference $\Delta M \equiv [M_B^{rest}]_{highz} - [M_B^{rest}]_{local} = [A]_{highz} - [A]_{local} = -0.68 \pm 0.17$ proves that galaxies of the same isophotal size had brighter absolute magnitudes at high redshift as today.

We will again remove the same objects from the high redshift galaxies as in Sec. 4.1 to match the isophotal size distribution perfectly (see Fig. 4.2). The offset obtained from Figure 4.8 agrees with the aforementioned measurements and the tests confirm this. Therefore, we will conclude that **objects of the same isophotal size have different absolute magnitude in the distant and the nearby universe**. We will adopt a difference of $\Delta M = -0.74 \pm 0.12$ mag as a compromise between the value from the fitting procedure and the value from Fig. 4.8.

4.4 The Central Surface Brightness μ_d^{rest}

The last morphological quantity we will consider is the central surface brightness, which was measured in the process of fitting light profiles. Here, the histograms again show a clean picture (see Fig. 4.9): all tests agree that **the central surface brightness distributions of the local and the high redshift galaxies are significantly different** (all tests result in $p \sim 0\%$). Although not necessarily required, we will also inspect the 2-dimensional plot μ_d^{rest} versus R_{25}. However, Fig. 4.10 shows that central surface brightness obviously does not correlate well with isophotal size. Although the high redshift galaxies indicate a relatively good correlation, the scatter about that relation for the local sample is very broad. The fitting technique will now fail to provide us with information about the relative surface brightnesses of objects with the same isophotal size. However, we also have to inspect the distributions of the two samples after matching the high redshift targets with the local galaxies in isophotal size (see Fig. 4.11). Comparing Fig. 4.11 with Fig. 4.9 shows that not only objects with the highest surface brightnesses got removed when matching the isophotal sizes, but sources with a wide range of surface brightnesses. This again indicates that if a correlation between central surface brightness and isophotal size exists it can only be weak. Another supporting factor for this is, that the mean of the high redshift distribution did not change by very much ($\Delta \langle \mu_d^{rest} \rangle = -1.44 \pm 0.32 \longleftrightarrow \Delta \langle \mu_d^{rest} \rangle = -1.56 \pm 0.38$). Considering the large measurement errors for this value we will adopt $\Delta \langle \mu_d^{rest} \rangle = -1.50 \pm 0.25$ mag arcsec^{-2}, corresponding to $\langle \mu_d^{rest} \rangle_{local} = 21.49 \pm 0.10$ mag arcsec^{-2} and $\langle \mu_d^{rest} \rangle_{local} = 19.99 \pm 0.25$ mag arcsec^{-2}. Apparently, the bulk of evolution we see when comparing galaxies at low and high redshift of the same isophotal size is in central surface brightness.

4.5 Morphological Evolution

In Sec. 3.5 we explained the basic formulae describing the four disc parameters isophotal size R_{25}, disc scale length R_d, absolute magnitude M_B^{rest} and central disc surface brightness $\mu_{0,d}^{rest}$. Since all of them are connected the various mean values we estimated in the previous sections should constitute a consistent picture of disc parameters at low and high redshift.

From eq. 3.1 we find:

$$\mu_d^{rest}(R) = \mu_{0,d}^{rest} + 2.5 \cdot \log e \cdot \frac{R}{R_d}$$

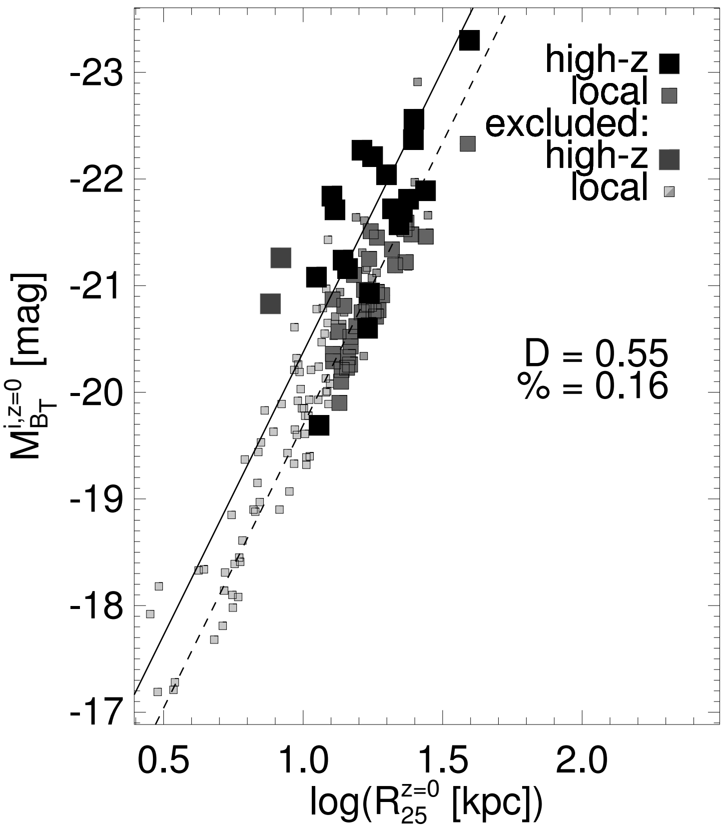

Figure 4.7: M_B^{rest} as a function of R_{25}

The absolute magnitudes M_B^{rest} versus the isophotal radius R_{25} for high redshift (large symbols) and local galaxies (small symbols). Symbols are the same as in Fig. 4.4. A KS-test indicates that both samples are significantly different (middle right).

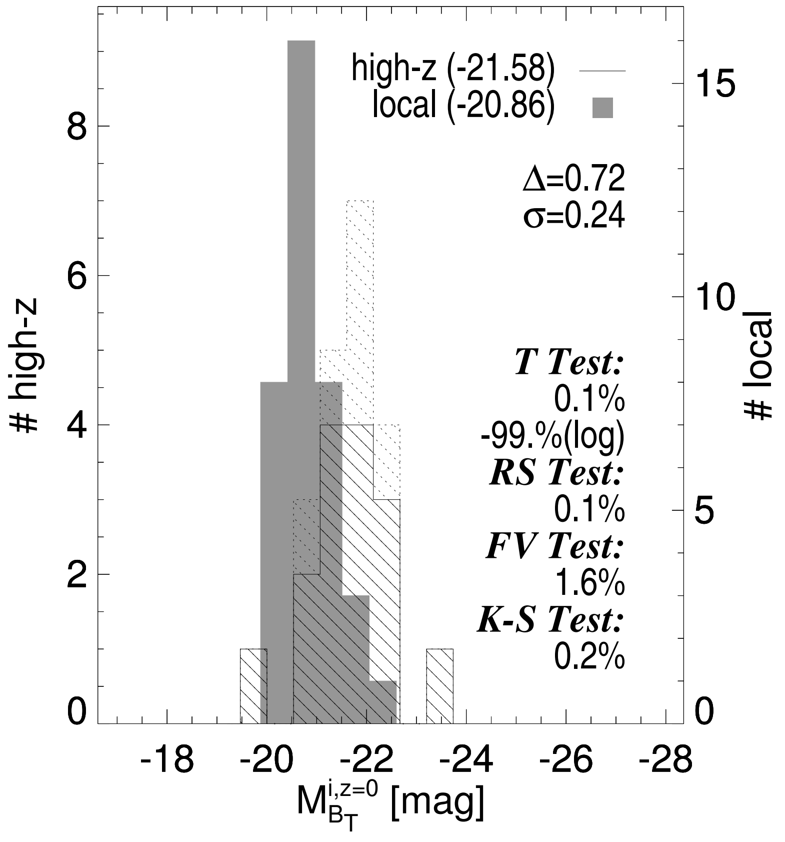

Figure 4.8: Histograms of the absolute magnitudes after matching the samples

Same plot as Fig. 4.6. The same four high redshift galaxies as in Fig. 4.2 were removed. In comparison to Fig. 4.6 the difference of the means got smaller. However, the tests still indicate that both samples are significantly different.

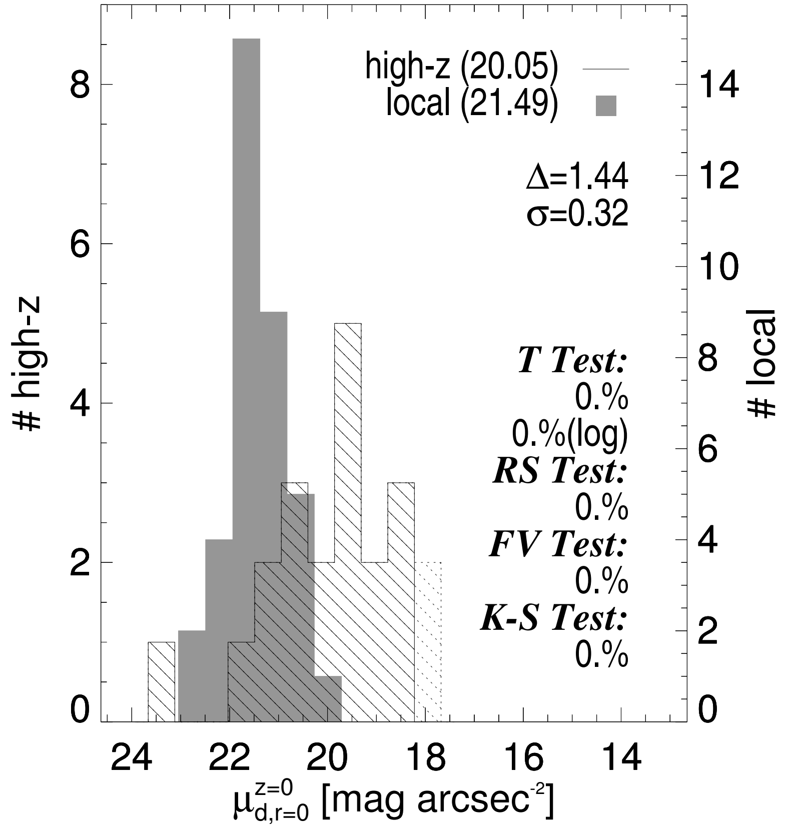

Figure 4.9: Histograms of the central surface brightnesses

Histograms of the rest-frame central surface brightnesses μ_d^{rest} of the low (shaded region) and high redshift (striped region) samples. The symbols and annotations are the same as in Fig. 4.1. The difference of the means of both distributions is 4.5σ, which gets confirmed by the statistical tests. However, the FV-test also indicates a significantly broader distribution for the high redshift galaxies as the local sample.

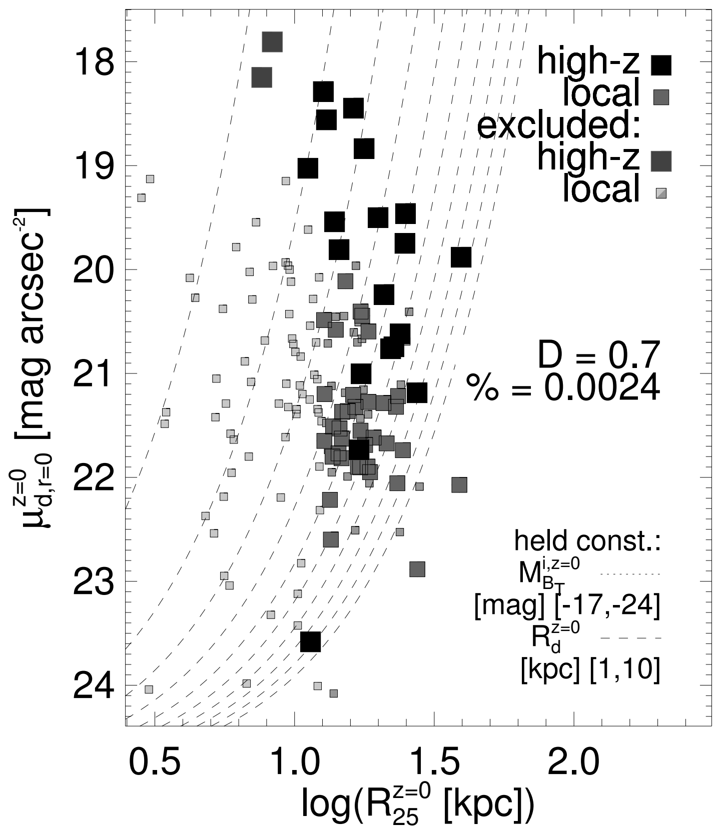

Figure 4.10: μ_d^{rest} as a function of R_{25}

The rest-frame central surface brightness μ_d^{rest} versus the isophotal radius R_{25} for high redshift (large symbols) and local galaxies (small symbols). Symbols are the same as in Fig. 4.4. The dashed lines are lines of constant disc scale length ranging from $1 < R_d < 10$. A KS-test indicates that both samples are significantly different (middle right).

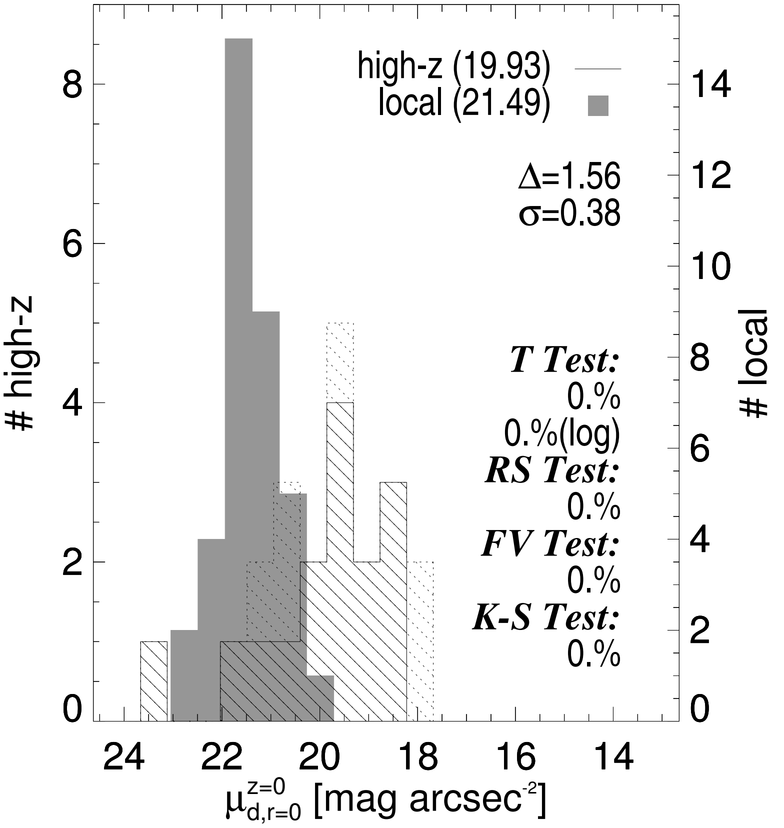

Figure 4.11: Histograms of the central surface brightnesses after matching the samples

Same plot as Fig. 4.9. The same four high redshift galaxies as in Fig. 4.2 were removed. The difference of the means of the two distributions has not changed significantly compared to Fig. 4.9. As expected, the standard deviation of this difference is somewhat larger than that of Fig. 4.9.

At a surface brightness 25 mag arcsec^{-2} this equation transforms into the defining equation for the isophotal size R_{25}:

$$R_{25} = \frac{25 - \mu_{0,d}^{rest}}{2.5 \cdot \log e} \cdot R_d \tag{4.2}$$

Inserting the high and low redshift sample values from Fig. 4.11 for a constant R_{25} we find:

$$\tilde{\alpha} \equiv \frac{[R_d]_{highz}}{[R_d]_{local}} = \frac{\left[\frac{25-\mu_{0,d}^{rest}}{2.5\cdot\log e}\right]_{local}}{\left[\frac{25-\mu_{0,d}^{rest}}{2.5\cdot\log e}\right]_{highz}} = \frac{25 - \left[\mu_{0,d}^{rest}\right]_{local}}{25 - \left[\mu_{0,d}^{rest}\right]_{highz}} = 0.70 \pm 0.04$$

It is comforting that $\tilde{\alpha}$ and α agree so well. As a first result we remark that **the disc scale lengths of the high redshift galaxies of our sample are only on average** $\sim 68\%$ **of those of local galaxies with the same isophotal radius**.

One might wonder whether it is indeed the disc scale lengths that increase with time or rather the isophotal sizes that decrease with time. In other words, one could in contrast to our preceeding discussion also try to examine the problem from the point of view of constant disc scale radii. Behind these two approaches we find two underlying pictures of disc galaxy evolution. On one hand there is scale evolution, i.e. with time disc scale lengths grow while isophotal sizes roughly stay constant. the disc grows from the inside out (see e.g. Bouwens et al., 1997). This also implies that to keep the absolute magnitudes constant the central surface brightnesses have to dim. This would then compensate the increase of disc scale lengths. On the other hand, one could imagine that the disc scale lengths stayed constant. This then requires that, with central surface brightnesses decreasing with time, the isophotal sizes also decrease. As a result of this absolute magnitudes should also get fainter with time. This scenario could be termed self-similar evolution of disc galaxies. To test the two scenarios we calculate the difference of the absolute disc magnitudes at high and low redshift

$$\Delta M = \left[M_{B,disc}^{rest}\right]_{highz} - \left[M_{B,disc}^{rest}\right]_{local} \approx \left[M_{B}^{rest}\right]_{highz} - \left[M_{B}^{rest}\right]_{local}$$

For simplicity we will assume that this difference is roughly equal to the difference of absolute magnitudes. We find:

$$\begin{aligned}
\Delta M &= \left[-5 \cdot \log R_d - 38.568 + \mu_{0,d}^{rest}\right]_{highz} - \left[-5 \cdot \log R_d - 38.568 + \mu_{0,d}^{rest}\right]_{local} \\
&= -5 \cdot \log \frac{[R_d]_{highz}}{[R_d]_{local}} + \left[\mu_{0,d}^{rest}\right]_{highz} - \left[\mu_{0,d}^{rest}\right]_{local} \\
&= -5 \cdot \log \alpha + \Delta \left\langle \mu_{0,d}^{rest} \right\rangle
\end{aligned} \tag{4.3}$$

Inserting values for the central surface brightness from Fig. 4.11 we find $\Delta M_{IO} = -0.66$ mag in the case of scale evolution (IO = inside-out, $\alpha = 0.68$) and $\Delta M_{SS} = -1.5$ mag for a self-similar evolutionary scenario (SS = self-similar, $\alpha = 1$). Our measured value of $\Delta M = -0.74$ mag is much closer to the prediction for scale evolution than for self-similar evolution. However, since both processes may be at work at the same time and without better statistics to reduce the error bars we conclude that **scale length evolution is likely to provide the main part driving disc evolution, in comparison to self similar evolution**.

To provide further support for this theory we will now try to match the R_d distributions by rejecting small high redshift galaxies and repeating the exercises from above. This should then put the absolute magnitude distributions as much in favour of a self-similar evolutionary scenario as possible. Removing the smallest three objects essentially leads to a match between the two R_d distributions (see Fig. 4.12). As a result of this the high redshift mean values for R_{25}, M_B^{rest} and $\mu_{0,d}^{rest}$ change as well: $[R_{25}]_{highz} = 19.65 \pm 1.18$ kpc, $[M_B^{rest}]_{highz} = -21.69 \pm 0.22$ mag and $\left[\mu_{0,d}^{rest}\right]_{highz} = 20.10 \pm 0.23$ mag arcsec^{-2} (see Fig. 4.13, 4.14 and 4.15). Solving eq. 4.1 for R_{25} we can calculate a new ratio $\beta \equiv [R_{25}]_{highz} / [R_{25}]_{local} = \left([A]_{local} / [A]_{highz}\right)^{1/B} = (1/\alpha)^{1/B} = 1.38$.

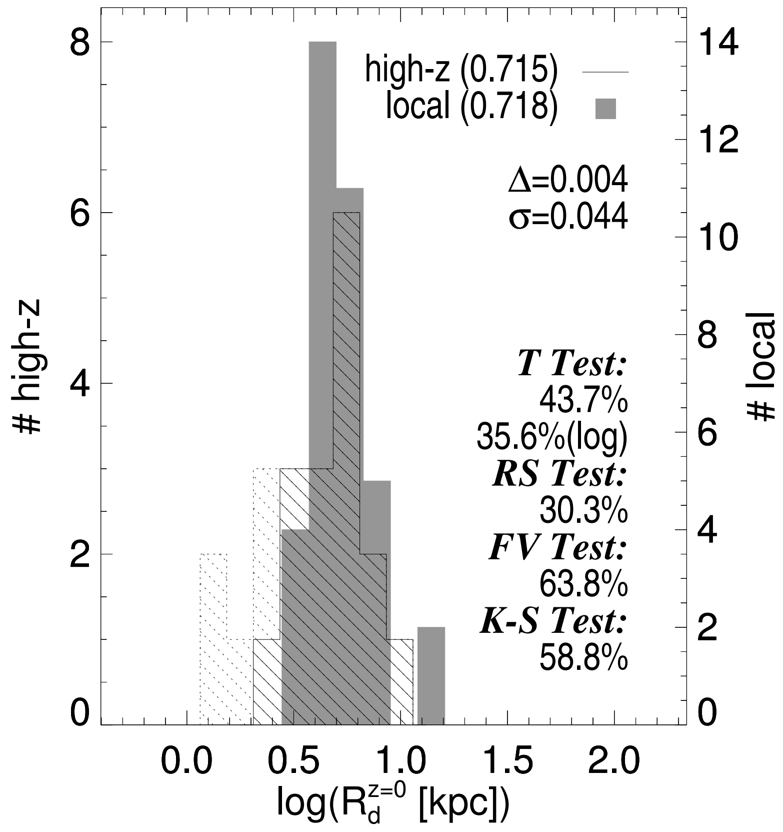

Figure 4.12: Histograms of the matched disc scale lengths

Matched histograms of the disc scale lengths of the low (shaded region) and high redshift (striped region) samples. The symbols and annotations are the same as in Fig. 4.1. After removing the three smallest galaxies from the high redshift sample the difference of the means of both distributions is almost zero. The statistical tests confirm this result.

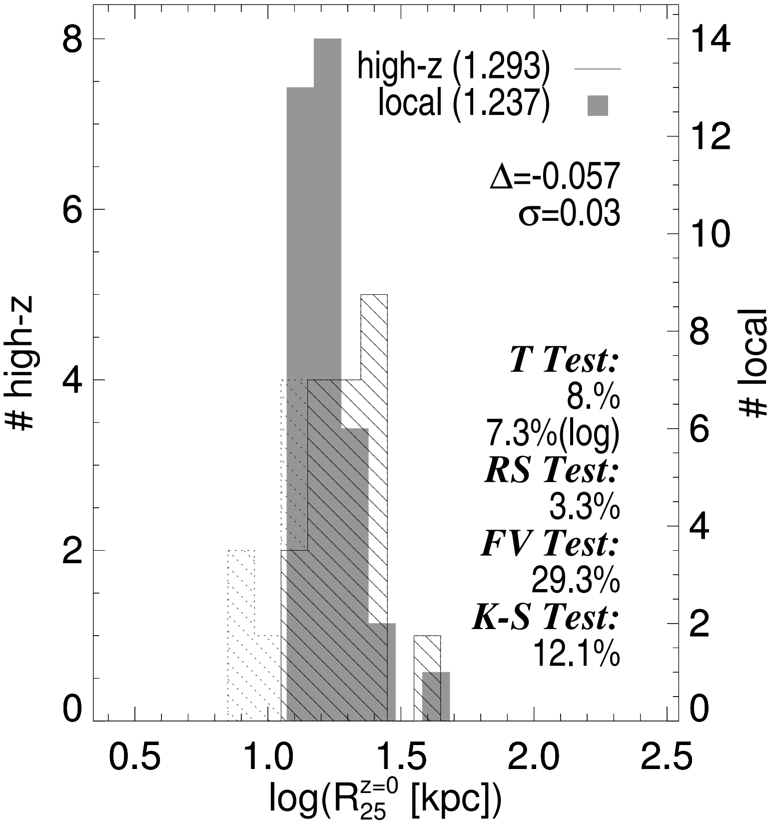

Figure 4.13: Histograms of the isophotal sizes after matching R_d

Histograms of the isophotal radius of the low (shaded region) and high redshift (striped region) samples after matching the disc scale lengths (see Fig. 4.12). The symbols and annotations are the same as in Fig. 4.1. After removing the three smallest high redshift galaxies from the sample we measure a difference of the means of the two distributions of almost 2σ. The tests fail to confirm this measurement. Only the RS-test indicates a marginal differenece.

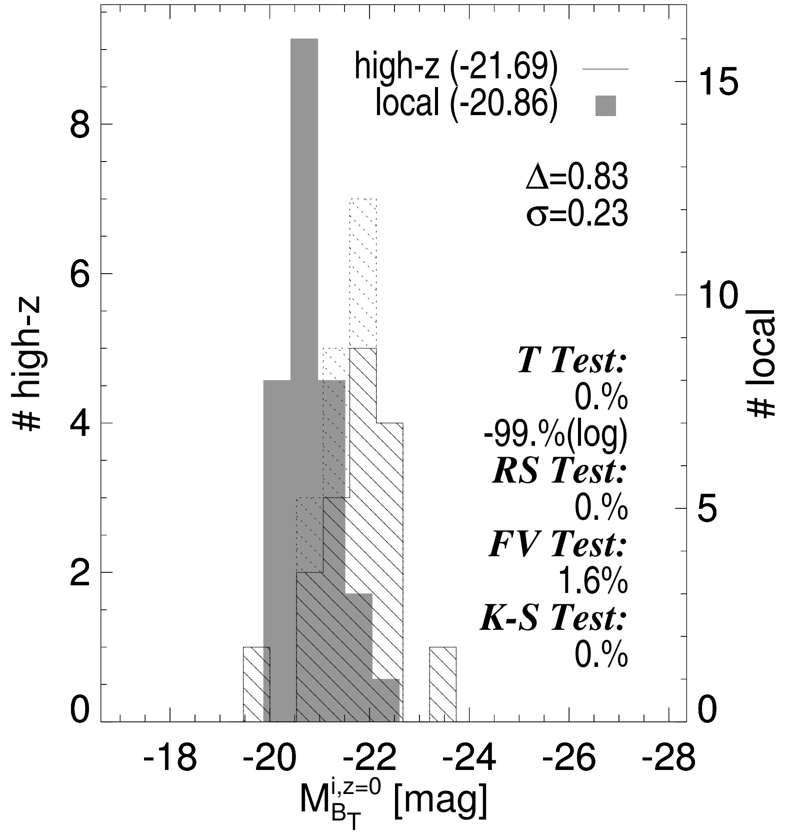

Figure 4.14: Histograms of the absolute magnitudes after matching R_d

Histograms of the absolute magnitude of the low (shaded region) and high redshift (striped region) samples after matching the disc scale lengths (see Fig. 4.12). The symbols and annotations are the same as in Fig. 4.1. The difference of the means of the two distributions is still almost 4σ after removing the three smallest high redshift galaxies from the sample. The statistical tests clearly separate the two samples.

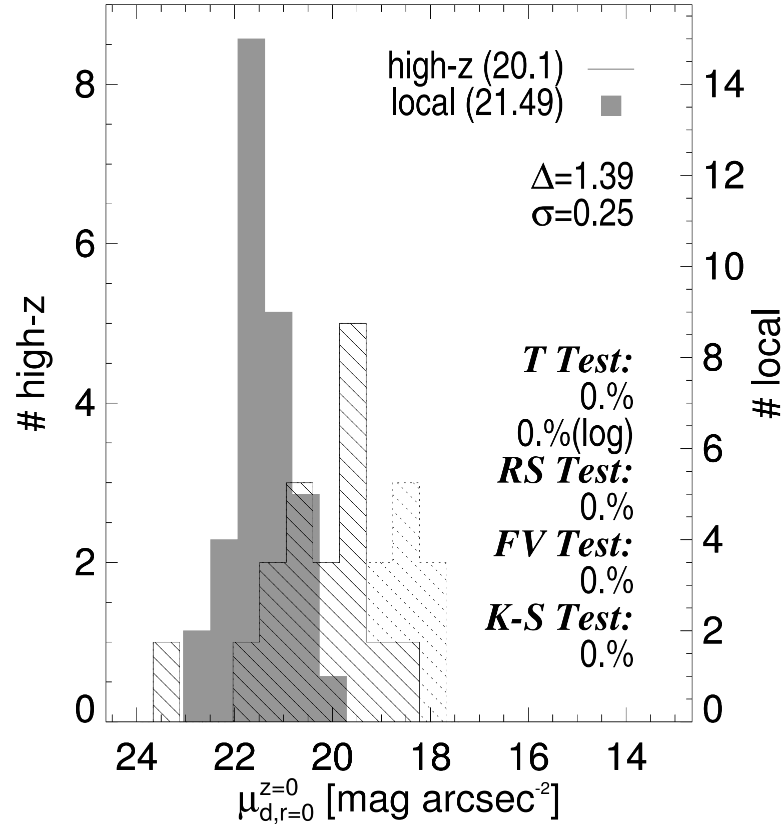

Figure 4.15: Histograms of the central surface brightnesses after matching R_d

Histograms of the central disc surface brightness of the low (shaded region) and high redshift (striped region) samples after matching the disc scale lengths (see Fig. 4.12). The symbols and annotations are the same as in Fig. 4.1. The difference of the means of the two distributions got smaller by removing the smallest sources, which had predominantly the highest surface brightnesses, but is still about 5.5σ.

Furthermore, eq. 4.2 leads to a new variable $\tilde{\beta} = \left[25 - \mu_{0,d}^{rest}\right]_{highz} / \left[25 - \mu_{0,d}^{rest}\right]_{local} = 1.40 \pm 0.08$. So far, self-similar evolution is consistent after matching the disc scale length distributions. Now we have to check whether the new absolute magnitude distributions (see Fig. 4.14) deliver a difference ΔM, which matches the self-similar evolution model. Using $\alpha = 1$, which is required by construction for self-similar evolution, we calculate $\widetilde{\Delta M}_{SS} = -1.39$. For scale evolution we now calculate $\widetilde{\Delta M}_{IO} = -0.55$. This implies using $\alpha = 0.68$ again. The previously measured value $\Delta M = -0.74 \pm 0.12$ is not too different from the new measurement after matching the disc scale lengths $\Delta M = -0.76 \pm 0.14$ (Fig. 4.14). Although the predicted value $\widetilde{\Delta M}_{SS} = -1.39$ from the self-similar evolution model got a little closer to the measured value, $\widetilde{\Delta M}_{IO} = -0.55$ from the inside-out model still provides a much better match even after optimising the disc scale lengths. Therefore, even using the other extreme, i.e. matching the disc scale lengths of the high redshift and low redshift samples, we do not measure the correct absolute magnitude difference that would be required to make self-similar evolution the most probable model.

Since the mean values of the histograms of the absolute magnitudes become the critical numbers to decide which of the two models is the most probable one, one might conjecture that our local sample contains more and brighter bulges, which could “artificially” decrease the observed difference between the two populations. We used our bulge-to-disc information to compute disc-only-magnitudes for all our objects. The resulting mean magnitudes, however, lead only to a very mild increase of the difference of $\Delta M_d = -0.93 \pm 0.2$ mag, again confirming the validity of the inside-out scenario.

We conclude that, **independent of the specific choice of selection, an inside-out model in which the isophotal radius stays roughly constant, while the mean central surface brightness and absolute magnitude dim and the mean disc scale length increases with time is the most probable mechanism for morphological evolution in contrast to self-similar evolution where the mean disc scale lengths stay constant, the mean central surface brightness and absolute magnitude dim and the isophotal radius decreases with time**.

4.6 The Rotation Speed v_{rot} and Mass $M_{2.2}$

Besides these striking morphological results we can now also address the dynamical properties of the local and distant populations. Firstly, we will show the distributions of the inclination corrected rotation speed for both the high and low redshift galaxy samples (see Fig. 4.16). As indicated by the mean tests the high redshift galaxies clearly rotate slower than their local counterparts (all mean-tests have < 1%). On the other hand, the variances and therefore the overall shape of the distributions have not changed (FV-test: 20%). As in the case of the morphological parameters, we will also inspect the correlation between R_{25} and v_{rot}. It appears that isophotal size also scales well with rotation speed (see Fig. 4.17). Therefore, subtracting a fit from the data will produce a meaningful estimate of the ratio of the rotation speeds of high and low redshift galaxies at a fixed isophotal size. We adopt a similar formula as eq. 4.1:

$$v_{rot} = A \cdot R_{25}^{B} \longleftrightarrow \log v_{rot} = \log A + B \cdot \log R_{25} \tag{4.4}$$

A chi-square fit results in $B = 0.8520$ and $\left[\tilde{A}\right]_{local} = \log A_{local} = 1.3198 \rightarrow [A]_{local} = 20.88$ and $\left[\tilde{A}\right]_{highz} = \log A_{highz} = 1.1046 \rightarrow [A]_{highz} = 12.72$. The ratio $\alpha \equiv [v_{rot}]_{highz} / [v_{rot}]_{local} = [A]_{highz} / [A]_{local} = 0.61 \pm 0.06$ determines the drop in rotation speed at a constant isophotal size. This value is in fair agreement with the value derived from the means of the high ($\langle v_{rot} \rangle_{highz} = (153 \pm 11)$ km s^{-1}) and low ($\langle v_{rot} \rangle_{local} = (202 \pm 8)$ km s^{-1}) redshift samples: $\alpha = 0.76 \pm 0.06$. Using the mean local rotation velocity $\langle v_{rot} \rangle_{local} = (202 \pm 8)$ km s^{-1} we derive a high redshift mean rotation velocity determined from the 2-dimensional fit of $\langle v_{rot} \rangle_{highz} = (123 \pm 13)$ km s^{-1}. Furthermore, this value is fairly independent of the specific selection of the sample. Matching the distant sample in isophotal size with the local galaxies the same way we did before (by rejecting four

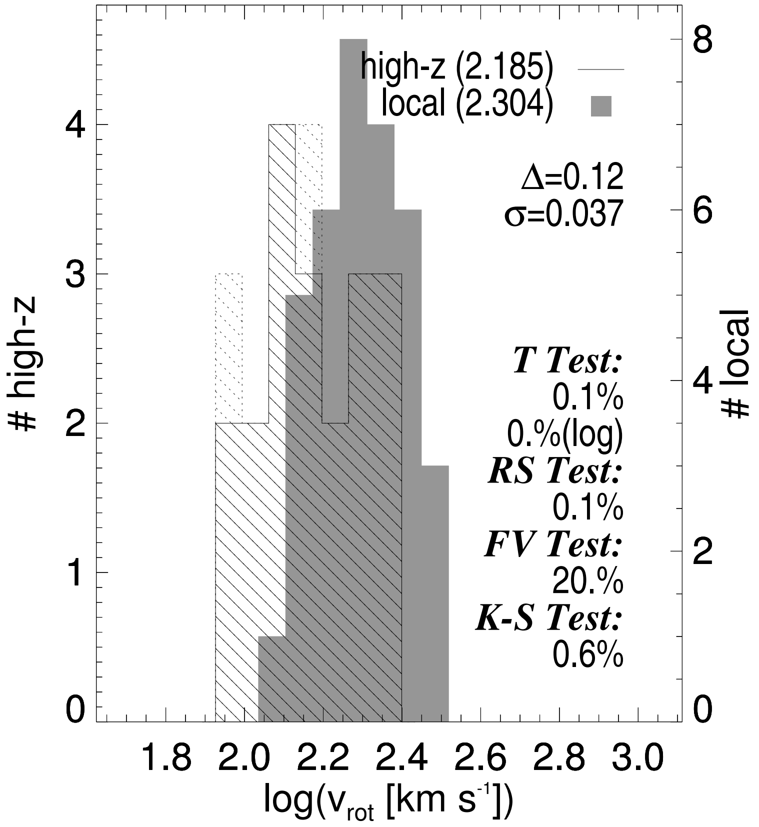

Figure 4.16: Histograms of the rotation speeds

Histograms of the inclination corrected rotation speed v_{rot} of the low (shaded region) and high redshift (striped region) samples. The symbols and annotations are the same as in Fig. 4.1. The difference of the means of both distributions is more than 3σ, which gets confirmed by the statistical tests. The FV-test indicates that the two distributions have a similar shape.

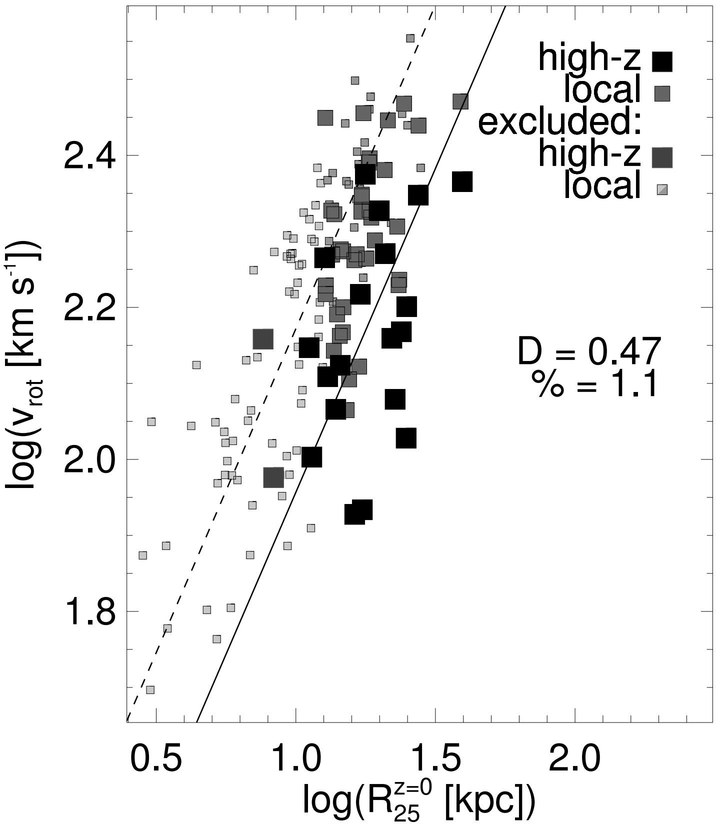

Figure 4.17: v_{rot} as a function of R_{25}

The rotation velocity v_{rot} versus the isophotal radius R_{25} for high redshift (large symbols) and local galaxies (small symbols). Symbols are the same as in Fig. 4.4. A KS-test indicates that both samples are significantly different (middle right).

galaxies with large R_{25}) results in mean a value $\langle v_{rot}\rangle = (150 \pm 13)$ km s^{-1} for the high redshift targets (see Fig. 4.18). Selecting the samples on R_d gives the same result ($\langle v_{rot}\rangle = (153 \pm 13)$; see Fig. 4.19). This is somewhat surprising since because of the correlation between R_{25} and v_{rot} one should expect a trend of primarily rejecting objects with large rotation speeds on one hand and small ones on the other. The scatter of the relation eq. 4.6 is large enough, though, to blur any such trend.

Since at large radii the dark matter is the dominant fraction of the total matter content even in a massive disc galaxy, we can now on first order assume an approximately spherical mass distribution, that is rotationally supported and where peculiar motions are negligible ($v_{peculiar} \ll v_{circular}$), to convert the rotation speeds to masses to derive a mass ratio between local galaxies and galaxies at a redshift $z \approx 0.9$:

$$\frac{\left[\langle v_{rot}\rangle^2\right]_{local}}{\left[\langle v_{rot}\rangle^2\right]_{highz}} = \frac{GM_{local}}{R} \Big/ \frac{GM_{highz}}{R} = \frac{M_{local}}{M_{highz}} \equiv \alpha_M \tag{4.5}$$

The radius R, which defines the enclosed area, is assumed to be the same at low and high redshift. With the local and high redshift mean rotation velocities $\left[\langle v_{rot}\rangle^2\right]_{local} = \left((202 \pm 8)\ \text{km s}^{-1}\right)^2$ and $\left[\langle v_{rot}\rangle^2\right]_{highz} = \left((142 \pm 7)\ \text{km s}^{-1}\right)^2$, which we use as a compromise between the values from the 2-dimensional fit and the histograms, we calculate a mean mass ratio $\alpha_M = 2.02 \pm 0.26$.

Furthermore, we can derive disc masses $M_{2.2}$ for all our galaxies at a specified radius $R_{2.2} = 2.2 \cdot R_d$ using:

$$M_d(R) = 2\pi\Sigma_0 R_d^2 \left[1 - e^{-\frac{R}{R_d}} \cdot \left(1 + \frac{R}{R_d}\right)\right]$$

and eq. 3.8 to find:

$$M_{2.2} = M_d(R \equiv R_{2.2} = 2.2 \cdot R_d) = 1.668 \cdot \frac{v_{d,circ}^2(R_{2.2}) \cdot R_d}{G}$$

We assume that $v_{d,circ}(R_{2.2})$ is approximated well by our rotation velocity v_{rot}. The validity of the approximation is proven by Fig. 3.23.

We plot the distributions of the disc mass enclosed at 2.2 disc scale radii $M_{2.2}$ for both the high and low redshift galaxy samples in Fig. 4.20. The high redshift galaxies have a significantly lower mass than the local galaxies (linear T-test: 2%, log. T-test: 0%, RS-test: 0%, KS-test: 0.2%), with the overall shape of the distributions not having changed (FV-test: 38%). Next we will also inspect the correlation between R_{25} and $M_{2.2}$. As expected, the isophotal sizes scale well with $M_{2.2}$ (see Fig. 4.21). We will now use fits to the low and high redshift data to produce an estimate of the ratio of the disc masses at a fixed isophotal size for both samples. Again, we adopt a similar formula than eq. 4.1:

$$M_{2.2} = A \cdot R_{25}^B \longleftrightarrow \log M_{2.2} = \log A + B \cdot \log R_{25} \tag{4.6}$$

We find $B = 2.4158$ and $\left[\tilde{A}\right]_{local} = 8.0055 \rightarrow [A]_{local} = 1.013 \cdot 10^8$ and $\left[\tilde{A}\right]_{highz} = 7.4984 \rightarrow [A]_{highz} = 3.150 \cdot 10^7$. Therefore, the ratio of disc masses at low and at high redshift is $\alpha \equiv [M_{2.2}]_{local} / [M_{2.2}]_{highz} = [A]_{local} / [A]_{highz} = 3.21 \pm 0.54$. The agreement with the value obtained from the means ($\langle M_{2.2}\rangle_{highz} = (3.57 \pm 0.49) \cdot 10^{10}$ M$_\odot$, $\langle M_{2.2}\rangle_{local} = (7.48 \pm 0.57) \cdot 10^{10}$ M$_\odot$) of the individual distributions $\alpha = 2.10 \pm 0.33$ is only fair within the error bars. Adopting $\langle \log(R_{25})\rangle = 1.25$ as a compromise for the mean isophotal radius at low and high redshift, we derive $\langle M_{2.2}\rangle_{local} = (10.60 \pm 0.45) \cdot 10^{10}$ M$_\odot$ and $\langle M_{2.2}\rangle_{highz} = (3.30 \pm 0.54) \cdot 10^{10}$ M$_\odot$ for the corresponding mean masses from the two-dimensional fit.

Now we will check whether our distributions withstand matching the R_{25}-distributions. The high redshift $M_{2.2}$ distribution after removing four galaxies did not change significantly ($\langle M_{2.2}\rangle_{highz} = (3.40 \pm 0.59) \cdot 10^{10}$ M$_\odot$, see Fig. 4.22). A selection based on R_d gives the same result ($\langle M_{2.2}\rangle_{highz} =$

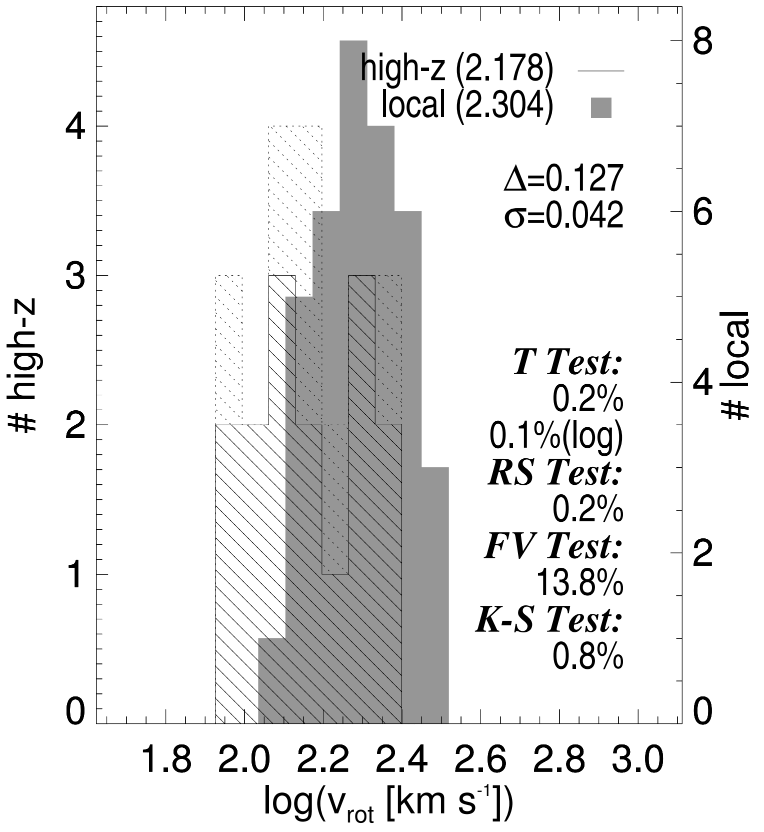

Figure 4.18: Histograms of the rotation speeds after matching the samples

Same plot as Fig. 4.16. The same four high redshift galaxies as in Fig. 4.2 were removed. In comparison to Fig. 4.16 the difference of the means did not change significantly. Furthermore, the tests indicate that the samples are indeed different.

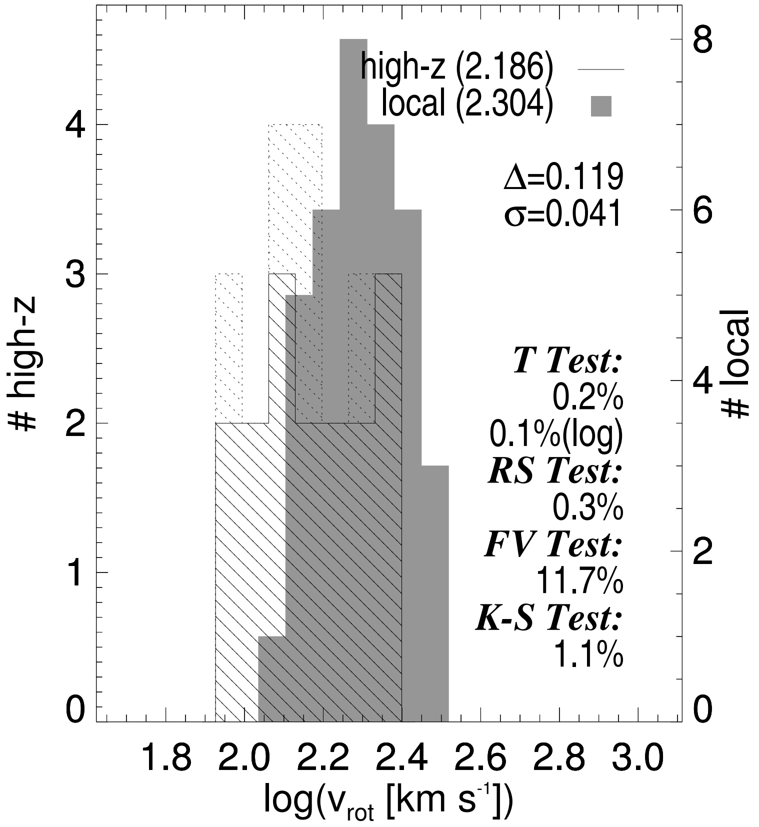

Figure 4.19: Histograms of the rotation speeds after matching R_d

Histograms of the rotation velocity of the low (shaded region) and high redshift (striped region) samples after matching the disc scale lengths (see Fig. 4.12). The symbols and annotations are the same as in Fig. 4.1. The difference of the means of the two distributions did not change by removing the smallest sources.

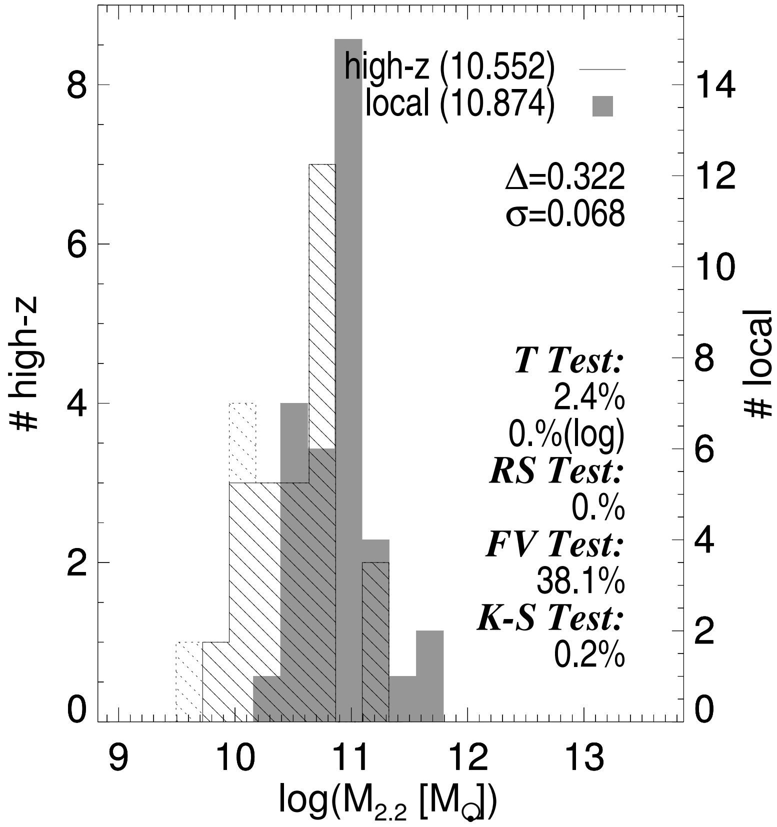

Figure 4.20: Histograms of the disc mass within 2.2 disc scale radii

Histograms of the disc mass $M_{2.2}$ enclosed within 2.2 disc scale radii R_d of the low (shaded region) and high redshift (striped region) samples. The symbols and annotations are the same as in Fig. 4.1. The difference of the means of both distributions is more than 4.5σ. This gets confirmed by the statistical tests. The FV-test indicates that the two distributions have a similar shape.

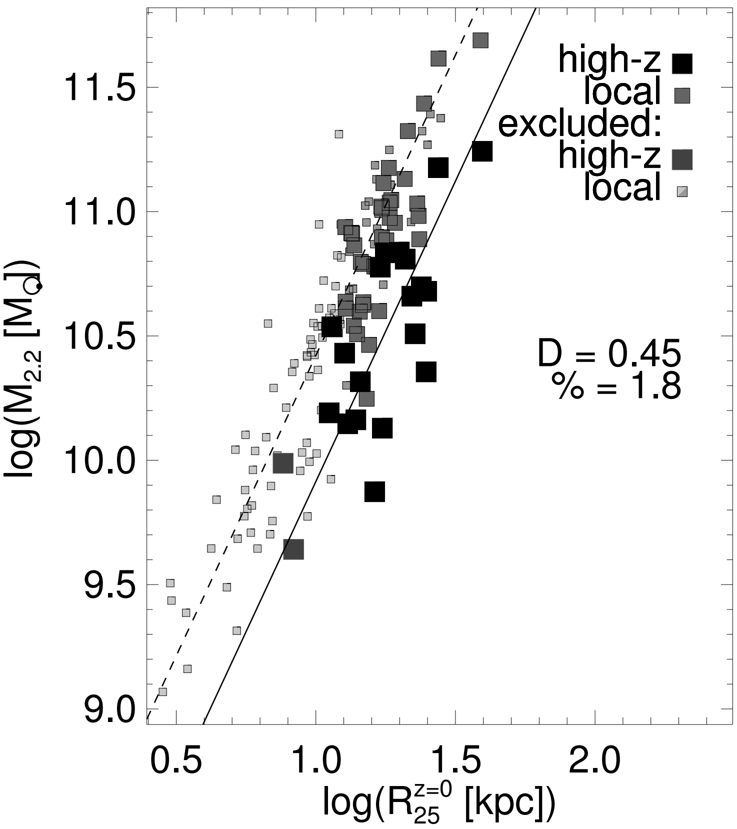

Figure 4.21: $M_{2.2}$ as a function of R_{25}

The disc mass $M_{2.2}$ versus the isophotal radius R_{25} for high redshift (large symbols) and local galaxies (small symbols). Symbols are the same as in Fig. 4.4. A KS-test indicates that both samples are significantly different (middle right).

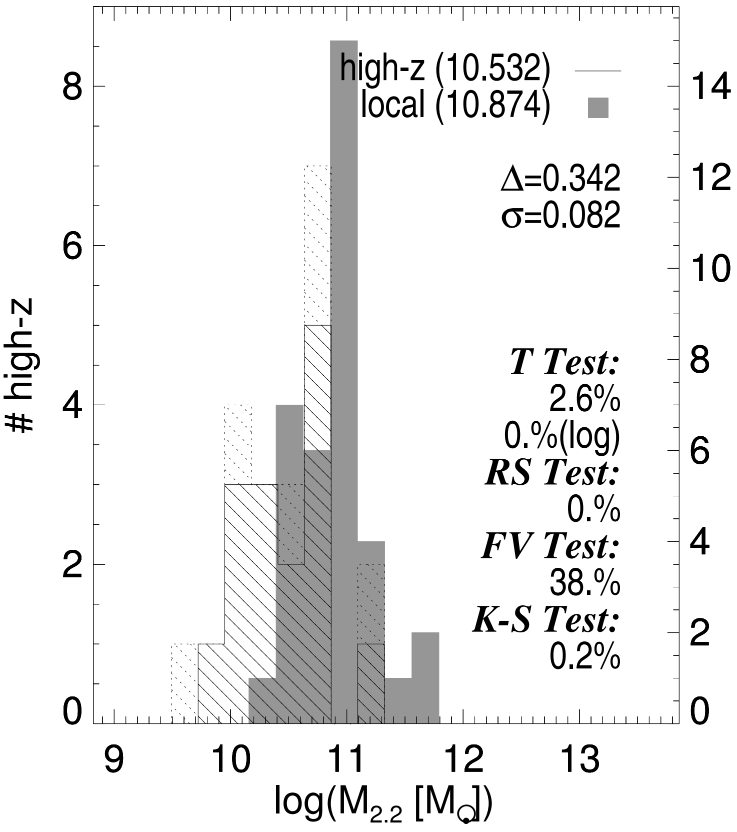

Figure 4.22: Histograms of the enclosed mass after matching the samples

Same plot as Fig. 4.20. The same four high redshift galaxies as in Fig. 4.2 were removed. The difference of the means of the distributions did not change significantly in comparison to Fig. 4.20. Again, the tests indicate that the means are indeed different, with the same overall profile shape.

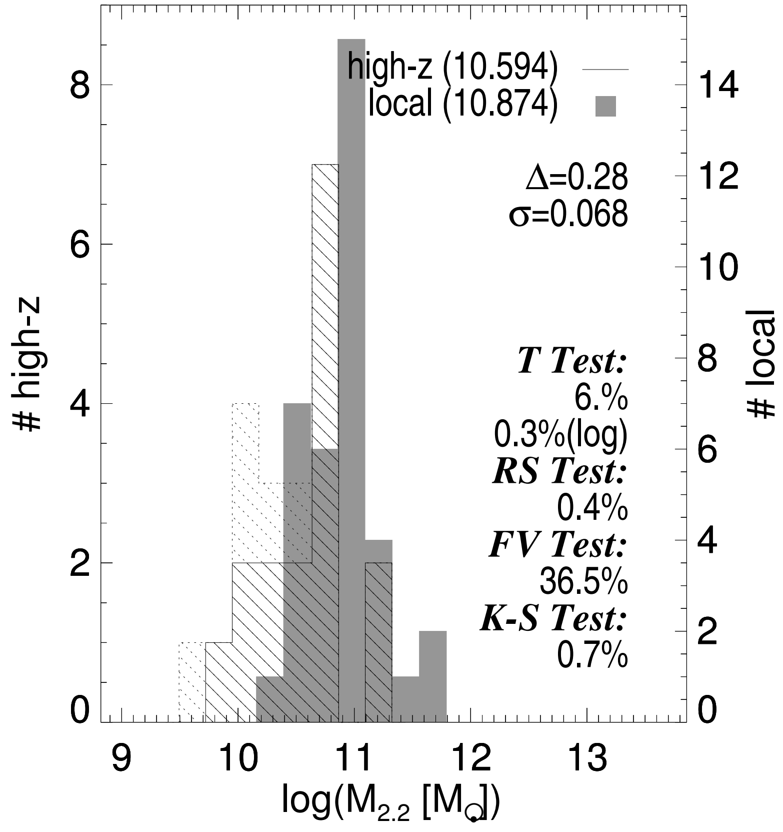

Figure 4.23: Histograms of the enclosed mass after matching R_d

Histograms of the enclosed mass of the low (shaded region) and high redshift (striped region) samples after matching the disc scale lengths (see Fig. 4.12). The symbols and annotations are the same as in Fig. 4.1. The difference of the means of the two distributions did not change by removing the smallest sources.

$(3.93 \pm 0.54) \cdot 10^{10}$ $M_\odot$, see Fig. 4.23). The strong correlation between R_{25} and $M_{2.2}$ gets nicely reflected in those mean values. Rejecting the smallest sources delivers the highest mean value while rejecting the largest sources results in the lowest mean value.

Since the largest discrepancy between the values of the mean masses from the histograms and the two-dimensional fit was in the local measurement, we adopt in the following for the within $2.2 \cdot R_d$ enclosed mass $\langle M_{2.2} \rangle_{highz} = (3.42 \pm 0.31) \cdot 10^{10}$ $M_\odot$ and $\alpha \equiv [M_{2.2}]_{local} \, / \, [M_{2.2}]_{highz} = [A]_{local} \, / \, [A]_{highz} = 2.50 \pm 0.25$ resulting in $\langle M_{2.2} \rangle_{local} = (8.52 \pm 0.31) \cdot 10^{10}$ $M_\odot$ for the high and low redshift samples.

4.7 The Tully-Fisher Relation

To further elucidate on the dynamical evolution of spiral galaxies we plot the Tully-Fisher relation for both our samples (see Fig. 4.24). Comparing all our local galaxies with the relation by Tully and Pierce (2000) reveals that the scatter of the Tully-Fisher relation was not affected by the process of clipping the profiles. Figure 4.25 shows the Tully-Fisher relation for our two samples after subtracting the local relation by Tully and Pierce (2000). Overall we find very few local galaxies beyond the 3σ-level (only $\sim 10\%$ of the total sample). Comparing this plot with a similar version for the local sample before clipping the light profiles (see Fig. 3.9), allows us to gauge the impact of the profile clipping. We show a vector version of both samples plotting the offsets from the local Tully-Fisher relation against each other (see Fig. 4.26) to disentangle the fractional influence of the clipping on the magnitude estimate and the inclinations. We conclude that the clipping of the light profiles has almost no effect on the magnitude estimates. However, the rotation speed gets affected quite substantially. Overall, the change in the individual data points does only slightly affect the characteristics of the whole ensemble. We measure but a slight shift of the mean values of the local population towards lower rotation velocities, i.e. "brighter" magnitudes. The offset $\langle \Delta M \rangle = -0.02 \pm 0.05$ is not shifted significantly towards smaller values $\langle \Delta M \rangle = -0.03 \pm 0.10$ in the truncation process.

Since we have shown by plausibility arguments (see Sec. 3.5.4) that the rotation velocity is unlikely to be affected by the low signal-to-noise quality of the high redshift Hα rotation curves, we can now conclude that clipping the profiles of galaxies does not have a significant impact on the data and does not affect our conclusions drawn from the high redshift sample. Since we might have $\sim 10\%$ outliers in our high redshift sample we exclude the three objects with the largest offset before calculating mean Tully-Fisher offsets $\langle \Delta M \rangle_{highz}$. Now we can examine how the drop in rotation velocity impacts on the Tully-Fisher relation without having to consider observational trade-offs any further.

4.7.1 The Tully-Fisher Offset

Assuming a slope taken from Tully and Pierce (2000), we find a significant offset from the Tully-Fisher relation for the high redshift sample (Fig. 4.24). This offset amounts to $\langle \Delta M \rangle = -1.50 \pm 0.19$ mag in a Λ-dominated universe (H_0=70, Ω_M=0.3, Ω_Λ=0.7). Although this offset is highly significant, due to the limited magnitude range of our sample we can not meaningfully constrain the slope of the high redshift Tully-Fisher relation. Figure 4.25 impressively demonstrates this offset in the magnitude dimension as well as for the rotation speeds. This offset is also fairly insensitive to the specific selection of our sample. After matching the isophotal sizes we find $\langle \Delta M \rangle = -1.38 \pm 0.19$ mag. As a compromise between those two values **we adopt an offset difference between our high and low redshift galaxies of $\langle \Delta M \rangle = -1.44 \pm 0.13$ mag**.

4.7.2 Phenomenological Explanation of the Tully-Fisher Relation

It is our task now to self-consistently explain the various differences that we discovered between the two samples. Especially, we have to disentangle which part of the total evolution results from the change in luminosity and which part from the change in mass. Although we have spoken so

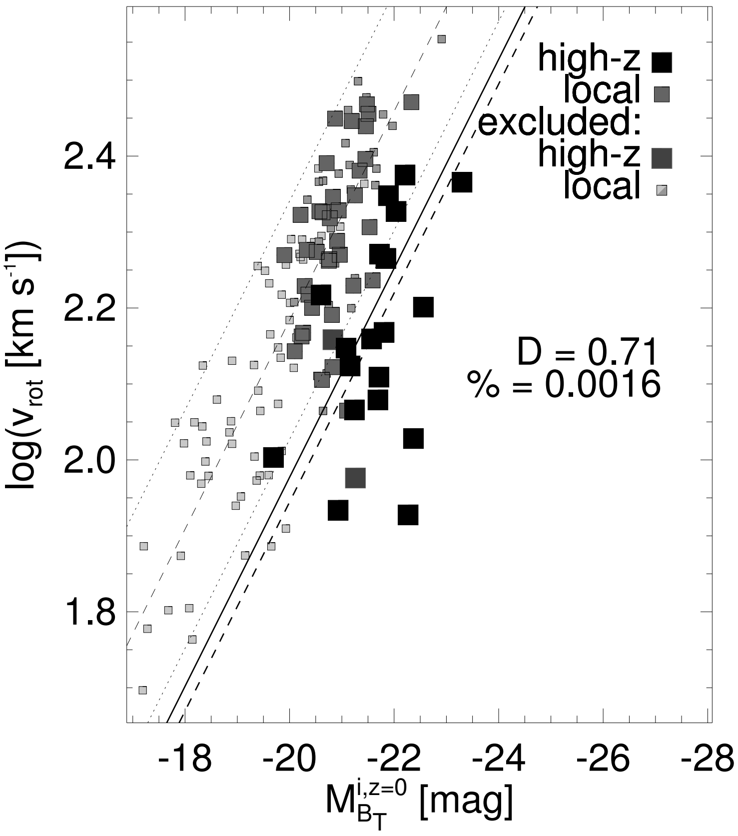

Figure 4.24: The Tully-Fisher relation

The absolute magnitude M_B^{rest} versus the rotation speed v_{rot}, the Tully-Fisher relation, for high redshift (large symbols) and local galaxies (small symbols). Symbols are the same as in Fig. 4.4. A KS-test indicates that both samples are significantly different (middle right). The thin dashed and dotted lines indicate the local Tully-Fisher relation by Tully and Pierce (2000) and its 3σ errors. The thick solid line is a fit to the high redshift data. The thick dashed line corresponds to the from the disc scale length, surface brightness and rotation velocity differences of local and distant samples expected change of the Tully-Fisher relation (see Sec. 4.7.2).

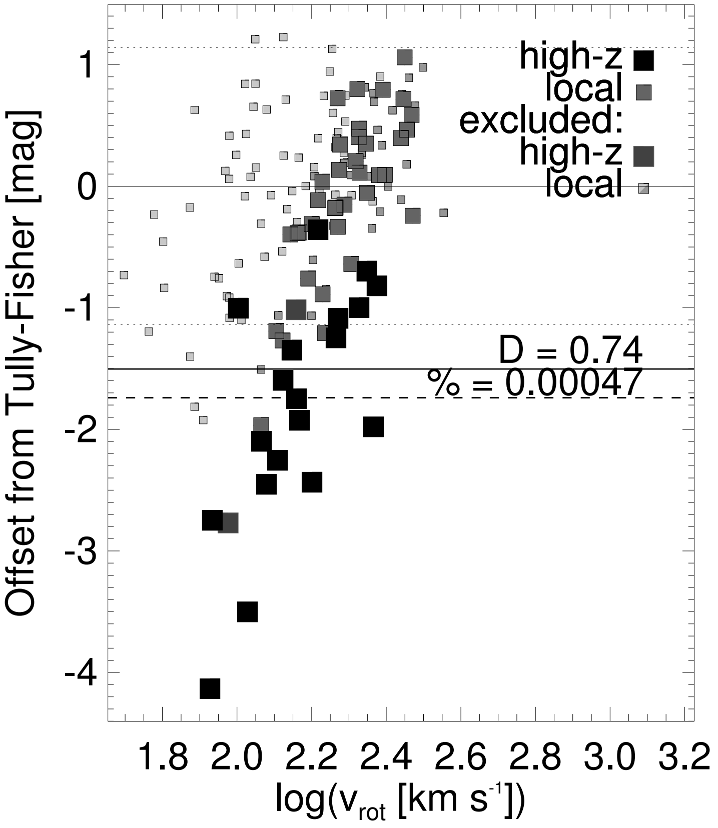

Figure 4.25: The offset from the Tully-Fisher relation

Here we plot the difference between the absolute magnitudes of our galaxies and the from the rotation speed expected Tully-Fisher magnitude as a function of rotation speed. Symbols and lines are the same as in Fig. 4.24. The offset between the two samples is almost 1.7 magnitudes.

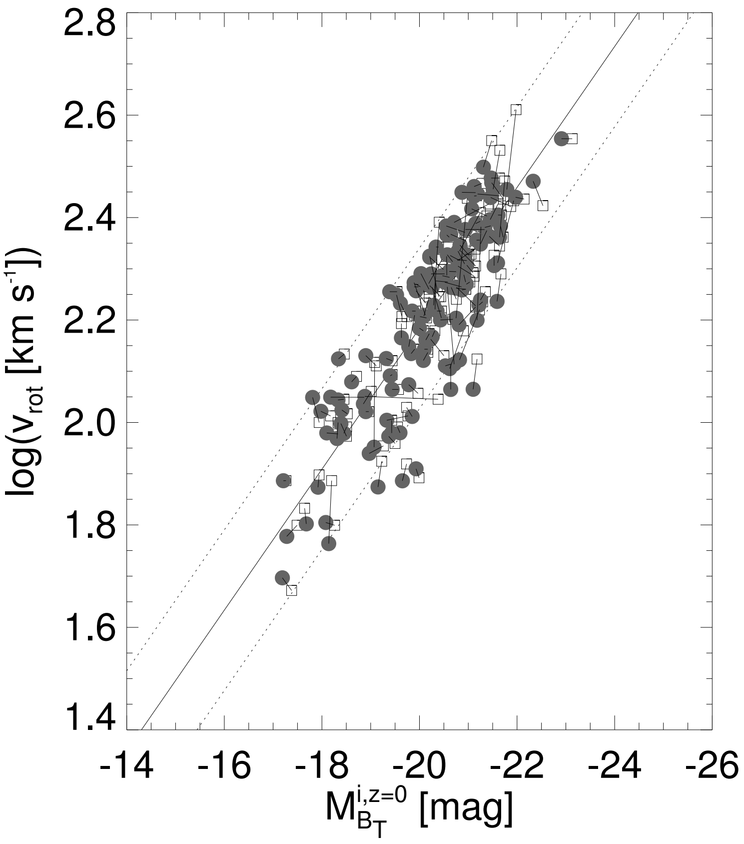

Figure 4.26: The Tully-Fisher relation and the impact of profile truncation

The Tully-Fisher relation for our local galaxies before (open boxes) and after (solid circles) applying the surface brightness truncation. Primarily the rotation velocity is affected by measuring imprecise inclinations. The inclination only has a minor impact on the absolute magnitude via the internal extinction correction.

far only in terms of magnitudes when describing the evolution of the Tully-Fisher relation, it is obvious from the change of rotation speeds, which also tends to increase the magnitude offset, that some fraction of the evolution is not only connected to star-formation, but an increase in mass as well.

However, separating the two ingredients may possibly not provide much further insight into the processes that drove the evolution of galaxies 6 Gyrs ago, since the processes leading to higher star-formation rates may at least to some extent be directly related to the mass increasing processes. Our individual findings of the mass and luminosity evolution should be consistent with the overall trend we see in the Tully-Fisher relation, though. Furthermore, since on one hand every merger event –especially in the early universe when galaxies on average contained more gas– is connected to a star-formation event, but on the other hand not every star-formation event –e.g. normal star-formation in spiral arms– is necessarily connected to an increase in mass, a surplus of star-formation should indicate that even "normal", i.e. mass-conserving, star-formation occurred more frequently or more intensely than today.

Empirically, we will now try to explain the Tully-Fisher relation. For this purpose we recast the local calibration by Tully and Pierce (2000):

$$M_B = -7.27 \cdot [\log(2 \cdot v_{rot}) - 2.5] - 20.11 \tag{4.7}$$

onto:

$$M_B = s \cdot \log\left(\frac{v_{rot}}{v_0}\right) + m_0 \tag{4.8}$$

Equation 4.8 contains three free parameters: the slope $s = -7.27$, which we cannot constrain, because of our limited magnitude range, a magnitude zeropoint $m_0 = -20.11$ mag and a rotation velocity zero point $v_0 = 10^{2.5}/2 = 158$ km s^{-1}. We will now try to estimate from our measurements new values for the high redshift population and we will calculate the relative contributions by the increase in mass and disc scale length. eq. 4.3 shows that including the redshift dependence of the morphological parameters a correction for m_0 should look like: $m_0' = m_0 + \Delta m_R + \Delta m_\mu$. From our analysis of the sizes of the discs at the two epochs we already know that the drop in disc scale length of $\sim 30\%$ results in a difference of $\Delta m_R = 0.74 \pm 0.12$ mag. From the evolution of the central surface brightnesses we get $\Delta m_\mu = -1.39 \pm 0.25$ mag. We can translate this directly into an offset from the Tully-Fisher relation, setting $m_0' = -20.11 + 0.74 - 1.39 = -20.76 \pm 0.28$ mag. Assuming that the Tully-Fisher relation had the same form at all times we also have to keep the ratio v_{rot}/v_0 constant. From the local value of $v_{rot}\,(local)\,/v_0\,(local) = 202/158 = 1.28$ we derive $v_0\,(highz) = 111 \pm 7$ km s^{-1}. In its original form the high redshift Tully-Fisher relation now takes the following appearance:

$$M_B = -7.27 \cdot [\log(2 \cdot v_{rot}) - 2.35] - 20.76 \tag{4.9}$$

For two galaxies of the same mass at the two epochs we therefore obtain a magnitude offset of -0.65 ± 0.28 mag from the morphological evolution and another -1.09 ± 0.20 mag from mass evolution resulting in a total of $\langle \Delta M \rangle = -1.74 \pm 0.34$ mag, which agrees very well with our measured offset of $\langle \Delta M \rangle = -1.44 \pm 0.13$ mag. Keeping in mind that we rejected the three most deviant objects, the agreement is almost perfect (without rejection one would have measured a mean value of $\langle \Delta M \rangle = -1.68 \pm 0.21$).

4.8 Colours and Mass-to-Light-Ratios

In Fig. 4.27 we plot the B-V histogram for high and low redshift galaxies. We find a significant offset Δ (B-V) = 0.1 between the means of the two distributions. The statistical tests confirm this result (T-Test: linear 1.7%, log. 1.9%; RS-Test: 1.1%). Furthermore, the variance test indicates that the shapes of the distributions are indistinguishable (FV-Test: 32%). Therefore, we conclude that our high redshift galaxies are on average slightly bluer than our local sample galaxies.

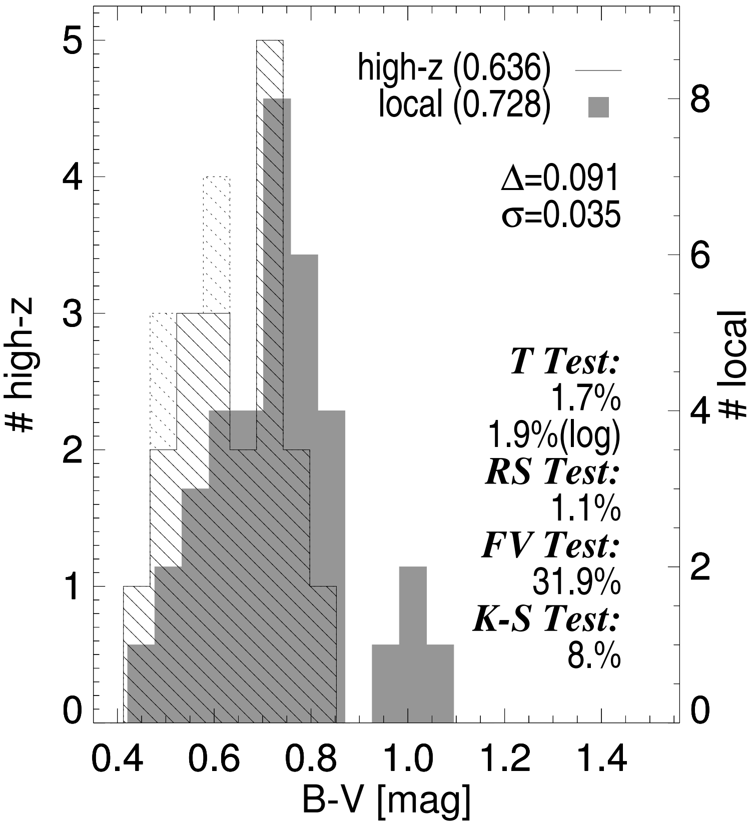

Figure 4.27: Histograms of the B-V colours

Histograms of the B-V colours of the low (shaded region) and high redshift (striped region) samples. The symbols and annotations are the same as in Fig. 4.1. The difference of the means of both distributions is more than 2.5σ. The means tests confirm this result while the FV-test indicates that the variances of the two samples are the same.

Next, we will employ a colour dependent model according to Bell and de Jong (2001) to derive stellar mass-to-light ratios in the B-band for our samples, assuming an exponential star formation history:

$$\log\left(\frac{M}{L}\right)_{stel} = a_B + b_B \cdot \text{(B-V)}$$

with $a_B = -0.994$ and $b_B = 1.804$ (see Fig. 4.28). We find that the high redshift galaxies have mass-to-light ratios almost 0.2dex smaller than the local galaxies. The problem with this formalism is that we cannot be sure about the precise star formation histories of our two samples. One might expect, since at high redshift one predominantly picks high surface brightness galaxies and since the overall star formation rate at high redshift was much higher than today, that we observe high redshift galaxies in a more "exited" state, i.e. in a state where the galaxies were forming more stars than today. Therefore, this would mean that the adopted star formation model, which converts colour to a mass-to-light ratio, is not steep enough, i.e. galaxies of similarly blue colour are forming dramatically more stars during a burst than in a quiescent mode, hence the stellar mass-to-light ratio is much lower. Therefore, we will also take this effect into account by converting colour to mass-to-light ratio using a strong burst model. We achieve this by taking the stellar mass-to-light ratios calculated with an exponential star formation history of the high redshift sample and convert those to B-R colours. From those we convert back to mass-to-light by using an exponential star formation history with an additional starburst added at a specific time, which is much steeper than the exponential model (see Fig. 5 in Bell and de Jong, 2001). As a result of this the offset in the mass-to-light ratio distributions gets a lot more pronounced (see Fig. 4.29). Furthermore, the scatter in the high redshift distribution gets larger just as expected from a steeper functional dependence.

Apart from the stellar mass-to-light ratios, we can calculate dynamical "mass-to-light" ratios by relating our mass estimate with the absolute B-band magnitude:

$$\log\left(\frac{M}{L}\right)_{dyn} = \log M_{2.2} - \log L = \log M_{2.2} + 0.4 \cdot (M - M_{\odot})$$

The histogram shows a highly significant offset (7.5σ) of more than 0.6dex (see Fig. 4.30). One could ask now whether the ratio of dynamical over stellar mass-to-light ratio changed over the course of the last 7 Gyrs. This is essentially a "mass ratio" of dynamical over stellar mass, i.e. an indicator for the change of the halo mass with respect to the increase in the number of stars. We compute the ratio ρ:

$$\rho = \log\left(\frac{\left(\frac{M}{L}\right)_{dyn}}{\left(\frac{M}{L}\right)_{stel}}\right) = (\log M_{2.2} + 0.4 \cdot (M - M_{\odot})) - (a_B + b_B \cdot \text{(B-V)})$$

In Fig. 4.31 we present the histograms of the mass ratios ρ for the low and high redshift sample for both star formation history extremes (normal mode left, with added burst right). As a result of the large uncertainties of the star formation histories the mass ratio ρ may vary over a factor of two. Therefore, we conclude that without further detailed studies of the star formation history of individual high redshift galaxies **to first order the mass ratio of dynamical over stellar mass stays roughly constant**. This would imply that the increase in dynamical mass is totally compensated for by the increase in the mass of stars. Or in other words, both disc populations have not changed their ratio of dark over luminous matter at least over the inner parts.

4.9 Dynamical Evolution

In the following section we will compare the (normalised) specific angular momenta for our two samples. According to Sommer-Larsen et al. (1999) we define the specific angular momentum j_d and the normalised specific angular momentum $\tilde{j}_d$:

$$\begin{aligned} j_d &= \tfrac{1.68}{1.1} R_d \cdot v_{rot} \\ \tilde{j} &= \tfrac{j_d}{v_{rot}^2} = \tfrac{1.68}{1.1} \tfrac{R_d}{v_{rot}} \end{aligned} \tag{4.10}$$

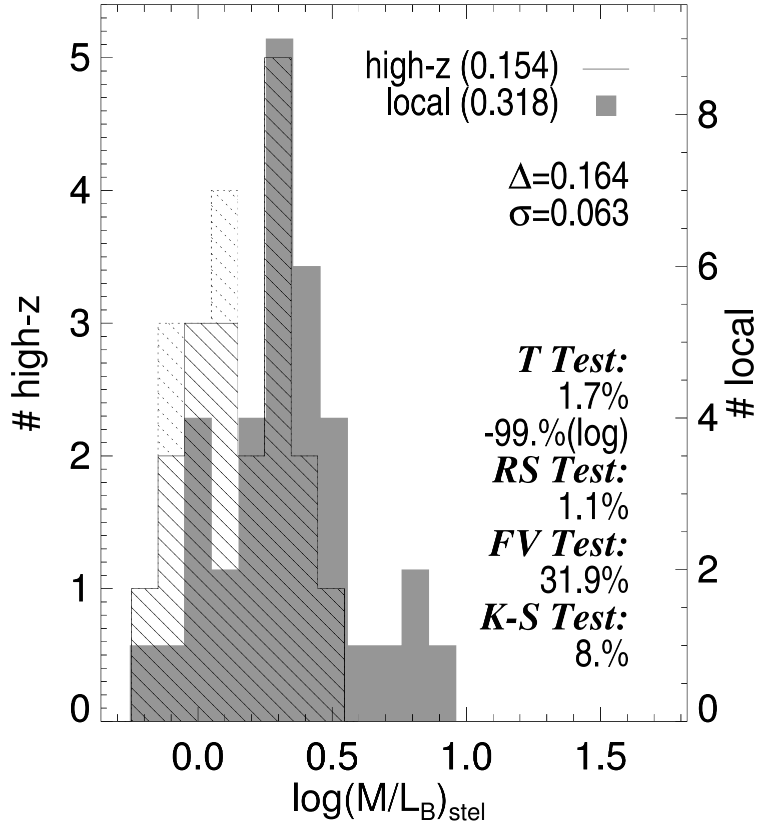

Figure 4.28: Histograms of stellar mass-to-light ratio

Histograms of the logarithm of the stellar mass-to-light ratios of the low (shaded region) and high redshift (striped region) samples. The symbols and annotations are the same as in Fig. 4.1. The high redshift galaxies have mass-to-light ratio about 0.16dex smaller than the local galaxies, at the 2.6σ level. The means tests confirm this result while the FV-test indicates that the variances of the two samples are the same.

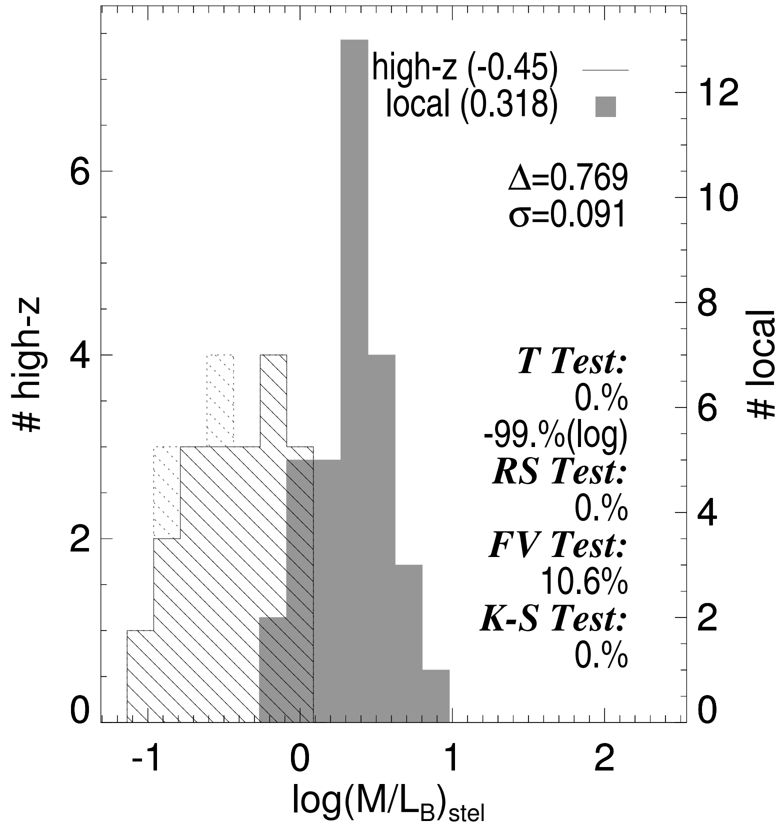

Figure 4.29: Histograms of stellar mass-to-light ratio

Histograms of the logarithm of the stellar mass-to-light ratios of the low (shaded region) and high redshift (striped region) samples. The symbols and annotations are the same as in Fig. 4.1. In contrast to Fig. 4.28 now a model was used for the high redshift galaxies only, which included a starburst at a specific time, thus making the conversion relation from colour to mass-to-light much steeper. The high redshift galaxies now have mass-to-light ratios about 0.8dex smaller than the local galaxies, almost at the 8.5σ level. The means tests confirm this result while the FV-test still shows that the shapes of the two samples are the same.

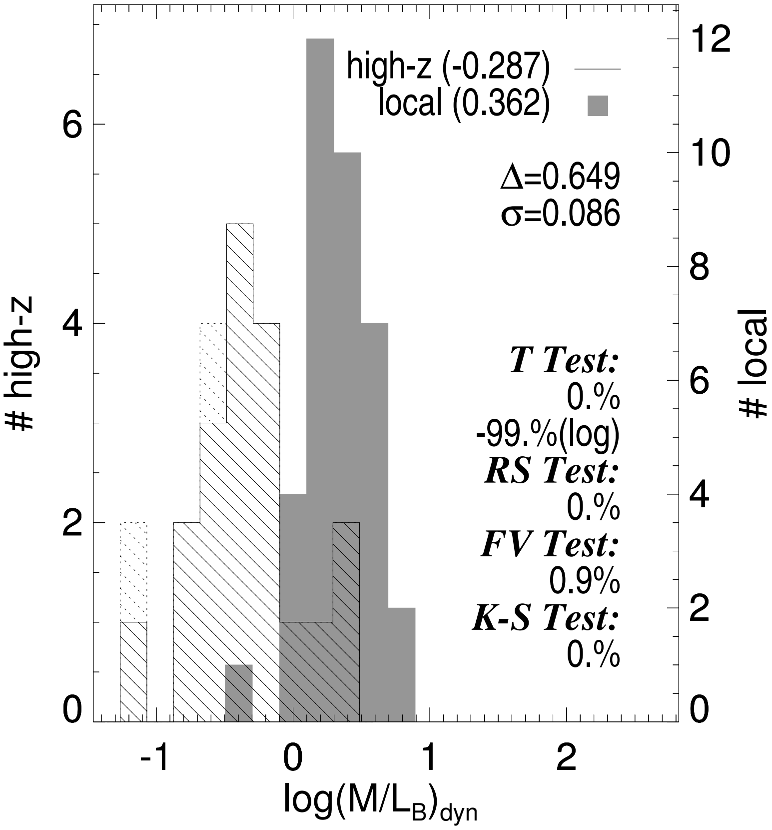

Figure 4.30: Histograms of dynamical mass-to-light ratio

Histograms of the logarithm of the dynamical mass-to-light ratios of the low (shaded region) and high redshift (striped region) samples. The symbols and annotations are the same as in Fig. 4.1. The high redshift galaxies have mass-to-light ratios signifanctly smaller than the local galaxies, at the 7.5σ level, owing to the lower masses and brighter absolute magnitudes. The means tests confirm this, while the FV-test indicates that the shape of the two distributions has changed.

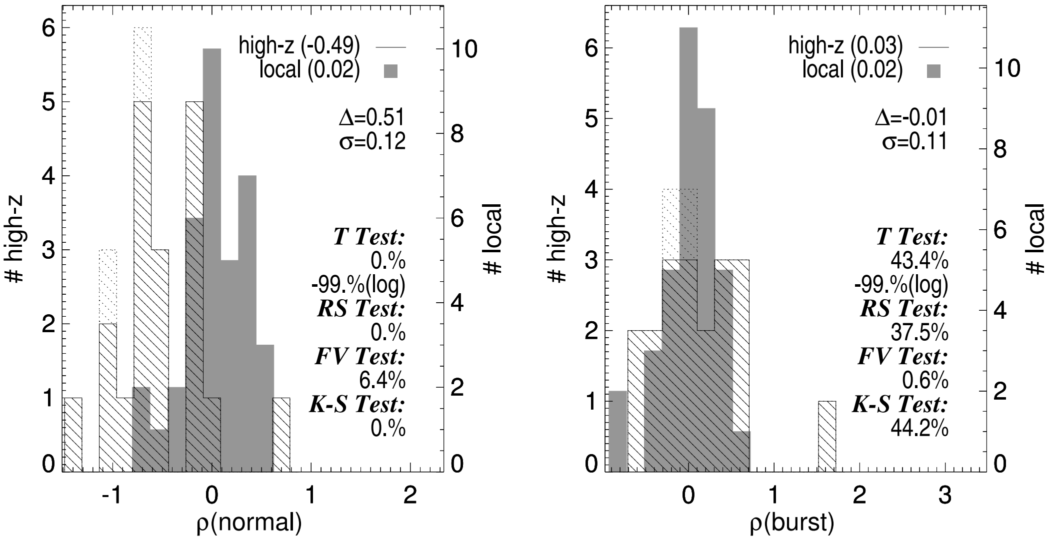

Figure 4.31: Histograms of the mass ratios ρ

Histograms of the mass ratios ρ of the low (shaded region) and high redshift (striped region) samples for normal high redshift star formation (left, same star formation history as local galaxies) and normal exponential star formation plus an added burst (right). The symbols and annotations are the same as in Fig. 4.1. Given the large uncertainties in the star formation history for the high redshift galaxies we find mean offsets of the two distributions as large as -0.49dex to +0.03dex.

This relation holds exactly for pure discs (without bulge), with a flat rotation curve, which is truncated at 4 disc scale lengths. The truncation radius at 4 disc scale lengths was found by van der Kruit and Searle (1982). Sommer-Larsen et al. (1999) calibrated the specific disc angular momentum j_d using a subset of 203 galaxies from the sample of Mathewson et al. (1992) with HI line width and resolved HI rotation curves and I-band disc scale lengths. To correct our rest-frame B-band disc scale lengths to I-band we apply a correction factor of $R_d^I = R_d^B/1.1$ (see Fig. 3.18). We compare our measurements to those of Mathewson et al. (1992) plotting R_d as a function of v_{rot} (see Fig. 4.32). Our local data are consistent with the largest galaxies in the literature sample, while the complete local sample roughly spans the same range as the Mathewson et al. (1992) data. Furthermore, our high redshift data are offset from our local sample towards smaller disc scale lengths and smaller rotation velocities. Since the high redshift galaxies are offset from the local sample in such a way that they populate a region sampled by other local galaxies might imply that the evolution we see in the rotation speed is only an effect introduced by selecting objects with slightly smaller disc scale lengths at high than at low redshift. However, Fig. 4.19 showed that even after matching the samples by disc scale length the offset of 0.1dex in rotation speed still remains. This offset is still significant at the 2.9σ level. Therefore, **the evolution in rotation speed and dynamical mass we measure cannot be explained with pure sample selection arguments**.

With respect to Fig. 4.33, we find a significant difference between the distributions of specific angular momentum at low and high redshift. This difference is prominent enough that it gets picked up even by the statistical tests (linear T-test: 2.2%, log. T-test: 0.1%, RS-test: 0.2%, KS-test: 1.5%). Since we are mainly interested in properties for objects with similar isophotal sizes we also present the same plot after matching the R_{25} distribution (see Fig. 4.34). Basically, the same picture is presented to us. Again, the tests already indicate the difference between the two samples (linear T-test: 1.7%, log. T-test: 0%, RS-test: 0.1%, KS-test: 1%). Nevertheless, we will also check the correlation between isophotal size and specific angular momentum (see Fig. 4.35). Applying the fitting technique again using:

$$j_d = A \cdot R_{25}^B \longleftrightarrow \log j_d = \log A + B \cdot \log R_{25} \tag{4.11}$$

we find $\left[\tilde{A}\right]_{local} = \log A_{local} = 1.1046 \rightarrow [A]_{local} = 12.72$ and $\left[\tilde{A}\right]_{highz} = \log A_{highz} = 0.8088 \rightarrow [A]_{highz} = 6.44$ after fixing $B = 1.70266$. The ratio $\alpha \equiv [j_d]_{highz} / [j_d]_{local} = [A]_{highz} / [A]_{local} = 0.51 \pm 0.04$ we now compare with the ratio of the means of the two distributions: 0.59 ± 0.06. The two estimates agree reasonably well.

In the history of theoretical galaxy modelling the specific angular momentum has received a lot of attention. This was primarily due to the fact that to the present day even the best predictions of the angular momenta of local disc galaxies were off be at least a factor of a few. Our consistent measurements of high and low redshift galaxies will place even stronger constraints now.

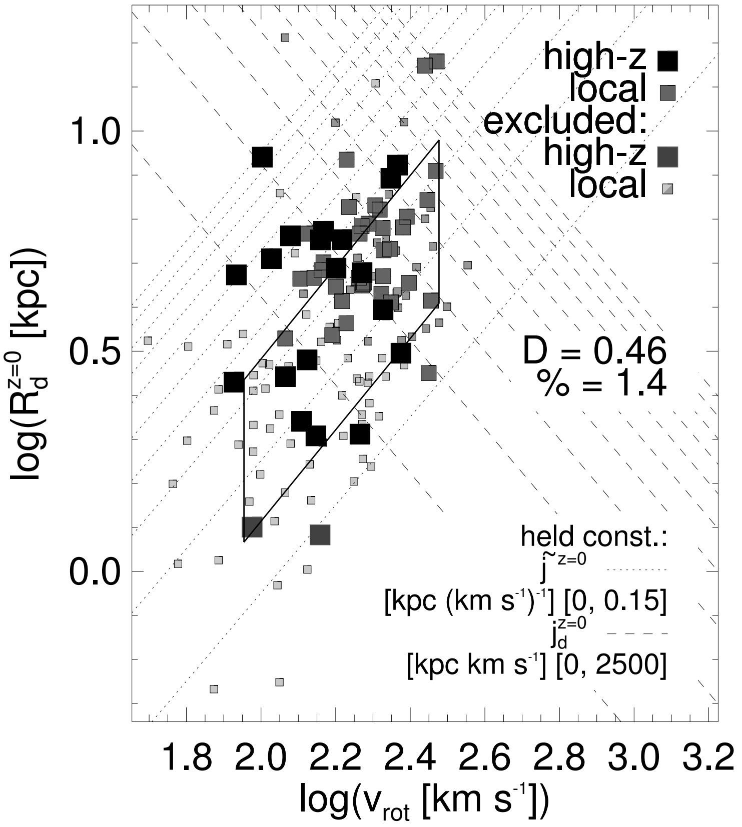

Figure 4.32: R_d as a function of v_{rot}

The disc scale length R_d versus the rotation speed v_{rot} for high redshift (large symbols) and local galaxies (small symbols). Symbols are explained in Fig. 4.4. A KS-Test (middle right) shows a marginal difference between the two samples. The diagonal lines are lines of constant specific angular momentum j_d (dashed) and constant normalised specific angular momentum $\tilde{j}_d$ (dotted). The Mathewson et al. (1992) data are indicated by the solid box. Our local sample is somewhat at the high end of the literature data, however, the complete local set is fairly consistent with Mathewson et al. (1992).

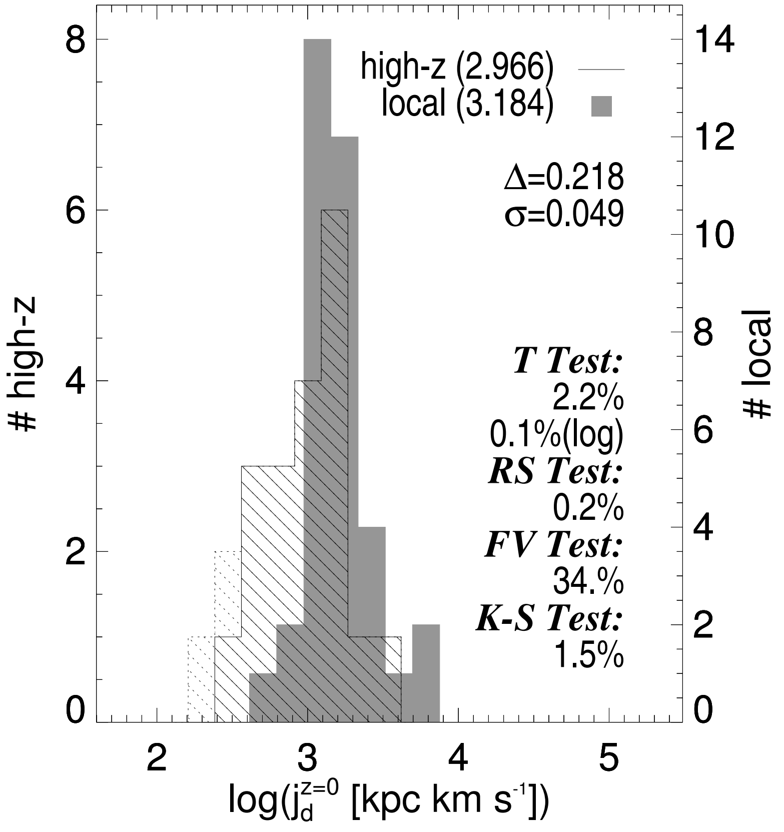

Figure 4.33: Histograms of the specific angular momenta

Histograms of the ispecific angular momenta j_d of the low (shaded region) and high redshift (striped region) samples. The symbols and annotations are the same as in Fig. 4.1. The difference of the means of both distributions is $\approx 4.5\sigma$, which gets confirmed by the statistical tests. The FV-test indicates that the two distributions have a similar shape.

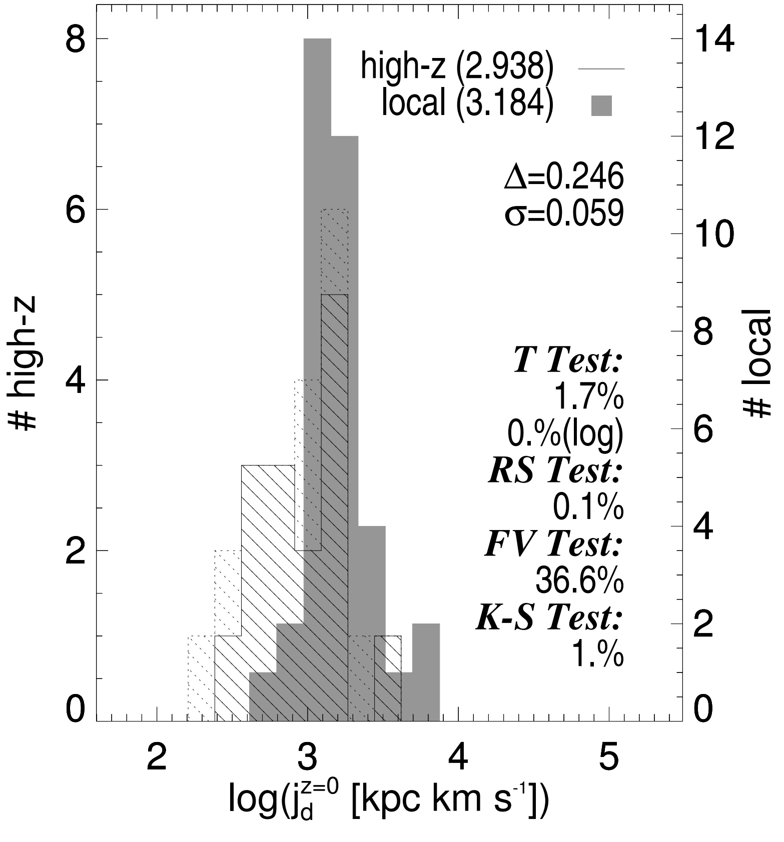

Figure 4.34: Histograms of j_d after matching the samples

Same plot as Fig. 4.33. The same four high redshift galaxies as in Fig. 4.2 were removed. In comparison to Fig. 4.33 the difference of the means got even larger. The tests again indicate that both samples have different means and the same shape.

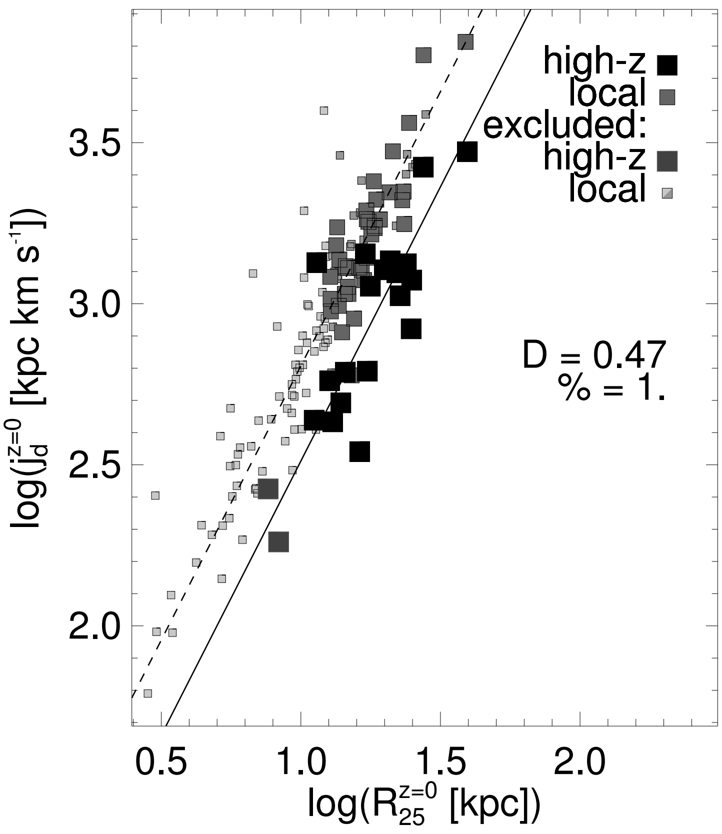

Figure 4.35: j_d as a function of R_{25}

The specific angular momentum j_d versus the isophotal radius R_{25} for high redshift (large symbols) and local galaxies (small symbols). Symbols are explained in Fig. 4.4. A 2-dimensional KS-Test (middle right) indicates that the two samples are significantly different (dashed line: local fit; solid line: high redshift fit).

Chapter 5

Discussion

5.1 Comparison with Observations

In the following section we will compare our Tully-Fisher sample to the available observational data in the literature. Basically, there are three different groups that have pushed the measurement of rotation velocities out to redshifts $0.5 < z < 1$: Vogt et al. (1993; 1996; 1997) and Ziegler et al. (2002); Böhm et al. (2003) and Milvang-Jensen (2003); Milvang-Jensen et al. (2003). All three groups work with rotation curves taken in the optical wavelength regime (usually [OII]λ3727, but in some cases [OIII] or Hβ for very nearby sources) taken with multi-object spectrographs. However, details about the corresponding imaging and observational setup vary.

5.1.1 The Vogt et al. Data

Vogt et al. used LRIS on KECK to obtain a total of 18 large ($\langle R_d \rangle \sim 3.5$kpc) disc galaxies at redshifts $0 < z < 1$ with $\langle z \rangle \sim 0.5$. A main complication for the reduction of their early rotation curves was the limitation to slits perpendicular to the dispersion axis of the spectrograph. As a result of this it was impossible to rotate the slit according to the position angle of the targets. The majority of the data, though, were taken with the slits being aligned to the major axis of their targets. Their galaxies were selected from HST WFPC2 images of fields flanking the Hubble Deep Field. Converted to our cosmology their data imply an offset from the Tully-Fisher relation of almost 0.7mag (see Fig. 5.1). Considering their lower mean redshift, the offsets they find are actually very compatible with the ones presented here, though. Their original conclusion that only very modest amounts of surface brightness evolution were compatible with their data resulted mainly from using a different cosmology ($q_0 = 0.05$, $H_0 = 75$km s^{-1} Mpc^{-1}) and also a different local comparison Tully-Fisher relation (Pierce and Tully, 1992), which in the B-band uses a different normalisation for field and cluster galaxies. Furthermore, since the offset from the Tully-Fisher was largest for their bluest galaxies, they concluded that the amount of offset could depend on sample selection. They plotted the magnitude-size relation for their galaxies and found that the data lay in between the area populated by local galaxies and the high redshift data $\langle z \rangle \approx 0.7$ of Schade et al. (1996). Although their magnitude range is "only" 3 magnitudes –similar to ours– they argue that the slope of the Tully-Fisher relation at high and at low redshift is the same. Since their data span the whole range of redshifts from as low as $z \sim 0$ out to $z \sim 1$ some fraction of their data did not actually have the time to evolve into a different slope, which complicates drawing strong conclusions about this point.

Additionally, another set of ~ 100 galaxies was recently advertised by Vogt and collaborators on various conferences (Vogt, 1999, 2000, 2001a,b) including the previously published data set. Although, those data were taken along the same round of observations (as part of the DEEP project), the conclusions drawn from those have changed. The offset from the Tully-Fisher relation got much smaller and is apparently not a function of redshift (see Fig. 5.2 and Fig. 5.3). In fact, the mean values of the offset from the Tully-Fisher relation is for most bins compatible with zero.

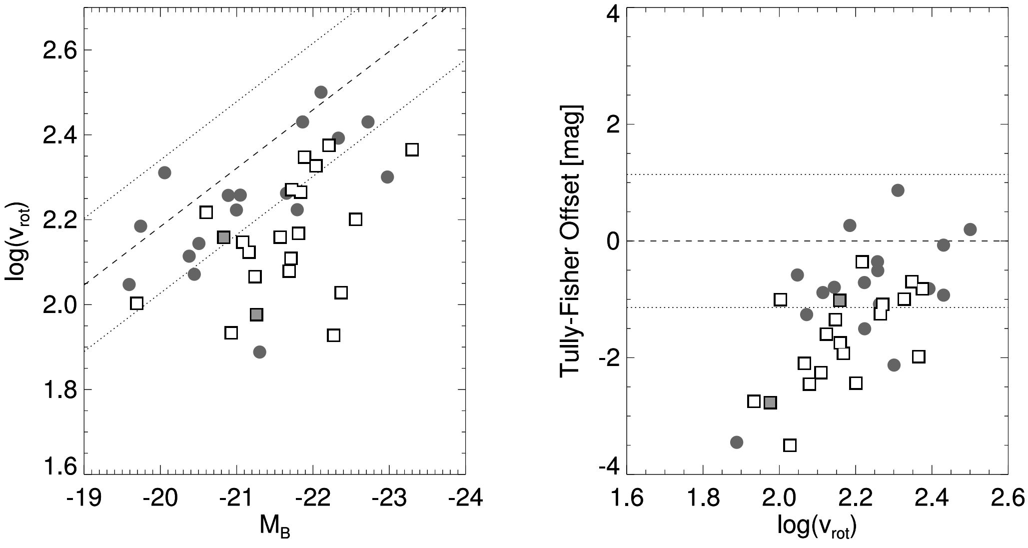

Figure 5.1: Tully-Fisher relation for Vogt et al. (1993; 1996; 1997)

The Tully-Fisher relation (left) and the magnitude offset from the Tully-Fisher relation as a function of rotation velocity (right) for the Vogt et al. (1993; 1996; 1997) data (filled circles) in comparison to our high redshift data (boxes; dark boxes excluded from sample). Their magnitude and rotation velocity range agrees well with ours; their offset from the Tully-Fisher relation is only 60% of ours, though. Thick dashed and dotted lines represent the local Tully-Fisher relation and its scatter, respectively.

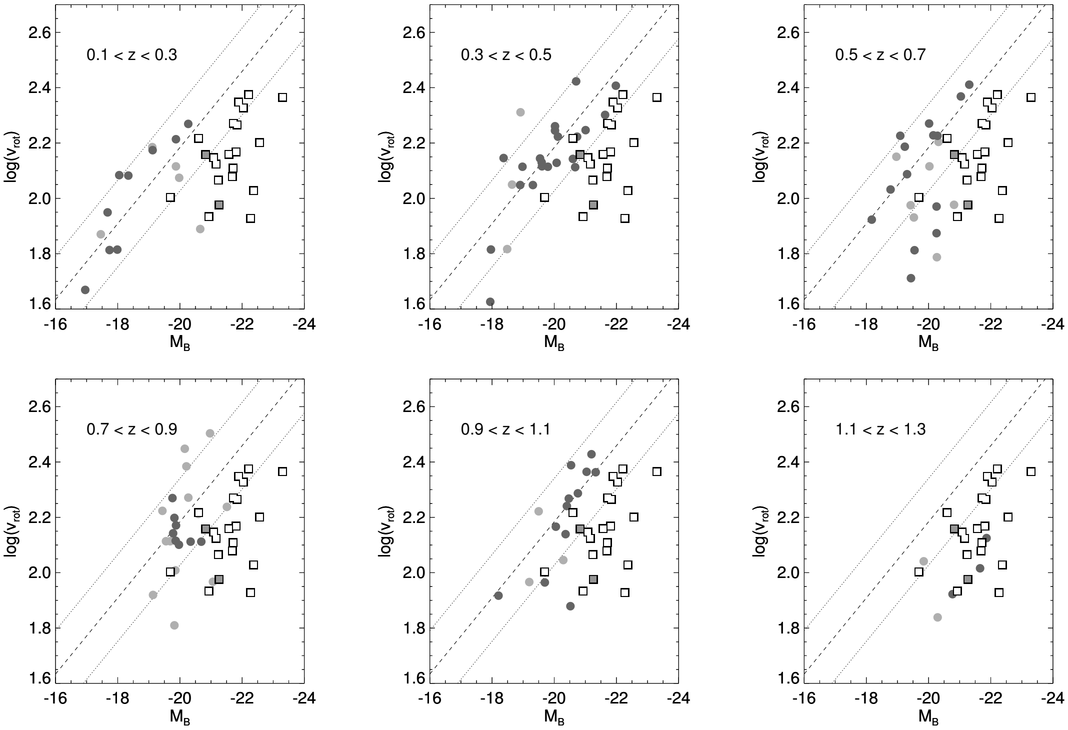

Figure 5.2: Tully-Fisher relation for Vogt (1999, 2000, 2001a,b)

The Tully-Fisher relation for different redshift bins for the Vogt (1999, 2000, 2001a,b) data (filled circles: dark - high quality; light - low quality) in comparison to our high redshift data (boxes). Their galaxies do not show a significant trend with redshift. Only their highest redshift bin agrees well with our data points. The lines indicate the local Tully-Fisher relation.

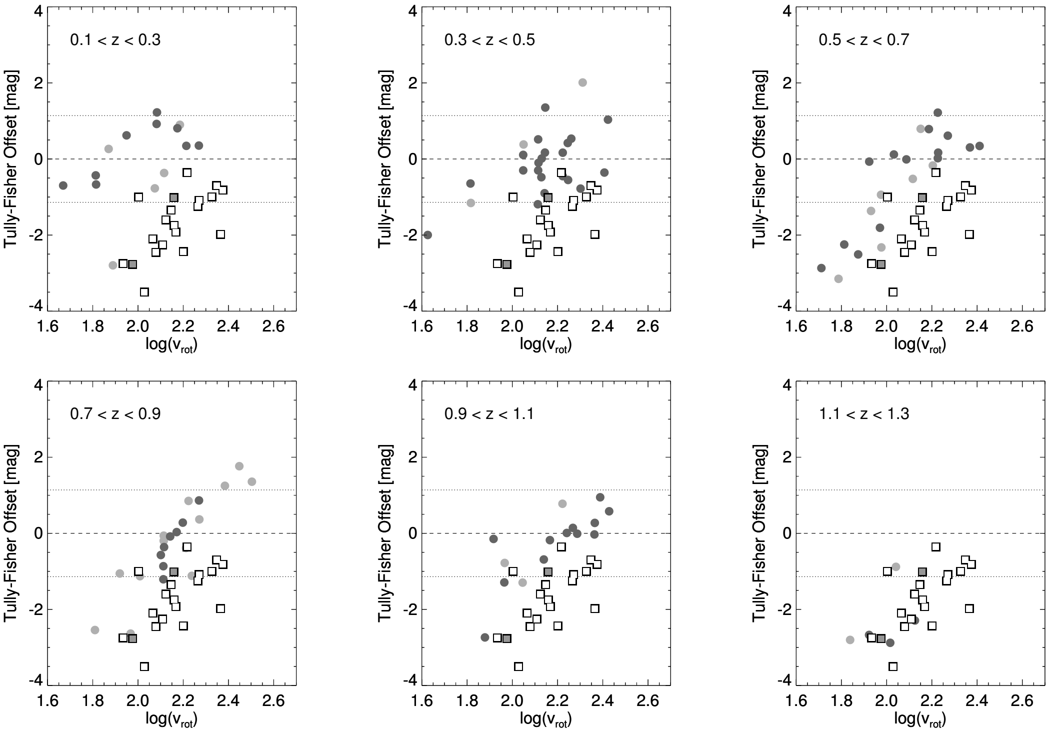

Figure 5.3: Tully-Fisher relation for Vogt (1999, 2000, 2001a,b)

The Tully-Fisher offset as a function of rotation velocity v_{rot} for different redshift bins for the Vogt (1999, 2000, 2001a,b) data (filled circles: dark - high quality; light - low quality) in comparison to our high redshift data (boxes; dark boxes excluded from sample). There is no obvious offset from the local relation for the Vogt data. It is interesting, though, that the apparent slope of their relation is the same as for our galaxies. We argue that this is a selection effect rather than a true intrinsic slope difference.

There is one exception, though. At the highest redshift their high quality data are based on H_α rotation curves also taken with ISAAC/VLT. Those data do show a huge offset of more than 2.6mag from the Tully-Fisher relation. Although that offset appears to be pretty large it is in very good agreement with our data, especially considering that those galaxies were selected to be very strong line emitters. The reason for the discrepancy between the two data sets is probably mainly found in their different mean characteristics, e.g. the mean disc scale decreased by almost 1kpc to $\langle R_d \rangle \sim 2.5$kpc.

5.1.2 The Ziegler et al. Data

Ziegler et al. (2002) and Böhm et al. (2003) used FORS2 on the VLT to obtain [OII] (plus [OIII], H_β) rotation velocities of 60 relatively small ($\langle R_d \rangle \sim 2.5$kpc) galaxies. Their mean redshift was also about $\langle z \rangle \approx 0.5$, with 18 galaxies at redshifts $z > 0.6$. Although FORS2 offers the possibility to place slits at arbitrary position angles Ziegler et al. (2002) chose not make use of this and did not align the slits. However, they remark that for their Tully-Fisher study they only picked galaxies with misalignments less than 15°, in order to minimise the effect. No additional correction was applied to overcome this problem. Furthermore, the sample was selected on basis of ground-based images (the FORS deep field) taken with the VLT. The seeing of almost 0.7" limits their ability to estimate disc scale lengths and especially inclinations for galaxies with apparent sizes of that order. We plot their data in comparison to ours in Fig. 5.4. Again, considering their lower mean redshift, their data are in fair agreement to ours. We find a mean offset from the local Tully-Fisher relation of almost 0.9mag for their high and low quality data and an offset of 0.65mag for their high quality data alone. This is in very good agreement with the Vogt et al. (1997) data, especially when keeping in mind that their main conclusion was that at high redshift galaxies would apparently follow a different Tully-Fisher slope. Therefore, the high offset including the low quality data is easily explained in terms of a slope change, since especially low luminosity / mass objects are of low quality. However, since their faint galaxies basically determine this trend of lower than expected rotation velocities at faint magnitudes, this result gets affected by the fact that the faint galaxies also tend to be the small objects (both apparent and absolute size, see Fig. 4.7 and Fig. 3.19), where the seeing limits recovering inclination angles. Since the adopted inclination has a huge impact on the rotation velocity the slope change could result from systematically overestimating the inclinations of small sources. In fact, we estimate from Fig. 5.5, Fig. 4.7 and Fig. 3.19 that about one half of their galaxies have apparent sizes less than an arcsecond, and indeed all those faint sources are classified as "low quality" by Böhm et al. (2003).

5.1.3 The Milvang-Jensen et al. Data

Milvang-Jensen et al. (2003) have also used FORS2 on the VLT supplemented with HST/WFPC2 imaging to study the properties of especially cluster galaxies at high redshift. The accompanying field sample to their cluster data has a mean redshift $z \approx 0.5$. Their field is centered around the cluster MS1054.4-0321 (Gioia et al., 1990) at a redshift $z = 0.83$. In contrast to Ziegler et al. (2002) they made use of the tilted slits available for FORS2 when obtaining their [OII] rotation curves.

Fortunately, their sample has one galaxy in common with ours to allow a unique direct comparison between [OII] and H_α. For MS1054-03 1403 (van Dokkum, 1999) they find values in very good agreement with ours after conversion to the same cosmology and keeping in mind that their error bars do not include systematic effects like the surface brightness effects explained in Sec. 3.6.1 (see Tab. 5.1). The largest difference we find in the rotation velocity v_{rot}. Since the inclination angles are pretty similar, this difference must be an intrinsic difference between the H_α and the [OII] measurement. In fact, we find a flat part of the rotation curve only on one side at a distance of the nominal centre of 10-15kpc, but not on the other. If the rotation curve were symmetric, as is suggested from the [OII] data, we would measure ≈ 280km s^{-1} in perfect agreement with Milvang-Jensen (2003). Even the extent out to which the rotation curve is traced is the same in both studies (10-15kpc).

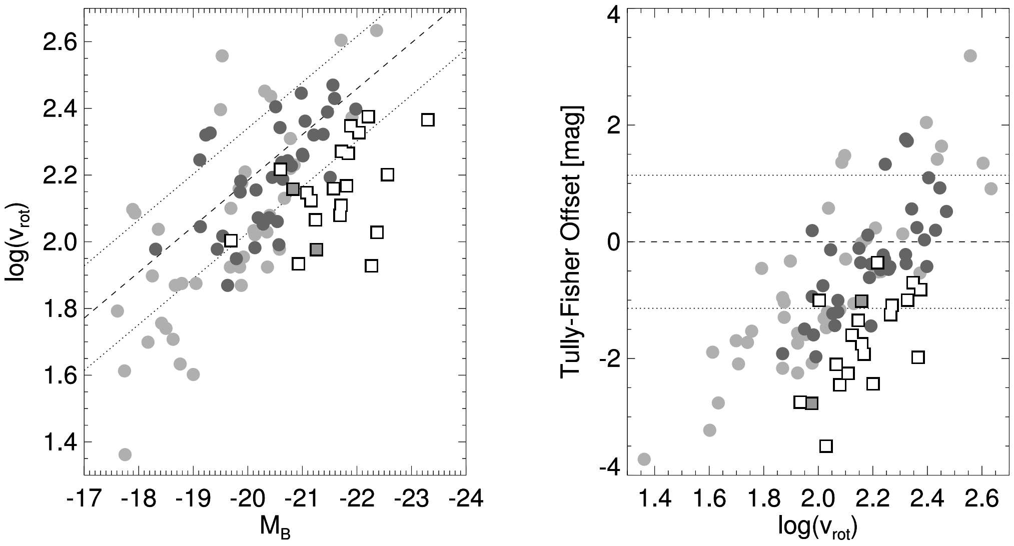

Figure 5.4: Tully-Fisher relation for Ziegler et al. (2002)

The Tully-Fisher relation (left) and the magnitude offset from the Tully-Fisher relation as a function of rotation velocity (right) for the Ziegler et al. (2002) data (filled circles) in comparison to our high redshift data (boxes; dark boxes excluded from the sample). Ziegler et al. (2002) high quality data are marked with dark and low quality data with light symbols. Their magnitude range gets about 4mag fainter than our data. However, no high quality points were measured in that regime. Thick dashed and dotted lines represent the local Tully-Fisher relation and its scatter, respectively. Thin lines correspond to a fit (plus scatter) to the Ziegler et al. (2002) data.

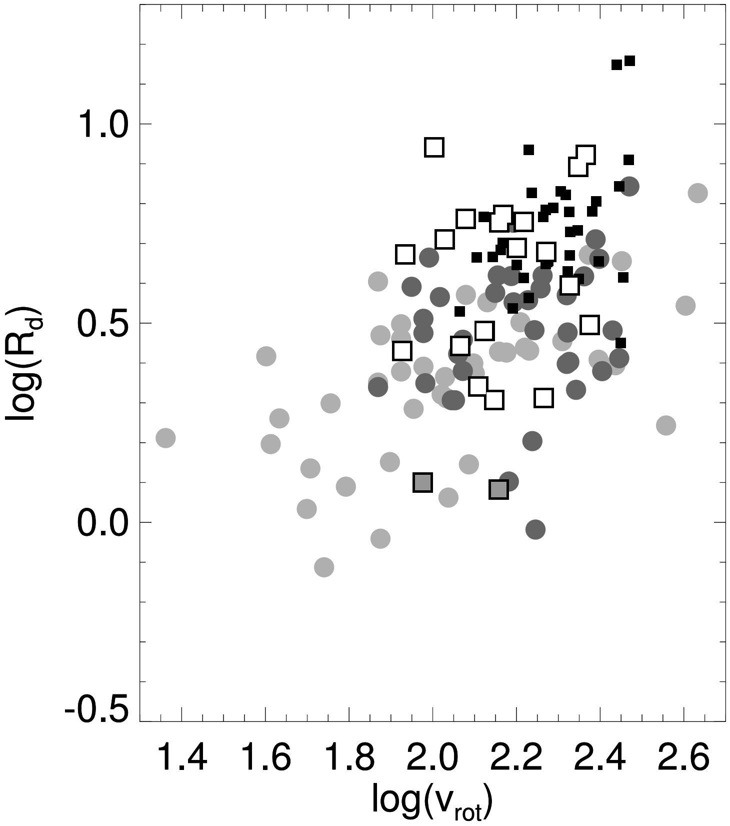

Figure 5.5: R_d versus v_{rot} for the Ziegler et al. (2002) data

The disc scale length R_d as a function of rotation velocity v_{rot}. The Ziegler et al. (2002) data (circles) are on average a factor of two smaller than our galaxies (boxes: large - high redshift; small - low redshift; large dark boxes excluded from the sample). Interestingly, their low quality sources (light circles) are found amongst all rotation velocities, while high quality sources (dark symbols) are only found above $v_{rot} > 90\text{km s}^{-1}$.

Comparing the Tully-Fisher relations for their and our data we find good agreement (see Fig. 5.6).The mean offsets from the Tully-Fisher relation are -0.37 ± 0.21mag for their low redshift field galaxies ($z < 0.6$), -1.08 ± 0.20mag for the high redshift field galaxies ($z > 0.6$, excluding the cluster) and -1.67 ± 0.36mag for their cluster galaxies. Milvang-Jensen (2003) claim to have found evidence for a systematic difference between the cluster and field population. Converted to the concordance cosmology we find an offset of 0.59 ± 0.41mag between the two populations. However, our mean value lies right in the middle between their field and cluster galaxies measurements. Having a five times larger field sample at high redshift we conclude that such a cluster-field difference is insignificant and requires much more data in order to decrease the error bars.

Table 5.1: MS1054-03 1403

	z	R$_d$ kpc	i deg	M$_B^{rest}$ mag	v$_{rot}$ km s^{-1}
	(1)	(2)	(3)	(4)	(5)
Milvang-Jensen (2003)	0.8132	8.79 ± 0.09	72.3 ± 0.3	-23.08 ± 0.01	271^{+8}_{-13}
Our values	0.81325	8.4 ± 1	76 ± 5	-23.30 ± 0.20	232 ± 50

Note. – (1) spectroscopic redshift z , (2) disc scale length R$_d$, (3) inclination i , (4) total absolute rest-frame magnitude M$_B^{rest}$, (5) adopted inclination corrected rotation velocity v$_{rot}$.

Furthermore, Milvang-Jensen (2003) report that they do not find strong evidence for a difference of the cluster and field population in terms of rotation velocity or disc scale length. Their high redshift field galaxies with $z > 0.6$ have a mean disc scale length of $\langle R_d \rangle = 3.8 \pm 0.3$kpc matching well with the Vogt et al. (1997) data, but significantly smaller than our galaxies ($\langle R_d \rangle = 4.7 \pm 0.5$kpc). However, the range of disc scale lengths spanned is about the same in their and our sample. Their cluster galaxies have a mean disc scale length $\langle R_d \rangle = 3.1 \pm 0.3$kpc, which is marginally different from their field galaxies. Their lower redshift galaxies ($z < 0.6$) have a mean disc scale length of $\langle R_d \rangle \approx 2.3$kpc similar to Ziegler et al. (2002). Finally, we compare the mean rotation velocities of their high redshift field and cluster galaxies with our high redshift galaxies. They agree very well (field: 150 ± 13km s^{-1}; cluster: 141 ± 28km s^{-1}; our data: 142 ± 7km s^{-1}). Their low redshift sample galaxies have a much lower mean rotation velocity, though (110 ± 10km s^{-1}).

5.1.4 Intercomparison and Redshift Evolution

Finally, we will compare the absolute magnitudes, disc scale lengths and rotation velocities as a function of redshift of the Vogt (2001a), Milvang-Jensen (2003), Ziegler et al. (2002) and our data sets. In Fig. 5.7 we show the redshift evolution of disc scale lengths for their and our galaxies. From the large spread of sizes in our complete local catalogue we find that all samples are consistent with the range of object sizes in the local universe. However, the limited number of observed high redshift objects and the lack of understanding of the selection function as a result of this makes predictions about the evolution absolutely impossible. The mean sizes found by Vogt (2001a), Milvang-Jensen (2003) and Ziegler et al. (2002) are rather consistent with each other and a medium sized local galaxy, though. In contrast to this, we have made a first attempt at selecting just one particular class of objects, i.e. the largest galaxies, to minimise observational limitations that would impact severly on the selection function. That in mind, attempts at distinguishing field and cluster populations at high redshift appear to be rather challenging and only large samples in combination with well determined selection functions will eventually allow solving such questions.

The selection function has an even worse effect on the magnitude distributions (see Fig. 5.8). Basically all high redshift surveys line up in a tight sequence connecting low luminosity systems at

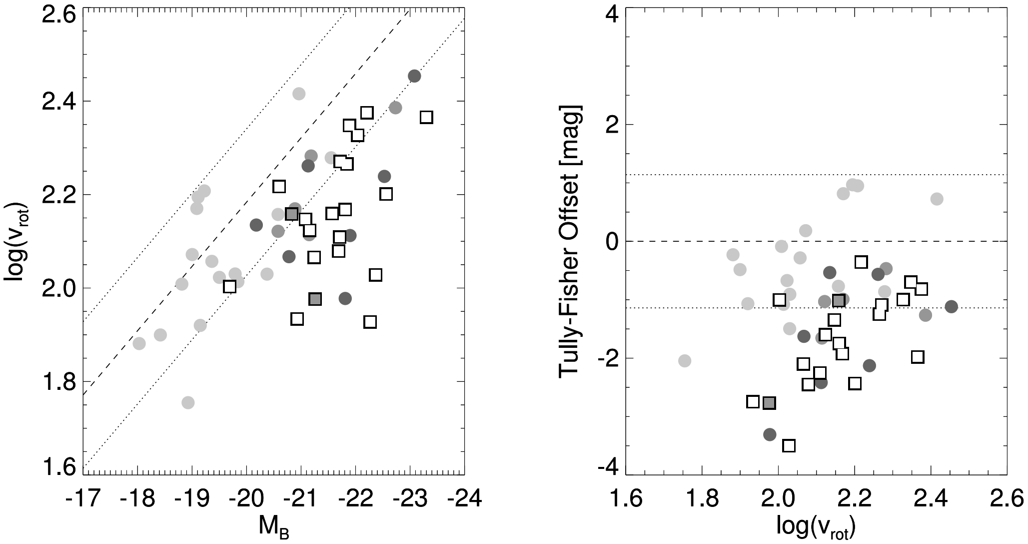

Figure 5.6: Tully-Fisher relation for Milvang-Jensen (2003)

The Tully-Fisher relation (left) and the magnitude offset from the Tully-Fisher relation as a function of rotation velocity (right) for the Milvang-Jensen (2003) data (filled circles) in comparison to our high redshift data (boxes; dark boxes excluded from sample). The different shades of grey going from light to dark circles indicate field galaxies at $z < 0.6$, field galaxies at $z > 0.6$ (excluding the cluster) and galaxies at the redshift of the cluster $0.81 < z < 0.84$. The magnitude and rotation velocity ranges for the Milvang-Jensen (2003) $z > 0.6$ galaxies agree well with ours; their offset from the Tully-Fisher relation is even larger at those redshifts. Thick dashed and dotted lines represent the local Tully-Fisher relation and its scatter, respectively.

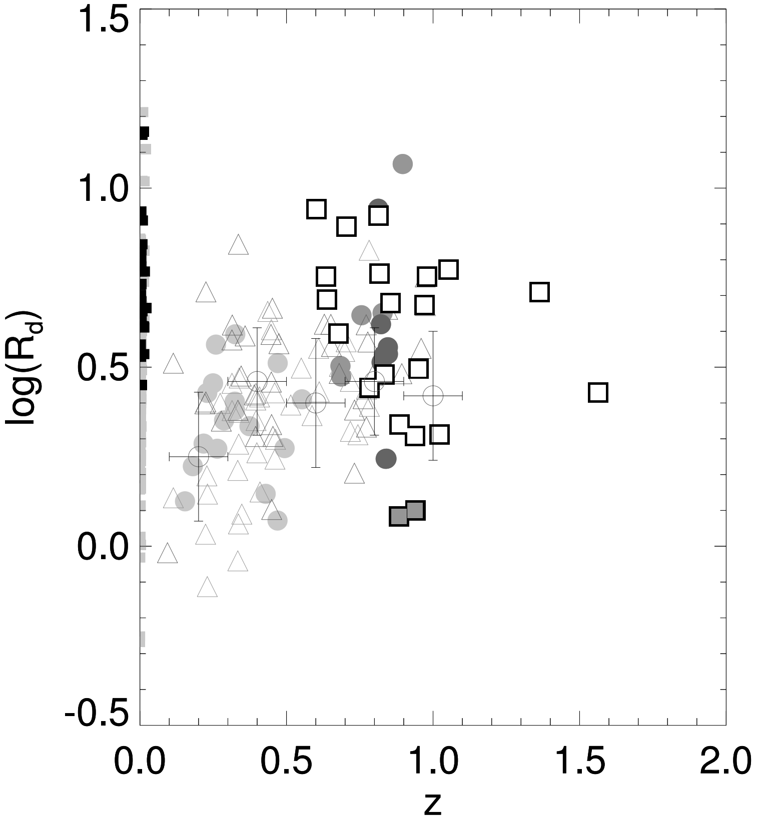

Figure 5.7: R_d as a function of redshift

The disc scale length R_d as a function of redshift. The Milvang-Jensen (2003) data are shown as solid circles; the Ziegler et al. (2002) data are shown as open triagnles (dark symbols: high quality, bright symbols: low quality). We distinguish in three shades of grey –going from light to dark– low redshift field, high redshift field and high redshift cluster galaxies. Open circles mark the Vogt (2001a) data. Since redshifts were not available for individual galaxies, we plot their redshift bins together with the mean values in that bin and 3σ error bars. The horizontal error bar for those data just show the width of the redshift bin. We plot our high redshift data with large boxes (dark boxes were excluded from the sample) and our local comparison sample with small boxes (dark - restricted sample; light - complete local sample). Without defining a specific selection Vogt (2001a), Milvang-Jensen (2003) and Ziegler et al. (2002) pick typically much smaller galaxies than can be found in our samples.

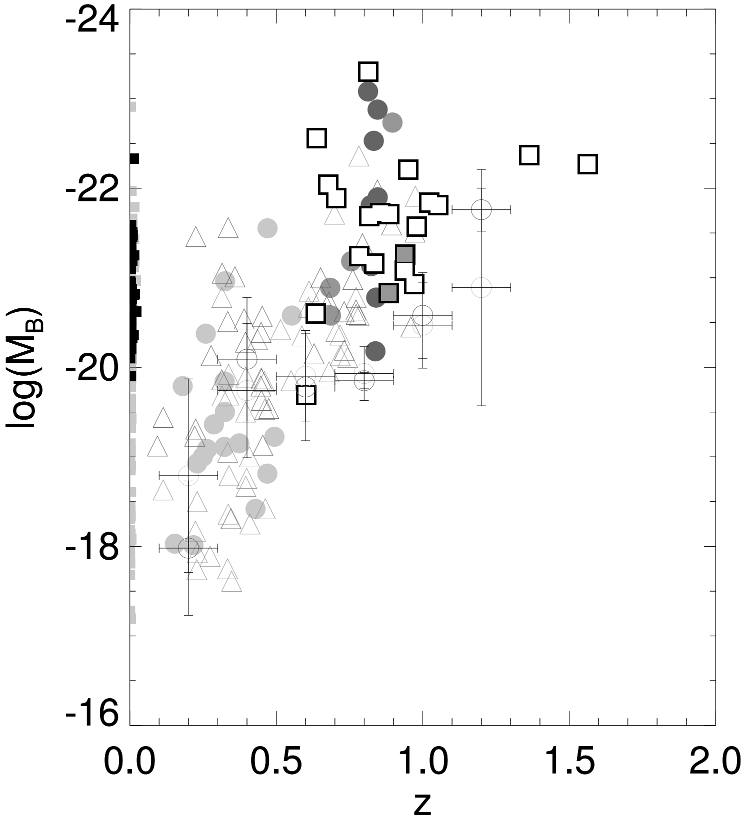

Figure 5.8: M_B as a function of redshift

The absolute rest-frame magnitude M_B as a function of redshift. Symbols are the same as in Fig. 5.7 except for the Vogt (2001a) data. We now plot their combined high and low quality objects in light grey and their high quality objects alone in dark grey. With increasing redshift the intrinsic surface brightness cut of the various surveys makes it impossible to observe fainter objects.

low redshift with high luminosity galaxies at high redshift. Although this is being interpreted as luminosity evolution the real effect of luminosity evolution is masked for two reasons. On one hand the sharp cut at low magnitudes is a result of the strongly redshift dependent surface brightness dimming of the targets. With increasing redshift it becomes impossible to pick up objects at faint absolute magnitudes. On the other hand, the limited survey area helps at high redshift where the covered comoving area is much larger than at low redshift. Therefore, it is easier to detect many bright objects at high redshift than at low redshift. Any evolution in absolute magnitude can only be traced taking this selection and the proper comoving volumes into account. Taking mean values from any of the mentioned surveys at different redshifts therefore cannot provide reasonable estimates of pure magnitude evolution. As our data show, for objects of similar isophotal size the apparent evolution in absolute magnitude is much smaller. Apart from that, at high redshift the various surveys agree fairly well. Milvang-Jensen (2003) find $\langle M_B \rangle = -20.95 \pm 0.12$ for their high redshift field galaxies and $\langle M_B \rangle = -21.79 \pm 0.37$ for their high redshift cluster galaxies, while our data has $\langle M_B \rangle = -21.60 \pm 0.12$. This value is compatible with both the cluster and the field population. Although always being somewhat at the low luminosity side compared to our data even the Vogt (2001a) data are successively pushed to brighter and brighter magnitudes at high redshift. At their highest redshift bin our data agree quite well. This again stresses how dominant the selection effects are at $z > 0.6$ when surveys with completely different selection criteria (large $\longleftrightarrow$ small) end up at the same values (same range of absolute magnitudes).

One gets a similar picture, though with larger scatter, when looking at the evolution of the rotation velocities (see Fig. 5.9). Only when applying a sensible selection it becomes possible to observe the from the hierarchical theory predicted evolution in mass. To show this effect without preselection one would need by far larger samples than are available today. But perhaps even more interesting is the evolution in the offset from the Tully-Fisher relation (see Fig. 5.10). Keeping in mind that galaxies were selected amongst the various surveys in very different ways, e.g. mixing up large and small galaxies, bright and faint, and so on, and keeping in mind the huge spread in the various variables, a very consistent picture is presented to us. Assuming the slope of the Tully-Fisher relation to be the same at all redshifts, one finds a consistently increasing offset with increasing redshift. Ziegler et al. (2002) have argued for a change of the slope of the Tully-Fisher relation. However, our previous discussion of the various selection effects buried in apparent magnitude limited surveys gives reason to suspect that this change of slope was artificially introduced by mixing galaxies of different absolute magnitudes at different redshifts. Therefore, we argue that until larger Tully-Fisher samples with several hundred objects per redshift bin spanning at least 4 - 5 mag in absolute magnitude and a thorough understanding of the survey selection function is available, strong statements about the evolution of the Tully-Fisher relation have to be taken with some care. However, the data available today suggest a systematically increasing offset from the Tully-Fisher relation with redshift. In conclusion, we find:

- Current surveys pick up galaxies in a magnitude range which gets narrower with redshift. At the faint end the apparent magnitude cut of the surveys limits the data, while at the bright end the comoving volume sampled is usually too small to contain the brightest objects.
- A similar effect occurs when looking at size or rotation velocity distributions as a function of redshift. Since those quantities are correlated with the absolute magnitude, it is the intrinsic apparent magnitude and surface brightness cut that limits the ability to detect smaller and less massive systems.
- From looking at plots of absolute magnitude, disc scale length or rotation velocity as a function of redshift one cannot deduce that strong evolution is occurring. Since selection effects dominate those distributions much larger samples than those available today are needed to address such issues directly.
- It is possible though, to make a statement about the evolution of the Tully-Fisher relation. Combining the available Tully-Fisher data we find a systematically increasing offset from the local relation with redshift. To address the incompleteness at faint absolute magnitudes one has to assume a slope of the Tully-Fisher relation that is constant with redshift.

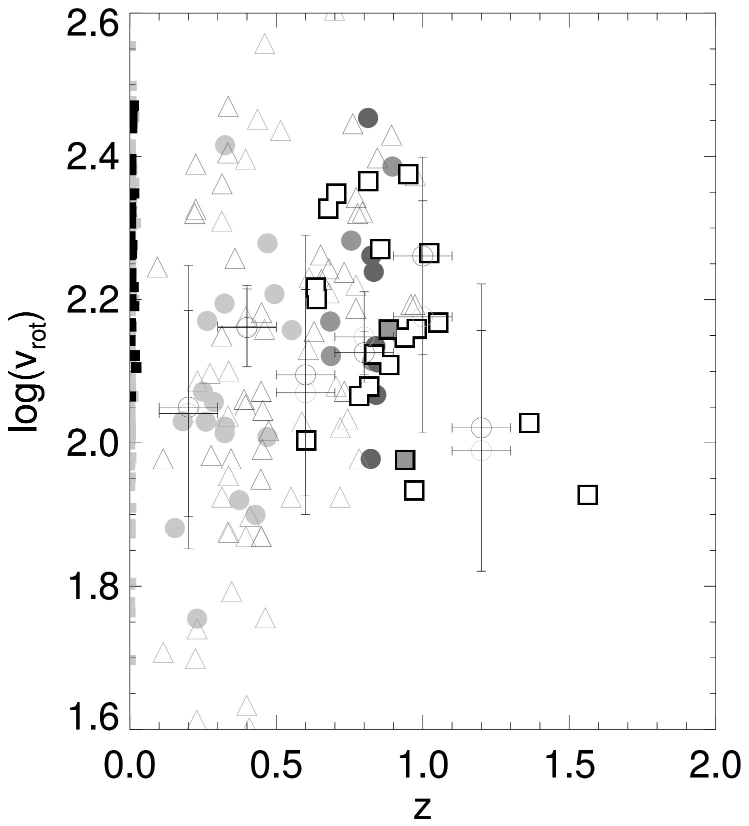

Figure 5.9: v_{rot} as a function of redshift

The rotation velocity v_{rot} as a function of redshift. Symbols are the same as in Fig. 5.7 except for the Vogt (2001a) data. We now plot their combined high and low quality objects in light grey and their high quality objects alone in dark grey. Again, with increasing redshift the intrinsic surface brightness cut of the various surveys makes it impossible to observe fainter objects and therefore less massive objects.

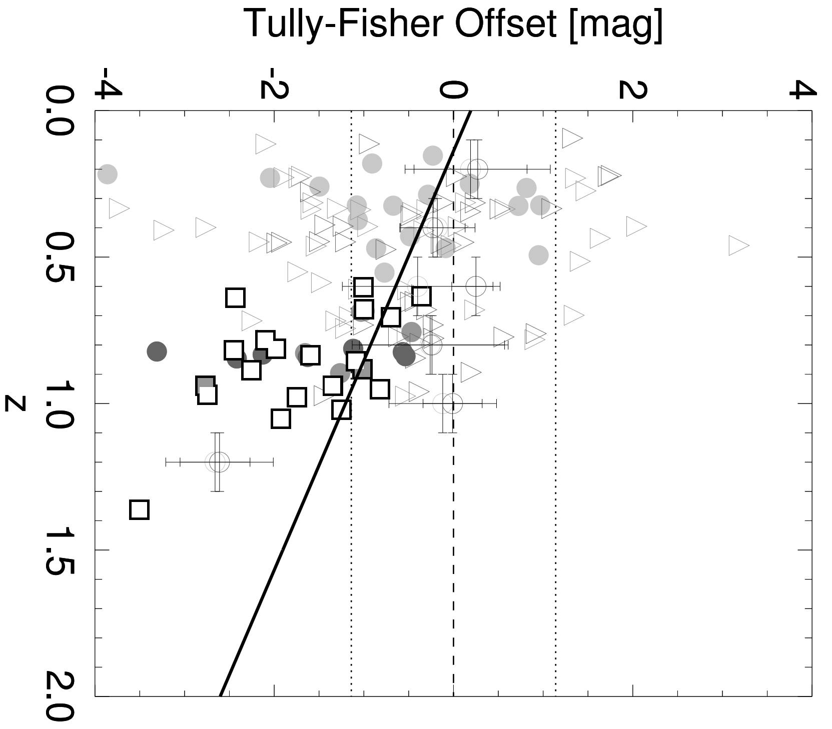

Figure 5.10: The Tully-Fisher offset as a function of redshift

The offset from the Tully-Fisher relation as a function of redshift. Symbols are the same as in Fig. 5.7 except for the Vogt (2001a) data. We now plot their combined high and low quality objects in light grey and their high quality objects alone in dark grey. With increasing redshift we observe a systematically increasing offset from the local relation (horizontal lines) regardless of the specific sample selection. The diagonal line is a free robust linear fit to all the data. The Vogt and Ziegler et al. data are weighted according to the number of galaxies in the respective bins.

5.2 Comparison with Theory

Very substantial progress has been made in the understanding of the evolution of galaxies not only from the observational point, but also concerning the theoretical modelling of the histories of galaxies. We will compare our work in this section with the scaling relations presented in Boissier and Prantzos (2001, 2000). They apply the simple scaling relations resulting from semi-analytical models (Mo et al., 1998) to derive initial gaseous profiles for which then subsequently the full chemical and spectrophotometric evolution is calculated. The properties of ensembles of disc galaxies thus formed are calibrated with a detailed template model of the Milky Way by Boissier and Prantzos (1999). Furthermore, we compare our data to predictions by Bouwens and Silk (2002) employing especially their hierarchical model appropriate for our adopted cosmology. Their so-called "backwards" approach, predicting high redshift properties starting from a detailed model of the Milky Way, gives similar results, though.

5.2.1 Evolution of the Disc Scale Length

We start by plotting the predicted evolution of the disc scale length with redshift (see Fig. 5.11). The simulations nicely span the whole range of observed galaxies in the local universe. Our selection of corresponding low and high redshift samples occupy the larger half of the simulations, though. To perform an elaborate comparison of data and simulations one would have to convolve the simulations with the same selection function as the data. Since this is beyond the scope of this work we just compare relative locations of our local and distant data points at the corresponding redshifts with the range spanned by the simulated galaxies. Both simulations and data are well fitted by a line with $R_d \propto (1+z)^{-0.5}$. This is inconsistent with the relation derived by Mao et al. (1998) where $R_d \propto (1+z)^{-1}$. However, they argued that this result was strongly dependent of the observational data by Vogt et al. (1997). Therefore, their scaling relations might change form using the new data. Additionally, we plotted the hierarchical model by Bouwens and Silk (2002), which represents a compromise between the two proposed scaling relations. Compared with our distant galaxies this model is too steep to be a perfect fit. Furthermore, both our high and low redshift samples are on average slightly larger than the Milky Way as predicted by Boissier and Prantzos (2001). The Milky Way behaves slightly different than the average galaxy in the simulations and actually follows closely the prediction by Mao et al. (1998).

5.2.2 Evolution of the Absolute Magnitude

Plotting the redshift evolution of the absolute magnitude reveals a similar picture (see Fig. 5.12). The simulations span about the same range as our complete local sample. However, our full local sample apparently misses some of the faintest objects. Both our restricted local sample and our high redshift sample range from the $+1\sigma$ line to the upper limit of the simulations at the respective redshifts. The Milky Way is representative of the faintest third of our data at both redshifts. Again we overplot the model by Bouwens and Silk (2002), normalised to our restricted local galaxy sample. Their hierarchical model agrees extremely well with our high redshift data set. Again, we refrain from more detailed analyses, which would necessitate the application of the selection function to the simulations.

5.2.3 Evolution of the Central Surface Brightness

Here we show the evolution of the central surface brightness in our models and the theoretical predictions (see Fig. 5.13). In this case the Milky Way model by Boissier and Prantzos (2001) provides a better estimate for the evolution of our galaxies than their general simulations, although the agreement between simulations and our distant galaxies is still fair. The simulations by Bouwens and Silk (2002) provide a match to the data of a slightly worse degree than the Milky Way model. Overall the model by Boissier and Prantzos (2001) recovers the distribution of our complete local sample well. However, the discrepancies between the relative central surface brightnesses of

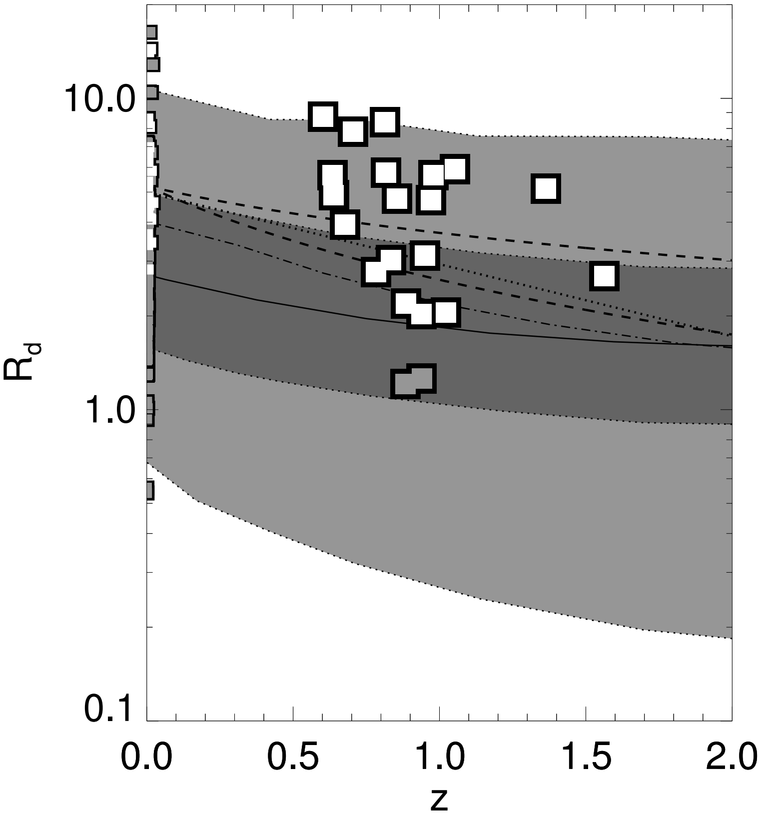

Figure 5.11: Evolution of the disc scale length

The evolution of the disc scale length as predicted by Boissier and Prantzos (2001). Boxes symbolise our high and low redshift galaxies (dark boxes were excluded from the sample). The dark shaded area represents the $\pm 1\sigma$ variation around the mean (solid line) of the simulations; the light shaded area shows the remaining galaxies. The dash-dotted line marks the evolution of the Milky Way disc. Thick dashed lines show the evolution predicted by Mao et al. (1998), which are proportional to $R_d \propto (1+z)^{-1}$ and $R_d \propto (1+z)^{-0.5}$. Given the fact that the restricted local sample only spans the "upper" half of the range spanned by the full local sample, which agrees with the prediction for local galaxies by Boissier and Prantzos (2001), our high redshift data are very consistent with the models by Boissier and Prantzos (2001). Our data rule out extremely strong evolution of the disc scale lengths towards smaller high redshift galaxies (decrease can be no larger than $\sim 30\%$) as well larger high redshift galaxies than locally. Both data and simulations favour a scaling relation $R_d \propto (1+z)^{-0.5}$ in contrast to what was predicted by Mao et al. (1998). The dotted line indicates the model by Bouwens and Silk (2002).

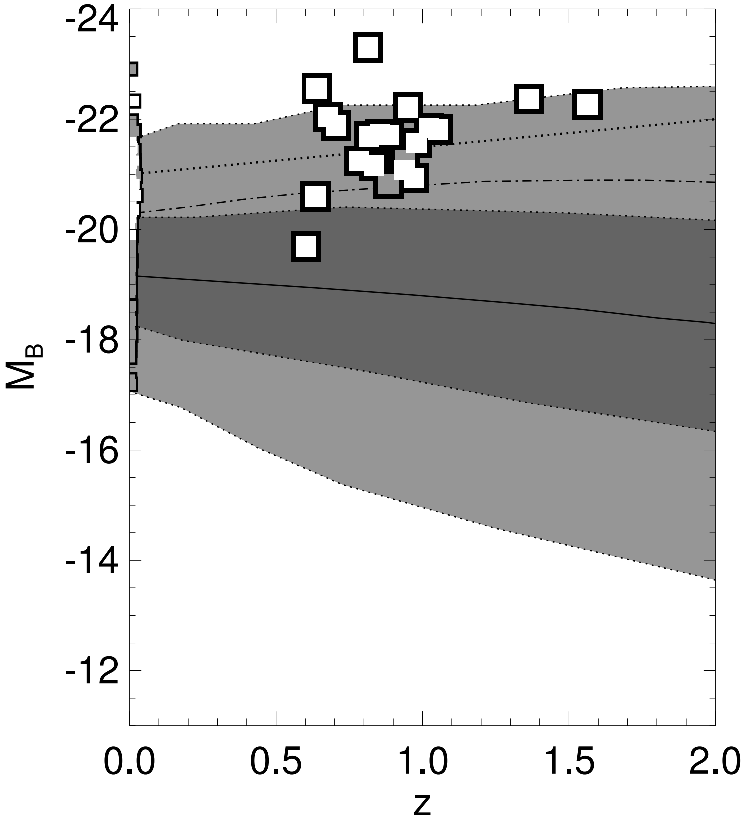

Figure 5.12: Evolution of the absolute magnitude

The evolution of the absolute magnitude as predicted by Boissier and Prantzos (2001). Boxes symbolise our high and low redshift galaxies (dark boxes were excluded from the sample). The dark shaded area represents the $\pm 1\sigma$ variation around the mean (solid line) of the simulations; the light shaded area shows the remaining galaxies. The dash-dotted line marks the evolution of the Milky Way disc. The model by Boissier and Prantzos (2001) and the model by Bouwens and Silk (2002, dotted line) both agree well with the data, again, considering the fact that the restricted local sample is basically a "bright" sub-sample of the full local sample. Our data rule out scenarious in which the brightest and largest high redshift galaxies were on average much fainter or brighter than in the local universe. However, the scatter of the observations is too large (even given our strong selection) to discriminate between various models.

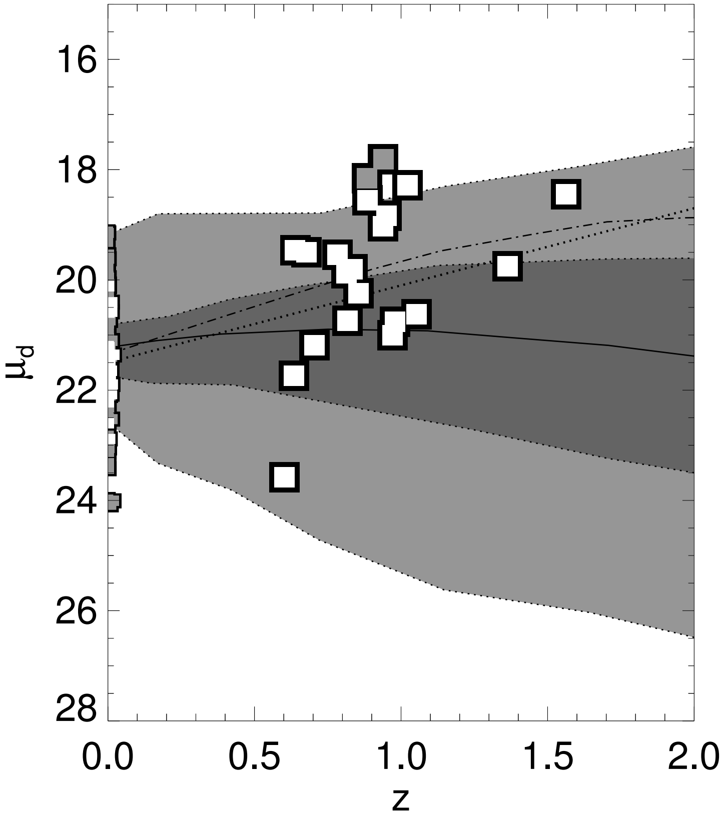

Figure 5.13: Evolution of the central surface brightness

The evolution of the central surface brightness as predicted by Boissier and Prantzos (2001). Boxes symbolise our high and low redshift galaxies (dark boxes were excluded from the sample). The dark shaded area represents the $\pm 1\sigma$ variation around the mean (solid line) of the simulations; the light shaded area shows the remaining galaxies. The Milky Way model (dash-dotted line) by Boissier and Prantzos (2001) agrees best with the data. The Bouwens and Silk (2002) model is indicated by the dotted line.

the observations and the models may hint at differential evolution of individual galaxy populations. Certainly, much larger samples are required to test such hypotheses.

5.2.4 Evolution of the B-V Colour

As another test we compare theoretical and observational measurements of the colours of local and high redshift galaxies (see Fig. 5.12). Since Boissier and Prantzos (2001) do not tabulate B-V colours, but only $[\text{U-V}]_{\text{AB}}$ we convert their colour using the relation found by Larson and Tinsley (1978):

$$[\text{U-B}] = 1.5 \cdot [\text{B-V}] - 0.9 \Rightarrow [\text{B-V}] = 0.4 \cdot ([\text{U-V}]_{\text{AB}} + 0.69 + 0.9)$$

Again our complete local sample nicely spans the range of colours predicted by the model. Interestingly, our restricted local sample spans the same range of values as the complete local sample, in contrast to the results from other quantities, where the restricted set usually only spanned a small part of the possible range. This nicely reflects the fact that our local galaxies were not selected for a specific colour. Although slightly bluer in absolute colour our high redshift galaxies still follow the general trend predicted by the simulations. Even the scatter appears to be similarly large as that of the local galaxies with respect to the simulations. Again we take that as proof that our conclusions are not severely biased by selecting blue star forming galaxies at high redshift.

5.2.5 Evolution of the Tully-Fisher relation

Finally, we provide a comparison of the B-band Tully-Fisher relation from the simulations and the data (see Fig. 5.15). Comparing the zeropoint of the simulations with the zeropoint of our observations at low redshift we observe an offset of 0.5-1mag, while at high redshift it gets as large as 1.5-2.5mag. Boissier and Prantzos (2001) state that their Tully-Fisher relation is in better agreement to the Tully-Fisher relation given in Willick et al. (1996) than the one by Tully et al. (1998). The reason being that the latter one was concerning cluster rather than field spiral galaxies, due to the impact of tidal interactions on the star formation rate, which was not included in the model. On the other hand, Bouwens and Silk (2002) claim good agreement, even in an absolute sense, between their data and the observations by Vogt et al. (1996; 1997) and the local Tully-Fisher relation by Pierce and Tully (1992). However, including the observations by Ziegler et al. (2002); Milvang-Jensen et al. (2003); Vogt (2001a) and our own data, their models are not in agreement with the observations any more. We find that their local relations are already off by almost 1mag from our local Tully-Fisher relation (Tully and Pierce, 2000). This can be largely attributed, though, to the choice of the local Tully-Fisher relation. Using the Pierce and Tully (1992) Tully-Fisher relation apparently provides a much better match to the simulations. This raises the question, of which local Tully-Fisher relation to choose for normalising the models. However, even after assuming the same local Tully-Fisher relation for both models and observations, i.e. after shifting the models by about 1 mag, the model prediction for evolution of the Tully-Fisher zeropoint does not match the observed one. Both Boissier and Prantzos (2001) and Bouwens and Silk (2002) predict almost no evolution of the zeropoint of the Tully-Fisher relation. It is not obvious, though, what the driving parameters are in the models to achieve a better agreement. One might speculate, since the star formation recipes that are used in the codes are relatively uncertain, that those may under- / overestimate the star formation rates at early / late times. On the other hand cooling mechanisms would also have some influence on the timescales over which matter settles in a disc and hence have some control over star formation rates. Furthermore, the problem may relate to the halo / disc spin parameters or the parameterisation of friction in the disc, which both influence the angular momentum of the discs and therefore also the amount of matter that settles in the disc and the measured rotation velocity or via the star formation rate the luminosity of the object. This last point gets supported by the fact that the rotation velocities in at least the Bouwens and Silk (2002) models are about 0.1 dex lower on average than the observational data at redshifts $z > 0.6$ at constant disc scale length (see Fig. 5.16). Although this cannot completely alleviate the problem. Furthermore, inspection of the

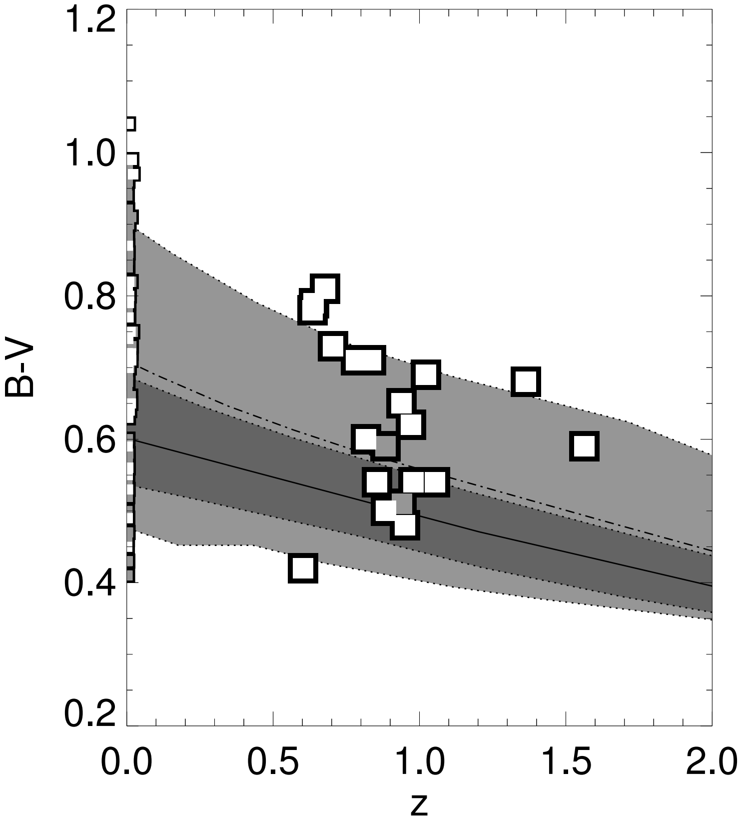

Figure 5.14: Evolution of the B-V colour

The evolution of the B-V colour as predicted by Boissier and Prantzos (2001). Boxes symbolise our high and low redshift galaxies (dark boxes were excluded from the sample). The dark shaded area represents the $\pm 1\sigma$ variation around the mean (solid line) of the simulations; the light shaded area shows the remaining galaxies. The model agrees well with the data, although the scatter in the observed data is relatively large. The Milky Way model by Boissier and Prantzos (2001) is indicated by the dash-dotted line.

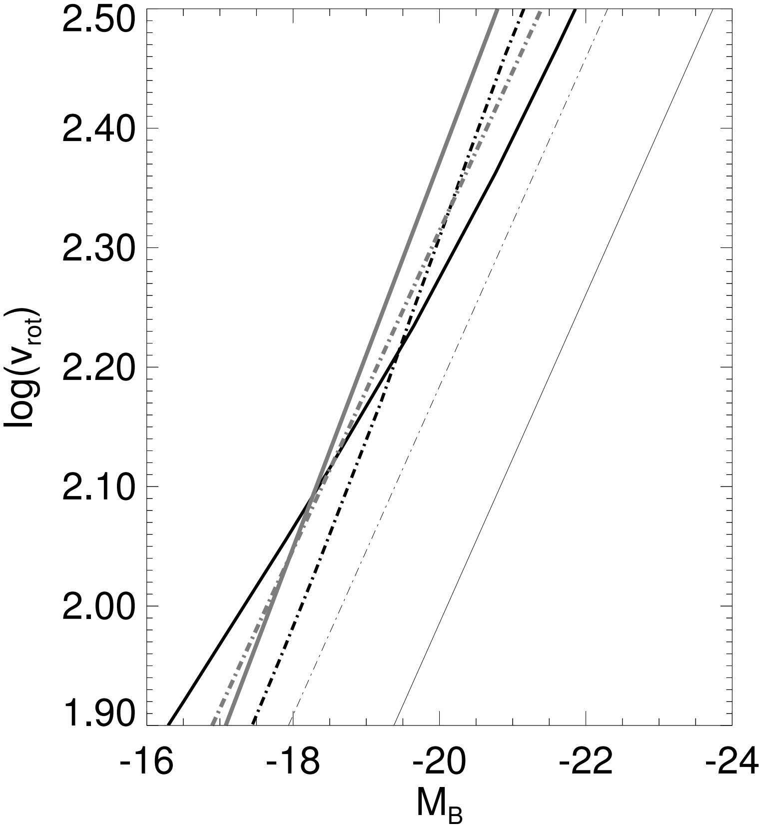

Figure 5.15: Evolution of the Tully-Fisher relation

The evolution of the Tully-Fisher relation as predicted by Boissier and Prantzos (2001) (thick black lines) and Bouwens and Silk (2002) (grey lines) in comparison to observational data (thin lines). The local Tully-Fisher relations for both models and observations are indicated by dot-dashed lines; the high redshift relations are marked by solid lines. The local observational data were taken from Tully and Pierce (2000); the observed high redshift data have the same slope as the local observed relation and are offset by -1.44mag, consistent with our own high redshift sample. Observations and simulations do not agree.

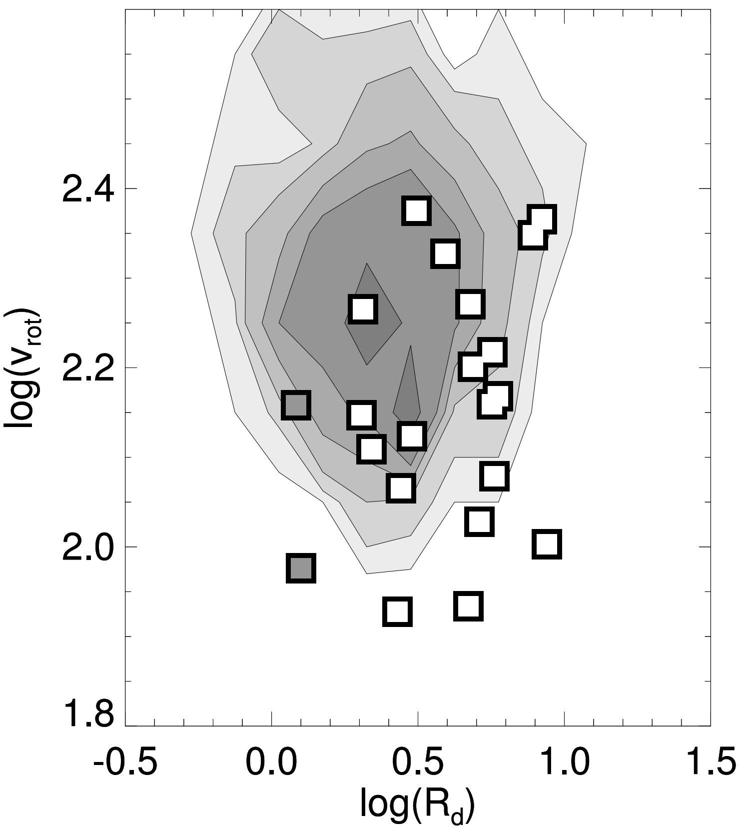

Figure 5.16: The size-rotation velocity relation

The rotation velocity as a function of disc scale length for redshifts $z > 0.6$. While spanning the same range of disc scale lengths, our data (boxes; dark boxes excluded from the sample) have systematically lower rotation velocities than the Bouwens and Silk (2002) simulations (iso-density contours).

magnitude-size relation for observations and simulations (see Fig. 5.17) shows that our data are selected on the large and bright side, but are well within the range predicted by the simulations by Boissier and Prantzos (2001). This again provides some evidence for the rotation velocities of the simulations being too large at high redshift.

Interestingly, in contrast to those semi-analytical models there are numerical simulations that do agree with the observations with respect to the evolution of the Tully-Fisher zeropoint (see Fig. 5.18). Steinmetz and Navarro (1999) have performed extensive numerical simulations of disc galaxies both at low and high redshift. Unfortunately, due to inconsistencies in the normalisation of their power spectrum they fail to reproduce the local Tully-Fisher relation. However, Eke et al. (2001) have shown that this problem can be strongly alleviated in a λ-dominated universe. Therefore, we have converted the Steinmetz and Navarro (1999) data to our cosmology and offset them by -2mag to match the local Tully-Fisher relation by Tully and Pierce (2000). The $z = 1$ simulations show an offset of -1.5mag after applying the offset, which agrees very well with our observed data. The reason for the numerical models providing better estimates for the evolution of the Tully-Fisher zeropoint may again have to do with the treatment of the cooling processes leading to the assembly of the discs. Since the numerical models solve the full set of hydrodynamical equations they may be better constrained in terms of relative evolution although the overall angular momentum problem still persists. On the other hand, semi-analytical models sometimes (e.g. Baugh et al., 1998; Cole et al., 2000) are normalised to match simultaneously luminosity functions in several bands, which has lead to a mismatch between observed and modeled Tully-Fisher relations. However, semi-analytical models that were normalised to match the Tully-Fisher relation usually fail to reproduce luminosity functions. Unfortunately, it is very hard to apply this test also to numerical models because of the lack of sufficient numbers of galaxies.

The Boissier and Prantzos (2001) simulations predict evolution of the Tully-Fisher relation in the sense that at high redshift the slope a was apparently steeper than at low redshift ($a_{highz} \sim -8.6 \Leftrightarrow a_{local} \sim -6.1$). The two relations intersect at $M_B \sim -19.5$. Furthermore, especially at high redshift the simulated Tully-Fisher relation apparently changes its slope from -8.1 at the high velocity end to -10.2 at the low velocity end. Analysing the simulations by Bouwens and Silk (2002) we again find a change of the slope comparing low ($a_{local} \sim -7.5$) and high redshift ($a_{highz} \sim -6.2$). The two relations intersect at $M_B \sim -18.7$. In those latter simulations we do not observe an intrinsic change of slope of the Tully-Fisher relation at one given redshift in contrast to the Boissier and Prantzos (2001) data. Interestingly, although their zeropoint roughly agree, those two simulations do not agree on their values of the Tully-Fisher slope at a given redshift. In fact, while the one predicts a steepening of the Tully-Fisher relation with redshift the other proclaims just the opposite. It was noted in the literature (e.g. Boissier and Prantzos, 2001) that the local estimates of observed Tully-Fisher slopes vary quite dramatically ($a = -6.8$: Mathewson et al., 1992; $a = -8.17$: Tully et al., 1998). Apparently, with theoretical predictions one faces the same problem. Again, this stresses the importance of converging on one fixed slope for local galaxies before actually trying to address the evolution of the Tully-Fisher slope, especially keeping in mind that very often theoretical work uses observations to calibrate mass-to-light ratios etc.

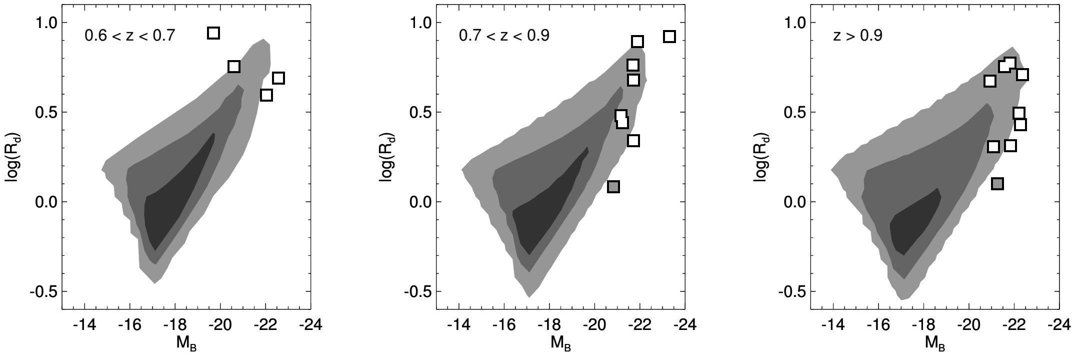

Figure 5.17: The magnitude-size relation

The disc scale length as a function of absolute magnitude for different redshift bins. Although generally on the large and bright side, our data (boxes; dark boxes excluded from the sample) agree well with the simulations (iso-density contours) by Boissier and Prantzos (2001).

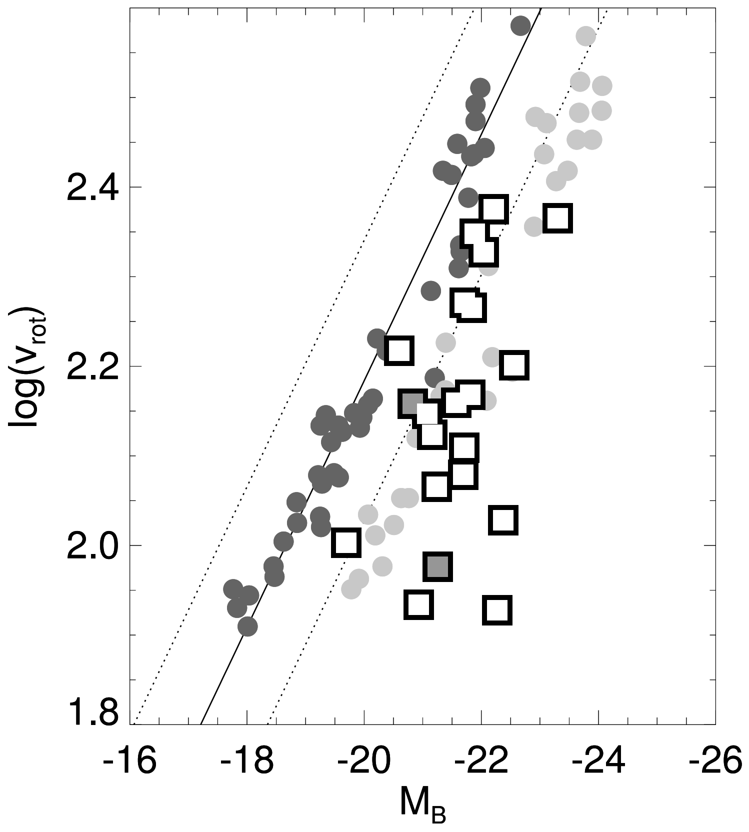

Figure 5.18: The Tully-Fisher relation for the Steinmetz and Navarro (1999) data

The Tully-Fisher relation for the simulations of Steinmetz and Navarro (1999). Dark circles indicate their local data, while light circles mark their simulations at $z = 1$. Their local galaxies where adjusted to match the local Tully and Pierce (2000) relation (solid line; 3σ error bars: dotted line). The accordingly shifted high redshift simulations agree well with the observed data (boxes; dark boxes excluded from sample).

Chapter 6

Conclusions

We have presented a large set of disc galaxy rotation curves at high redshift complemented with high resolution imaging in order to evaluate the Tully-Fisher relation at $z \sim 0.9$. Our sample was selected on the basis of available spectroscopic redshifts in combination with HST imaging (with a few exceptions with only VLT imaging). To maximise our chances of detecting resolved rotation curves we required our sample galaxies to have isophotal sizes $R_{25} > 12.5$kpc corresponding to apparent sizes $R_{lim}^{app} \sim 1''$. No further constraints based on luminosity or line strength were imposed (the minimum redshift of our targets was $z > 0.6$). We used ISAAC at the VLT to take spectra at the restframe wavelength of the H_α line. From those we extracted rotation curves to study the Tully-Fisher relation at high redshift. To quantify the evolution of disc galaxies over the second half of the lifetime of the universe we compared our high redshift data to a set of local galaxies based on the same size selection criteria. Furthermore, we made an effort to degrade the high signal-to-noise local data to a degree that matches the high redshift data. This also enabled us to obtain realistic error estimates for the morphological properties of high redshift galaxies. From those data in comparison to the literature we found the following:

- For the majority of the high redshift data we can trace the rotation curves out to the radius where the peak rotation velocity is expected $R_{2.2}$ or the optical limiting radius R_{lim}. We do not find systematical differences between the "better" and "worse" half of the data. Estimation of the rotation velocity should therefore not be influenced by observational limitations. However, properties like inclination or disc scale length do depend on the depth, i.e. signal-to-noise ratio, of the imaging data and the morphology of the data. We find that the appearance of bars and/or rings makes measuring shapes of distant objects very difficult.

- Although only a lower cut was implied by our selection criterion we find that the distributions of disc sizes at low and high redshift are the same. Therefore, we conclude that the appearance of large galaxies lies more than $\sim$ 8Gyr back. The disc scale lengths of the high redshift sample appear to be a little smaller on average than the local ones. Moreover, the high redshift galaxies are slightly brighter at the same isophotal size. We do find a dramatic increase in the central surface brightness with redshift, though. On one hand, to some extent this was expected since our data are to a large fraction a subset of the data of Schade et al. (1996). On the other hand, this does contradict the results by Simard et al. (1999) according to which the mean surface brightness of disc galaxies does not evolve with redshift. We tested two scenarios of disc evolution to explain the changes in the various variables: inside-out, and self-similar evolution. We find that self-similar evolution, i.e. at constant disc scale length only the central surface brightness evolves, cannot have been the major mode of disc evolution; inside-out formation, where disc scale lengths grow with time and the central surface brightness gets fainter, provides a much better fit to the data.

- Furthermore, we find significant evolution of the rotation velocity of objects of the same isophotal size with redshift. Converting rotation velocity to mass we find that our high redshift galaxies were about a factor of 2 less massive than the largest present day galaxies. This increase in mass follows the general trend of the increase in disc scale length (see Fig. 6.1). Deriving stellar mass-to-light ratios from the observed B-V colour we find mass ratios $\rho = M_{dyn}/M_{stel}$ that are about the same at high and at low redshift, thus implying that the mass-to-light ratios have changed systematically. Moreover, the angular momenta of the high redshift galaxies are significantly smaller than locally as a result of the decrease of mass and disc scale length.

- We compared our data to other samples in the literature (Vogt et al., 1993, 1996, 1997; Vogt, 1999, 2000, 2001a,b; Ziegler et al., 2002; Böhm et al., 2003; Milvang-Jensen et al., 2003; Milvang-Jensen, 2003). Combining all the data sets we find that over a redshift range $0 < z < 1$ ~ 200 galaxies are not sufficient considering the large diversity of objects to allow detailed measurements, like e.g. Tully-Fisher slopes or cluster-field differences. Before adressing such issues one has to have a thourough understanding of the selection effects of the individual sample. We find that imposing a selection similar to our approach (namely in R_{25}) constrains a complete local sample –spanning the full range of disc scale lengths, absolute magnitudes and rotation velocities– in such a way that (subjective) biases (when selecting targets for spectroscopy) get minimised, thus presenting a closer picture of galaxy evolution. Our high redshift sample ($z > 0.6$) comprises the largest and most distant objects while at intermediate redshift ($0.1 < z < 0.6$) observed galaxies from the literature are a factor of two smaller than ours (see Fig. 5.7). However, this is not a result of redshift evolution, but rather sample selection. On one hand total numbers in the various surveys are so small that they are far from complete in the respective redshift bins, and on the other hand our restricted local sample, after applying the same selection function, consists of objects of the same size as the high redshift sample. If anything the expectation is that galaxy disc scale lengths increase with time (Mao et al., 1998). A similar picture is presented to us looking at the absolute magnitudes. Although maybe expected from the general increase of star formation with redshift (Madau et al., 1996, 1998; Dickinson et al., 2003) we argue that what we see here is again rather a result of the limited surface brightness range on the faint end and limited volume sampling at the bright end when selecting the target galaxies than true evolution. It would be very surprising if the brightest galaxies at intermediate redshift would be over a magnitude fainter as in the local universe or at high redshift. At redshifts $z \sim 1$ the observable range gets so limited that the various samples independent of their intrinsic sizes span the same magnitudes. Along that line of reasoning one should also expect that very low rotation velocities at intermediate redshifts result mainly from limitations imposed on the samples and not from evolution. The highest redshift data compared with our restricted local sample suggest a general increase of rotation velocity with redshift as expected from the theory.

- The Tully-Fisher relation of high redshift galaxies is offset by ~ 1.1mag from the local relation. This is a result of the increase of surface brightness and absolute magnitude on one hand, and of the systematic decrease of rotation velocity on the other hand. In combination with other data in the literature we find that there is significant evidence for a systematic increase of Tully-Fisher offset with redshift, regardless of the specific selection of the samples. Combining all the data, a free robust fit to the Tully-Fisher offset Δ_{TF} as a function of redshift gives $\Delta_{TF} = -(0.19 \pm 0.19) - (1.40 \pm 0.32) \cdot z$. It is remarkable, that even the zero-point comes out to be right. Although not as steep as expected from our data alone (the Vogt data have a high weight) the slope predicts an offset at $z \sim 0.9$ very compatible to our data ($1.1 \pm 0.4 \longleftrightarrow 1.44 \pm 0.12$).

- We cannot constrain the slope of the Tully-Fisher relation since our magnitude range is too small, though. However, given the result of the redshift dependence of the Tully-Fisher offset, trying to estimate the Tully-Fisher slope becomes increasingly difficult. Even the largest Tully-Fisher samples today only have of order 10-20 galaxies per redshift bin. Ziegler et al. (2002), who have claimed to have found evidence for a change in slope, only have 14 galaxies

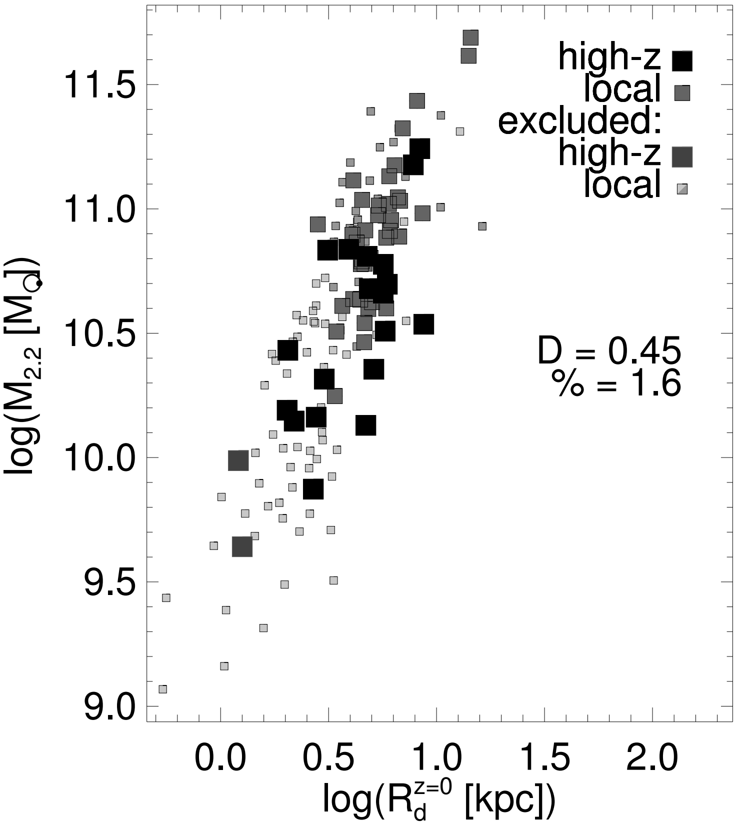

Figure 6.1: Mass as a function of disc scale length

The dynamical mass derived at $R_{2.2}$ as a function of R_d for high redshift (large symbols) and local galaxies (small symbols). Symbols are the same as in Fig. 4.4. The lower average mass of the high redshift galaxies is completely compensated by the slightly smaller mean disc scale lengths to make them stay on the same global relation as the local galaxies.

in the critical magnitude range $M_B > -19$ at redshifts $0 < z < 0.5$, which encompasses certainly a time interval large enough for galaxies to undergo significant evolution. At redshifts $z > 0.6$ they have a magnitude range similar to ours and therefore lack the possibility to constrain the slope enough to draw strong conclusions. Even the theory cannot make reliable predictions about the Tully-Fisher slope at the moment. Boissier and Prantzos (2001) and Bouwens and Silk (2002) for example predict opposite directions for the evolution of the Tully-Fisher slope.

- We have also compared our data to theoretical predictions. Our high and restricted low redshift data are consistent with the largest disc galaxies in the Boissier and Prantzos (2001) simulations. Both simulations and data suggest evolution of the disc scale length $R_d \propto (1+z)^{-0.5}$ in contrast to the relation $R_d \propto (1+z)^{-1}$ as was derived by Mao et al. (1998) for the Vogt et al. (1993, 1996, 1997) data. The region spanned by our data on the $z - R_d$-plane is also fairly consistent with the evolution of the Milky Way and the model by Bouwens and Silk (2002). We come to simliar conclusions comparing the absolute magnitude distributions of simulations and data. Both Boissier and Prantzos (2001) and Bouwens and Silk (2002) agree very well with our data, and although our galaxies are slightly more luminous than the Milky Way our data are very consistent with its evolution. In terms of surface brightness we find similar results. The Milky Way model agrees very well, while Bouwens and Silk (2002) and Boissier and Prantzos (2001) provide a slightly worse fit. Since we cannot derive equivalent widths from our data it is reassuring that the B-V colours of our high redshift galaxies exactly follow the trend predicted by the models. However, in contrast to those results the Tully-Fisher relation does neither match the models by Boissier and Prantzos (2001) nor those of Bouwens and Silk (2002). Although to some extent this results from not matching the local Tully-Fisher relation, which may be attributed to normalisation problems, the predicted relative evolution with redshift does not agree with the observational data. Since observational and theoretical sizes and magnitudes agreed so well the difference may be accounted to the rotation velocities. However, after adjusting the zero-point of the numerical simulations by Steinmetz and Navarro (1999) (the angular momentum problem) to match our local data we find perfect agreement between the amount of evolution in the Tully-Fisher zeropoint they and we see from $z \sim 1$ to $z \sim 0$.

Although the results from the literature encompass a wide range of conclusions, so far no consensus has been found to resolve issues about the evolution of the Tully-Fisher relation. What is direly needed to make more progress in the field of the evolution of spiral galaxies are larger samples with several hundred galaxies per redshift bin and a good understanding of the underlying selection functions. In the optical such sample sizes are finally becoming available with the advent of wide-field multi-object spectrographs (e.g. VIMOS on the VLT). At redshifts $z \sim 1$ those optical techniques reach a natural limit. To extend to even higher redshift one has to push forward to obtain as many H_α rotation curves as possible in the near-infrared, possibly including adaptive optics, which could greatly enhance the efficiency of detecting the flat part of the rotation curve (Koo, 2000). Eventually, the first generation of cryogenic near-infrared multi-object spectrographs will deliver a decisive answer to those questions on a 5-10 years time-scale.

Chapter 7

Acknowledgements

This work would not have been possible without the help and support of several people. First of all, I would like to thank Matt Lehnert for his inspiration and guidance. Without all his suggestions and ideas in countless discussions this thesis would have been much thinner. I am grateful to Reinhard Genzel for his constructive input throughout the years and his critical reading of the first draft. This led to many improvements and helped me see things from different perspectives. Furthermore, I am indebted to Linda Tacconi and Dimitra Rigopoulou, who supported this work through their input as my thesis committee.

Hans-Walter Rix is thanked for his encouragements and patience with me to finally get finished. It is also a pleasure to thank Helmut Dannerbauer, Eric Bell, Catherine Heymans and Martina Kleinheinrich who shared offices with me. They sustained all my bad moods in times when things were not as smoothly as I wanted them to be. And it was joyful spending the better times in their company. I would also like to thank all the people who worked in closer contact with me, especially Boris Häussler and the GEMS team.

Generous allocation of ISAAC/VLT time by the OPC at ESO is gratefully acknowledged. This research has made use of the NASA/IPAC Extragalactic Database (NED), which is operated by the Jet Propulsion Laboratory, California Institute of Technology, under contract with the National Aeronautics and Space Administration.

Bibliography

Aaronson, M., Huchra, J., and Mould, J.: 1979, *ApJ* **229**, 1

Abadi, M. G., Navarro, J. F., Steinmetz, M., and Eke, V. R.: 2003, *ApJ* **591**, 499

Abell, G. O., Corwin, H. G., and Olowin, R. P.: 1989, *ApJS* **70**, 1

Abraham, R. G., Merrifield, M. R., Ellis, R. S., Tanvir, N. R., and Brinchmann, J.: 1999, *MNRAS* **308**, 569

Böhm, A., Ziegler, B. L., Fricke, K. J., and FDF Team, t.: 2003, *Ap&SS* **284**, 689

Barnes, J. E.: 1992, *ApJ* **393**, 484

Barnes, J. E. and Hernquist, L.: 1992, *ARA&A* **30**, 705

Barnes, J. E. and Hernquist, L.: 1996, *ApJ* **471**, 115

Barton, E. J., Bromley, B. C., and Geller, M. J.: 1999, *ApJ* **511**, L25

Barton, E. J., Geller, M. J., Bromley, B. C., van Zee, L., and Kenyon, S. J.: 2001, *AJ* **121**, 625

Baugh, C. M., Cole, S., and Frenk, C. S.: 1996a, *MNRAS* **283**, 1361

Baugh, C. M., Cole, S., and Frenk, C. S.: 1996b, *MNRAS* **282**, L27

Baugh, C. M., Cole, S., Frenk, C. S., and Lacey, C. G.: 1998, *ApJ* **498**, 504

Bell, E. F. and de Jong, R. S.: 2001, *ApJ* **550**, 212

Bender, R., Burstein, D., and Faber, S. M.: 1992, *ApJ* **399**, 462

Benson, A. J., Pearce, F. R., Frenk, C. S., Baugh, C. M., and Jenkins, A.: 2001, *MNRAS* **320**, 261

Bernstein, G. M., Guhathakurta, P., Raychaudhury, S., Giovanelli, R., Haynes, M. P., Herter, T., and Vogt, N. P.: 1994, *AJ* **107**, 1962

Binney, J. and Tremaine, S.: 1987, *Galactic dynamics*, Princeton, NJ, Princeton University Press, 1987, 747 p.

Boissier, S. and Prantzos, N.: 1999, *MNRAS* **307**, 857

Boissier, S. and Prantzos, N.: 2000, *MNRAS* **312**, 398

Boissier, S. and Prantzos, N.: 2001, *MNRAS* **325**, 321

Bond, J. R., Cole, S., Efstathiou, G., and Kaiser, N.: 1991, *ApJ* **379**, 440

Bottinelli, L., Gouguenheim, L., Paturel, G., and Teerikorpi, P.: 1995, *A&A* **296**, 64

Bouwens, R. and Silk, J.: 2002, *ApJ* **568**, 522

Bouwens, R. J., Cayon, L., and Silk, J.: 1997, *ApJ* **489**, L21+

Bower, R. G.: 1991, *MNRAS* **248**, 332

Cheng, K. P., Collins, N., Angione, R., Talbert, F., Hintzen, P., Smith, E. P., Stecher, T., and The UIT Team (eds.): 1997, *Uv/visible Sky Gallery on CDROM*

Cole, S., Aragon-Salamanca, A., Frenk, C. S., Navarro, J. F., and Zepf, S. E.: 1994, *MNRAS* **271**, 781

Cole, S., Lacey, C. G., Baugh, C. M., and Frenk, C. S.: 2000, *MNRAS* **319**, 168

Couch, W. J., Barger, A. J., Smail, I., Ellis, R. S., and Sharples, R. M.: 1998, *ApJ* **497**, 188+

Courteau, S.: 1992, *PASP* **104**, 976

Courteau, S.: 1997, *AJ* **114**, 2402

Courteau, S. and Rix, H.: 1999, *ApJ* **513**, 561

Cowie, L. L., Songaila, A., Hu, E. M., and Cohen, J. G.: 1996, *AJ* **112**, 839+

Dalcanton, J. J., Spergel, D. N., and Summers, F. J.: 1997, *ApJ* **482**, 659

de Jong, R. S.: 1996a, *Journal of Astronomical Data* **2**, 1+

de Jong, R. S.: 1996b, *A&AS* **118**, 557

de Vaucouleurs, G., de Vaucouleurs, A., Corwin, J. R., Buta, R. J., Paturel, G., and Fouque, P.: 1991, in *Third reference catalogue of Bright galaxies, 1991, New York : Springer-Verlag.*, pp 0+

Dickinson, M., Papovich, C., Ferguson, H. C., and Budavári, T.: 2003, *ApJ* **587**, 25

Distefano, A., Rampazzo, R., Chincarini, G., and de Souza, R.: 1990, *A&AS* **86**, 7

Domínguez-Tenreiro, R., Tissera, P. B., and Sáiz, A.: 1998, *ApJ* **508**, L123

Drozdovsky, I. O. and Karachentsev, I. D.: 2000, *A&AS* **142**, 425

Dubinski, J. and Carlberg, R. G.: 1991, *ApJ* **378**, 496

Duval, M. F. and Monnet, G.: 1985, *A&AS* **61**, 141

Efstathiou, G., Frenk, C. S., White, S. D. M., and Davis, M.: 1988, *MNRAS* **235**, 715

Eke, V. R., Navarro, J. F., and Steinmetz, M.: 2001, *ApJ* **554**, 114

Elizondo, D., Yepes, G., Kates, R., Müller, V., and Klypin, A.: 1999, *ApJ* **515**, 525

Evrard, A. E., Summers, F. J., and Davis, M.: 1994, *ApJ* **422**, 11

Faber, S. M.: 1982, in *Astrophysical Cosmology Proceedings*, pp 191–214

Fall, S. M.: 1983, in *IAU Symp. 100: Internal Kinematics and Dynamics of Galaxies*, pp 391–398

Fall, S. M. and Efstathiou, G.: 1980, *MNRAS* **193**, 189

Ferrarese, L., Ford, H. C., Huchra, J., Kennicutt, R. C., Mould, J. R., Sakai, S., Freedman, W. L., Stetson, P. B., Madore, B. F., Gibson, B. K., Graham, J. A., Hughes, S. M., Illingworth, G. D., Kelson, D. D., Macri, L., Sebo, K., and Silbermann, N. A.: 2000, *ApJS* **128**, 431

Freedman, W. L., Madore, B. F., Gibson, B. K., Ferrarese, L., Kelson, D. D., Sakai, S., Mould, J. R., Kennicutt, R. C., Ford, H. C., Graham, J. A., Huchra, J. P., Hughes, S. M. G., Illingworth, G. D., Macri, L. M., and Stetson, P. B.: 2001, *ApJ* **553**, 47

Frei, Z., Guhathakurta, P., Gunn, J. E., and Tyson, J. A.: 1996, *AJ* **111**, 174+

Frenk, C. S., White, S. D. M., Davis, M., and Efstathiou, G.: 1988, *ApJ* **327**, 507

Fruchter, A. S., Hook, R. N., Busko, I. C., and Mutchler, M.: 1997, in *The 1997 HST Calibration Workshop with a new generation of instruments /edited by Stefano Casertano, Robert Jedrzejewski, Charles D. Keyes, and Mark Stevens. Baltimore, MD : Space Telescope Science Institute (1997) QB 500.268 C35 1997, p. 518.*, pp 518+

Gavazzi, G.: 1993, *ApJ* **419**, 469

Gioia, I. M., Maccacaro, T., Schild, R. E., Wolter, A., Stocke, J. T., Morris, S. L., and Henry, J. P.: 1990, *ApJS* **72**, 567

Giovanelli, R., Haynes, M. P., Herter, T., Vogt, N. P., da Costa, L. N., Freudling, W., Salzer, J. J., and Wegner, G.: 1997, *AJ* **113**, 53

Giuricin, G., Marinoni, C., Ceriani, L., and Pisani, A.: 2000, *ApJ* **543**, 178

Glazebrook, K., Ellis, R., Colless, M., Broadhurst, T., Allington-Smith, J., and Tanvir, N.: 1995, *MNRAS* **273**, 157

Guiderdoni, B., Hivon, E., Bouchet, F. R., and Maffei, B.: 1998, *MNRAS* **295**, 877

Han, M.: 1991, *Ph.D. Thesis*

Heavens, A. F. and Jimenez, R.: 1999, *MNRAS* **305**, 770

Helly, J. C., Cole, S., Frenk, C. S., Baugh, C. M., Benson, A., Lacey, C., and Pearce, F. R.: 2003, *MNRAS* **338**, 913

Heyl, J. S., Cole, S., Frenk, C. S., and Navarro, J. F.: 1995, *MNRAS* **274**, 755

Holmberg, E.: 1946, *Medd. Lund Obs. II* 117

Howk, J. C. and Savage, B. D.: 1999, *AJ* **117**, 2077

Karachentsev, I. D. and Sharina, M. E.: 1997, *A&A* **324**, 457

Karachentsev, I. D., Sharina, M. E., and Huchtmeier, W. K.: 2000, *A&A* **362**, 544

Kauffmann, G.: 1995a, *MNRAS* **274**, 153

Kauffmann, G.: 1995b, *MNRAS* **274**, 161

Kauffmann, G., Guiderdoni, B., and White, S. D. M.: 1994, *MNRAS* **267**, 981

Kauffmann, G., Nusser, A., and Steinmetz, M.: 1997, *MNRAS* **286**, 795

Kauffmann, G., White, S. D. M., and Guiderdoni, B.: 1993, *MNRAS* **264**, 201+

Kinney, A. L., Calzetti, D., Bohlin, R. C., McQuade, K., Storchi-Bergmann, T., and Schmitt, H. R.: 1996, *ApJ* **467**, 38+

Koo, D. C.: 2000, in *Building Galaxies; from the Primordial Universe to the Present*, pp 279–+

Kormendy, J.: 1989, *ApJ* **342**, L63

Lacey, C. and Cole, S.: 1993, *MNRAS* **262**, 627

Larsen, S. S. and Richtler, T.: 1999, *A&A* **345**, 59

Larson, R. B. and Tinsley, B. M.: 1978, *ApJ* **219**, 46

Lilly, S. J., Le Fevre, O., Crampton, D., Hammer, F., and Tresse, L.: 1995, *ApJ* **455**, 50+

Madau, P., Ferguson, H. C., Dickinson, M. E., Giavalisco, M., Steidel, C. C., and Fruchter, A.: 1996, *MNRAS* **283**, 1388

Madau, P., Pozzetti, L., and Dickinson, M.: 1998, *ApJ* **498**, 106

Mao, S., Mo, H. J., and White, S. D. M.: 1998, *MNRAS* **297**, L71

Mathewson, D. S., Ford, V. L., and Buchhorn, M.: 1992, *ApJS* **81**, 413

Milvang-Jensen, B.: 2003, *Ph.D. thesis*, University of Nottingham

Milvang-Jensen, B., Aragón-Salamanca, A., Hau, G. K. T., Jørgensen, I., and Hjorth, J.: 2003, *MNRAS* **339**, L1

Mo, H. J., Mao, S., and White, S. D. M.: 1998, *MNRAS* **295**, 319

Mo, H. J., Mao, S., and White, S. D. M.: 1999, *MNRAS* **304**, 175

Mutchler, M. and Fruchter, A.: 1997, *American Astronomical Society Meeting* **29**, 1271+

Naab, T., Burkert, A., and Hernquist, L.: 1999, *ApJ* **523**, L133

Navarro, J. F., Frenk, C. S., and White, S. D. M.: 1995, *MNRAS* **275**, 56

Navarro, J. F., Frenk, C. S., and White, S. D. M.: 1996, *ApJ* **462**, 563

Navarro, J. F., Frenk, C. S., and White, S. D. M.: 1997, *ApJ* **490**, 493

Navarro, J. F. and White, S. D. M.: 1993, *MNRAS* **265**, 271

Navarro, J. F. and White, S. D. M.: 1994, *MNRAS* **267**, 401

Pearce, F. R., Jenkins, A., Frenk, C. S., Colberg, J. M., White, S. D. M., Thomas, P. A., Couchman, H. M. P., Peacock, J. A., Efstathiou, G., and The Virgo Consortium: 1999, *ApJ* **521**, L99

Peletier, R. F. and Willner, S. P.: 1993, *ApJ* **418**, 626

Pierce, M. J. and Tully, R. B.: 1988, *ApJ* **330**, 579

Pierce, M. J. and Tully, R. B.: 1992, *ApJ* **387**, 47

Press, W. H. and Schechter, P.: 1974, *ApJ* **187**, 425

Prugniel, P., Zasov, A., Busarello, G., and Simien, F.: 1998, *A&AS* **127**, 117

Puche, D. and Carignan, C.: 1988, *AJ* **95**, 1025

Raychaudhury, S., von Braun, K., Bernstein, G. M., and Guhathakurta, P.: 1997, *AJ* **113**, 2046

Regan, M. W. and Vogel, S. N.: 1994, *ApJ* **434**, 536

Rhoads, J. E.: 1998, *AJ* **115**, 472

Samland, M. and Gerhard, O.: 2003

Schade, D., Lilly, S. J., Le Fevre, O., Hammer, F., and Crampton, D.: 1996, *ApJ* **464**, 79

Schlegel, D. J., Finkbeiner, D. P., and Davis, M.: 1998, *ApJ* **500**, 525

Schommer, R. A., Bothun, G. D., Williams, T. B., and Mould, J. R.: 1993, *AJ* **105**, 97

Silk, J.: 1997, *ApJ* **481**, 703

Simard, L., Koo, D. C., Faber, S. M., Sarajedini, V. L., Vogt, N. P., Phillips, A. C., Gebhardt, K., Illingworth, G. D., and Wu, K. L.: 1999, *ApJ* **519**, 563

Somerville, R. S. and Primack, J. R.: 1999, *MNRAS* **310**, 1087

Sommer-Larsen, J., Gelato, S., and Vedel, H.: 1999, *ApJ* **519**, 501

Spergel, D. N., Verde, L., Peiris, H. V., Komatsu, E., Nolta, M. R., Bennett, C. L., Halpern, M., Hinshaw, G., Jarosik, N., Kogut, A., Limon, M., Meyer, S. S., Page, L., Tucker, G. S., Weiland, J. L., Wollack, E., and Wright, E. L.: 2003

Steinmetz, M. and Mueller, E.: 1994, *A&A* **281**, L97

Steinmetz, M. and Navarro, J. F.: 1999, *ApJ* **513**, 555

Strauss, M. A. and Willick, J. A.: 1995, *Phys. Rep.* **261**, 271

Tissera, P. B., Lambas, D. G., and Abadi, M. G.: 1997, *MNRAS* **286**, 384

Tully, R. B. and Fisher, J. R.: 1977, *A&A* **54**, 661

Tully, R. B. and Fouque, P.: 1985, *ApJS* **58**, 67

Tully, R. B., Mould, J. R., and Aaronson, M.: 1982, *ApJ* **257**, 527

Tully, R. B. and Pierce, M. J.: 2000, *ApJ* **533**, 744

Tully, R. B., Pierce, M. J., Huang, J., Saunders, W., Verheijen, M. A. W., and Witchalls, P. L.: 1998, *AJ* **115**, 2264

Tully, R. B., Verheijen, M. A. W., Pierce, M. J., Huang, J., and Wainscoat, R. J.: 1996, *AJ* **112**, 2471+

Unsöld, A. and Baschek, B.: 1991, *Der neue Kosmos*, Springer-Verlag Berlin Heidelberg New York

van den Bosch, F. C.: 2000, *ApJ* **530**, 177

van den Bosch, F. C.: 2002, *MNRAS* **332**, 456

van den Bosch, F. C., Abel, T., Croft, R. A. C., Hernquist, L., and White, S. D. M.: 2002, *ApJ* **576**, 21

van der Kruit, P. C. and Searle, L.: 1982, *A&A* **110**, 61

van Dokkum, P. G.: 1999, *Ph.D. thesis*, Rijksuniversiteit Groningen, Kapteyn Institute for Astronomy

Verheijen, M. A. W.: 1997, *Ph.D. Thesis*

Visvanathan, N.: 1981, *Journal of Astrophysics and Astronomy* **2**, 67

Vogt, N. P.: 1999, in *ASP Conf. Ser. 193: The Hy-Redshift Universe: Galaxy Formation and Evolution at High Redshift*, pp 145–+

Vogt, N. P.: 2000, in *ASP Conf. Ser. 197: Dynamics of Galaxies: from the Early Universe to the Present*, pp 435–+

Vogt, N. P.: 2001a, in *ASP Conf. Ser. 240: Gas and Galaxy Evolution*, pp 89–+

Vogt, N. P.: 2001b, in *Deep Fields*, pp 112–+

Vogt, N. P., Forbes, D. A., Phillips, A. C., Gronwall, C., Faber, S. M., Illingworth, G. D., and Koo, D. C.: 1996, *ApJ* **465**, L15

Vogt, N. P., Herter, T., Haynes, M. P., and Courteau, S.: 1993, *ApJ* **415**, L95+

Vogt, N. P., Phillips, A. C., Faber, S. M., Gallego, J., Gronwall, C., Guzman, R., Illingworth, G. D., Koo, D. C., and Lowenthal, J. D.: 1997, *ApJ* **479**, L121

White, S. D. M. and Rees, M. J.: 1978, *MNRAS* **183**, 341

Willick, J. A.: 1991, *Ph.D. Thesis*

Willick, J. A., Courteau, S., Faber, S. M., Burstein, D., Dekel, A., and Kolatt, T.: 1996, *ApJ* **457**, 460

Willick, J. A., Strauss, M. A., Dekel, A., and Kolatt, T.: 1997, *ApJ* **486**, 629

Ziegler, B. L., Böhm, A., Fricke, K. J., Jäger, K., Nicklas, H., Bender, R., Drory, N., Gabasch, A., Saglia, R. P., Seitz, S., Heidt, J., Mehlert, D., Möllenhoff, C., Noll, S., and Sutorius, E.: 2002, *ApJ* **564**, L69

Appendix A

Statistical Tests

We discuss the distributions of several morphological and dynamical parameters of our target galaxies. We will overplot the histograms of the high and low redshift populations onto one diagram to illustrate whether there are differences in the two populations. Furthermore, we will apply several statistical tests to quantify at which level we can prove or disprove how different the two samples are. Mainly, we are interested in differences of the means and of the variances of the distributions. The T-means test, or student's T-test, and the Wilcoxon's rank-sum test (RS-test) are both sensitive to differences of the means of two distributions. Differences of the variance, i.e. the overall shape or width of the distributions, we will quantify using an F-variance test (FV-test). Finally we will apply a Kolmogorov-Smirnov test (KS-test) to check for general differences including mean and variance. All four tests will be applied to linearly and logarithmically spaced data. Since the RS- and the KS-tests are non-parametric tests the results for linear and logarithmic spacing should be the same, while depending on the dynamic range of the data the results of the parametric T- and FV-tests may be quite different. The four tests provide the user with an estimate of how probable the null-hypothesis is, i.e. that the two samples were drawn from the same global population. This probability value ranges from 0% to 100%. If the probability value p exceeds 5% we assume that at the 5% percent level the two distributions are equal, if p lies below 5% we reject the null-hypothesis and assume any measured differences to be real. Or in other words, $p > 5\%$ means both samples were drawn from the same population, at $p < 1\%$ the samples are significantly different, and at $1\% < p < 5\%$ the samples are marginally different.

These tests should reveal obvious differences between the two populations. However, since we have only a relatively limited number of sources in both samples, the statistical tests may fail in cases of broad distributions. The reason for this is, that broad distributions have a very low peak signal compared to a narrow distribution with the same sample size. The weaker the signal in one bin of a histogram gets, the more sensitive it gets to noise and outliers. Therefore, in the cases of histograms with small variances the means-tests will be much more sensitive as in the cases of histograms with large variances.

We will simulate two data sets in two variables to examine the performance of the various statistical tests. We will assume two data samples L and H of which two quantities, x and y, are to be measured. Sample L shall consist of 40 objects while sample H will contain 20 targets, similar to our low and high redshift galaxy samples. One of those two quantities, say x, shall have the same distribution for both samples, e.g. by selection. We will simulate 1000 realisations of each sample in each variable (L_x, L_y, H_x, and H_y) with exactly specified properties (see Tab. A.1). The random Gaussian distributions L_x and H_x will have slightly different means and variances ($\langle L_x \rangle = 19$ / $\langle H_x \rangle = 20$ and $\sigma(L_x) = 5$ / $\sigma(H_x) = 5.5$), which will resemble the remaining differences even after selection in the case of the real data. A single sample shows a similar visual appearance as the real data (see Fig. A.1), while a sum of all 1000 realisations displays the overall Gaussian nature of the random numbers and their means and widths quite nicely (see Fig. A.2). The second quantity y shall be related to the first variable x to form a linear dependence between

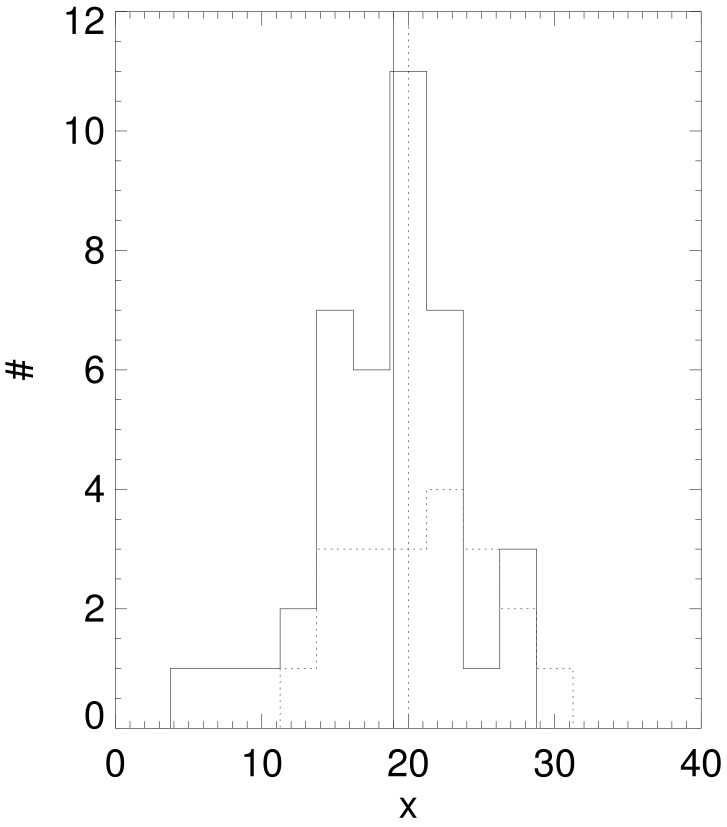

Figure A.1: Random Gaussian distribution of variable x

Histograms of the random Gaussian distributions L_x (solid line) and H_x (dotted line). The vertical lines represent the expected mean values of the two distributions (L_x: solid, H_x: dotted). L_x and H_x consist of 40 and 20 elements, respectively.

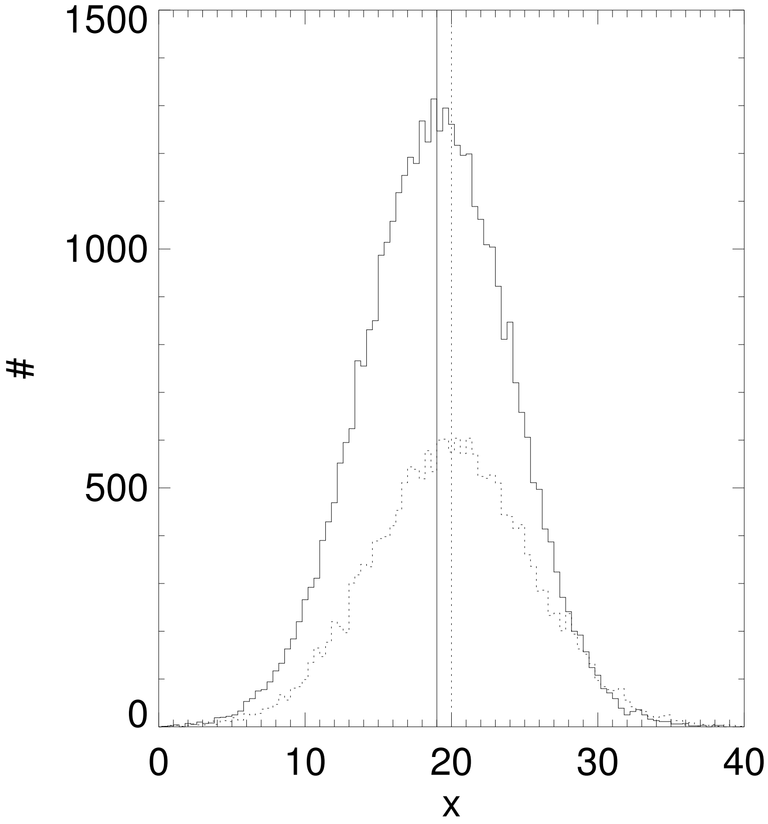

Figure A.2: Sum of 1000 random Gaussian distributions of variable x

Histograms of the sums of 1000 realisations of the random Gaussian distributions L_x (solid line) and H_x (dotted line). The vertical lines represent the expected mean values of the two distributions (L_x: solid, H_x: dotted). The total distributions L_x and H_x consist of 40000 and 20000 elements, respectively.

the two:

$$y_i = 0.263 \cdot x_i + G_i \tag{A.1}$$

Each y_i consists of a scaled value x_i plus a random value G_i shifted by 1 (see Fig. A.3 and Fig. A.4). All G_i form a Gaussian distribution with a width $\sigma(G_i) = 0.8$ and a mean $\langle G_i \rangle = 0$ in the case of L_y and $\langle G_i \rangle = -0.76$ in the case of H_y. As a result of this the second variable y also shows a Gaussian distribution with the means $\langle L_y \rangle = 5$ / $\langle H_y \rangle = 4.5$ and widths $\sigma(L_y) = 0.8$ / $\sigma(H_y) = 0.8$ (see Fig. A.5 and Fig. A.6).

Table A.1: Random Distributions

	L_x	L_y	H_x	H_y	$G_i(L_y)$	$G_i(H_y)$
mean	19	5	20	4.5	0	-0.76
σ	5	0.8	5.5	0.8	0.8	0.8

Note. – Mean and σ values for the various statistical distributions used in this analysis.

Now we will apply the four aforementioned tests to quantify whether the means and/or variances of the two samples L_x and H_x are different. Although we find a peak in the probability distributions of T- and RS-tests (see Fig. A.7 and Fig. A.8) below 5% the majority of all measurements (88% and 81%, respectively) exceed the 5% limit, thus indicating that randomly picked samples L_x and H_x would probably have the same means. The most likely probability values for T- and RS-tests would be 42% and 22%, respectively. The FV-test does not show the peak at low probabilities (see Fig. A.9). All values from 0% to 100% are roughly evenly distributed. There is but a slight trend of increasing numbers towards small values left. More than 92% of all simulated samples had FV-probability values exceeding 5%, the mean of all probability values was 44%. The KS-test shows similar results as the variance test. More than 91% of all measurements had KS-probabilities $p > 5\%$ with a mean $\langle p \rangle = 47\%$. The KS-statistic has a rather peculiar distribution, though. Individual values are not evenly distributed, but certain values seem to be preferred while others are never measured (see Fig. A.10).

The same assessment for the second variable y delivers similar results. The probability distributions of T- and RS-tests show a peak below 5%, but the majority of all measurements results in values > 5% (80% and 71%, respectively, see Fig. A.11 and Fig. A.12). The mean values for a T- and a RS-test are 34% and 17%, respectively. Furthermore, the FV-test does not show a peak at low probability values, but only a slight trend of increasing numbers towards 0% (see Fig. A.13). More than 93% of all values exceed 5%, resulting in an expected mean value of 47%. The KS-test is again distributed amongst several discrete values with more than 86% beyond 5% and a mean value of $\langle p \rangle = 38\%$ (see Fig. A.14).

To summarise, we find from evaluating the statistical tests that the two samples L and H are indistinguishable from each other in both variables x and y. For L_x and H_x this was expected, since by selection those two samples were roughly constructed to show the same mean values. However, the offset of the mean in L_y and H_y could not be confirmed. It seems that the tests can not distinguish between small differences of the mean values of two distributions in cases when the difference is small compared to the width of the distribution. In such a case a 2-dimensional plot might help to remove the ambiguity. However, prerequisite for this is that a correlation exists between the two variables x and y. Since y was constructed to depend linearly on x the 2-dimensional plot (see Fig. A.3 and Fig. A.4) reveals an offset between the two variables. We will now recast the question of whether L_y and H_y are significantly different slightly. Instead we will ask whether for a *fixed* value of x the expected values of $L_y(x)$ and $H_y(x)$ differ significantly. To recover the offset between $L_y(x)$ and $H_y(x)$ we assume that both samples follow the same functional form, in our case eq. A.1. We fit L_y and H_y and subtract the fit, thus enabling comparison of $L_y(x)$ and $H_y(x)$ at the same x-value. This is equivalent to examining only an infinitesimal portion of the

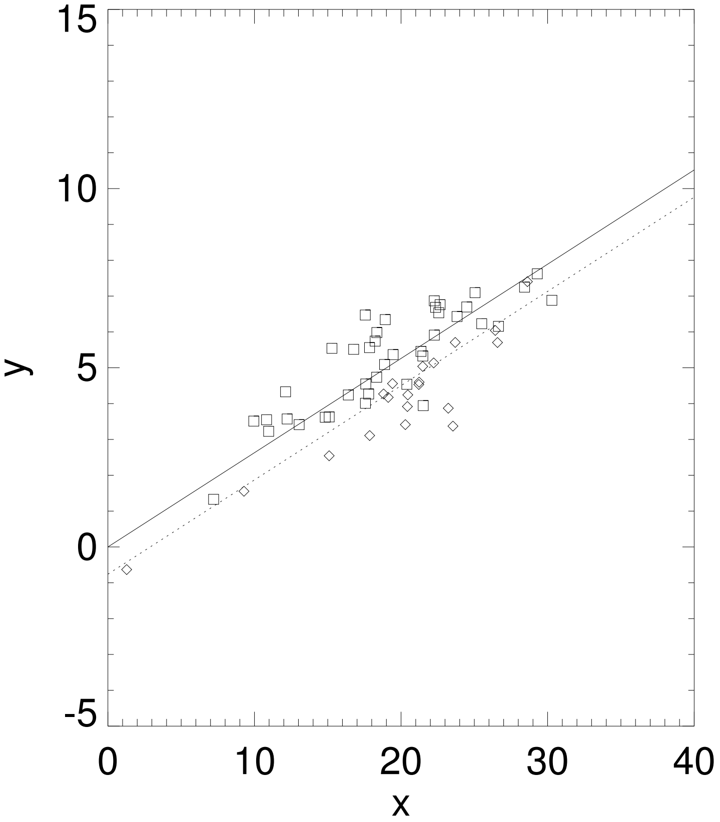

Figure A.3: Random variable y versus x

Plot of the Gaussian distributions L_x (boxes) and H_x (diamonds) versus L_y and H_y. The lines represent the expected mean relations of the two distributions (L_x: solid, H_x: dotted). $L_{x/y}$ and $H_{x/y}$ consist of 40 and 20 elements, respectively.

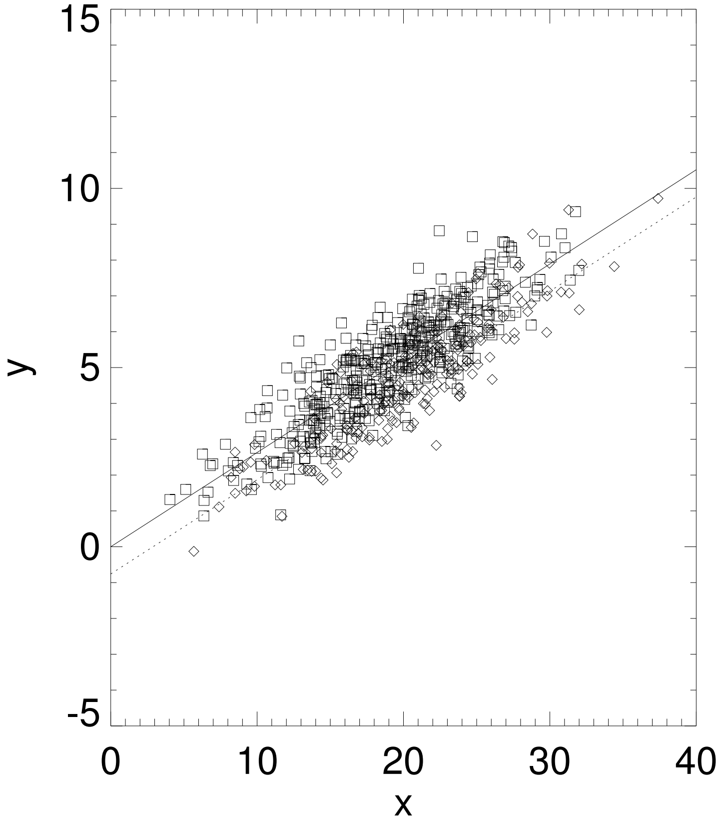

Figure A.4: Sum of 10 random distributions of variable y versus x

The same plot of L_x, H_x versus L_y, H_y for 10 times the number of object as in plot Fig. A.3.

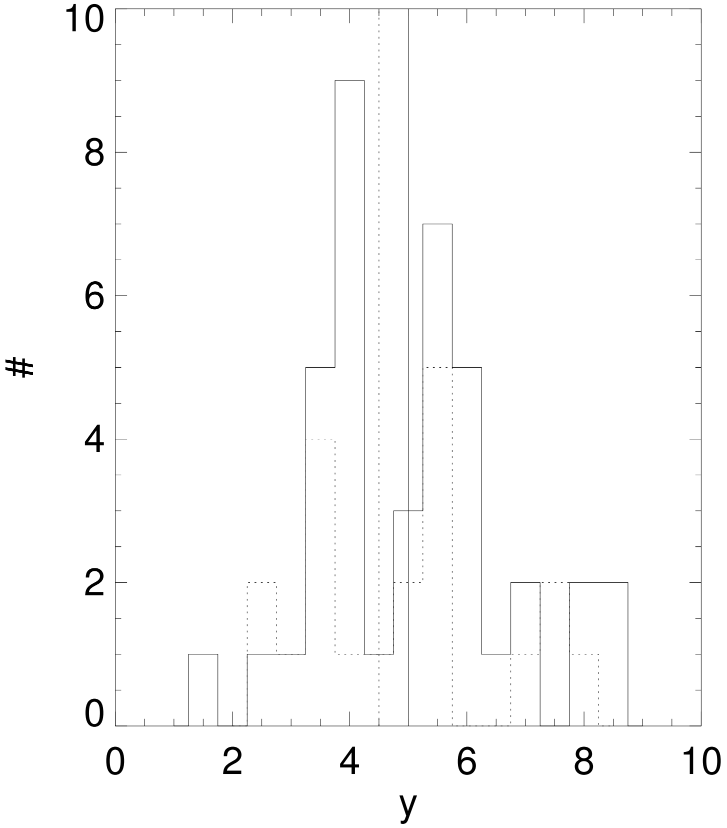

Figure A.5: Random Gaussian distribution of variable y

Histograms of the random Gaussian distributions L_y (solid line) and H_y (dotted line). The vertical lines represent the expected mean values of the two distributions (L_y: solid, H_y: dotted). L_y and H_y consist of 40 and 20 elements, respectively.

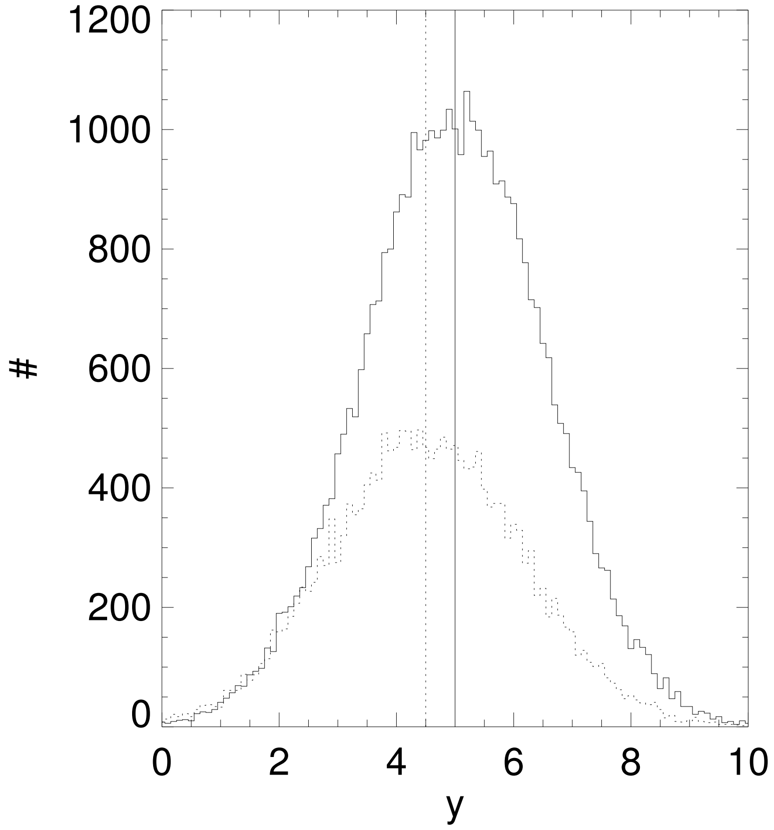

Figure A.6: Sum of 1000 random Gaussian distributions of variable y

Histograms of the sums of 1000 realisations of the random Gaussian distributions L_y (solid line) and H_y (dotted line). The vertical lines represent the expected mean values of the two distributions (L_y: solid, H_y: dotted). The total distributions L_y and H_y consist of 40000 and 20000 elements, respectively.

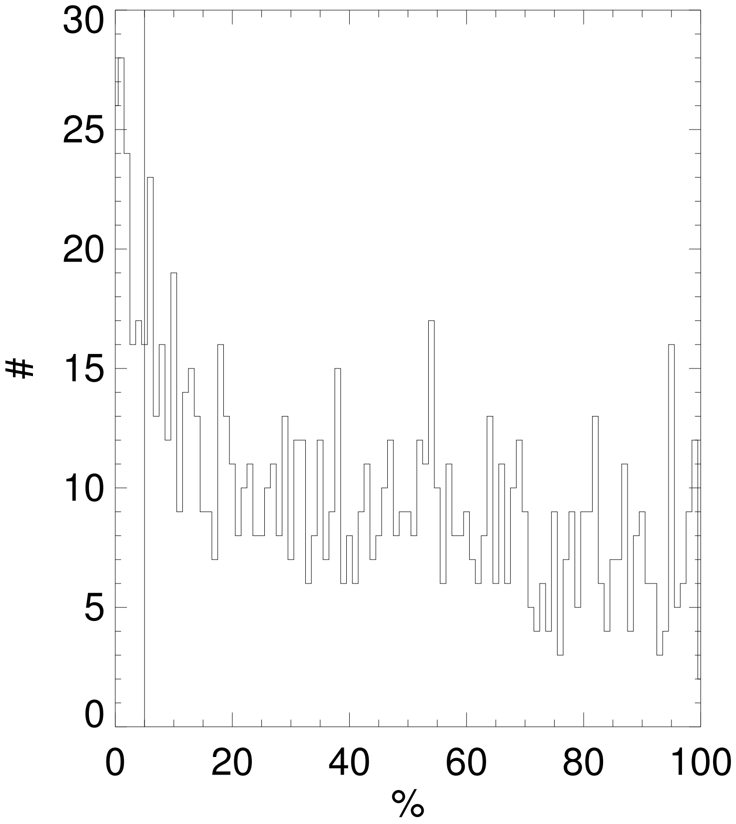

Figure A.7: T-test probability distribution of L_x and H_x

Histogram of T-tests to each of the 1000 realisations of L_x and H_x (40 and 20 elements, respectively). Although we find a peak in the distribution at values stating that the two data sets are different (below 5%, vertical line) the majority of all tests indicate that the two are the same. Therefore, a random measurement would probably have a value exceeding 5%.

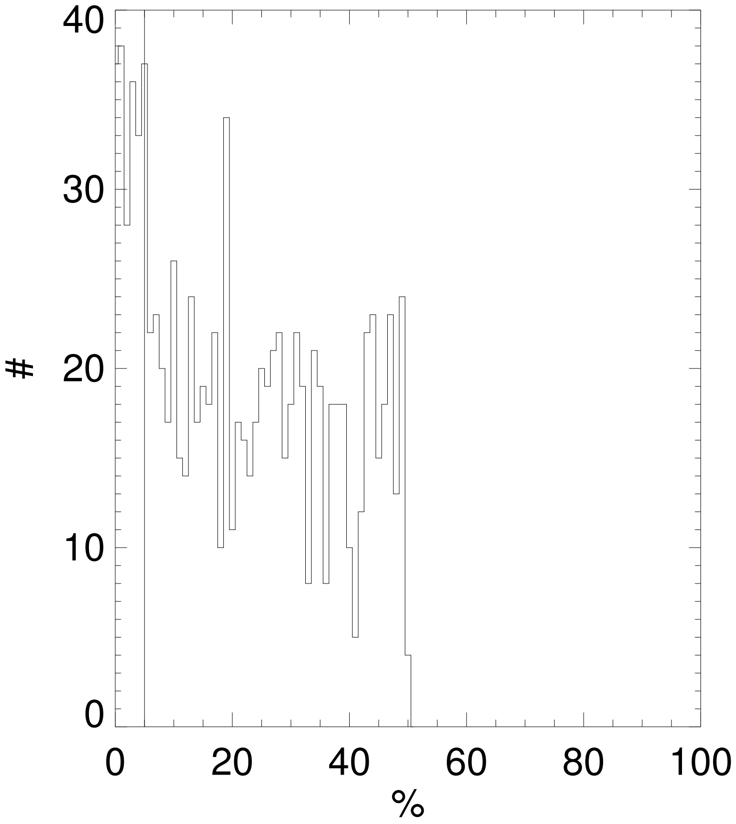

Figure A.8: RS-test probability distribution of L_x and H_x

Similar histogram as Fig. A.7, but for an RS-test. Again, we find a peak in the distribution at low values stating that the two data sets are different (below 5%, vertical line). However, the majority of all tests indicate that the two are the same and a random measurement would therefore probably have a value exceeding 5%.

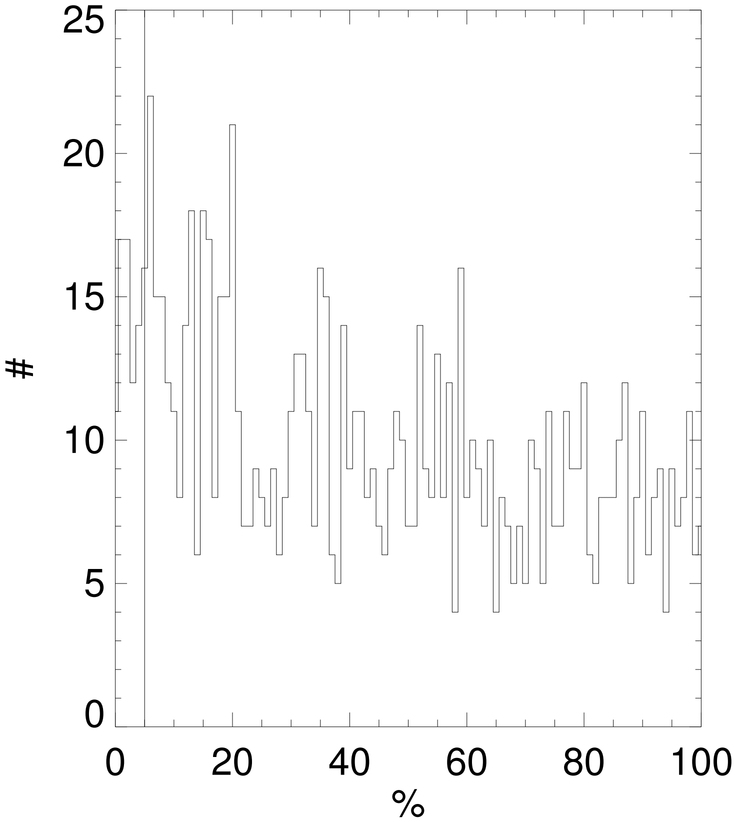

Figure A.9: FV-test probability distribution of L_x and H_x

Histogram of FV-tests similar to Fig. A.7. There is almost no peak in the distribution at low values stating that the two data sets are different (below 5%, vertical line). The majority of all tests indicate that the two distributions are the same and a random measurement would again probably have a value exceeding 5%.

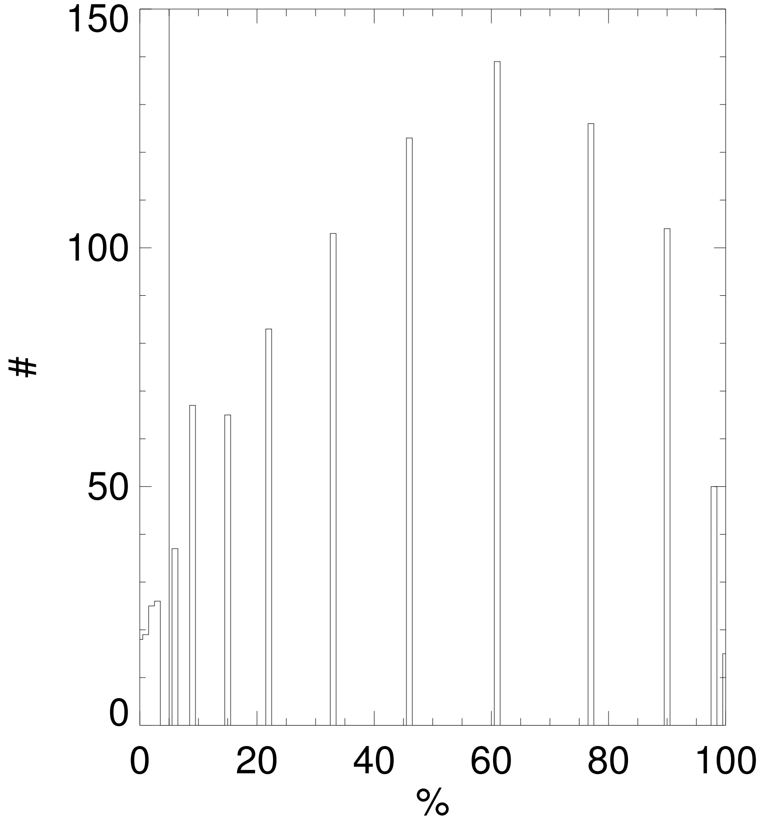

Figure A.10: KS-test probability distribution of L_x and H_x

A histogram of KS-tests for L_x and H_x (see Fig. A.7). The test results are highly concentrated to certain values. The overall distribution of test results peaks at extremely high values. Thus, a random measurement would probably indicate that the two samples are the same.

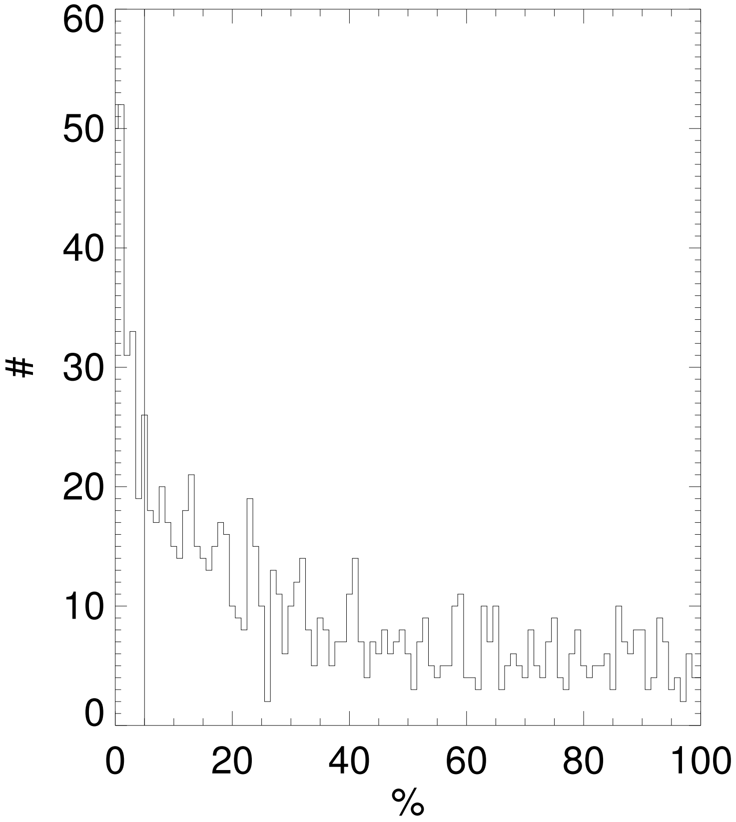

Figure A.11: T-test probability distribution of L_y and H_y

Similar histogram as Fig. A.7, no for L_y and H_y. We find a peak in the distribution at low values stating that the two data sets are different (below 5%, vertical line), even stronger than in the case of Fig. A.7. However, the majority of all tests still has a value exceeding 5%, thus, indicating that the two distributions are the same. A random measurement would therefore probably have a value exceeding 5%.

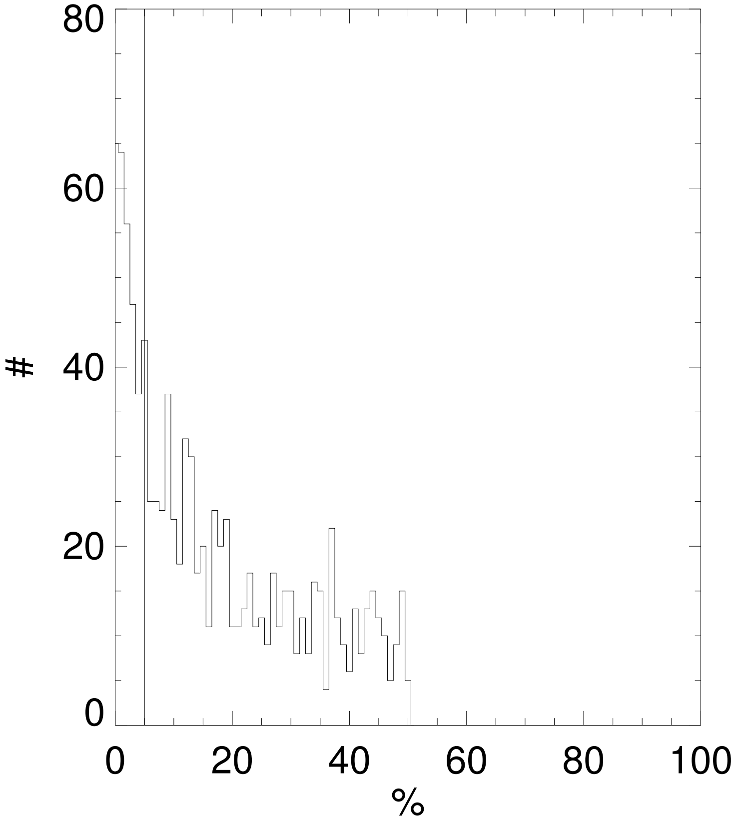

Figure A.12: RS-test probability distribution of L_y and H_y

Same histogram as Fig. A.11, but for the RS-test. The peak in the distribution at low values stating that the two data sets are different (below 5%, vertical line) does not make up for the majority of all tests. Therefore, a random measurement would have a value exceeding 5%.

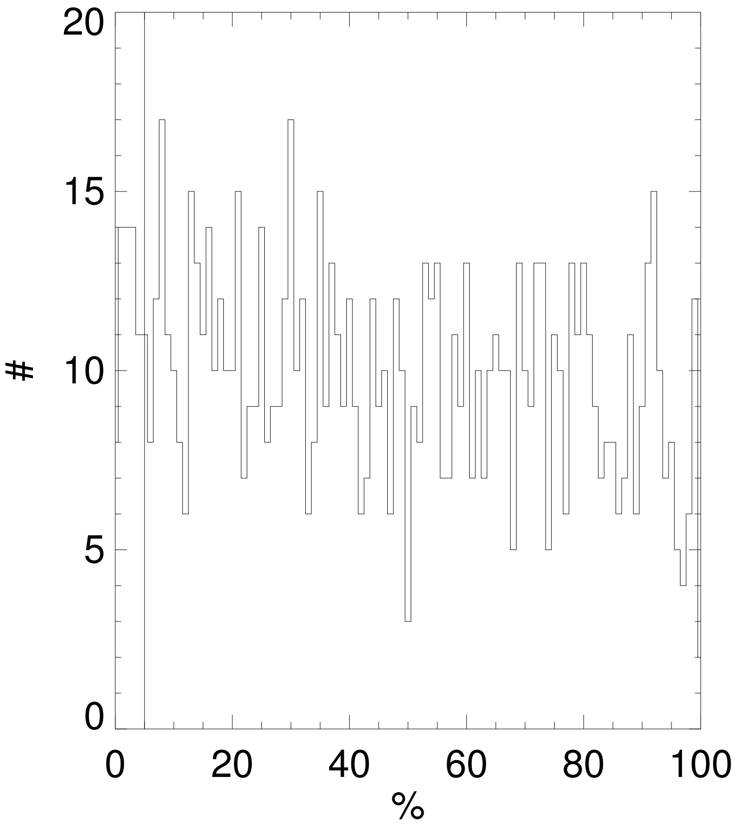

Figure A.13: FV-test probability distribution of L_y and H_y

Same histogram as Fig. A.11, but for the FV-test. We find an almost flat distribution of test outcomes. Therefore, a random measurement would have a value exceeding 5% (vertical line)

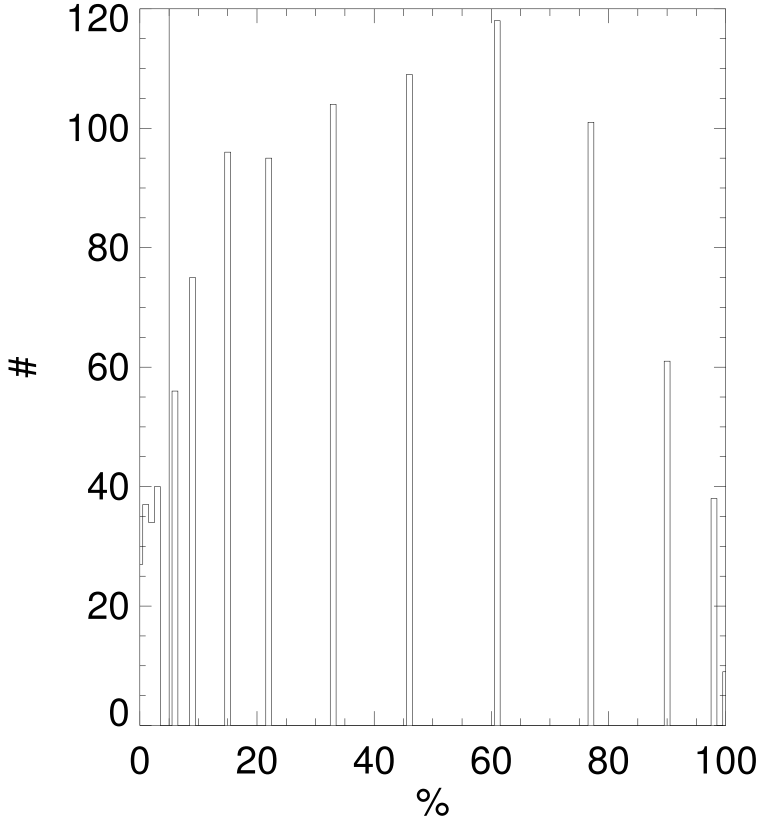

Figure A.14: KS-test probability distribution of L_y and H_y

The histogram of KS-test result similar as Fig. A.11. Again we find a discrete distribution of values that peaks at high values. Therefore, a random measurement would have a value exceeding 5% (vertical line).

data on the x-axis and still maintaining information about the hypothetical value of a member of the other sample at the same x-position. Subtracting the fit from the two samples will conserve the intrinsic scatter of the variable y at a specific value of the variable x.

Now we will repeat the same statistical tests again on the "reduced" data. As expected from the correlation of x and y, the T- and RS-tests clearly reject the trivial result. Only 7.2% and 4.5% of all measurements for the T- and RS-test, respectively, exceed the 5%-level that would result in the two distributions being equal (see Fig. A.15 and Fig. A.16). The expected mean probability value for both tests is 2% and 1%, respectively. At the same time the FV-test results do not change (see Fig. A.17). More than 95% of the values are above 5%, the mean probability value is $\langle p \rangle = 51\%$. Therefore, as expected, the shape parameter is not influenced by the procedure of subtracting a fit. Finally, the KS-test also confirms the T- and RS-test (see Fig. A.18). Here, 17.8% of the probability values lie beyond 5%, not enough to shift the mean value $\langle p \rangle = 4\%$ above 5%.

Therefore, we conclude that the statistical tests cannot distinguish between two distributions if the widths of the two are much larger than their offset. However, in cases where the variable in question is related to another variable, which is the same for both samples, by e.g. selection, it is possible to enhance the sensitivity of the tests by subtracting a fit of the data from both samples. It has to be stressed that this procedure will only produce meaningful results when a correlation exists between the two variables, though. Furthermore, the statistical problem gets re-phrased slightly in the process. As a result of this during our discussion we focus on the relation of our two samples amongst each other and especially on how the properties of objects of the same isophotal size change, and refrain from questions how the general high redshift population evolves. This would be extremely dangerous also from the point of very small number statistics. Nevertheless, the existence of a correlation between two variables may be the only way to discriminate between small intrinsic differences of two samples. Furthermore, this theoretical example shows that with samples of only a few tens of members the statistical tests are pushed to their limits and only small changes of a few sources more or less may already impact on the outcome of the tests. We will therefore only use them as an indicator and stick to general sample mean values and estimated measurement errors to confirm the existence of differences between our samples.

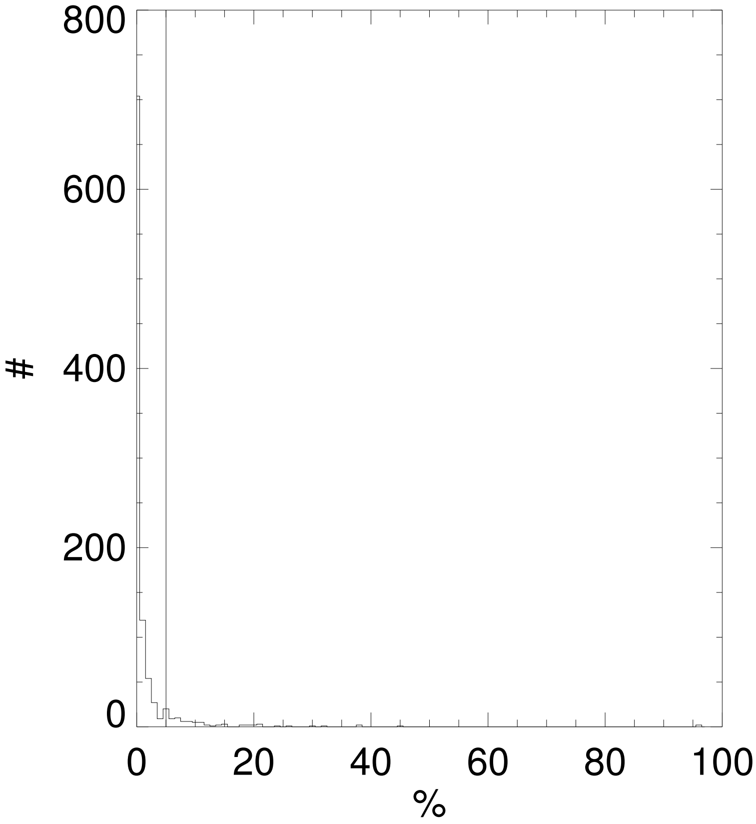

Figure A.15: T-test probability distribution of the “reduced” L_y and H_y

Similar histogram as Fig. A.11, but now after subtracting a fit to the data, thus, effectivly compressing the range of y-values. In contrast to the previous tests now almost all measurements are below 5% (vertical line), indicating that the two samples are different. Therefore, we can enhance the “sensitivty” of the test in the case of correlated variables.

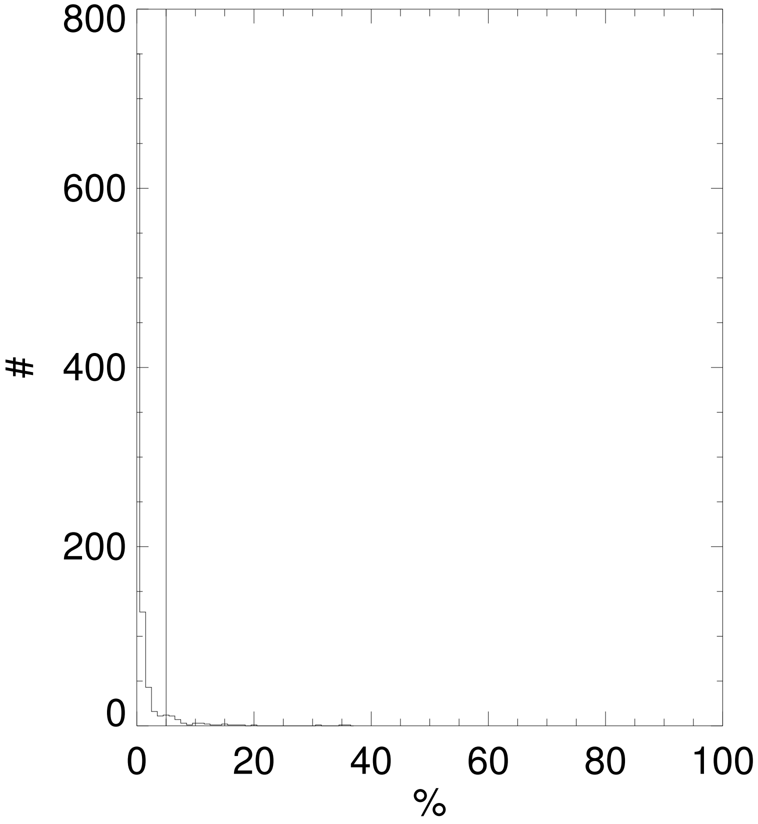

Figure A.16: RS-test probability distribution of the “reduced” L_y and H_y

We get the same result as in Fig. A.15 also for the RS-test. Again, almost all measurements are below 5% (vertical line). Therefore, a random measurement would indicate that the two samples are different.

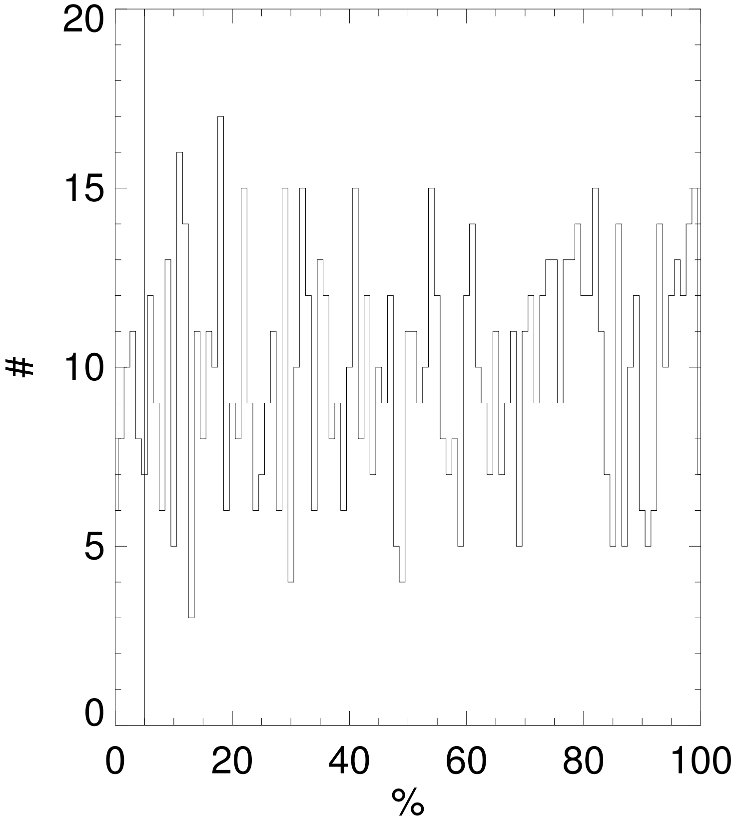

Figure A.17: FV-test probability distribution of the “reduced” L_y and H_y

The same histogram as in Fig. A.15 now for the FV-test. This plot is very similar to Fig. A.13. There, is no peak at values below 5% (vertical line). Therefore the variances of the samples are indeed the same, just as expected.

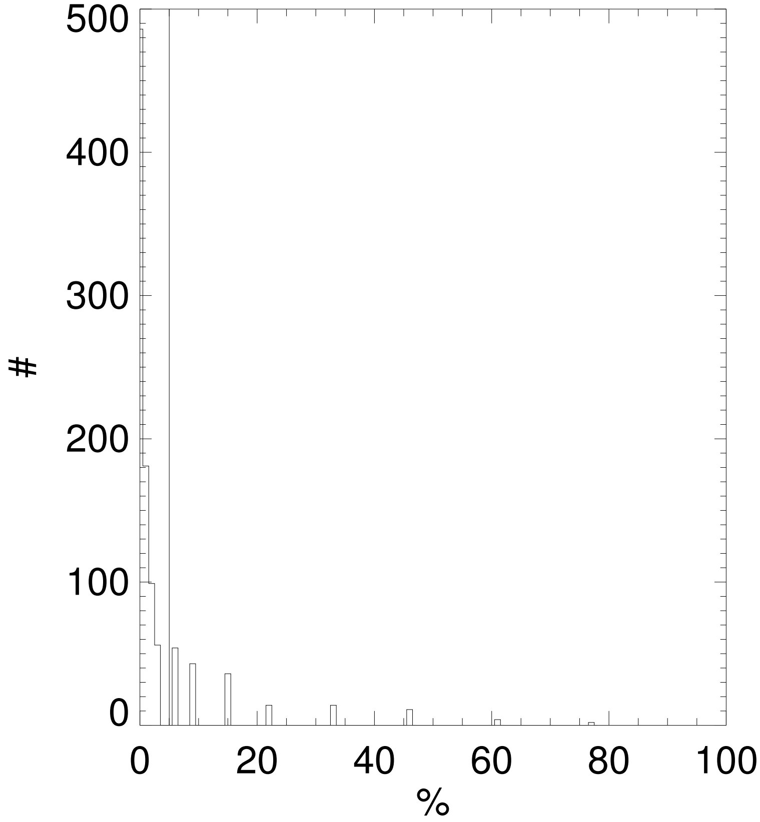

Figure A.18: KS-test probability distribution of the “reduced” L_y and H_y

The distribution of KS-values (see also Fig. A.14) after including the fit. Again, almost all measurements are below 5% (vertical line). A random measurement would indicate that the two samples are different.

Appendix B

Bulge-to-Disc Ratios

To estimate the impact of bulges on our data we define the bulge-to-disc ratio as the ratio of the bulge to the total luminosity of the object B/T in the rest-frame B-band:

$$B/T = \frac{L_b}{L_b + L_d} \tag{B.1}$$

with the bulge and disc luminosities $L_b = 7.22\pi R_b^2 \Sigma_{0,b}^{rest}$ and $L_d = 2\pi R_d^2 \Sigma_{0,d}^{rest}$, respectively. We do not find significant trends of any of our derived variables with bulge-to-disc ratio (see Fig. B.1, B.2, B.3, B.4, B.5, B.6, B.7).

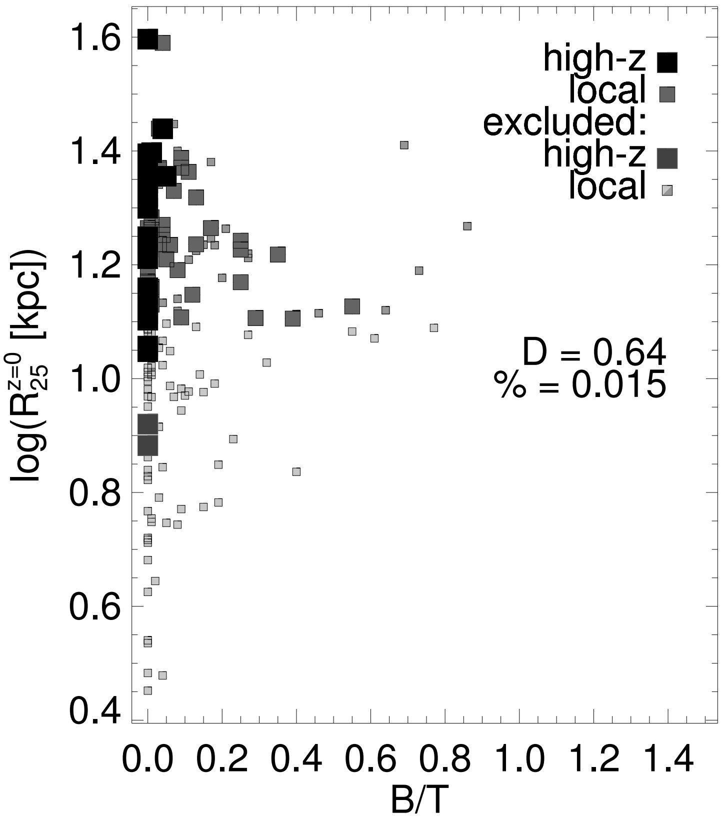

Figure B.1: R_{25} as a function of B/T

The isophotal radius R_{25} versus the bulge-to-disc ratio B/T for high redshift (large symbols) and local galaxies (small symbols). Symbols are the same as in Fig. 4.4. We do not observe significant trends with increasing bulge-to-disc ratio.

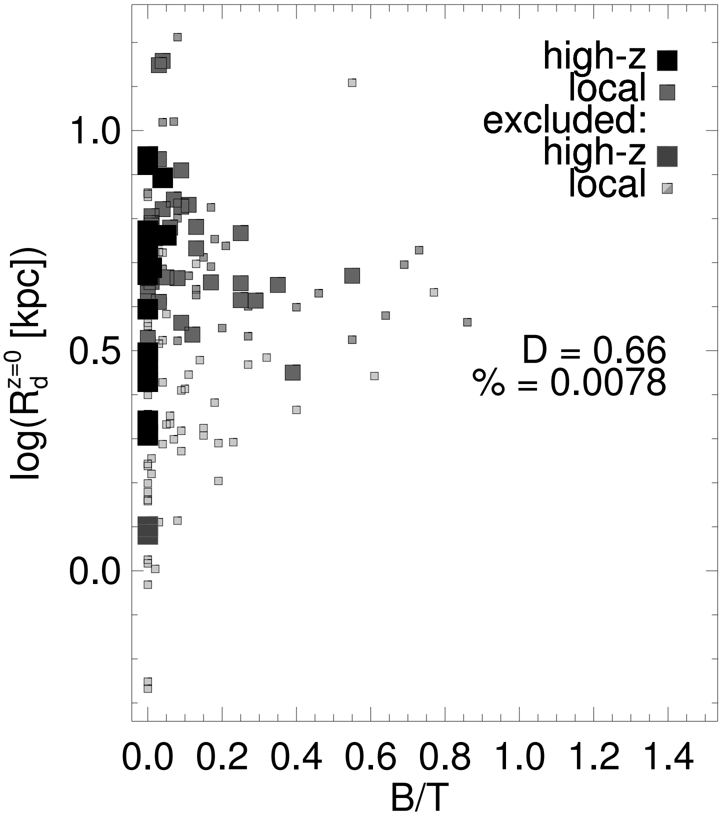

Figure B.2: R_d as a function of B/T

The disc scale length R_d versus the bulge-to-disc ratio B/T for high redshift (large symbols) and local galaxies (small symbols). Symbols are the same as in Fig. 4.4. We do not observe significant trends with increasing bulge-to-disc ratio.

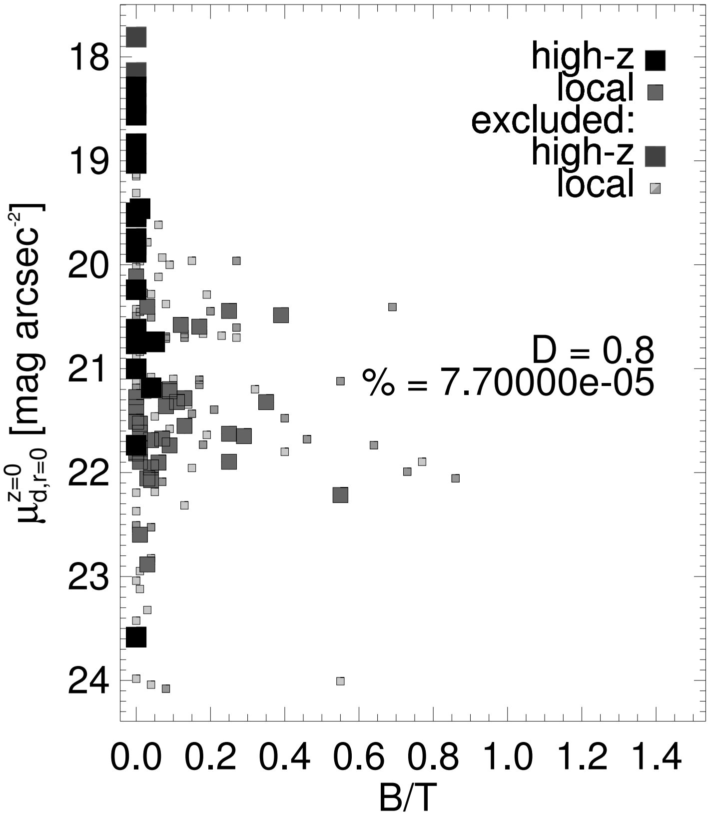

Figure B.3: μ_d as a function of B/T

The central surface brightness μ_d versus the bulge-to-disc ratio B/T for high redshift (large symbols) and local galaxies (small symbols). Symbols are the same as in Fig. 4.4. We do not observe significant trends with increasing bulge-to-disc ratio.

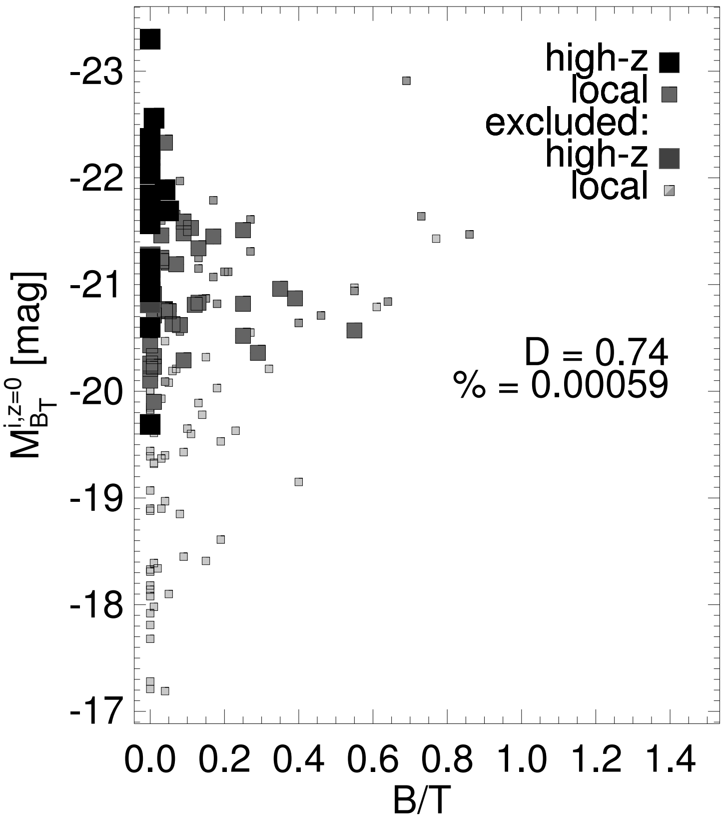

Figure B.4: M_B as a function of B/T

The absolute magnitude M_B versus the bulge-to-disc ratio B/T for high redshift (large symbols) and local galaxies (small symbols). Symbols are the same as in Fig. 4.4. We do not observe significant trends with increasing bulge-to-disc ratio.

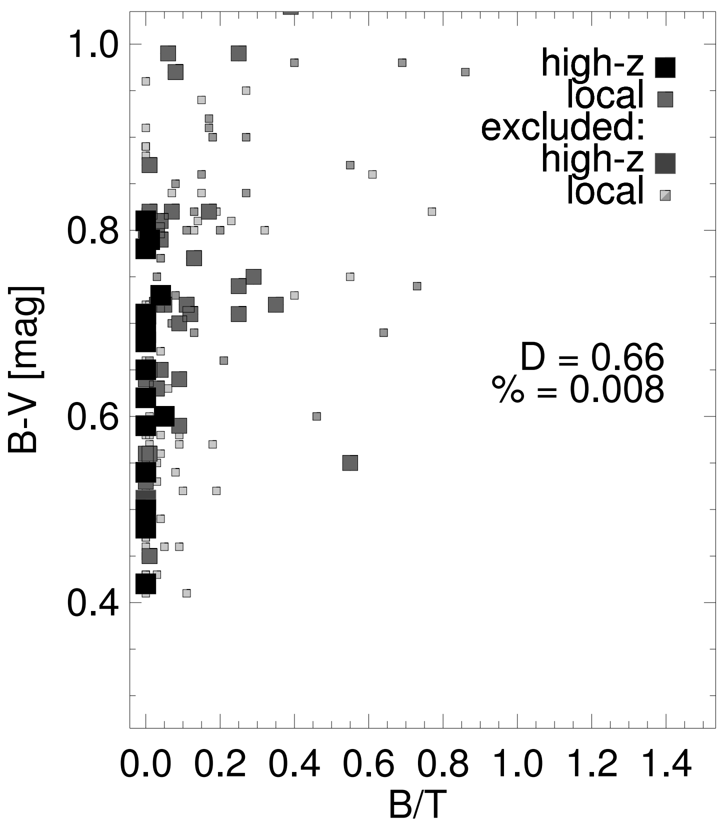

Figure B.5: B-V as a function of B/T

The rest-frame B-V colour versus the bulge-to-disc ratio B/T for high redshift (large symbols) and local galaxies (small symbols). Symbols are the same as in Fig. 4.4. We do not observe significant trends with increasing bulge-to-disc ratio.

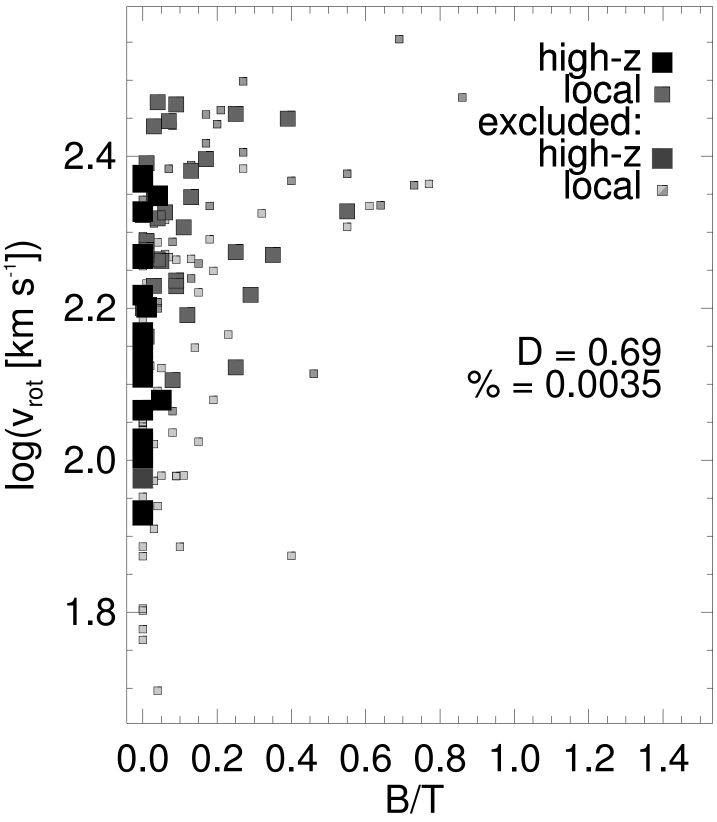

Figure B.6: v_{rot} as a function of B/T

The rotation velocity v_{rot} versus the bulge-to-disc ratio B/T for high redshift (large symbols) and local galaxies (small symbols). Symbols are the same as in Fig. 4.4. We do not observe significant trends with increasing bulge-to-disc ratio.

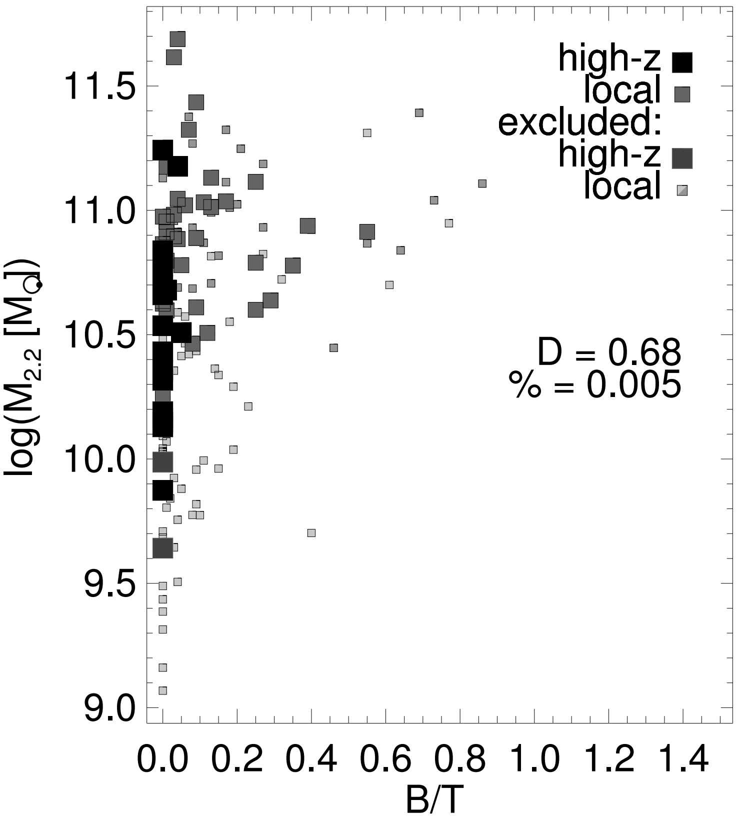

Figure B.7: $M_{2.2}$ as a function of B/T

The dynamical mass $M_{2.2}$ versus the bulge-to-disc ratio B/T for high redshift (large symbols) and local galaxies (small symbols). Symbols are the same as in Fig. 4.4. We do not observe significant trends with increasing bulge-to-disc ratio.

Appendix C

The Atlas

Here we present the rotation curves and light profile fits for our galaxies. Figure C.1 and Fig. C.2 show the "calibration" data for high and low redshift galaxies, respectively. In the case of the local galaxies these plots demonstrate at which limiting surface brightness μ_{lim} we chose to chop the light profile to read of our adopted values for disc scale length R_d, disc central surface brightness μ_d, bulge scale length R_b, bulge central surface brightness μ_b and inclination i; in the case of the high redshift galaxies the plots demonstrate the stabilising effect of using information obtained from measuring the light profile at different radii. In the next two figures (Fig. C.3 and Fig. C.4) we present the light profiles of the local and distant galaxies. For the local sample we mark the adopted surface brightness cut μ_{lim} and resulting limiting radius R_{lim}. Finally, we display the rotation curves and adopted rotation curve models for our high redshift galaxy sample (Fig. C.5). In those plots we also indicate disc scale lengths R_d and limiting radii R_{lim}. In the cases of CSH96-74 and CFRS-03.1284 our fitting algorithm failed and we obtained values for the rotation speed from a 1-dimensional line profile. Figure C.6 shows the spectrum of CFRS-00.0137. This was the only galaxy without any discernible spatial structure. In this case we did not even attempt to fit a 2-dimensional rotation curve.

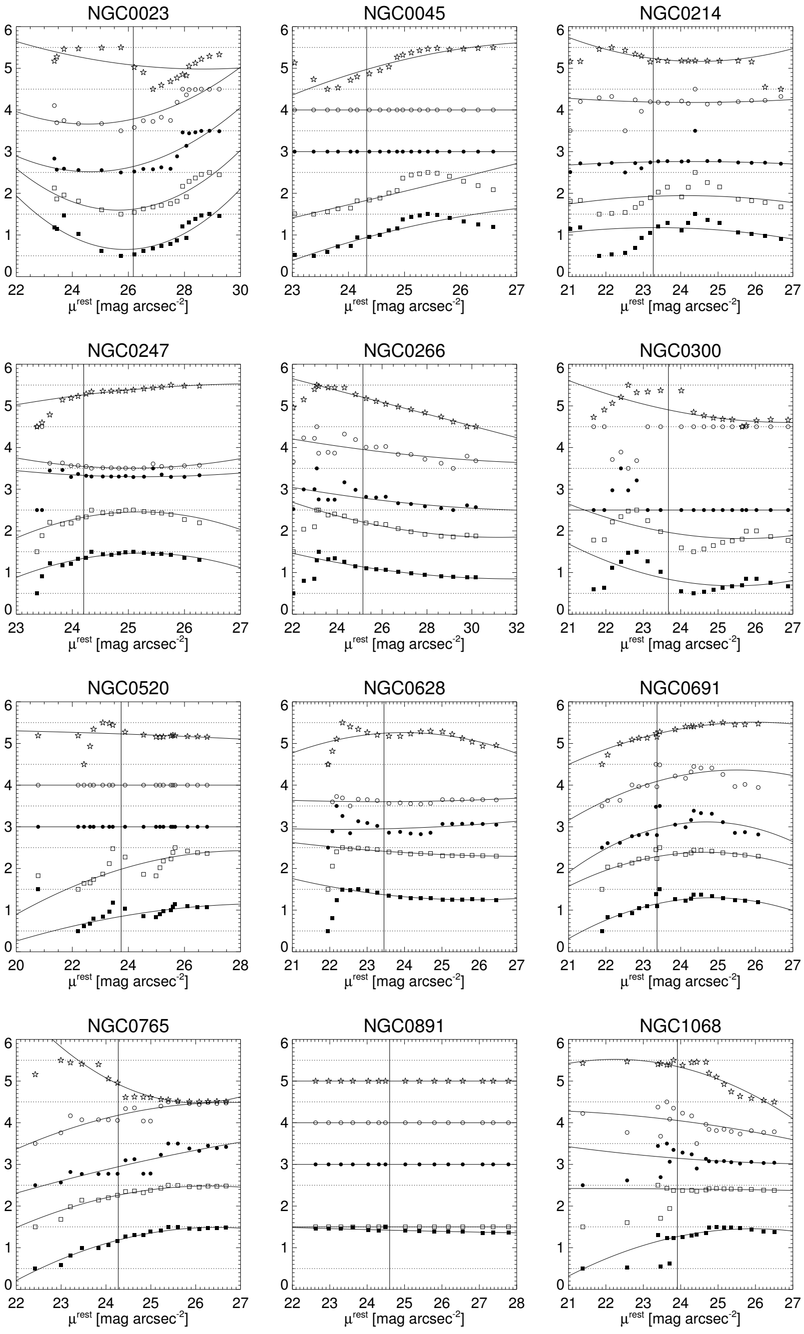

Figure C.1: Calibration for local galaxies

Resulting disc scale length (filled boxes), central disc surface brightness (open boxes), bulge scale length (filled circles), central bulge surface brightness (open circles) and inclination (open stars) as a function of limiting surface brightness (horizontal axis). The vertical axis is in arbitrary units. The adopted values are taken at the intersection of the quadratic fit (thin solid lines) with the thick vertical line.

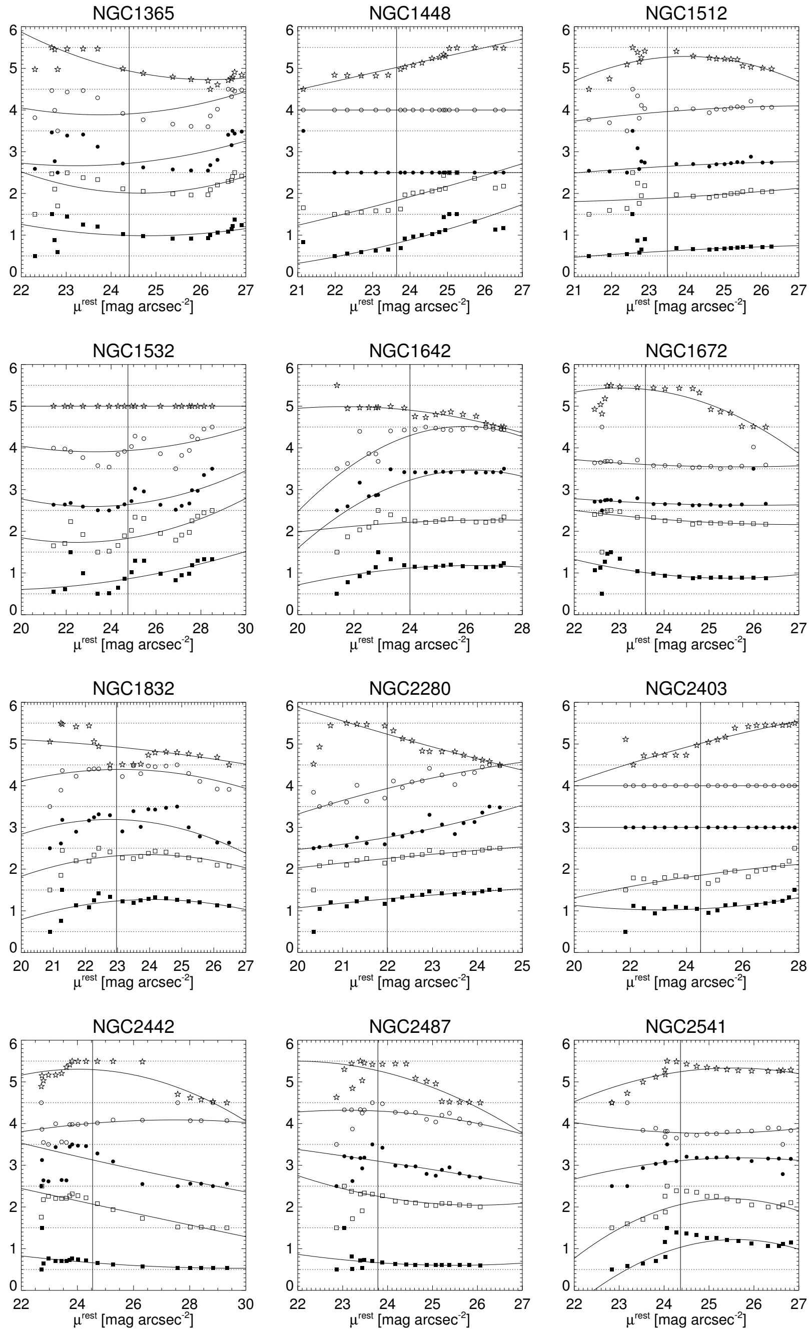

Figure C.1: Calibration for local galaxies

Resulting disc scale length (filled boxes), central disc surface brightness (open boxes), bulge scale length (filled circles), central bulge surface brightness (open circles) and inclination (open stars) as a function of limiting surface brightness (horizontal axis). The vertical axis is in arbitrary units. The adopted values are taken at the intersection of the quadratic fit (thin solid lines) with the thick vertical line.

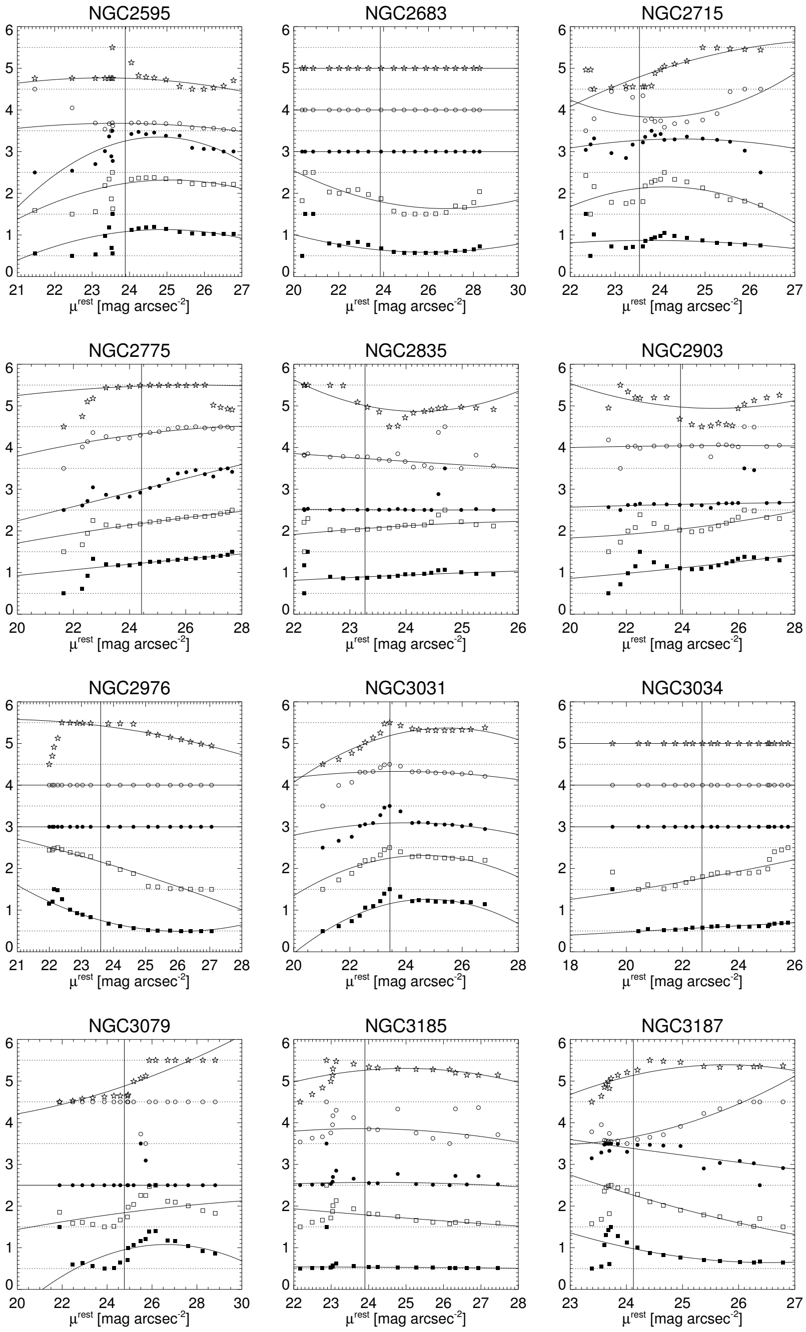

Figure C.1: Calibration for local galaxies

Resulting disc scale length (filled boxes), central disc surface brightness (open boxes), bulge scale length (filled circles), central bulge surface brightness (open circles) and inclination (open stars) as a function of limiting surface brightness (horizontal axis). The vertical axis is in arbitrary units. The adopted values are taken at the intersection of the quadratic fit (thin solid lines) with the thick vertical line.

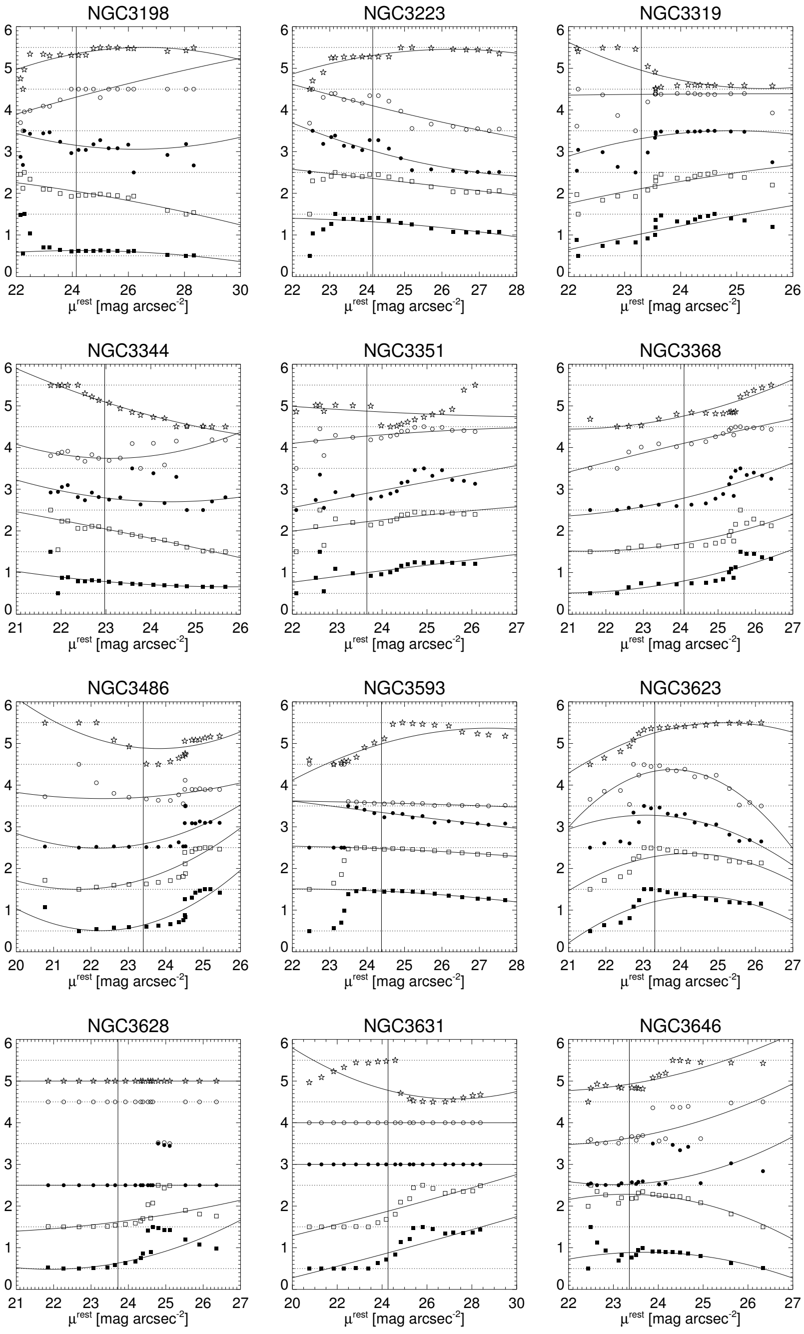
NGC3198 NGC3223 NGC3319 NGC3344 NGC3351 NGC3368 NGC3486 NGC3593 NGC3623 NGC3628 NGC3631 NGC3646

Figure C.1: Calibration for local galaxies

Resulting disc scale length (filled boxes), central disc surface brightness (open boxes), bulge scale length (filled circles), central bulge surface brightness (open circles) and inclination (open stars) as a function of limiting surface brightness (horizontal axis). The vertical axis is in arbitrary units. The adopted values are taken at the intersection of the quadratic fit (thin solid lines) with the thick vertical line.

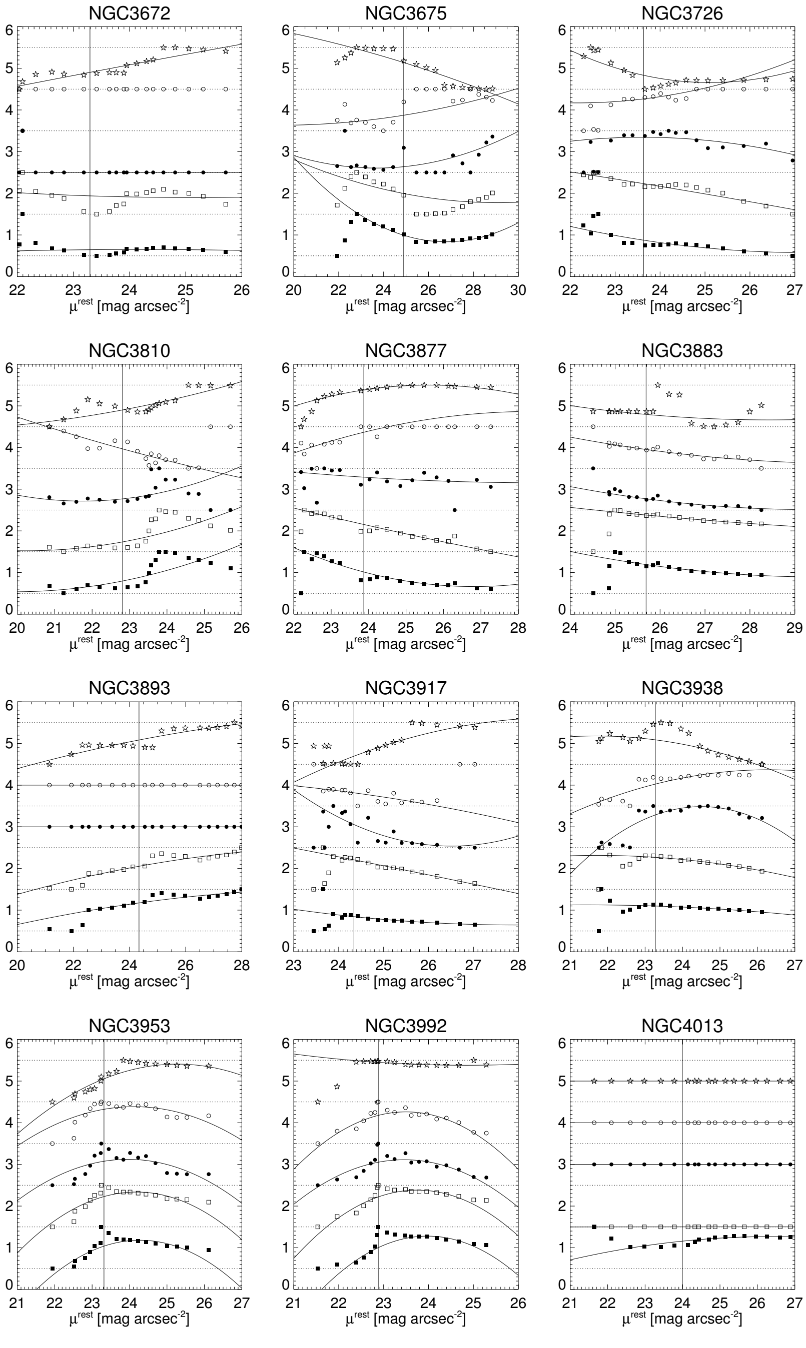

Figure C.1: Calibration for local galaxies

Resulting disc scale length (filled boxes), central disc surface brightness (open boxes), bulge scale length (filled circles), central bulge surface brightness (open circles) and inclination (open stars) as a function of limiting surface brightness (horizontal axis). The vertical axis is in arbitrary units. The adopted values are taken at the intersection of the quadratic fit (thin solid lines) with the thick vertical line.

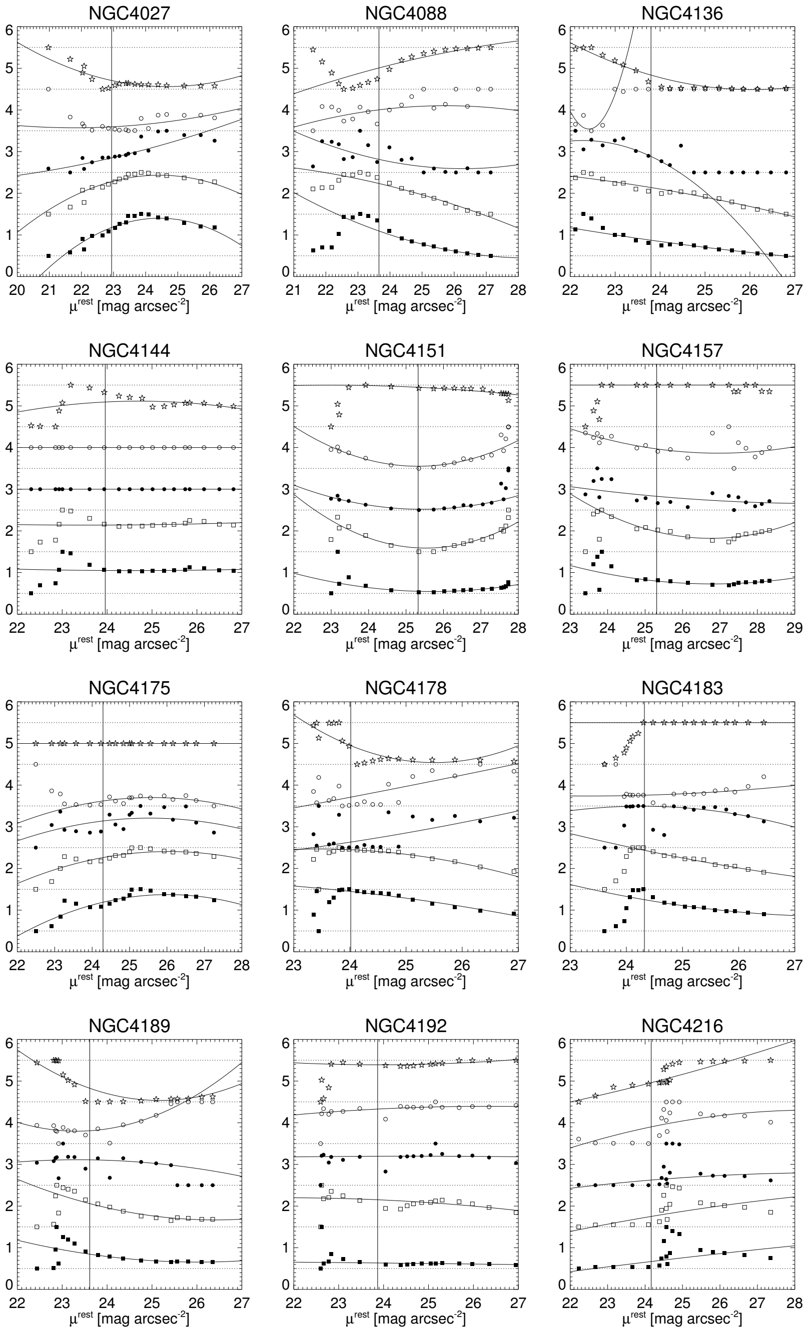

NGC4027 NGC4088 NGC4136 NGC4144 NGC4151 NGC4157 NGC4175 NGC4178 NGC4183 NGC4189 NGC4192 NGC4216

Figure C.1: Calibration for local galaxies

Resulting disc scale length (filled boxes), central disc surface brightness (open boxes), bulge scale length (filled circles), central bulge surface brightness (open circles) and inclination (open stars) as a function of limiting surface brightness (horizontal axis). The vertical axis is in arbitrary units. The adopted values are taken at the intersection of the quadratic fit (thin solid lines) with the thick vertical line.

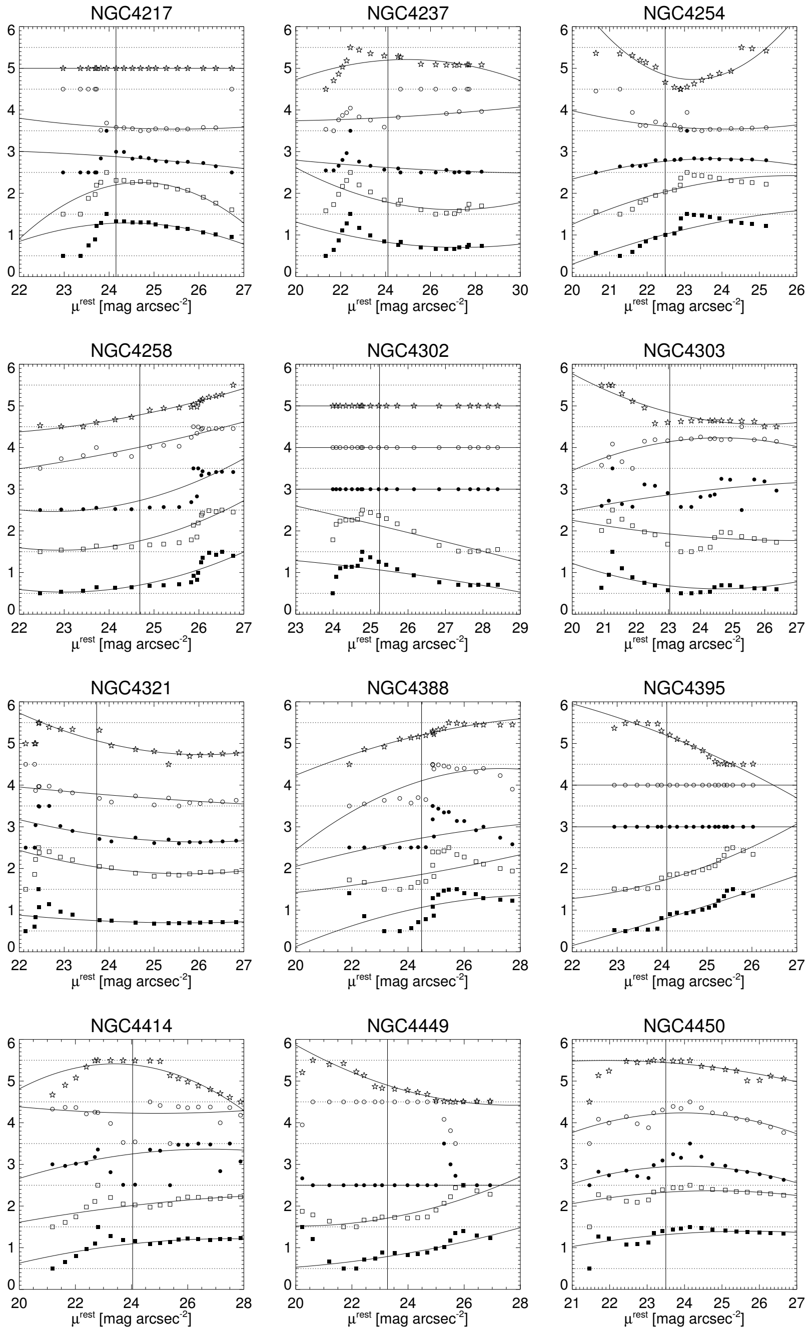

Figure C.1: Calibration for local galaxies

Resulting disc scale length (filled boxes), central disc surface brightness (open boxes), bulge scale length (filled circles), central bulge surface brightness (open circles) and inclination (open stars) as a function of limiting surface brightness (horizontal axis). The vertical axis is in arbitrary units. The adopted values are taken at the intersection of the quadratic fit (thin solid lines) with the thick vertical line.

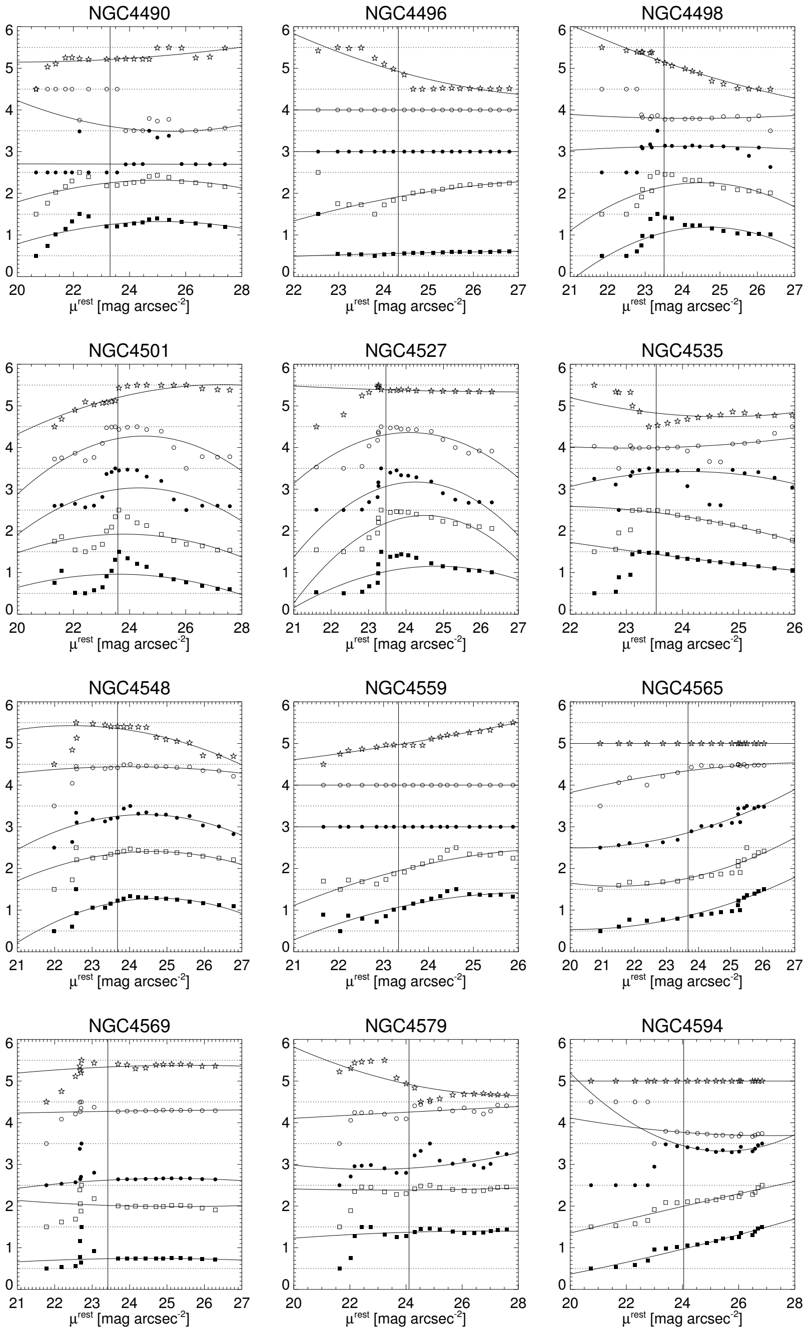

Figure C.1: Calibration for local galaxies

Resulting disc scale length (filled boxes), central disc surface brightness (open boxes), bulge scale length (filled circles), central bulge surface brightness (open circles) and inclination (open stars) as a function of limiting surface brightness (horizontal axis). The vertical axis is in arbitrary units. The adopted values are taken at the intersection of the quadratic fit (thin solid lines) with the thick vertical line.

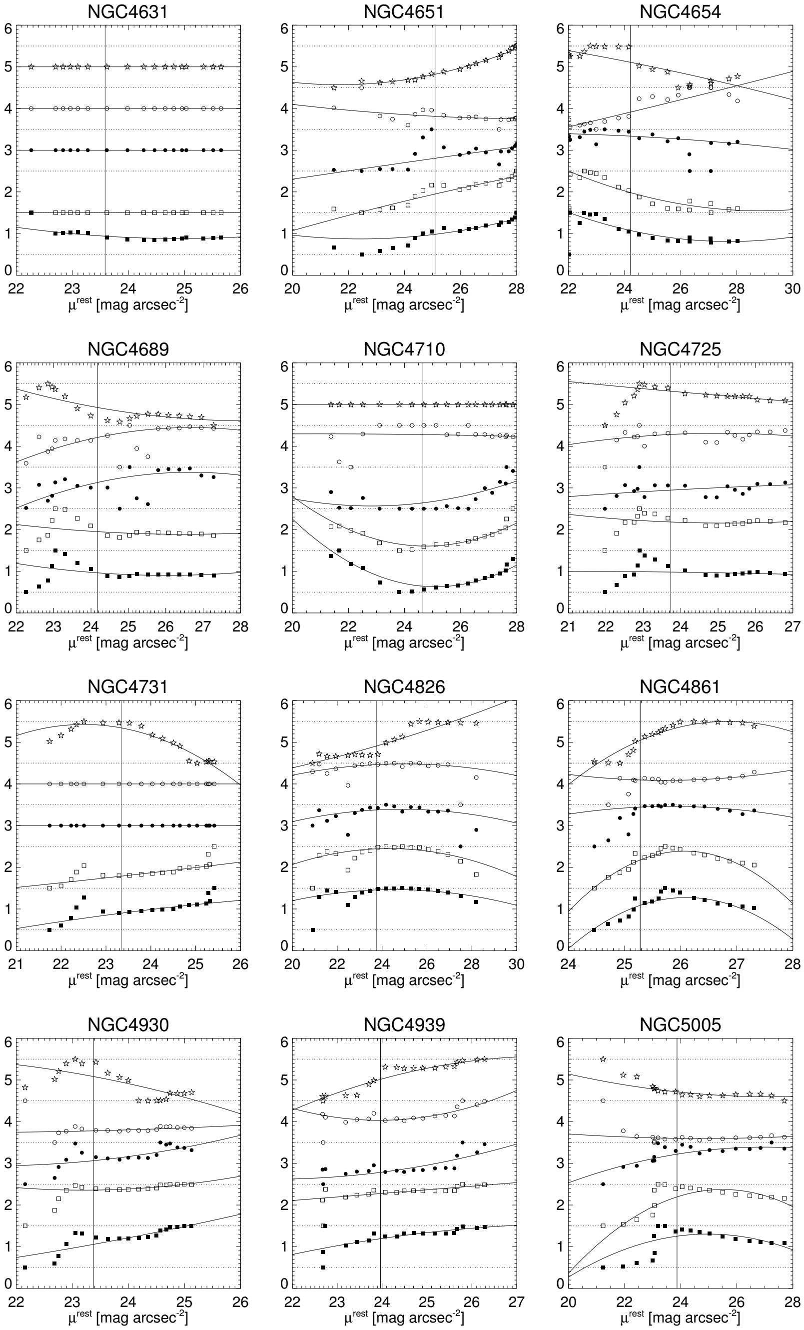

Figure C.1: Calibration for local galaxies

Resulting disc scale length (filled boxes), central disc surface brightness (open boxes), bulge scale length (filled circles), central bulge surface brightness (open circles) and inclination (open stars) as a function of limiting surface brightness (horizontal axis). The vertical axis is in arbitrary units. The adopted values are taken at the intersection of the quadratic fit (thin solid lines) with the thick vertical line.

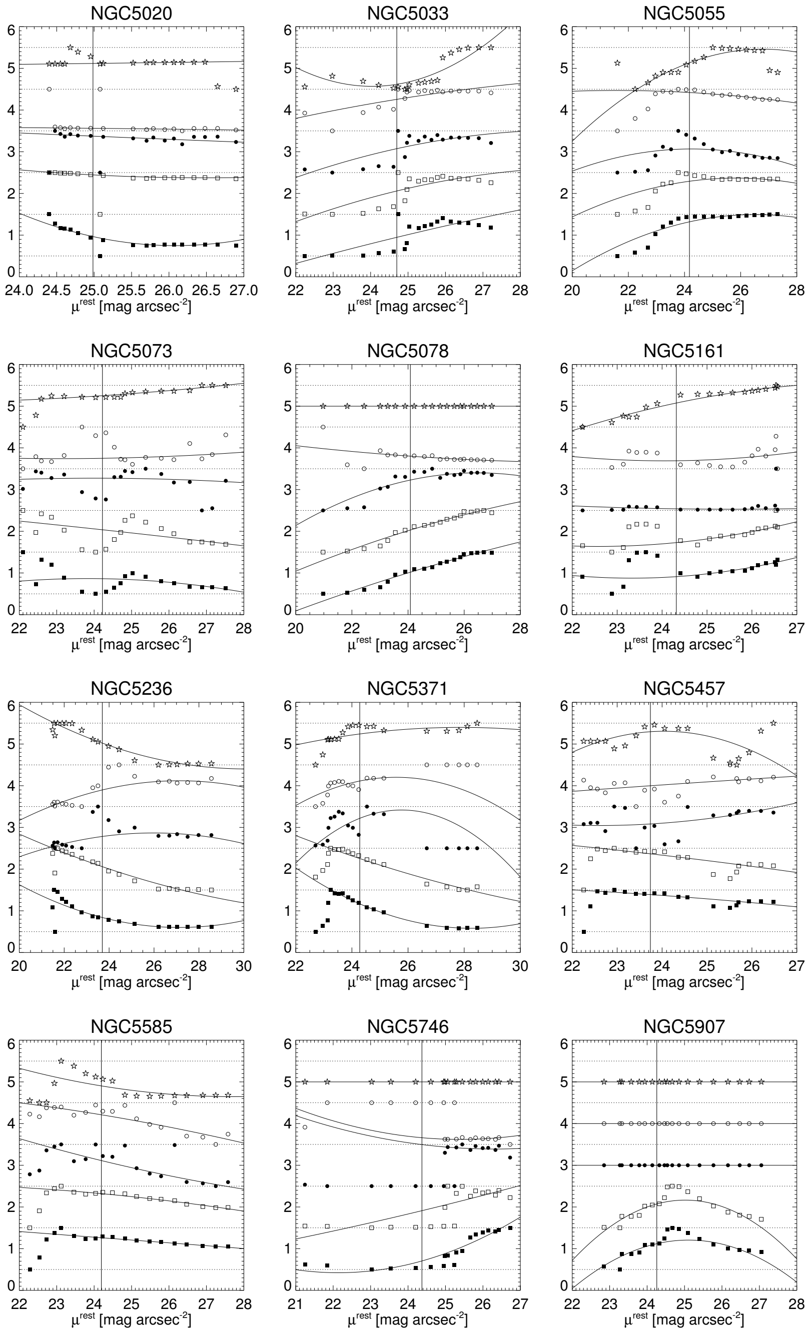

Figure C.1: Calibration for local galaxies

Resulting disc scale length (filled boxes), central disc surface brightness (open boxes), bulge scale length (filled circles), central bulge surface brightness (open circles) and inclination (open stars) as a function of limiting surface brightness (horizontal axis). The vertical axis is in arbitrary units. The adopted values are taken at the intersection of the quadratic fit (thin solid lines) with the thick vertical line.

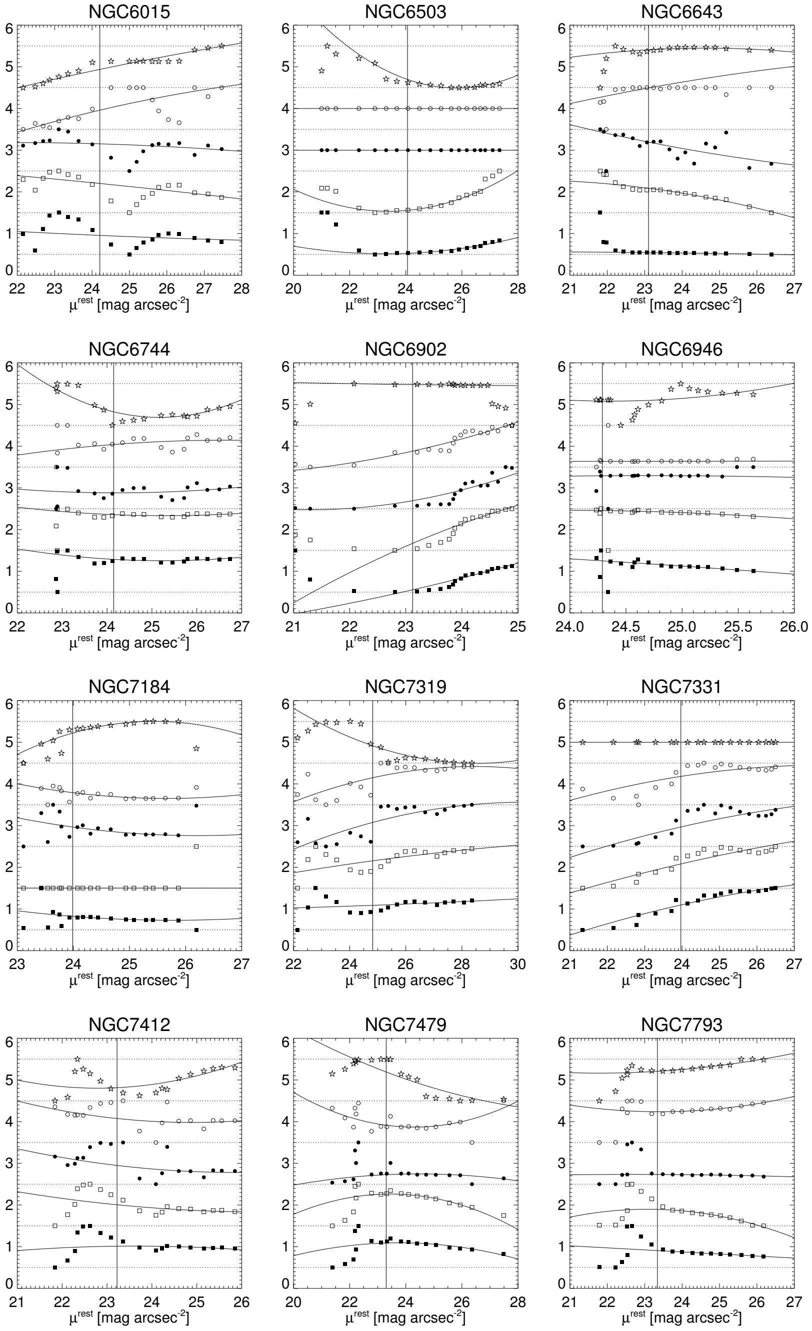

Figure C.1: Calibration for local galaxies

Resulting disc scale length (filled boxes), central disc surface brightness (open boxes), bulge scale length (filled circles), central bulge surface brightness (open circles) and inclination (open stars) as a function of limiting surface brightness (horizontal axis). The vertical axis is in arbitrary units. The adopted values are taken at the intersection of the quadratic fit (thin solid lines) with the thick vertical line.

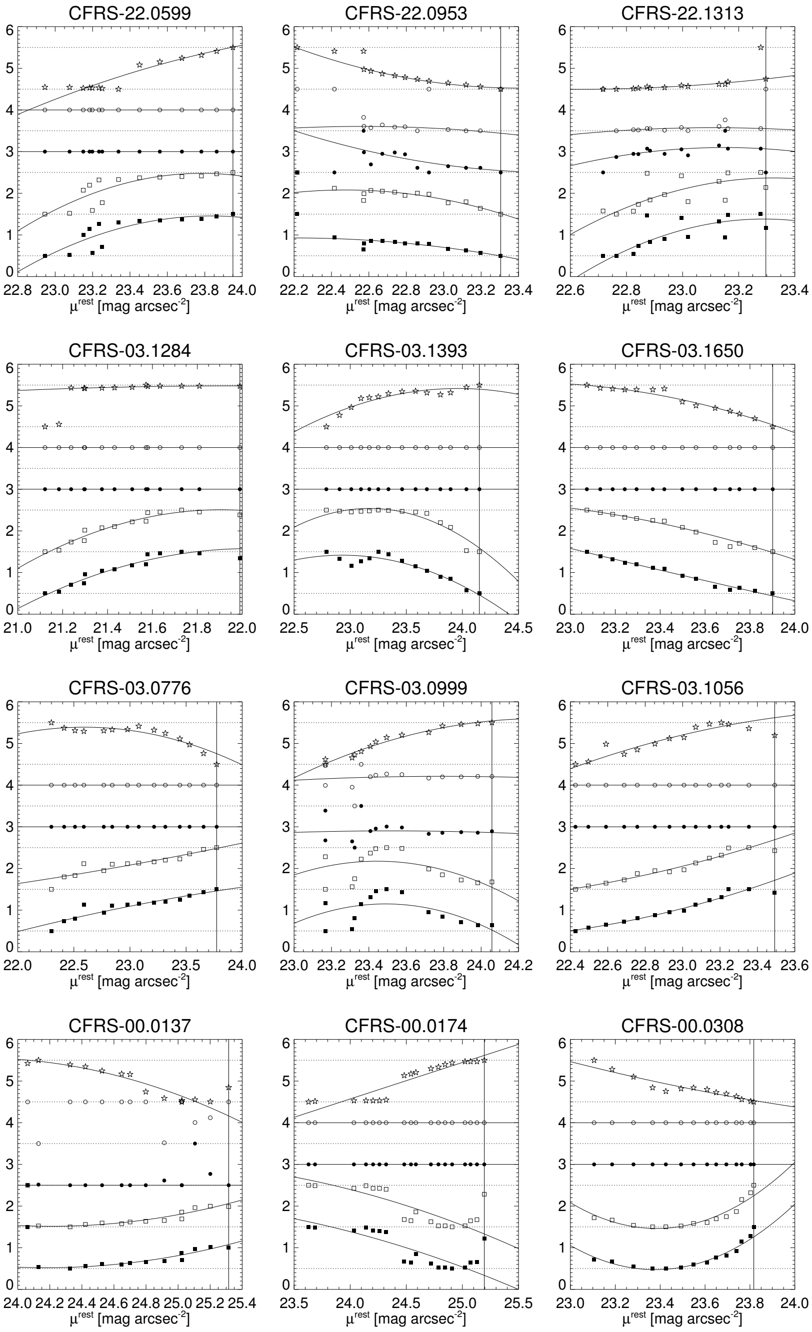
CFRS-22.0599
CFRS-22.0953
CFRS-22.1313
CFRS-03.1284
CFRS-03.1393
CFRS-03.1650
CFRS-03.0776
CFRS-03.0999
CFRS-03.1056
CFRS-00.0137
CFRS-00.0174
CFRS-00.0308

Figure C.2: Calibration for distant galaxies

Resulting disc scale length (filled boxes), central disc surface brightness (open boxes), bulge scale length (filled circles), central bulge surface brightness (open circles) and inclination (open stars) as a function of limiting surface brightness (horizontal axis). The vertical axis is in arbitrary units. The adopted values are taken at the intersection of the quadratic fit (thin solid lines) with the thick vertical line.

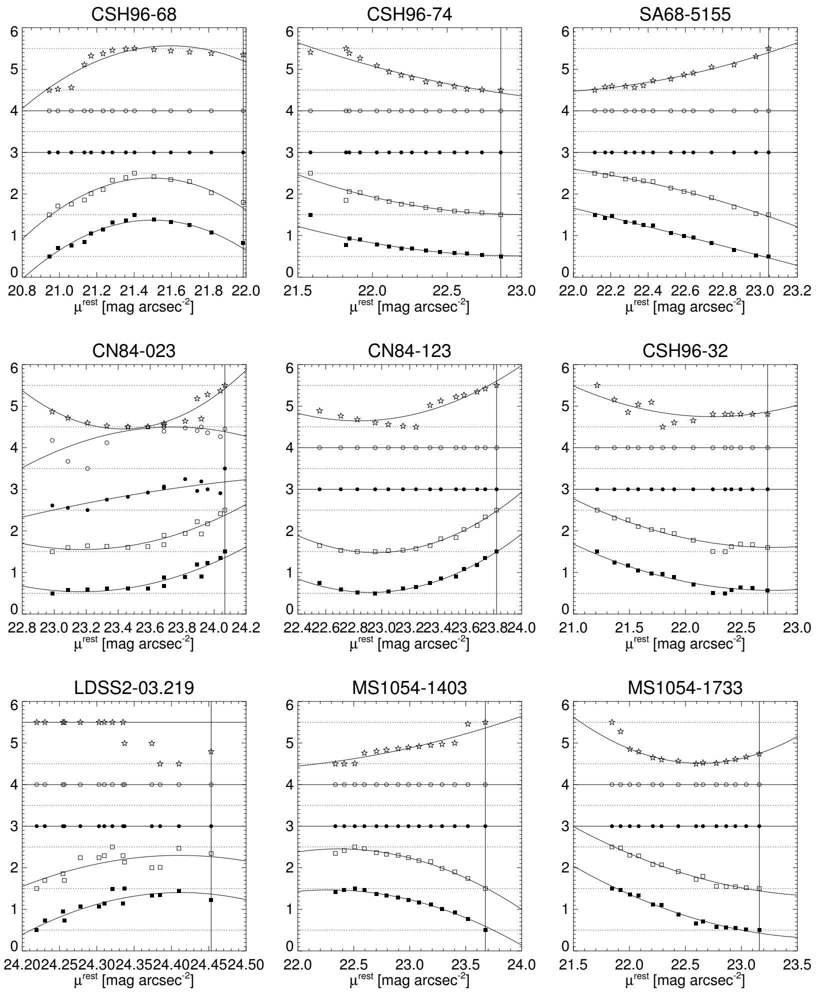

Figure C.2: Calibration for distant galaxies

Resulting disc scale length (filled boxes), central disc surface brightness (open boxes), bulge scale length (filled circles), central bulge surface brightness (open circles) and inclination (open stars) as a function of limiting surface brightness (horizontal axis). The vertical axis is in arbitrary units. The adopted values are taken at the intersection of the quadratic fit (thin solid lines) with the thick vertical line.

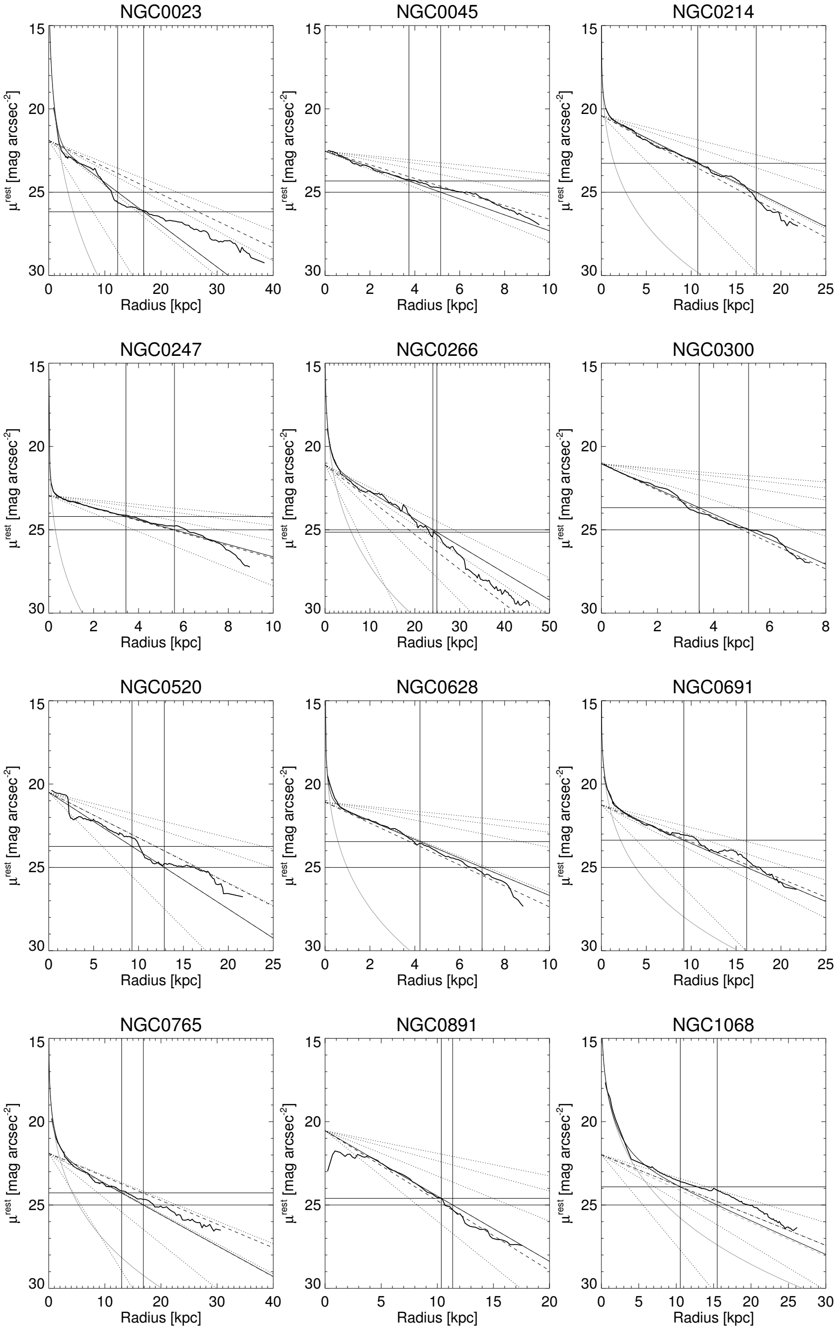

Figure C.3: Light profiles of nearby galaxies

Light profiles (thick solid line) of the local galaxies. An exponential (grey dashed line) and a de Vaucouleurs (grey solid line) model was fitted out to a characteristic radius R_{lim} (thick vertical and horizontal lines). The combined model defines R_{25} (thin horizontal and vertical lines). Using the total profile one would measure a disc scale length as indicated by the black dashed line. The thin dotted lines indicate disc scale lengths of 2, 4, 6, 8 kpc.

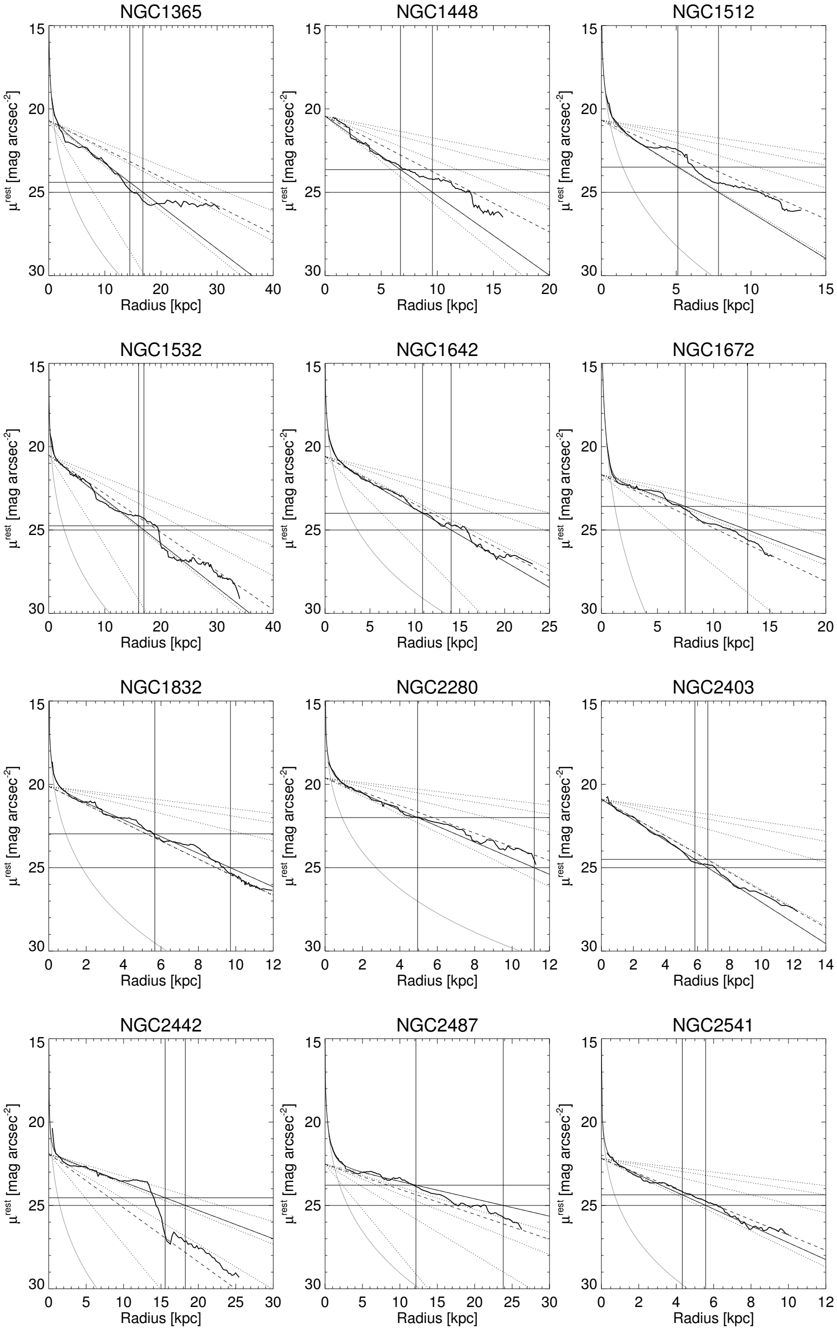

Figure C.3: Light profiles of nearby galaxies

Light profiles (thick solid line) of the local galaxies. An exponential (grey dashed line) and a de Vaucouleurs (grey solid line) model was fitted out to a characteristic radius R_{lim} (thick vertical and horizontal lines). The combined model defines R_{25} (thin horizontal and vertical lines). Using the total profile one would measure a disc scale length as indicated by the black dashed line. The thin dotted lines indicate disc scale lengths of 2, 4, 6, 8 kpc.

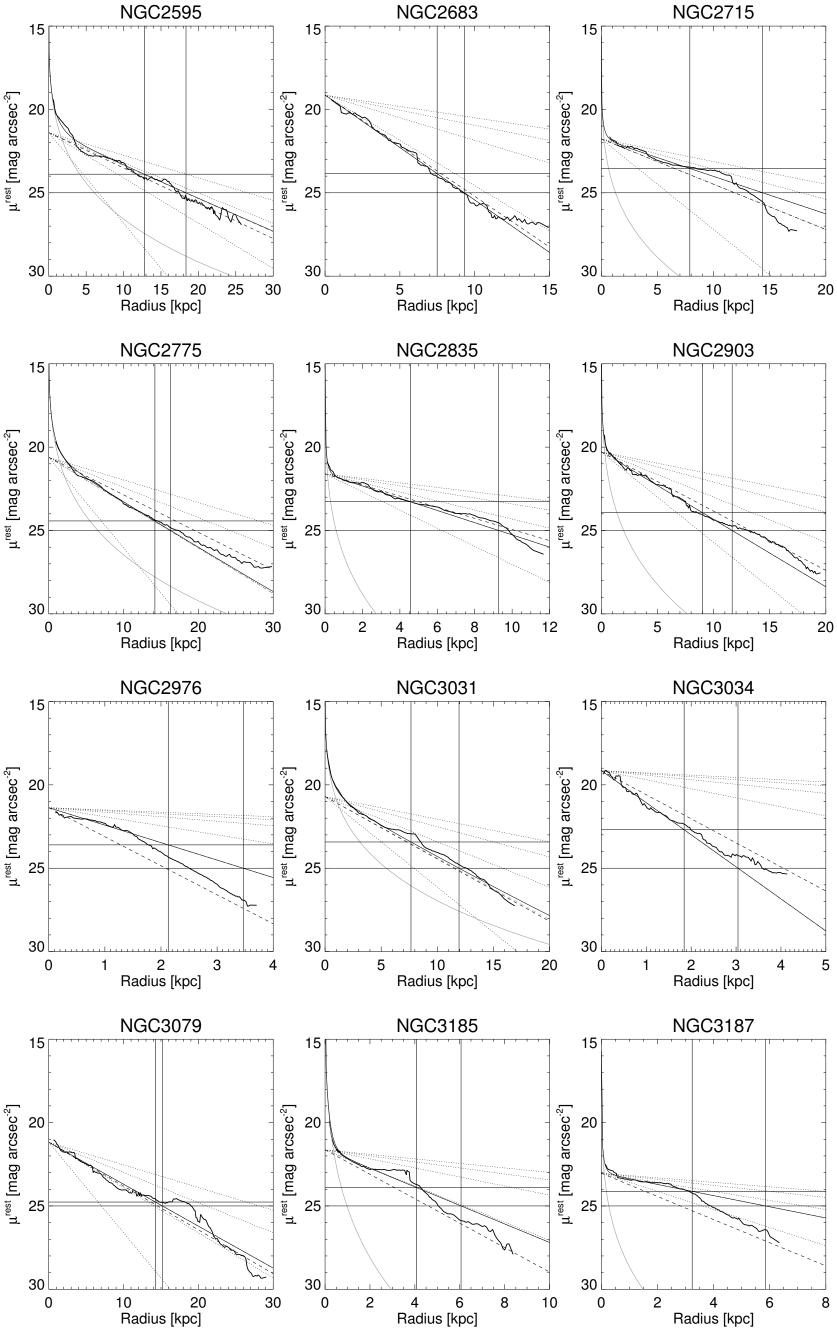

Figure C.3: Light profiles of nearby galaxies

Light profiles (thick solid line) of the local galaxies. An exponential (grey dashed line) and a de Vaucouleurs (grey solid line) model was fitted out to a characteristic radius R_{lim} (thick vertical and horizontal lines). The combined model defines R_{25} (thin horizontal and vertical lines). Using the total profile one would measure a disc scale length as indicated by the black dashed line. The thin dotted lines indicate disc scale lengths of 2, 4, 6, 8 kpc.

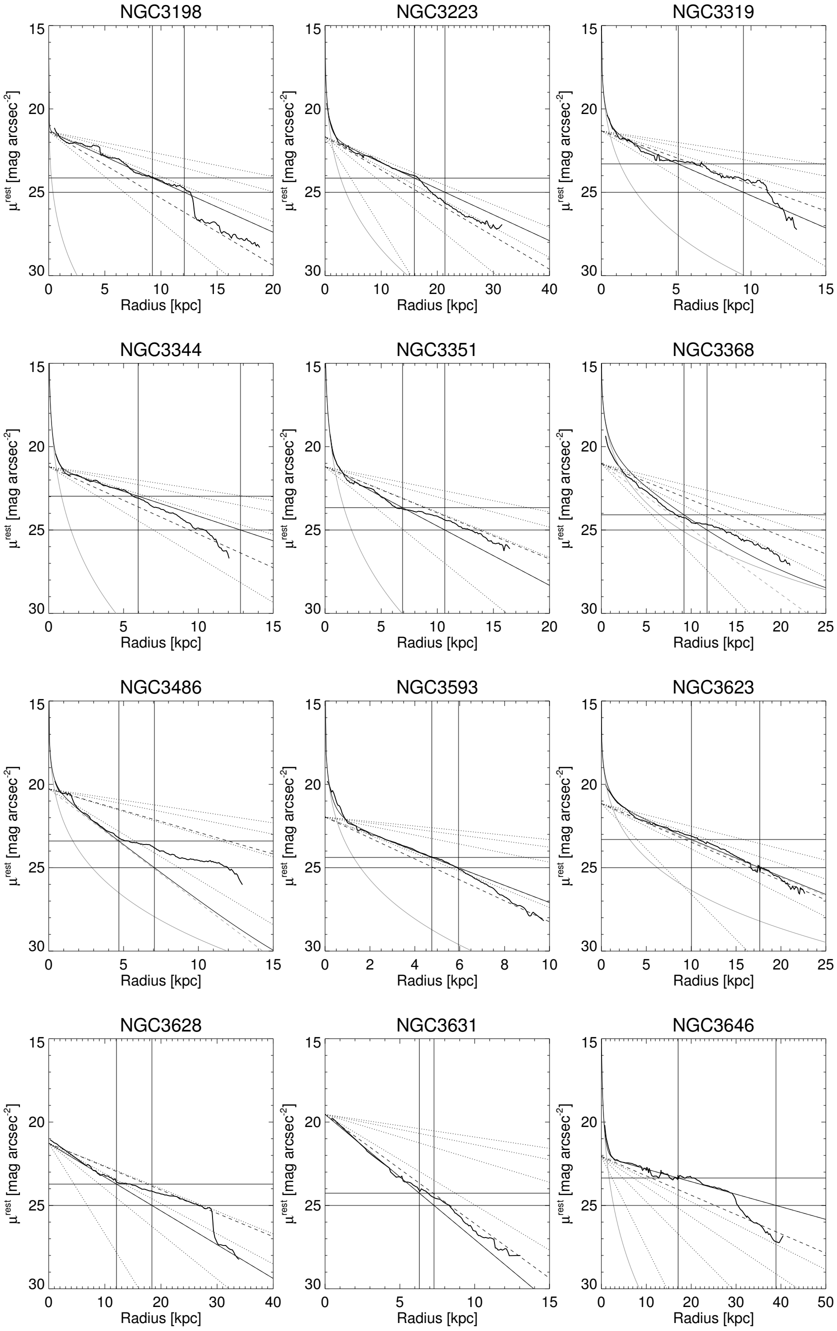
NGC3198 NGC3223 NGC3319 NGC3344 NGC3351 NGC3368 NGC3486 NGC3593 NGC3623 NGC3628 NGC3631 NGC3646

Figure C.3: Light profiles of nearby galaxies

Light profiles (thick solid line) of the local galaxies. An exponential (grey dashed line) and a de Vaucouleurs (grey solid line) model was fitted out to a characteristic radius R_{lim} (thick vertical and horizontal lines). The combined model defines R_{25} (thin horizontal and vertical lines). Using the total profile one would measure a disc scale length as indicated by the black dashed line. The thin dotted lines indicate disc scale lengths of 2, 4, 6, 8 kpc.

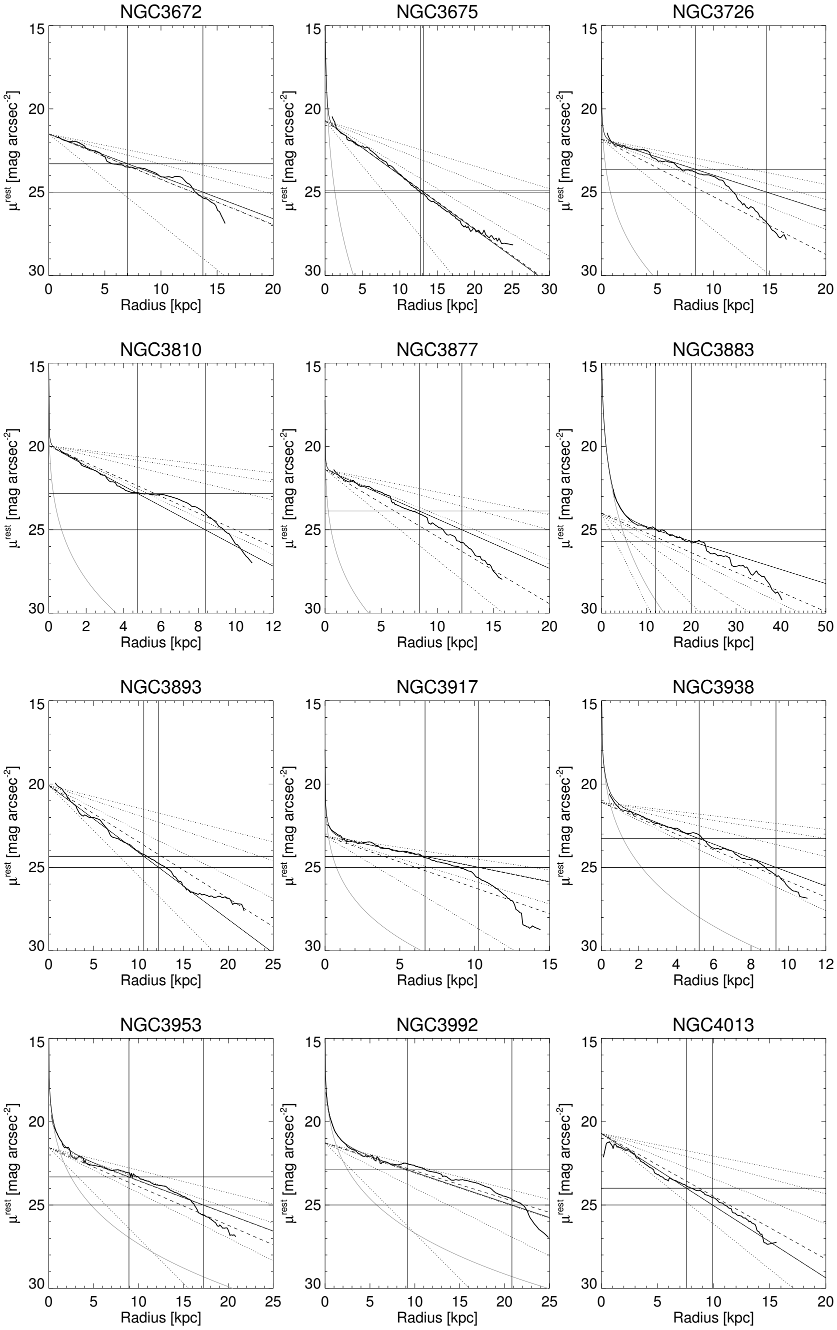

Figure C.3: Light profiles of nearby galaxies

Light profiles (thick solid line) of the local galaxies. An exponential (grey dashed line) and a de Vaucouleurs (grey solid line) model was fitted out to a characteristic radius R_{lim} (thick vertical and horizontal lines). The combined model defines R_{25} (thin horizontal and vertical lines). Using the total profile one would measure a disc scale length as indicated by the black dashed line. The thin dotted lines indicate disc scale lengths of 2, 4, 6, 8 kpc.

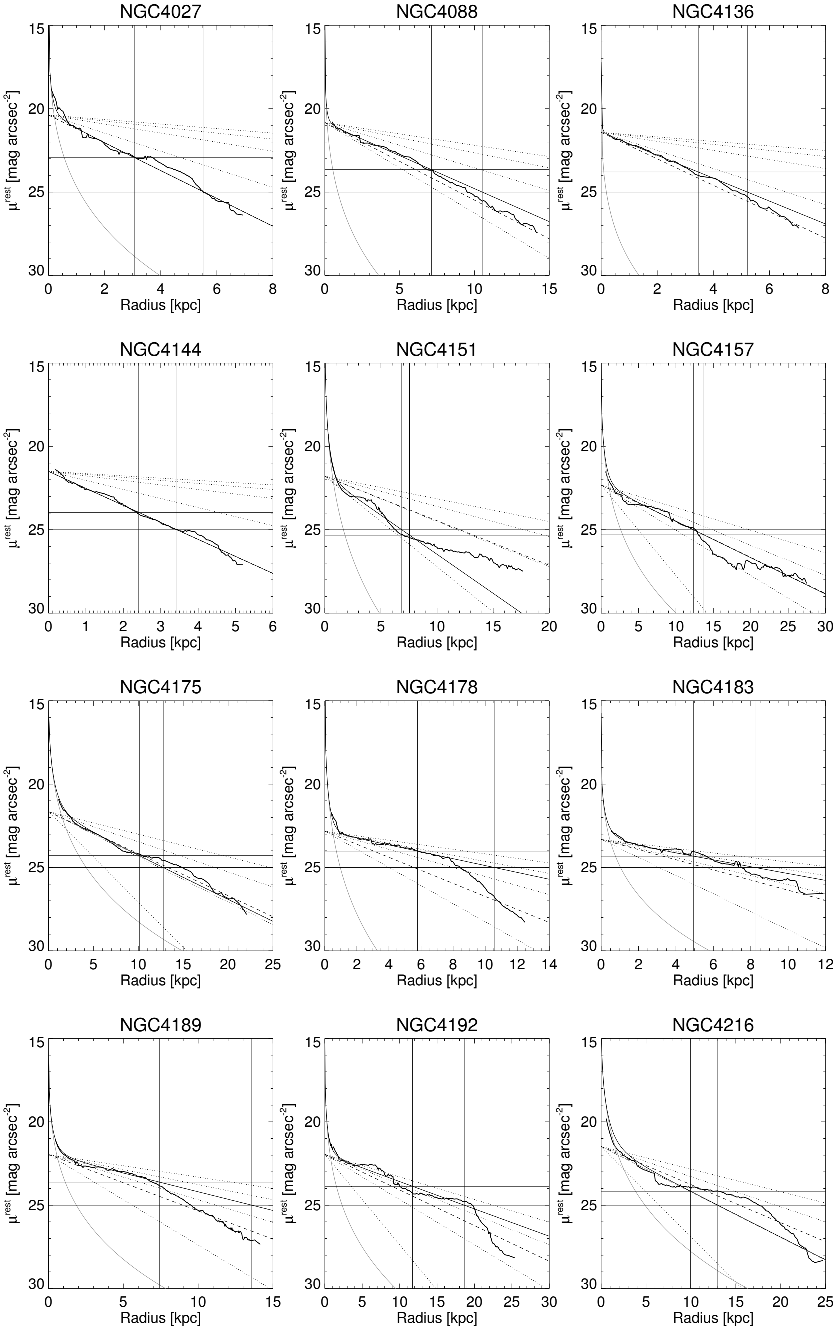

Figure C.3: Light profiles of nearby galaxies

Light profiles (thick solid line) of the local galaxies. An exponential (grey dashed line) and a de Vaucouleurs (grey solid line) model was fitted out to a characteristic radius R_{lim} (thick vertical and horizontal lines). The combined model defines R_{25} (thin horizontal and vertical lines). Using the total profile one would measure a disc scale length as indicated by the black dashed line. The thin dotted lines indicate disc scale lengths of 2, 4, 6, 8 kpc.

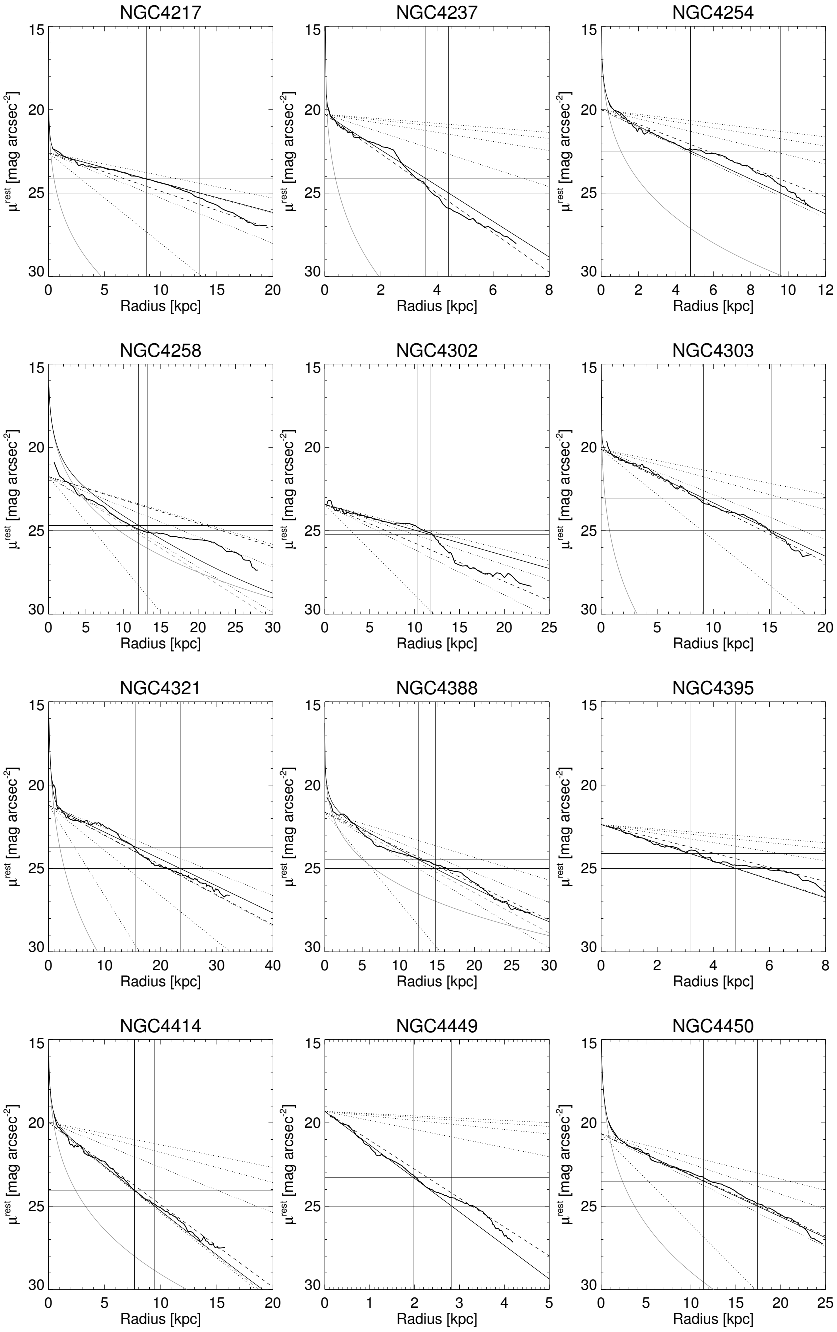

NGC4217 NGC4237 NGC4254 NGC4258 NGC4302 NGC4303 NGC4321 NGC4388 NGC4395 NGC4414 NGC4449 NGC4450

Figure C.3: Light profiles of nearby galaxies

Light profiles (thick solid line) of the local galaxies. An exponential (grey dashed line) and a de Vaucouleurs (grey solid line) model was fitted out to a characteristic radius R_{lim} (thick vertical and horizontal lines). The combined model defines R_{25} (thin horizontal and vertical lines). Using the total profile one would measure a disc scale length as indicated by the black dashed line. The thin dotted lines indicate disc scale lengths of 2, 4, 6, 8 kpc.

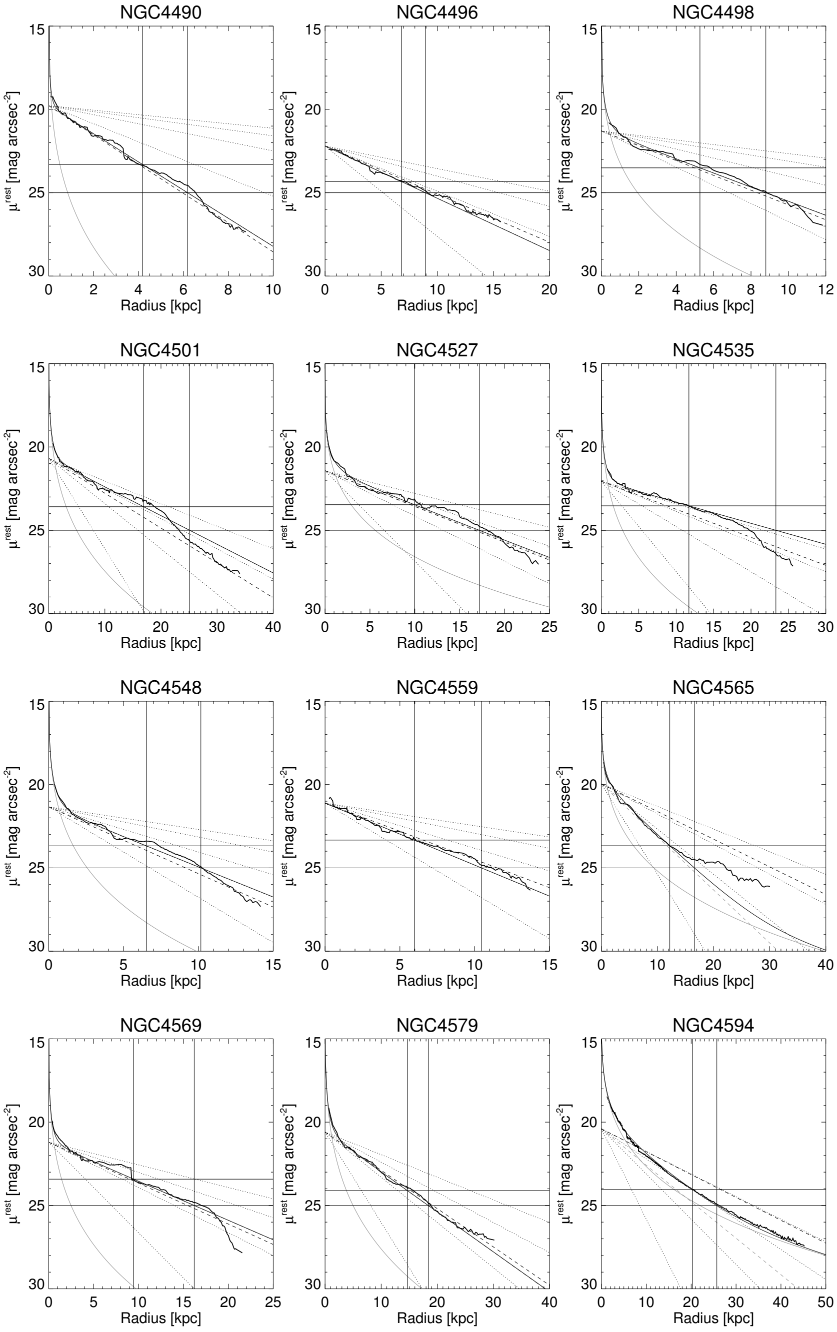

Figure C.3: Light profiles of nearby galaxies

Light profiles (thick solid line) of the local galaxies. An exponential (grey dashed line) and a de Vaucouleurs (grey solid line) model was fitted out to a characteristic radius R_{lim} (thick vertical and horizontal lines). The combined model defines R_{25} (thin horizontal and vertical lines). Using the total profile one would measure a disc scale length as indicated by the black dashed line. The thin dotted lines indicate disc scale lengths of 2, 4, 6, 8 kpc.

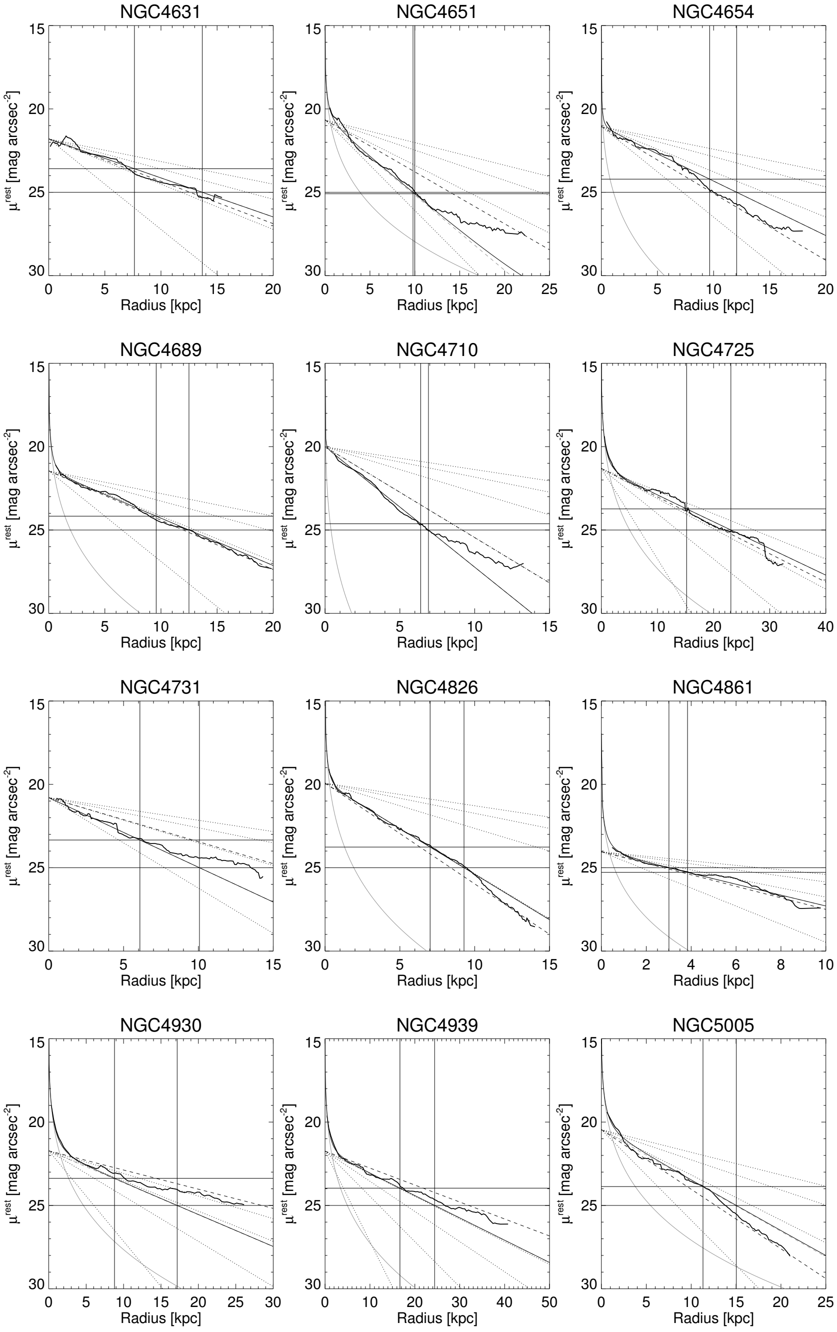

Figure C.3: Light profiles of nearby galaxies

Light profiles (thick solid line) of the local galaxies. An exponential (grey dashed line) and a de Vaucouleurs (grey solid line) model was fitted out to a characteristic radius R_{lim} (thick vertical and horizontal lines). The combined model defines R_{25} (thin horizontal and vertical lines). Using the total profile one would measure a disc scale length as indicated by the black dashed line. The thin dotted lines indicate disc scale lengths of 2, 4, 6, 8 kpc.

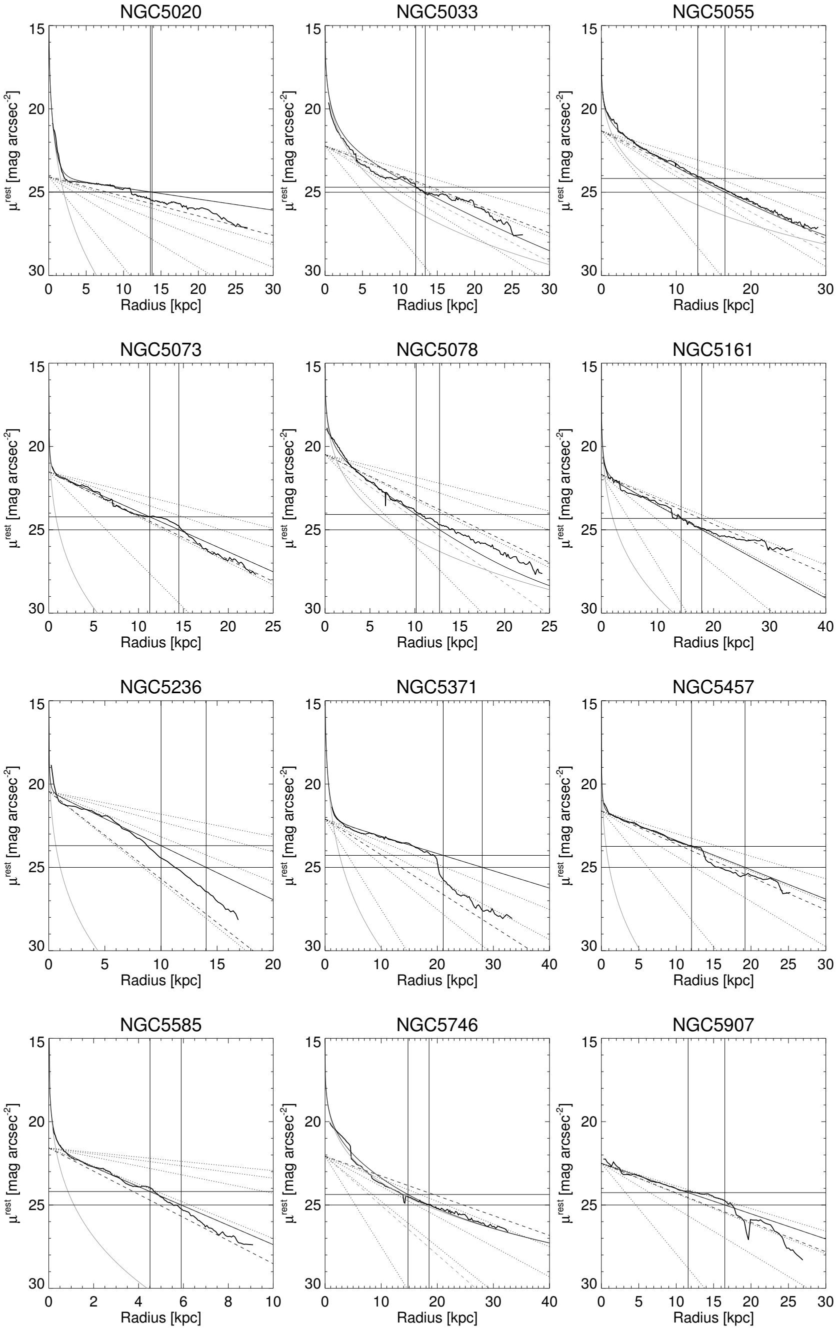

Figure C.3: Light profiles of nearby galaxies

Light profiles (thick solid line) of the local galaxies. An exponential (grey dashed line) and a de Vaucouleurs (grey solid line) model was fitted out to a characteristic radius R_{lim} (thick vertical and horizontal lines). The combined model defines R_{25} (thin horizontal and vertical lines). Using the total profile one would measure a disc scale length as indicated by the black dashed line. The thin dotted lines indicate disc scale lengths of 2, 4, 6, 8 kpc.

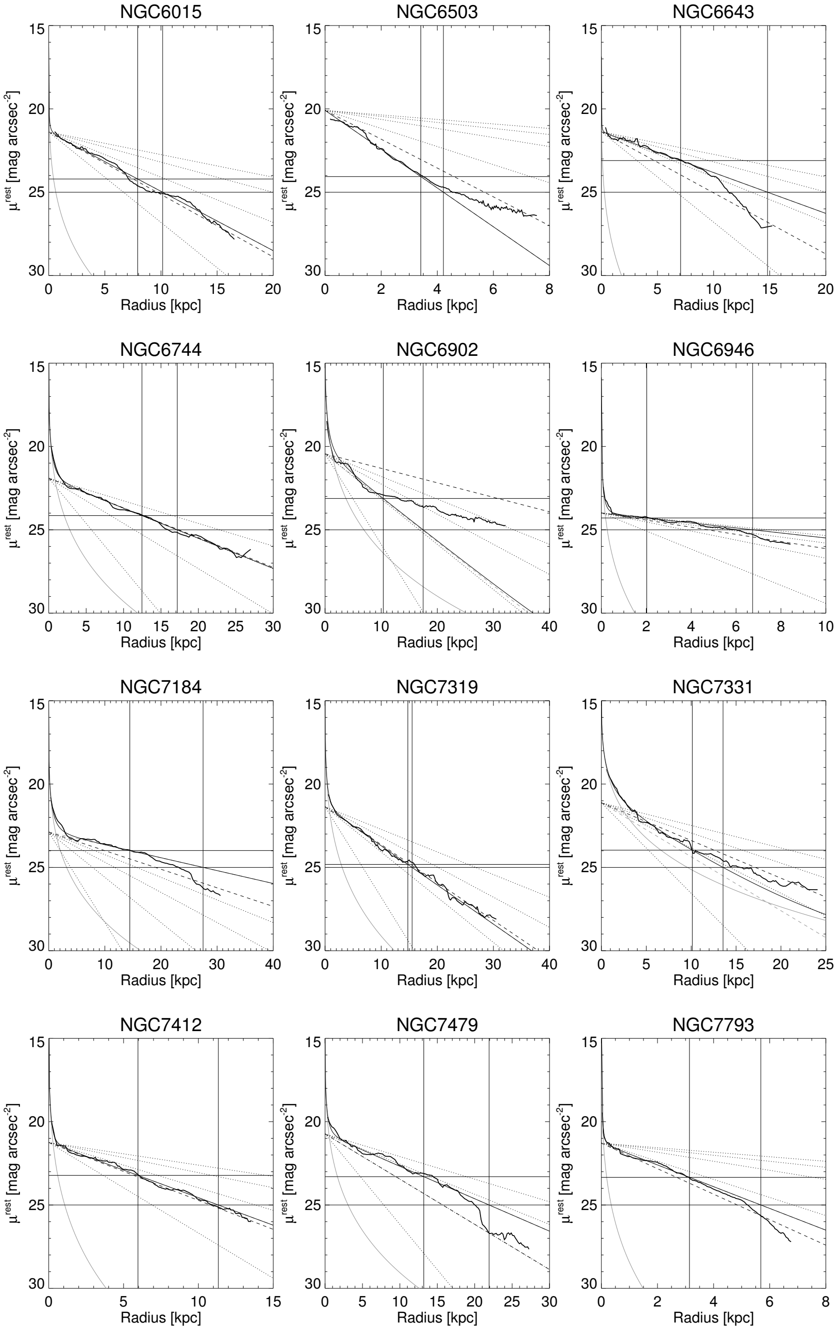

Figure C.3: Light profiles of nearby galaxies

Light profiles (thick solid line) of the local galaxies. An exponential (grey dashed line) and a de Vaucouleurs (grey solid line) model was fitted out to a characteristic radius R_{lim} (thick vertical and horizontal lines). The combined model defines R_{25} (thin horizontal and vertical lines). Using the total profile one would measure a disc scale length as indicated by the black dashed line. The thin dotted lines indicate disc scale lengths of 2, 4, 6, 8 kpc.

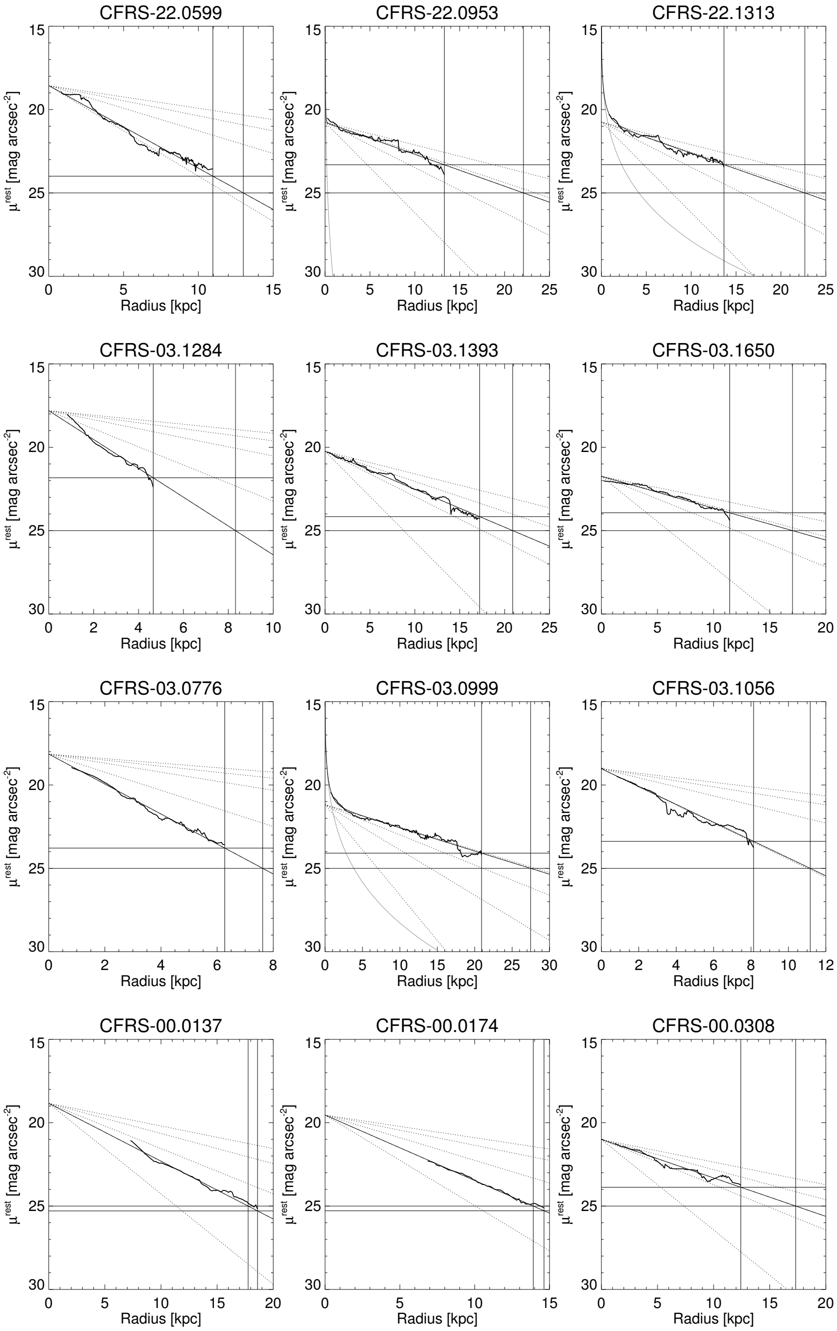

Figure C.4: Light profiles of distant galaxies

Light profiles (thick solid line) of the high redshift galaxies. An exponential (grey dashed line) and a de Vaucouleurs (grey solid line) model was fitted out to a characteristic radius R_{lim} (thick vertical and horizontal lines). The combined model defines R_{25} (thin horizontal and vertical lines).

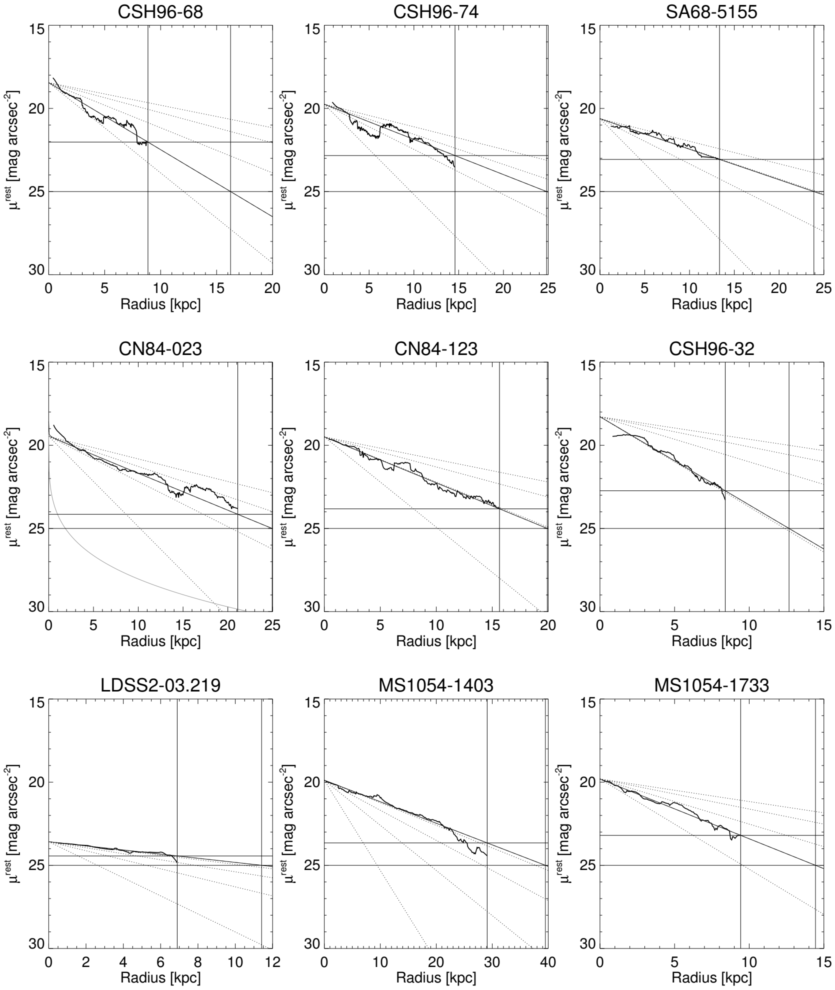

Figure C.4: Light profiles of distant galaxies

Light profiles (thick solid line) of the high redshift galaxies. An exponential (grey dashed line) and a de Vaucouleurs (grey solid line) model was fitted out to a characteristic radius R_{lim} (thick vertical and horizontal lines). The combined model defines R_{25} (thin horizontal and vertical lines).

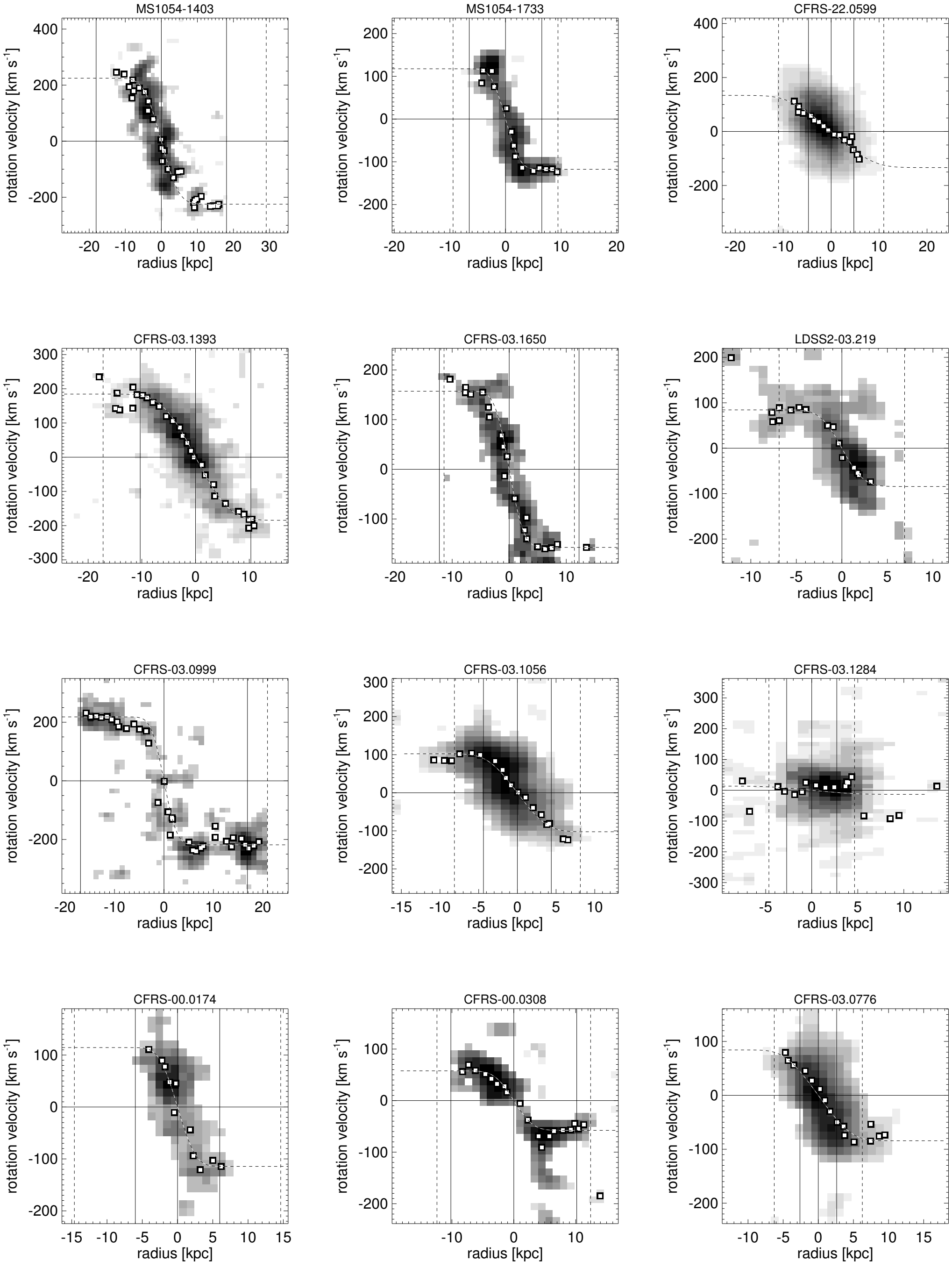

Figure C.5: Rotation curves of the high redshift galaxies

Rotation curves of the high redshift galaxies (grey scale). Vertical solid lines indicate $R_{2.2}$; vertical dashed lines show R_{lim}. Boxes represent the adopted rotation curves; the dashed line is our model fit from which we obtain the rotation velocity.

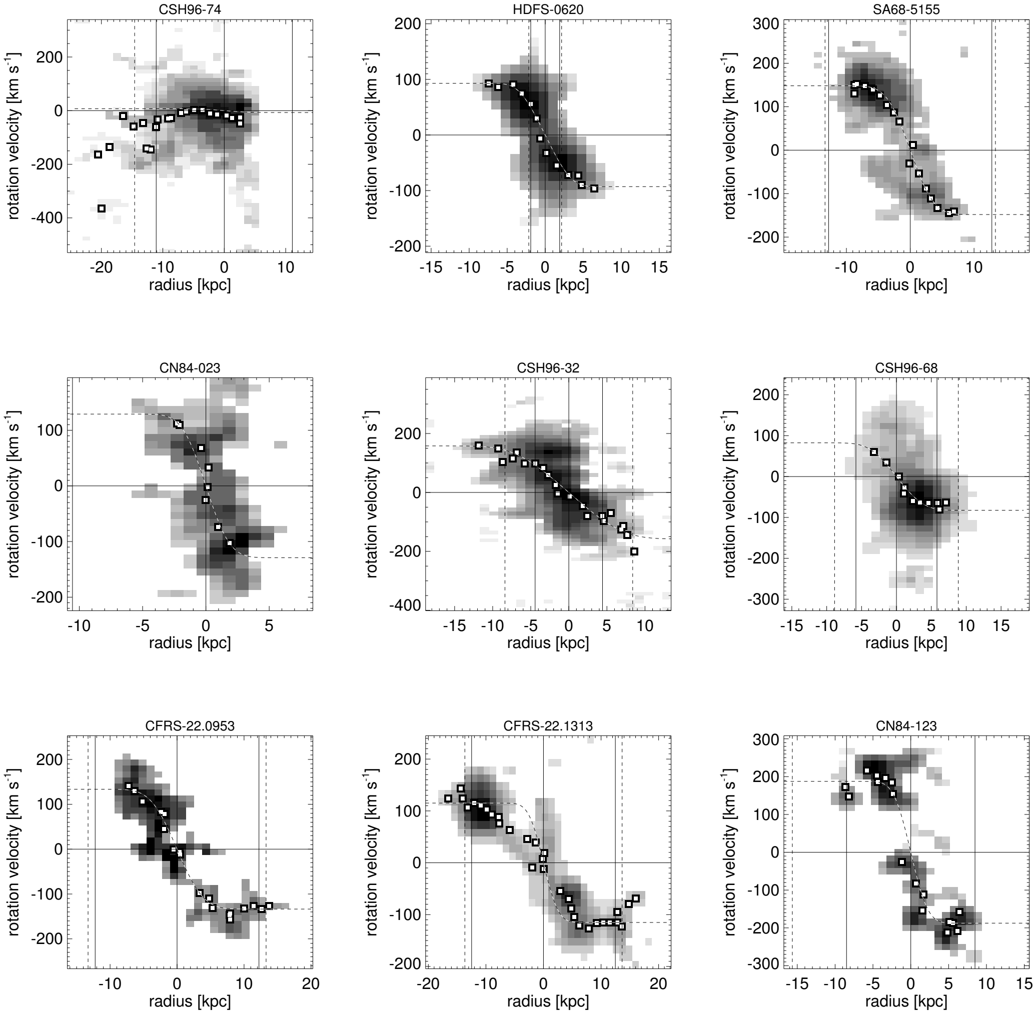

Figure C.5: Light profiles of distant galaxies

Rotationcurves of the high redshift galaxies (grey scale). Vertical solid lines indicate $R_{2.2}$; vertical dashed lines show R_{lim} . Boxes represent the adopted rotation curves; the dashed line is our model fit from which we obtain the rotation velocity.

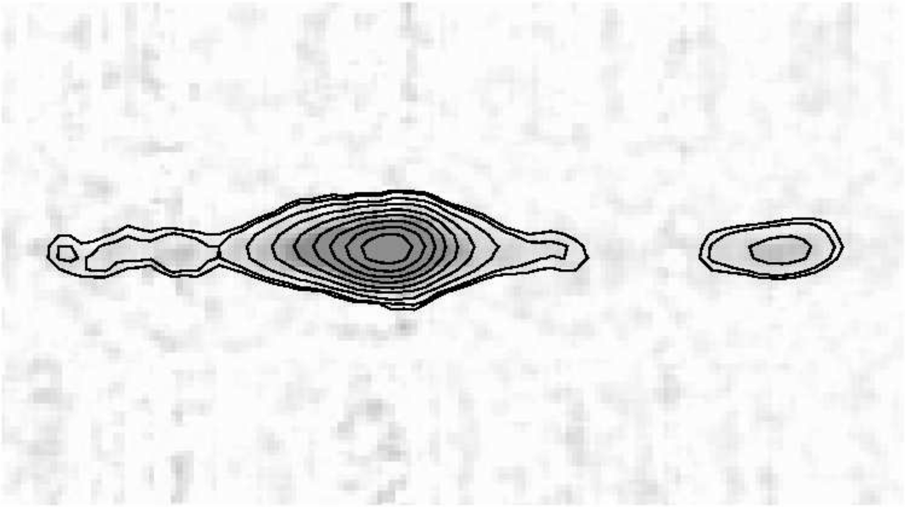

Figure C.6: Spectrum of CFRS-00.0137

The spectrum of CFRS-00.0137, the only galaxy with no spatial structure. The dispersion axis is horizontal; the spatial axis is vertical. The strong peak corresponds to Hα, the weaker peak to the right was identified as [NII].